Modelling of radiative transfer in light sources

Modelling of Radiative Transfer in Light Sources

PROEFSCHRIFT

ter verkrijging van de graad van doctor aan de
Technische Universiteit Eindhoven, op gezag van de
Rector Magnificus, prof.dr. R.A. van Santen, voor een
commissie aangewezen door het College voor
Promoties in het openbaar te verdedigen
op maandag 13 januari 2003 om 16.00 uur

door

Henricus Wilhelm Peter van der Heijden

geboren te Helmond

Dit proefschrift is goedgekeurd door de promotoren:

prof.dr.ir. D.C. Schram

en

prof.dr.ir. G.M.W. Kroesen

Copromotor:

dr. J.J.A.M. van der Mullen

This research is sponsored by the Dutch Technology Foundation STW as project ETN.3892 and by Philips Lighting Eindhoven, The Netherlands

CIP-DATA LIBRARY TECHNISCHE UNIVERSITEIT EINDHOVEN

Heijden, Henricus Wilhelm Peter van der

Modelling of Radiative Transfer in Light Sources / by Henricus Wilhelm Peter van der Heijden. - Eindhoven : Technische Universiteit Eindhoven, 2003. - Proefschrift.
ISBN 90-386-1595-7
NUR 924
Trefwoorden : plasma simulatie / stralingstransport / molecuulstraling / lichtbronnen
Subject headings : plasma simulation / radiative transfer / molecular radiation / software design / discharge lamps / sulfur lamp

Printed by: Universiteitsdrukkerij Technische Universiteit Eindhoven
Cover image: visualisation of part of the Franck-Condon table for the S_2 B-X radiative transition that is responsible for the sulfur lamp's bright sun-like spectrum

Contents

Chapter 1

General introduction

To man, that was in th'evening made,
Stars gave the first delight;
Admiring, in the gloomy shade,
Those little drops of light.

(Edmund Waller, 1664)

Nature's light sources, the stars, may appear to be "little drops of light", but they are in reality rather large yet dense concentrations of matter in the plasma state. The plasma state is often called the fourth state of matter and is characterised by the presence of charged particles and electromagnetic fields. A more detailed inspection of the cosmos reveals that the space between the stars is also enriched with various kinds of plasmas which are generally termed nebulae. Unlike stars these nebulae are characterised by extremely low densities. In fact, the cosmos shows that the fourth state of matter offers a rich variety and that consequently the classification of the plasma state is not at all an easy task.

Not only nature provides a rich variety of plasmas; a similar richness is found in man-made laboratory or technological plasmas. Changing operational settings such as the chemical composition, size, power, field-structure, current waveform, or operational pressure will create different types of plasmas. The huge parameter space of operational conditions has the consequence that the number of high-tech plasma applications in lighting, material sciences, and environmental technology is continually increasing. Another consequence of the size of the parameter space is that theory formation is difficult and lagging behind. As a result, the work on and with new plasma applications mostly follows the laborious way of trial and error. This inefficient procedure can, at least partly, be avoided if the task of plasma classification can be guided by a computational plasma model development system that is flexible enough to cover a significant part of the parameter space.

This thesis will focus on model descriptions of a small but significant slice of the full spectrum of artificial plasma sources. As the title, *Modelling of Radiative Transfer in Light Sources*, reflects, the main interest is in light sources or radiative plasmas, although an excursion into particle sources or reactive plasmas is also provided. Of all the processes in these plasmas, radiation generation and transport will receive the most attention, even though another excursion delves into the theory of density calculations in complicated mixtures.

1.1 Radiative transfer and plasma modelling

The field of modern radiative transfer can be said to have its origin in Holstein and Biberman's simultaneously published papers (Holstein, 1947; Biberman, 1947). The Holstein-Biberman equations are still in use, although naturally over the years refinements (Biberman, 1949; Holstein, 1951; Payne and Cook, 1970; van Trigt, 1976a), have been developed that remove some of the limiting assumptions in the original works. Some of these refinements are numerical, for example based on Monte Carlo techniques (Klots and Anderson, 1972) or analytical treatments (Payne *et al.*, 1974; van Trigt, 1976b), or a combination of analytical and numerical approaches (Goedheer, 1978).

Meanwhile, the descriptions of reactive plasmas usually consist of two main building blocks; one for the fluid-like effects (Patankar, 1980; Beulens *et al.*, 1991; vanden Abeele, 2000) and another for the description of the (local) chemistry. The fluid part consists of the balance equations for particles, momentum, and energy. In order to solve these, transport coefficients (Johnston, 2003) and source terms are needed which are strongly dependent on the composition of the plasma. This is described by the chemistry block, which consists of a set of reaction equations with corresponding rate coefficients.

In the case of radiative plasmas the models for radiative transfer and reactive plasmas have to be merged. Since apart from optically thick also optically intermediate and thin radiation have to be taken into account, the radiation transport problem cannot be treated in the framework of the fluid module. Therefore, beside the fluid and chemistry components found in models for reactive plasmas, models for plasma light sources contain an additional component for radiation.

This thesis deals with design aspects of, and computational studies performed using, the versatile PLASIMO plasma modelling package (van der Mullen *et al.*, 2002). Originally PLASIMO stands for PLAsma SImulation MOdel, but in recent years PLASIMO has become a model development package, capable of creating models for many different types of plasmas, rather than a single plasma code in the traditional meaning. However, in most cases the previous studies in which PLASIMO was used were devoted to laboratory plasmas which can be seen as reactive plasmas of simple chemical composition. The extension made in this work can be typified as an enhanced capability for handling chemical complexity and the addition of general transport of radiation.

Over the years, many people have worked on the PLASIMO code initiated and since supervised by van der Mullen (van der Mullen *et al.*, 2002). Further principal developments have been contributed by Benoy (Benoy *et al.*, 1991; Benoy, 1993), Janssen (Janssen *et al.*, 1999; Janssen, 2000), van Dijk (van Dijk *et al.*, 2001; van Dijk, 2001; van Dijk *et al.*, 2002), who all have written a Ph.D. thesis that is at least in part about their work on PLASIMO. After initial modelling work by Beulens *et al.* (1991), Benoy (1993) wrote the first version of PLASIMO and used it to model inductively coupled spectrochemical argon plasmas. Expanding plasmas, such as cascaded arcs (which this thesis is partly concerned with as well), both in and out of thermal equilibrium were studied by Janssen (2000). A major rewrite of the code base, making the transition from the programming language C to the more modern C++, was initiated by and described in the thesis of van Dijk (2001), who also worked on various high and low pressure mercury plasmas. At present, other work is in progress by Johnston on transport coefficients and sulfur light sources (Johnston, 1999; Johnston *et al.*, 2002; Johnston, 2003), by Hartgers on self-consistent diffusion and time dependence (Hartgers and van der Mullen, 2001; Hartgers *et al.*, 2002), and by Garloff on extreme ultra-violet (EUV) radiation sources.

1.2 Plasma (light) sources

Around 1930, the first mass-produced plasma light sources appeared: the low pressure mercury lamp, better known as the tubular fluorescent lamp (Waymouth, 1971), and the low pressure sodium lamp (the characteristic bright orange street light) (Meyer and Nienhuis, 1988). In later years high pressure mercury (Waymouth, 1971) and sodium light sources became available (de Groot and van Vliet, 1986; Meyer and Nienhuis, 1988). Still more recent are metal halide lamps (Meyer and Nienhuis, 1988) and electrode-less discharges such as the Philips QL lamp (van Dijk, 2001; Jonkers *et al.*, 1997; Jonkers, 1998) and the sulfur[1] lamp (Dolan *et al.*, 1992, 1995; Turner *et al.*, 1997).

This thesis will touch upon two radiative light sources (metal halide and sulfur lamps) though the chemistry and radiation transport theory presented here are applicable to more radiative plasmas. The theory of radiative plasmas can be applied to reactive plasmas as well. Even though radiation is a by-product in these plasmas, it may still play a vital role in experimental diagnostics. The last application is therefore a reactive plasma produced by a cascaded arc source (van de Sanden *et al.*, 1992, 1995, 1996).

An overview of the plasmas that this thesis deals with is given below.

- *Metal halide lamps*
  These high pressure plasmas used for lighting contain a bulk species, usually mercury, and various additives that are chosen for their radiative properties. The additives enter the plasma as constituents of metal halide molecules, and the calculation of the (thermal equilibrium) densities of these additives is the main subject of chapter 2.

- *The sulfur lamp*
  Mostly due to the fact that sulfur plasmas react aggressively with metal electrodes, the sulfur lamp is an electrode-less lamp and powered by microwaves, making the system one of the most strange-looking light sources ever seen. It does, however, have some quite interesting properties. The sulfur dimer radiates light that follows the eye-sensitivity curve well, which is desirable for a light source. The radiation generation by sulfur molecules is the subject of chapter 4. The transport of radiation inside the sulfur lamp, which gives rise to the net emitted spectrum of the lamp, is dealt with in chapters 5 and 6.

- *Cascaded arc*
  Although the cascaded arc generated plasmas usually produce visible light, they are not seen as light sources in the traditional sense of the word. However, the radiative transfer techniques developed in this thesis are not just applicable to light sources, but can also be used to investigate other radiation related effects. In chapter 8 a Monte Carlo radiative transfer method is used to analyse the results of a laser induced fluorescence experiment on an expanding hydrogen plasma.

1.3 Thesis outline

Most chapters in this thesis deal with both radiative transfer and light sources. Chapter 2, which deals with the calculation of species densities in plasmas that are in local thermal equilibrium

[1] IUPAC nomenclature is followed by calling this element “sulfur” instead of “sulphur”.

(LTE), is already an exception to this rule. However, without a knowledge of the relevant densities not much can be said about the radiative properties of a plasma, so it is fitting that the thesis starts off with this chapter. It also provides a first glimpse of the plasma simulation model PLASIMO. The subject of density calculations in LTE is not generally seen as very challenging. However, in some cases, which are highly relevant for certain types of light sources such as metal halide lamps, the geometry of the plasma makes the calculation of the mixture components not at all trivial.

After this excursion into the subject of mixtures in LTE, chapter 3 presents a gentle introduction into the core subject of this thesis: radiation. It includes a short discussion of general radiation topics, introduces often used formulae and gives an overview of existing work. It also introduces the notion of locally determined radiation properties and non-local transport effects, and discusses the design of the radiation modules in PLASIMO.

Chapter 4, which was originally published as a paper (van der Heijden and van der Mullen, 2001), discusses semiclassical (SC) and quantum-mechanical (QM) methods for calculating the radiative properties of diatomic molecules, applied to the sulfur dimer which is mainly responsible for the radiation in the sulfur lamp.

The following chapter, 5, also first appeared as a paper (van der Heijden *et al.*, 2002). It continues where the previous chapter left off, by using the molecular absorption and emission coefficients to a calculate the spectrum of the high pressure sulfur lamp — based on a fixed temperature profile that is obtained via educated guess work — which is then compared to experimentally obtained spectra.

The third installment of the sulfur series, originally published as van der Heijden and van der Mullen (2002) and in this thesis known as chapter 6, presents an efficient radiative transfer code that connects well with a control volume (CV) fluid model, such as PLASIMO. It is again applied to the sulfur lamp, where it is now possible to do a self-consistent calculation of the temperature profile and the effects of radiative transfer.

The validation chapter (7) contains validation tests of the radiative transfer method developed in the previous chapter. For these tests, two new methods are developed: (1) Analytical expressions, which are fast but valid for only a very narrow set of problems and (2) a Monte Carlo model which is relatively slow, but can be used for arbitrary geometries and density profiles.

An application of the Monte Carlo code is the analysis of hydrogen laser induced fluorescence decay time measurements in an expanding cascaded arc in chapter 8, which has been partly published as van der Heijden *et al.* (2000).

Chapter 9 is devoted to concluding remarks about each of the previous chapters.

Chapter 2

Particle densities in local thermal equilibrium

Abstract

In this chapter the calculation of particle densities in plasmas that are in local thermal equilibrium (LTE) is discussed. The subject matter is split into a local part, where the main parameters are pressure and temperature, and a non-local, transport-sensitive, part. The latter is of importance in plasmas like metal halide lamps, where the densities of some species are determined by transport effects around "salt reservoirs" at a so-called cold-spot temperature. The transport effects are calculated using "elemental diffusion" equations. Example calculations are presented for a Hg/Na/I high pressure mixture.

2.1 Introduction

Even though this thesis deals primarily with radiative transfer calculations in light sources, this chapter will not treat radiation at all but instead focus on a subject that in most radiative transfer treatments is considered a known quantity: the set of particle densities in confined plasmas in local thermal equilibrium (LTE).

As will be shown in the next section, even using the assumption of chemical equilibrium, in many systems commonly found in high pressure light sources it is not possible to calculate all particle densities given only the local plasma properties such as total pressure and temperature. If it were always possible — and there are plasma setups where this is a valid approximation — the theory in section 2.3 would be sufficient. However, it turns out that in general a treatment of transport effects is necessary in order to be able to calculate LTE densities.

Since, as will become clear, the chemical composition calculation is strongly linked to temperature and bulk flow properties, and utilises several different numerical solution methods, the treatment of the subject of this chapter also serves as an introduction of some of the plasma calculation modules in the plasma simulation model PLASIMO.

This chapter deals with a number of particle density related concepts, with very specific meanings, which are introduced here together along with related notational conventions:

- A *Mixture* is a (confined) volume of particles, with an associated temperature and pressure field. Such a mixture is subject to bulk convection flow, for example caused by gravity, in which the details of the confining vessel geometry play an important role. The bulk convection and LTE descriptions are closely linked; the densities determine the overall convection characteristics, while the convection calculation determines the pressure gradient and the bulk velocity.

- *Particles* or *species* consist of one or more elements, and are the primary items of which the density is to be calculated. Examples of particles in the current context are atoms, molecules, (molecular) ions and electrons. All quantities that appear in reactions (e.g. $A + B \leftrightarrow AB$) are considered particles. As this reaction illustrates, particles are by definition not conserved in reactions (if they were, the reaction would be trivial). The densities of specific particles are denoted with square brackets, for example $[A]$, $[B]$, and $[AB]$, while in general density equations the traditional symbol n is used. If particles are indexed, Roman subscripts i, j, etc. are used.

- *Elements* are the basic and indivisible building blocks of particles. In the current context, where ionisation and molecular formation processes are considered but not nuclear reactions, atomic cores and electrons are the basic building blocks. A chemical reaction is only considered valid if the elements on the right hand side are equal to the elements on the left hand side. The densities of elements are denoted with curly braces, and indexed with Greek subscripts α, β, etc. As an example, consider a mixture containing the species A, B, and AB_3, then $\{A\} = [A] + [AB_3]$ and $\{B\} = [B] + 3[AB_3]$.

After the general overview in the next section, the theory for the local aspect of LTE density calculations is given in section 2.3. The example calculation at the end of this section will show that for a sufficiently simple mixture, a local calculation will suffice. However, as more elements are introduced into the mixture, a purely local treatment is no longer possible.

A fairly detailed treatment of diffusive-convective transport is given in section 2.4. This introduces the concept of bulk flow, the mass averaged motion of the collection of particles that makes up a plasma, and gives equations for calculating the movements of individual species and elements. Once the transport properties are known, it is possible to calculate the actual densities of particles based on equilibrium laws and other locally known constraints that are described in section 2.3.

In section 2.5 a full-up calculation is presented, including local balances and constraints as well as transport effects. A discussion of the results and the conclusion are given in section 2.6.

2.2 Overview

The governing equation for a particular particle density n in a steady-state mixture is as follows,

$$\nabla \cdot \vec{\Gamma} = P - nD, \tag{2.1}$$

with flux density $\vec{\Gamma}$ the sum of convection and diffusion contributions, D [s^{-1}] the local destruction rate and P [$m^{-3}s^{-1}$] the local production term, both of which are generally due to chemical or radiative processes.

If the transport term, $\nabla \cdot \vec{\Gamma}$ is much smaller than the production and destruction terms nD and P, then the density n is mainly locally determined,

$$n \approx \frac{P}{D}, \tag{2.2}$$

by P and D (which are generally strongly temperature dependent).

However, as the following example will show, even if local production and destruction processes far outweigh the transport term $\nabla \cdot \vec{\Gamma}$ in equation (2.1), transport effects cannot be completely neglected. The reason for this is that local chemical reactions are by definition unable to create their own building blocks, the elements, which must therefore be supplied somehow.

Consider a mixture of Na and I elements, which occur in atomic form and as a molecule NaI. The LTE equation for the balance

$$Na + I \leftrightarrow NaI \tag{2.3}$$

has the following form,

$$[Na][I] = [NaI]f(T), \tag{2.4}$$

where $f(T)$ is a yet to be specified function of temperature T. In addition to the balance equation (2.4), a requirement for a uniform (average, in case there is a convective flow) pressure p may be given,

$$[Na] + [I] + [NaI] = \frac{p}{kT}. \tag{2.5}$$

Working with these two equations only, the solution in figure 2.1, with a complete separation of Na and I elements is allowed. This particular distribution of elements has the property that everywhere in the mixture one of the ingredients of NaI is missing so that the molecule is not formed at all, rendering equation (2.4) redundant.

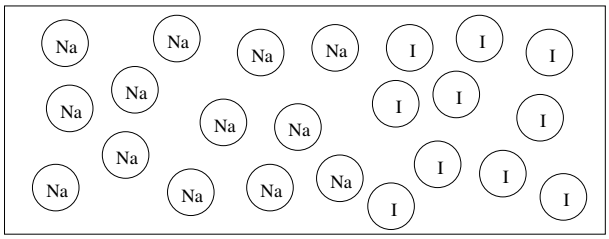

Figure 2.1: *An obviously absurd solution to an under-specified LTE system. The LTE balance equation, $[Na][I] = [NaI]f(T)$, is satisfied if $[NaI] = 0/m^3$ everywhere and $[Na] = 0/m^3, [I] = p/kT$ or $[Na] = p/kT, [I] = 0/m^3$, which also keeps the pressure uniform. Clearly this solution is not stable, because diffusion would mix it up.*

From figure 2.1 it is obvious that some mechanism of element distribution (read: diffusion) needs to be added to the LTE system. From a mathematical point of view it is also easy to understand that the system of equations is under-determined, since there are only two equations for the three unknowns $[Na]$, $[I]$, and $[NaI]$.

This poses an interesting dilemma. On the one hand, it is not desirable to resort to solving a transport-production-destruction balance as in equation (2.1) for each particle, since that would mean that no use can be made of the LTE balance equations. LTE equations give convenient

expressions for the production-to-destruction ratios P/D, but do not supply the production or destruction rates needed to evaluate $P - nD$. Solving the full transport balance (2.1) is also unattractive from a numerical point of view, exactly because the transport term is so small compared to the chemical production and destruction rates, which gives rise to stability problems. On the other hand, the previous example has made it clear that some transport effects must be accounted for in the density calculation.

A compromise can be found by rewriting the full transport equations for each particle. In the case of the Na, I, and NaI mixture, destruction of a NaI particle means that it is dissociated into — and therefore produces — a Na and I particle. The reverse is also true; destruction of a Na atomic particle means that it, together with an I atom, formed a NaI molecule. Therefore, the various production and destruction terms are related,

$$\begin{aligned} P_{Na} &= P_I = [NaI]D_{NaI} \\ P_{NaI} &= [Na]D_{Na} = [I]D_I, \end{aligned} \tag{2.6}$$

so that adding the transport equations for Na and NaI,

$$\begin{aligned} \nabla \cdot \vec{\Gamma}_{Na} &= P_{Na} - [Na]D_{Na} \\ \nabla \cdot \vec{\Gamma}_{NaI} &= P_{NaI} - [NaI]D_{NaI}, \end{aligned} \tag{2.7}$$

gives a transport equation for Na elements,

$$\nabla \cdot (\vec{\Gamma}_{Na} + \vec{\Gamma}_{NaI}) = \nabla \cdot \vec{\Gamma}_{\{Na\}} = 0, \tag{2.8}$$

which simply expresses that since Na elements are not created or destroyed by chemical reactions, the flux density of these elements must be divergence free. A similar equation can be given for I elements,

$$\nabla \cdot (\vec{\Gamma}_I + \vec{\Gamma}_{NaI}) = \nabla \cdot \vec{\Gamma}_{\{I\}} = 0. \tag{2.9}$$

In a general mixture, it is possible to define one such transport equation for each element, by demanding that no elements are created or destroyed[1]. For example, if the dimer Na_2 were also considered in the mixture, the transport equation for Na elements (2.8) would be $\nabla \cdot (\vec{\Gamma}_{Na} + \vec{\Gamma}_{NaI} + 2\vec{\Gamma}_{Na_2}) = 0$. The factor two is needed because the Na_2 flux carries two Na elements. The general form of the transport equation for element α is thus

$$\nabla \cdot \left(\sum_i R_{i\alpha} \vec{\Gamma}_i \right) = 0, \tag{2.10}$$

where the summation with index i is over every particle and $R_{i\alpha}$ is the number of elements α in particle i.

The meaning of elemental conservation rules is illustrated, for the Na, I, and NaI mixture, in figure 2.2. Instead of demanding that the divergence of the flux density of each particle is equal to the relatively small difference in chemical reaction rates $P - nD$, which is not known if LTE balance equations are used, the particle fluxes are left unspecified. However, since production and destruction terms for elements are by definition zero, it is possible to make a statement about the elemental flux density; it must be divergence free.

[1] The electron forms an exception since it is already constrained by charge neutrality, as will be shown later.

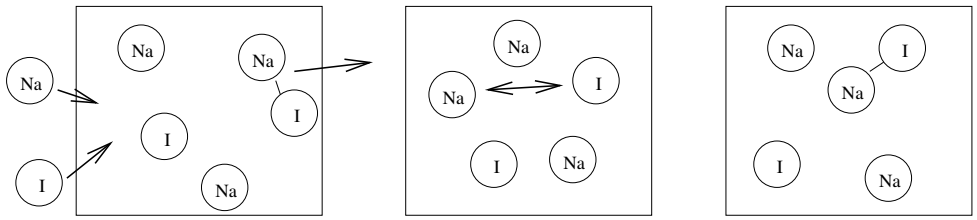

Figure 2.2: *An example of the conservation of elements. If (a) one Na and one I atom enter a volume, while a NaI molecule leaves at the same time, (b) the newly arrived Na and I atoms will instantly associate to satisfy the LTE balance between atoms and molecules, so that (c) the density distribution is unchanged.*

The following section will discuss balances, which give LTE equations for P/D in (2.2), and other locally determined constraints that together give rise to LTE density values. An overview of the implementation in PLASIMO is given, as well as a sample calculation. The transport equation for elements (2.10) is treated in section 2.4.

2.3 Local LTE balances and constraints

2.3.1 Chemical balances

Various equilibrium equations are known under different names, such as the Saha or Guldberg-Waage equations. While these equations do describe different effects, it is important to realize that both are a form of the law of mass action. Generally stated, all balances can be expressed as

$$a_1X_1 + a_2X_2 + \ldots + a_nX_n \longleftrightarrow b_1Y_1 + b_2Y_2 + \ldots + b_nY_m, \tag{2.11}$$

where a_i and b_j are positive integer numbers and X_i and Y_j denote the n and m different particles on either side. The densities $[X_i]$ and $[Y_j]$ of all particles involved are then related via

$$\frac{\Pi_i^n[X_i]^{a_i}}{\Pi_j^m[Y_j]^{b_j}} = \frac{\Pi_i^n(Q_{X_i})^{a_i}}{\Pi_j^m(Q_{Y_j})^{b_j}} \left(\frac{2\pi kT}{h^2}\right)^{\frac{3}{2}(\sum_i^n a_i - \sum_j^m b_j)} \left(\frac{\Pi_i^n(m_{X_i})^{a_i}}{\Pi_j^m(m_{Y_j})^{b_j}}\right)^{\frac{3}{2}} \exp\left(-\frac{\sum_i^n a_iE_{X_i} - \sum_j^m b_jE_{Y_j}}{kT}\right), \tag{2.12}$$

where Q_Z, m_Z, and E_Z are the partition sum, mass, and offset energy, respectively, of particle Z.

The offset energy E_Z is not a unique characteristic of the particle. For a given system of particles and balances, the offset energies are determined relative to each other and reaction energies are the only constant quantities. A collection of N particles is subject to at most $N-1$ unique balances, with each balance giving a linear requirement,

$$\sum_i^n a_iE_{X_i} - \sum_j^m b_jE_{Y_j} = \Delta E_{\rightarrow}, \tag{2.13}$$

where $\Delta E_{\rightarrow}$ is defined as the energy that is released by a left to right process of the balance (2.11). Since there are not more than $N-1$ linear equations for N offset energies, the offset energies are not uniquely specified. For example, the association reaction $A + A \rightarrow A_2$, implies

that $2E_A - E_{A_2} = \Delta E$, where ΔE is the amount of energy that is released when two A particles form the molecule A_2. It is customary to choose the zero offset energies for atoms, so that $E_{A_2} = -\Delta E$, but this is not required.

The general form of the partition sum Q_X of particle X is given by

$$Q_X = \sum_p g_p Z_p \exp\left(-\frac{E_p}{kT}\right), \tag{2.14}$$

where p iterates over all of the particle's internal states, g_p is the state degeneracy, Z_p the state's internal partition sum, and E_p is the state's energy relative to the particle offset energy. By definition, the first state is the ground state of the particle, so that $E_1 = 0$. The internal partition sum Z_p of atomic states is unity, while molecular states generally have complex internal partition sums (see also chapter 4).

A few special cases of the general equation (2.12) are given below.

- The *Guldberg-Waage* equation describes a molecular balance $A + B \leftrightarrow AB$,

$$\frac{[A][B]}{[AB]} = \frac{Q_A Q_B}{Q_{AB}} \left(\frac{2\pi\mu_{AB}kT}{h^2}\right)^{\frac{3}{2}} \exp\left(-\frac{D_{AB}}{kT}\right), \tag{2.15}$$

  with D_{AB} the dissociation energy of AB and μ_{AB} the reduced mass of the system $A+B$,

$$\mu_{AB} = \frac{m_A m_B}{m_{AB}} = \frac{m_A m_B}{m_A + m_B}. \tag{2.16}$$

- In order to obtain the well-known *Saha* ionisation-recombination balance, A is replaced with Z^+, B with e and AB with Z. Using $Q_e = 2$ (due to the two-fold spin degeneracy of electrons) and the approximation that $m_e + m_Z \approx m_Z$, so that $\mu_{Z^+e} \approx m_e$, gives

$$\frac{[Z^+][e]}{[Z]} = \frac{2Q_{Z^+}}{Q_Z} \left(\frac{2\pi m_e kT}{h^2}\right)^{\frac{3}{2}} \exp\left(-\frac{E_i}{kT}\right), \tag{2.17}$$

  where E_i is the ionisation energy of Z. Often Q_Z and Q_{Z^+} are approximated with the degeneracies g_Z and g_{Z^+} of the ground states of Z and Z^+ respectively.

- Another special case of equation (2.12) is the *Boltzmann* balance for excitation, $Z \leftrightarrow Z^*$,

$$\frac{[Z^*]}{[Z]} = \frac{Q_Z^*}{Q_Z} \exp\left(-\frac{\Delta E}{kT}\right), \tag{2.18}$$

  where $\Delta E = E_{Z^*} - E_Z$ is the energy difference and again $Q_{Z^{(*)}}$ is often replaced with $g_{Z^{(*)}}$.

Note that it makes no difference, at least for a system in LTE, whether for example an excitation balance is written as $Z \leftrightarrow Z^*$ or $Z + e \leftrightarrow Z^* + e$, since the electron terms (or indeed the terms of any particle that is conserved in the reaction) in equation (2.12) cancel. This is one of the fundamental characteristics of LTE. It is implicitly assumed that the means (such as electron or heavy particle collisions or other effects) for left or right going processes are available in abundance. From this it follows, for example, that in LTE there is no need to distinguish between two-particle or three-particle recombination, such as there is in non-LTE.

2.3.2 Local constraints

The balances discussed in the previous section provide only a subset of the equations related to LTE compositions. Depending on the assumptions made, the following equations may form part of the total system of LTE equations for a given mixture.

- *Pressure:* If the total pressure or the partial pressure of a set of particles is known, a pressure equation is to be added to the system of equations:

$$[Z_1] + [Z_2] + \ldots + [Z_n] = \frac{p}{kT}, \tag{2.19}$$

  where p is a partial pressure for the subset of particles $Z_1 \ldots Z_n$, or the total pressure if $Z_1 \ldots Z_n$ is the set of all particles in the mixture.

- *Charge conservation:* In a mixture containing electrons and ions, it is usually assumed that the positive and negative charge carriers are not spatially separated (at least not on the spatial scale that the model describes), so that the net local charge density is zero:

$$q_1[Z_1] + q_2[Z_2] + \ldots q_n[Z_n] = 0, \tag{2.20}$$

  with q_i the charge of particle Z_i. Unlike pressure constraints, which can give multiple equations for different subsets of the particles in the mixture, there can be only one equation for charge conservation.

- *Element conservation:* If the densities of elements are known, the following equation must hold

$$R_{\alpha 1}[Z_1] + R_{\alpha 2}[Z_2] + \ldots + R_{\alpha n}[Z_n] = \{A_\alpha\}, \tag{2.21}$$

  with $R_{\alpha i}$ the number of elements A_α in particle Z_i and $\{A_\alpha\}$ the density of elements A_α.

2.3.3 Composition constraints

In order to use a pressure constraint (2.19), it is obviously necessary to know what the (partial) pressure of a collection of particles actually is. In many types of closed discharges, most notably light sources, the (partial) pressure is not *a priori* known. Instead, what is given is the filling contents of the closed discharge, usually in the form of a pressure (for a filling species that is gaseous at room temperature) or a mass (for materials that are liquid or solid at power-off conditions). In the latter case, a distinction must be made between filling species that are evaporated completely during normal operation (and thus, ignoring startup effects, can be treated like a gaseous filling) and species that remain partly in solid or liquid state.

Filling components of the first kind are said to be "dosed", which in effect means that the exact number of the component's elements inside the plasma is known. For example, consider a sulfur lamp with a filling of $F_S = 30$ mg of sulfur powder, which is completely evaporated at operating conditions. The equations governing the total pressure p are then

$$[S] + [S_2] + [S_3] + \ldots = \frac{p}{kT}, \qquad (\text{local}) \tag{2.22}$$

$$\int_V ([S] + 2[S_2] + 3[S_3] + \ldots)\, dV = \frac{F_S}{m_S}, \quad (\text{non} - \text{local}) \tag{2.23}$$

where the various sulfur atomic and molecular ions have been omitted and m_S is the sulfur atomic mass.

2.3.4 Implementation details

The pressure, charge and elemental density equations are all linear, and suitable for representation as a matrix equation. However, all balances, except for the Boltzmann balance, are non-linear. These can be linearised by taking the (natural) logarithm of all densities, but this 'de-linearises' the pressure, charge, and element density equations. Therefore, PLASIMO employs a non-linear solver to solve a system of local LTE equations.

The core of the solver comes from the public MINPACK package. It is written in FORTRAN and available via many ftp and web sites on the Internet, such as www.netlib.org. The MINPACK package provides the functions `lmdif` and `lmder`, which use a modified Levenberg-Marquant algorithm, a least-squares minimiser for a set of non-linear equations. The difference between `lmdif` and `lmder` is that the former function requires the user to only provide callback functions $f_j(x_1, x_2, \ldots, x_n)$ for which a set $\overline{x}$ is to be found so that $f_j(\overline{x}) = 0$ for all equations f_j. `lmder`, on the other hand, also requires the user to provide functions $\frac{\partial f_j}{\partial x_i}(\overline{x})$, which can reduce the computational cost of the solver, since the Jacobian of the system of equations can be directly calculated.

The MINPACK functions can be used for problems with more equations than unknowns (for example, fitting a curve to data points) but PLASIMO currently requires that for each unknown (read 'LTE density') exactly one equation is specified.

Reducing the dynamic range of the LTE equations' solution increases the solver stability, so the equations are rewritten in terms of the logarithm of the densities. For LTE balances, this is very advantageous, since

$$\frac{[X_1]^{a_1}[X_2]^{a_2}\ldots[X_n]^{a_n}}{[Y_1]^{b_1}[Y_2]^{b_2}\ldots[Y_m]^{b_m}} = F(T) \tag{2.24}$$

becomes

$$a_1x_1 + a_2x_2 + \ldots + a_nx_n - b_1y_1 - b_2y_2 - \ldots - b_my_m - log(F(T)) = 0, \tag{2.25}$$

with $x_i = \log([X_i])$. However, the other LTE equations become less elegant. The pressure constraint is rewritten as

$$\log(\exp(x_1) + \exp(x_2) + \ldots + \exp(x_n)) - \log(p/kT) = 0. \tag{2.26}$$

The charge equation becomes

$$\log(C_1^+ \exp(x_1^+) + C_2^+ \exp(x_2^+)\ldots) - \log(-C_1^- \exp(x_1^-) - C_2^- \exp(x_2^-)\ldots) = 0, \tag{2.27}$$

where all charged particles are split in groups with positive (x_i^+, with $C_i^+ > 0$) and negative (x_i^-, with $C_i^- < 0$) charge numbers C, to ensure that the term in the logarithms is always positive. Finally, the element density equation for element A is

$$\log(R_{A1}\exp(x_1) + R_{A2}\exp(x_2) + \ldots + R_{An}\exp(x_n)) - \log(\{A\}) = 0. \tag{2.28}$$

PLASIMO's LTE solver provides the above functions and their derivatives (these derivative functions are trivial and not given here), so that the faster `lmder` function is used[2].

[2] A comparison of `lmdif` and `lmder` calculations of an LTE lookup table showed that `lmdif` required 5180 f_j evaluations and `lmder` required 770 f_j and 580 $\partial f_j/\partial x_i$ evaluations. Since the computational cost of f_j and $\partial f_j/\partial x_i$ is about equal, the `lmder` implementation requires four times less CPU time in callback functions.

2.3.5 Examples of local systems of equations

For a given mixture of particles, there are generally multiple systems of LTE equations that can be specified. The balances are usually quite obvious, though some care must be taken that no redundant equations are added.

Here is an example of a mixture containing two different elements, H and e, and five different particles, H, H^*, H^+, H_2, and e,

$$\begin{array}{lrcl}
\text{(i)} & H & \longleftrightarrow & H^+ + e \\
\text{(ii)} & H & \longleftrightarrow & H^* \\
\text{(iii)} & H + H & \longleftrightarrow & H_2 \\
\text{(iv)} & [H] + [H^*] + [H^+] + [H_2] + [e] & = & p/kT \\
\text{(v)} & [H^+] & = & [e].
\end{array}$$

This is only one way of specifying the system. For example, replacing balances (ii) and (iii) with

$$\begin{array}{lrcl}
\text{(ii*)} & H^+ + e & \longleftrightarrow & H^* \\
\text{(iii*)} & H + H^+ + e & \longleftrightarrow & H_2
\end{array}$$

gives a new system of equations with an identical solution.

Adding an argon element, in the form of atom and ion particles, makes the mixture more interesting,

$$\begin{array}{lrcl}
\text{(iv)} & [H] + [H^*] + [H^+] + [H_2] + [Ar] + [Ar^+] + [e] & = & p/kT \\
\text{(v)} & [H^+] + [Ar^+] & = & [e] \\
\text{(vi)} & [Ar^+] + [e] & \longleftrightarrow & \text{[Ar]}.
\end{array}$$

There are now 7 unknown densities (4 containing the hydrogen element, 2 containing argon, 1 electron), and only 6 equations. What is missing is a rule that specifies what the ratio of Ar to H is. One way of specifying this is by giving partial pressures, for example,

$$\begin{array}{lrcl}
\text{(iv-a)} & [H] + [H^*] + 2[H^+] + [H_2] & = & 0.2p/kT \\
\text{(iv-b)} & [Ar] + 2[Ar^+] & = & 0.8p/kT
\end{array}$$

which specifies a mixture that is 80% argon and 20% hydrogen. The electron density has been eliminated from these equations by doubling the ion contribution to the partial pressure (each singly ionised atom now also contributes one electron to the partial pressure). In this way, the electron density has been assigned to either the hydrogen or the argon "sub-mixture". The LTE densities of this mixture are plotted in figure 2.3.

This use of sub-mixtures with well defined partial pressures is an approximation that gives a locally solvable system of equations, but is not always applicable. In the current example, if the vast majority of particles are ground state H or Ar atoms, with very small ion and molecular fractions (say $< 10^{-6}$ or so), it can be a valid description.

However, if for example the temperature field is such that the central part of the mixture is mostly ionised while the outer regions are not, the solution of this local system of equations will give rise to significant gradients in atom and ion densities. A similar problem arises if the minimum and maximum values of the temperature field are significantly below and above the dissociation temperature of the molecules.

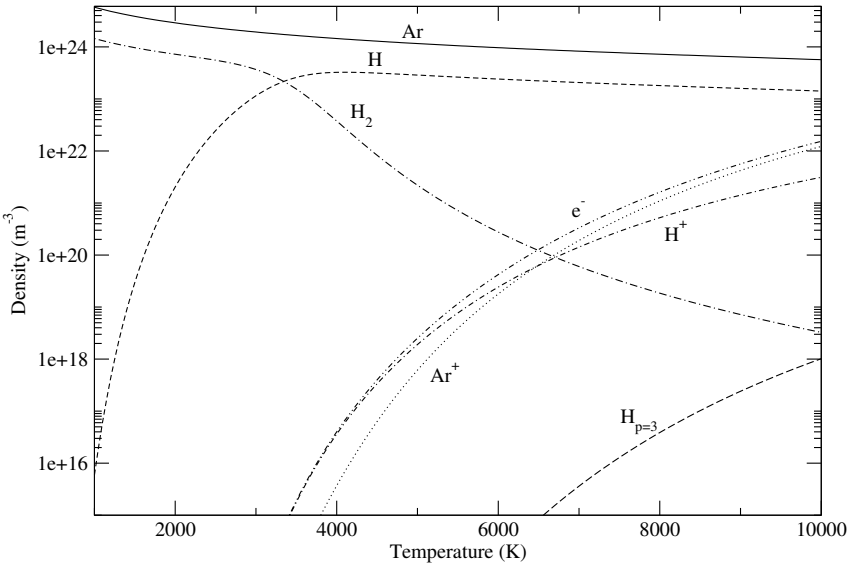

Figure 2.3: *Particle densities in a 20% H, 80% Ar (volume fractions) mixture in LTE as function of temperature for a total pressure of* 10^5 *Pa. Note that at low temperatures, the dominant ion is* H^+ *(ionisation energy 13.2 eV), while at higher temperatures* Ar^+ *(at 15.8 eV) takes over as the main positive charge carrier. Argon atoms are the dominant species, and the density effectively follows the ideal gas law,* $[Ar] \approx p/kT$.

2.4 Transport equations

2.4.1 Introduction

In PLASIMO, diffusion-convection transport equations are solved as a form of the general ϕ-equation (Patankar, 1980),

$$\nabla \cdot (f_\phi \rho \vec{c}_\phi \phi) - \nabla \cdot (\lambda_\phi \nabla \phi) = S_\phi, \tag{2.29}$$

where the precise meaning of the terms f_ϕ, $\vec{c}_\phi$, λ_ϕ, and S_ϕ is given by the details of the specific transport equations.

In the following section, it will be shown that the divergence of the diffusive-convective flux density of species i can be described by an equation of the form (2.29), where ϕ is the partial pressure p_i of species i.

In section 2.4.3, it will be shown how the equation for the divergence of the elemental flux density follows from the species transport equations, and how it too can be written in the form of a ϕ-equation. This makes it possible to use the existing PLASIMO ϕ-equation infrastructure to solve the equations for elemental fluxes.

2.4.2 Diffusion

Before the details of elemental diffusion are discussed an equation for particle diffusion is derived, starting from the conservation of mass and momentum and following the more general derivation of Janssen (2000). The advantage of giving a derivation rather than using a "standard" diffusion formula is that the used approximations are made visible.

The specific mass balance for species i in a steady-state plasma is given by

$$\nabla \cdot (\rho_i \vec{u}_i) = S_i = m_i(P - n_i D), \tag{2.30}$$

with $\rho_i = m_i n_i$ the mass density of species i, $\vec{u}_i$ the mean velocity of species i, S_i [kg m^{-3}s^{-1}] the volumetric rate of production of particles i, and m_i the mass of particle i. Equation (2.30) is equation (2.1) stated in terms of mass per unit of volume instead of particle densities, and can be obtained by multiplying (2.1) with m_i.

The specific momentum balance can be approximated by

$$\nabla \cdot (\rho_i \vec{u}_i \vec{u}_i) = -\nabla p_i + \vec{u}_i S_i + \rho_i \vec{f}_i + \sum_j \vec{R}_{ij}, \tag{2.31}$$

with p_i the partial pressure of particle i, $\vec{f}_i$ [ms^{-2}] the body force per unit mass acting on particles i, and $\vec{R}_{ij}$ the mean force per unit volume [Nm^{-3}] exerted by species j on species i. The complete momentum balance contains a term $\nabla \cdot \overline{\overline{P_i}} = \nabla p_i + \nabla \cdot \overline{\overline{\pi}}$, with $\overline{\overline{P_i}}$ the partial pressure tensor and $\overline{\overline{\pi}}$ the viscosity tensor. In equation (2.31) the viscosity is ignored. It will be shown that the full pressure tensor, including viscous terms, can be used in the calculation of the bulk flow properties.

In order to obtain equations for the bulk flow properties, equations (2.30) and (2.31) will be summed over all species i. Defining total pressure $p = \sum_i p_i$, density $\rho = \sum_i \rho_i$, bulk velocity $\vec{u}$,

$$\vec{u} = \sum_i \frac{\rho_i}{\rho} \vec{u}_i, \tag{2.32}$$

and making use of the fact that the divergence operator is linear, summing (2.30) gives

$$\nabla \cdot (\rho \vec{u}) = 0, \tag{2.33}$$

where the right hand side is zero since there can be no net mass production due to chemical reactions. This mass conservation is a less strict form of the requirement in (2.10), which states that mass conservation holds for each element independently.

For the momentum balance, it is convenient to define the deviation $\vec{v_i}$ of mean species velocity $\vec{u}_i$ from the bulk velocity $\vec{u}$,

$$\vec{u}_i = \vec{u} + \vec{v_i}. \tag{2.34}$$

Note that from the definition of the bulk velocity (2.32) it follows that $\sum_i \rho_i \vec{v_i} = 0$. Summing and expanding the $\nabla \cdot (\rho_i \vec{u}_i \vec{u}_i)$ term in (2.31) gives

$$\sum_i \nabla \cdot (\rho_i \vec{u}_i \vec{u}_i) = \sum_i \nabla \cdot (\rho_i (\vec{u}\vec{u} + 2\vec{u}\vec{v_i} + \vec{v_i}\vec{v_i})) = \nabla \cdot (\rho \vec{u}\vec{u}) + \nabla \cdot \left(\sum_i \rho_i \vec{v_i}\vec{v_i} \right). \tag{2.35}$$

The term containing $\vec{v_i}\vec{v_i}$ can be incorporated in the pressure tensor $\overline{\overline{P}}$ (a detailed treatment of which is beyond the scope of this text, see for example Holt and Haskell (1965)),

$$\overline{\overline{P}} = \sum_i p_i + \sum_i \rho_i \vec{v_i}\vec{v_i}. \tag{2.36}$$

The summation of (2.31) over all species eliminates terms describing forces between species due to Newton's third law, commonly known as the action equals reaction principle. Specifically, the momentum production $\vec{u}_i S_i$ due to chemical reactions cancels, as well as the $\vec{R}_{ij}$ force terms. The result is

$$\nabla \cdot (\rho \vec{u}\vec{u}) = -\nabla \cdot \overline{\overline{P}} + \sum_i \rho_i \vec{f}_i, \tag{2.37}$$

where only the external forces which affect the kinetic energy density of the bulk remain. This equation can be simplified using the general vector relation

$$\nabla \cdot (\rho \vec{u}\vec{u}) = (\rho \vec{u} \cdot \nabla)\vec{u} + \vec{u}\nabla \cdot (\rho \vec{u}), \tag{2.38}$$

and realizing that the second term cancels due to mass conservation (2.33). This leads to the expression

$$(\rho \vec{u} \cdot \nabla)\vec{u} = -\nabla \cdot \overline{\overline{P}} + \sum_i \rho_i \vec{f}_i. \tag{2.39}$$

It is important to realize that the force term $\sum_i \rho_i \vec{f}_i$ will not contain a net influence from an electric field $\vec{E}$. Since the electrical body force for species i equals $n_i q_i \vec{E}$, the charge neutrality constraint $\sum_i n_i q_i = 0$ (2.20) causes the net contribution of the electric field to be zero. Likewise, the charge neutrality implies that the bulk flow does not carry a current density, $\sum_i n_i q_i \vec{u} = 0$. All effects related to charged particles will only show up in the specific momentum balance, whereas the bulk momentum balance generally only contains the gravitational force, $\sum_i \rho_i \vec{g} = \rho \vec{g}$, with $\vec{g}$ the gravitational acceleration, or a centrifugal force[3], $\rho \omega^2 \vec{r}$, with ω the angular frequency of rotation and r the distance to the axis of rotation.

Returning to the specific momentum balance (2.31), the next approximation is to ignore thermophoretic forces and consider frictional forces only (Hartgers *et al.*, 2002),

$$\vec{R}_{ij} = f_{ij}(\vec{u}_j - \vec{u}_i). \tag{2.40}$$

The friction constant f_{ij} [kg m^{-3}s^{-1}] is zero for $i = j$, and otherwise given by

$$f_{ij} = n_i n_j m_{ij} \Omega_{ij}, \tag{2.41}$$

with m_{ij} the reduced mass of the i j system and Ω_{ij} [m^{3}s^{-1}] the rate coefficient for momentum transfer from species i to j. f_{ij} is related to the binary diffusion coefficient D_{ij} [m^{2}s^{-1}] via

$$f_{ij} = \frac{p_i p_j}{p D_{ij}}. \tag{2.42}$$

The most important approximation in this derivation is the assumption that there is an abundant background species that dominates the frictional forces, and which has a partial pressure that is close to the total pressure p. The summation over $\vec{R}_{ij}$ then contains only one term,

$$\sum_j \vec{R}_{ij} \approx \frac{p_i}{D_i}(\vec{u} - \vec{u}_i), \tag{2.43}$$

with D_i the binary diffusion coefficient for species i and the background gas.

[3]For example, the sulfur lamp (see chapter 4) is rotated during operation.

Expanding the divergence of $\rho_i \vec{u}_i \vec{u}_i$ in the specific momentum balance for species i (2.31) using equation (2.38) and substituting equation (2.43) then gives

$$(\rho_i \vec{u}_i \cdot \nabla)\vec{u}_i + \vec{u}_i \nabla \cdot (\rho \vec{u}_i) = -\nabla p_i + \vec{u}_i S_i + \rho_i \vec{f}_i + \frac{p_i}{D_i}(\vec{u} - \vec{u}_i), \tag{2.44}$$

from which the second term on the right and left hand side can be eliminated using the mass balance for species i (2.30), yielding

$$(\rho_i \vec{u}_i \cdot \nabla)\vec{u}_i = -\nabla p_i + \rho_i \vec{f}_i + \frac{p_i}{D_i}(\vec{u} - \vec{u}_i). \tag{2.45}$$

To estimate the importance of the remaining term, $(\rho_i \vec{u}_i \cdot \nabla)\vec{u}_i$, it is instructive to rewrite the partial pressure p_i in terms of the thermal velocity u_{ther},

$$p_i = n_i kT = \frac{1}{3} n_i m_i \frac{\frac{3}{2}kT}{\frac{1}{2}m_i} = \frac{1}{3}\rho_i u_{i,ther}^2, \tag{2.46}$$

The terms on the right hand side containing ∇p_i and p_i are therefore much larger than the term on the left hand side containing only the convective-diffusive velocity, so that the latter can be neglected,

$$-\nabla p_i + \rho_i \vec{f}_i + \frac{p_i}{D_i}(\vec{u} - \vec{u}_i) = 0. \tag{2.47}$$

What remains to be discussed is the force term $\rho_i \vec{f}_i$, which contains contributions from gravity (centrifugal forces will be ignored here, in the following argument they can be substituted for gravity), and the electrical field $\vec{E}$[4],

$$\rho_i \vec{f}_i = \rho_i \vec{g} + \rho_i \frac{q_i}{m_i}\vec{E}. \tag{2.48}$$

A typical value for q_i/m_i is 10^7 C/kg, so that even an electric field of a mere 1 V/m will give a body force that is 6 orders of magnitude larger than the gravitational force. For neutral particles the gravitational force can be ignored as well, as can be seen using $\nabla p_i \approx p/\Lambda$, with Λ the gradient length (order of millimetres in high pressure light sources), so that clearly $u_{ther}^2/3 \gg g\Lambda$. After substituting the electric field term for the force term, what remains is,

$$-\nabla p_i + \rho_i \frac{q_i}{m_i}\vec{E} + \frac{p_i}{D_i}(\vec{u} - \vec{u}_i) = 0. \tag{2.49}$$

Rearranging terms, and using $\rho_i = p_i m_i / kT$ then gives

$$(\vec{u}_i - \vec{u}) = -D_i \frac{\nabla p_i}{p_i} + \frac{D_i q_i}{kT}\vec{E}. \tag{2.50}$$

The electric field $\vec{E}$ is partly determined by external factors (such as the current density) and partly by the displacement of the charged particles. This can be clearly seen by using equation (2.50) to derive an expression for the current density $\vec{j}$,

$$\vec{j} = \sum_i n_i q_i \vec{u}_i = \sum_i n_i q_i (\vec{u}_i - \vec{u}) = -\sum_i \mu_i \nabla p_i + \sigma \vec{E}, \tag{2.51}$$

[4]The contribution from the magnetic field, the Lorentz force, will be ignored in this treatment.

with μ_i the mobility of species i,

$$\mu_i = \frac{D_i q_i}{kT}, \tag{2.52}$$

and σ the electrical conductivity,

$$\sigma = \sum_i n_i \mu_i q_i. \tag{2.53}$$

It is important to keep track of the signs of the various quantities. The mobility μ_i is negative for negatively charged particles such as electrons (in this case the electric current and diffusive velocities point in opposite directions). The conductivity σ contains a summation over q_i^2, so it is always positive (the current always points in the direction of the driving electric field). The expression for $\vec{j}$ leads to the following equation for the total electric field $\vec{E}$,

$$\vec{E} = \frac{1}{\sigma}\left(\vec{j} + \sum_i \mu_i \nabla p_i\right). \tag{2.54}$$

Equation (2.54) shows that even in the absence of an electric current, $\vec{E}$ can have a non-zero value. Even if there is an electric current density $\vec{j}$, the gradients of the charged particles may be pointing in any direction, so that generally $\vec{E}$ is not parallel with $\vec{j}$. It is common to introduce the ambipolar field $\vec{E}_{amb}$ to describe the electric field caused by the gradients of the charged particles,

$$\vec{E}_{amb} = \frac{1}{\sigma}\sum_i \mu_i \nabla p_i. \tag{2.55}$$

An approximate value for the ambipolar field can now be found by using the fact that the electrons have the highest mobility, so the summation over i can be approximated as just the contribution from the electrons (index e). Likewise, the electrical conductivity will be mainly determined by the electrons, so that $\sigma \approx n_e \mu_e q_e$, giving

$$\vec{E}_{amb} = \frac{\mu_e}{n_e \mu_e q_e}\nabla p_e = \frac{kT}{q_e}\frac{\nabla p_e}{p_e}. \tag{2.56}$$

Substituting (2.56) into equation (2.50) gives

$$p_i \vec{u}_i = -D_i \nabla p_i + p_i\left(\vec{u} + D_i \frac{q_i}{q_e}\frac{\nabla p_e}{p_e} + \frac{D_i q_i}{kT}\frac{\vec{j}}{\sigma}\right), \tag{2.57}$$

which is the basic equation that governs the transport of minority species i. The remainder of this section is devoted to a discussion of this equation.

If the current density $\vec{j}$ is alternating, the net effect on the species velocity u_i will be small, and the $\vec{j}/\sigma$ term can usually be ignored in the specific momentum balance (the Ohmic dissipation associated with the periodic electron motion must of course appear in the plasma energy balance).

It is important to note that the factor q_i/q_e is a negative integer for positive ions and 0 for neutrals. If there is one dominant positive ion i with charge number $Z_i = |q_i/q_e|$, so that the charge neutrality constraint gives $p_e \approx Z_i p_i$ and $\nabla p_e \approx Z_i \nabla p_i$, the ambipolar term in equation (2.57) can be incorporated in the diffusion term, yielding

$$p_i \vec{u}_i \approx -D_i(1 + Z_i)\nabla p_i + p_i \vec{u} \tag{2.58}$$

where the current density term is ignored, and the diffusion coefficient D_i is effectively multiplied by a factor $(1 + Z_i)$. This method for approximating the ambipolar term is numerically simpler, and thus more stable, than the original equation (2.57) with the p_e gradient.

Equation (2.57) is valid for both ions and electrons, but is only useful for ions. The approximation used in the derivation, $\sum_i \mu_i \approx \mu_e$, implies that substituting the values for electrons gives a trivial result,

$$p_e(\vec{u}_e - \vec{u}) = -D_e \nabla p_e + D_e \nabla p_e + \frac{\mu_e}{n_e q_e \mu_e} \vec{j}, \tag{2.59}$$

so that,

$$n_e q_e (\vec{u}_e - \vec{u}) = \vec{j}. \tag{2.60}$$

This result illustrates that in the current approach the electron density n_e is not directly governed by a transport equation, but instead is locally determined by the charge neutrality constraint. It is indirectly affected by transport effects since it must balance the net ion densities which are governed by the transport equation (2.57).

Using $n_i = p_i/kT$, and omitting the current density term, equation (2.57) can be written as a particle flux density that fits in the form of the general ϕ-equation (2.29),

$$\vec{\Gamma}_i = n_i \vec{u}_i = -\frac{D_i}{kT} \nabla p_i + \frac{p_i}{kT} \left(\vec{u} + D_i \frac{q_i}{q_e} \frac{\nabla p_e}{p_e} \right), \tag{2.61}$$

which is perhaps more familiar in terms of densities n_i,

$$\vec{\Gamma}_i = n_i \vec{u}_i = -D_i \nabla n_i + n_i \left(\vec{u} + D_i \frac{q_i}{q_e} \frac{\nabla n_e}{n_e} + \left(\frac{q_i}{q_e} - 1 \right) D_i \frac{\nabla T}{T} \right), \tag{2.62}$$

where the $\nabla T/T$ term, due to $\nabla p_i/(kT) = \nabla n_i + n_i \nabla T/T$, is sometimes neglected under the assumption that the ∇n_i term is dominant. This is not a safe assumption in high pressure light sources, where temperature gradients can be quite steep due to the effective heat transfer between electrons and heavy particles.

In order to find a unique solution to a differential equation of the type (2.57), boundary conditions need to be specified. In a closed configuration and neglecting wall interactions, these are obvious; At the walls, the flux density perpendicular ($\perp$) to the vessel wall must be zero,

$$(\Gamma_i)_\perp = 0. \tag{2.63}$$

The same condition applies to the bulk flux density $(\rho \vec{u})_\perp$ so that the convective term vanishes at the wall. The boundary condition for the elemental pressure at the vessel wall is thus

$$(\nabla p_i)_\perp = 0 \tag{2.64}$$

for neutrals, and

$$(\nabla p_i)_\perp = \frac{q_i p_i}{q_e p_e} (\nabla p_e)_\perp \tag{2.65}$$

for ions.

2.4.3 Elemental diffusion

In the introduction, it was shown that for each element α the following transport equation must hold,

$$\nabla \cdot \vec{\Gamma}_\alpha = \nabla \cdot \left(\sum_i R_{i\alpha} \vec{\Gamma}_i \right) = 0. \tag{2.66}$$

In order to solve a system of elemental transport equations and local balances, it is convenient to rewrite the elemental flux $\vec{\Gamma}_\alpha$ in an "elemental" form using the elemental partial pressure p_α which is defined as,

$$p_\alpha = \sum_i R_{i\alpha} p_i. \tag{2.67}$$

The general form of the elemental transport equation can than be written in the form of a ϕ-equation (2.29),

$$\nabla \cdot \vec{\Gamma}_\alpha = \nabla \cdot \left(-\frac{D_\alpha}{kT} \nabla p_\alpha + \frac{p_\alpha}{kT} \vec{c}_\alpha \right) = 0, \tag{2.68}$$

where the meanings of the elemental diffusion coefficient D_α and the convection-like velocity $\vec{c}_\alpha$ will follow from the derivation.

The elemental partial pressure is a somewhat artificial concept, since the value may be higher than the total pressure. For example, in a pure H_2 gas at 1 bar pressure, the H elemental partial pressure is 2 bar. The definition for the elemental density n_α is similar,

$$n_\alpha = \sum_i R_{i\alpha} n_i. \tag{2.69}$$

From definitions (2.67) and (2.69), it is easy to see that the ideal gas law, $p_i = n_i kT$, also holds for elemental densities and partial pressures.

Using equation (2.61) gives

$$\vec{\Gamma}_\alpha = \sum_i R_{i\alpha} \left(-\frac{D_i}{kT} \nabla p_i + \frac{p_i}{kT} \left(\vec{u} + D_i \frac{q_i}{q_e} \frac{\nabla p_e}{p_e} \right) \right). \tag{2.70}$$

The summation over the convection term is easily evaluated using (2.67),

$$\sum_i R_{i\alpha} \frac{p_i}{kT} \vec{u} = \frac{p_\alpha}{kT} \vec{u}. \tag{2.71}$$

However, the diffusion term is more problematic and requires a special trick:

$$\nabla p_i = \nabla \left(\frac{p_i}{p_\alpha} p_\alpha \right) = \frac{p_i}{p_\alpha} \nabla p_\alpha + p_\alpha \nabla \left(\frac{p_i}{p_\alpha} \right). \tag{2.72}$$

The meaning of $R_{i\alpha} p_i / p_\alpha$ is perhaps more easily understood by using $p = nkT$ and the definition of elemental density n_α (2.69),

$$\frac{R_{i\alpha} p_i}{p_\alpha} = \frac{R_{i\alpha} n_i}{n_\alpha} = \frac{R_{i\alpha} n_i}{\sum_j R_{j\alpha} n_j} \tag{2.73}$$

The value of $R_{i\alpha} n_i / n_\alpha$ is between 0 and 1 and gives the fraction of elements α that is contained in particles i. This fraction is strongly temperature dependent, and only moderately influenced

by pressure. For example, at temperatures significantly below the dissociation temperature of H_2, the ratio $2[H_2]/\{H\}$ will be close to unity, whereas $[H]/\{H\}$ is nearly zero. At higher temperatures, where the molecular balance shifts towards the atomic state, the situation will be reversed. This is illustrated in figure 2.4, which shows the particle to element ratios for H_2, H and H^+ in a hydrogen mixture as a function of temperature.

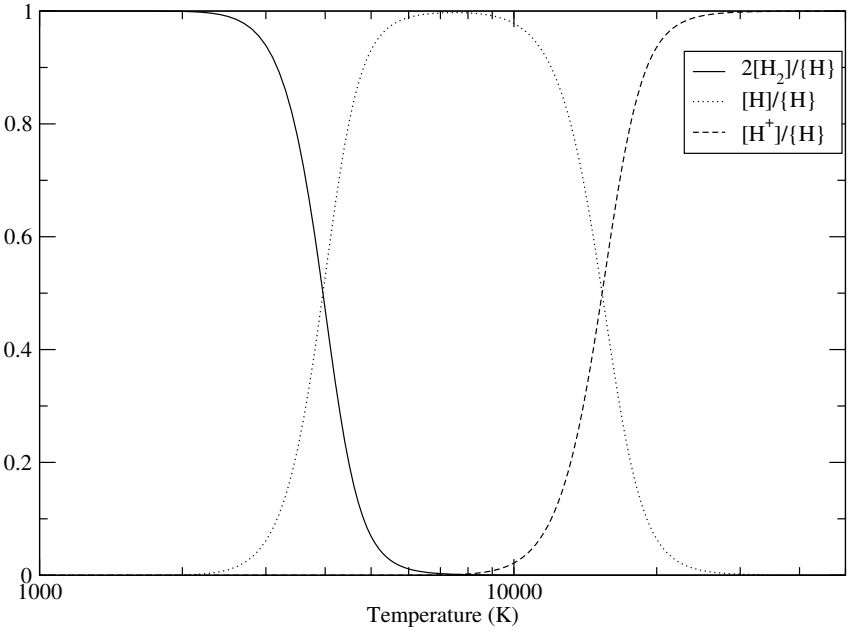

Figure 2.4: *Value of $R_{i\alpha}n_i/\{H\}$ for particles i=H_2, H, and H^+. Each species i dominates (that is, practically all H elements appear in the form of particle i) the mixture in a certain temperature range. At all temperatures $(2[H_2]+[H]+[H^+])/\{H\}=1$.*

Substituting equations (2.71) and (2.72) into (2.70) and rearranging terms yields

$$\vec{\Gamma}_\alpha = -\left(\sum_i R_{i\alpha}\frac{D_i}{kT}\frac{p_i}{p_\alpha}\right)\nabla p_\alpha + \frac{p_\alpha}{kT}\left(\vec{u}+\sum_i R_{i\alpha}D_i\left(\frac{q_i}{q_e}\frac{\nabla p_e}{p_e}-\nabla\left(\frac{p_i}{p_\alpha}\right)\right)\right). \tag{2.74}$$

The elemental diffusion coefficient is thus given by

$$D_\alpha = \frac{\sum_i R_{i\alpha}D_i p_i}{p_\alpha}, \tag{2.75}$$

and the convection term contains three contributions, labelled the bulk, ambipolar and reactive terms,

$$\vec{c}_\alpha = \underbrace{\vec{u}}_{\text{bulk}} + \underbrace{\sum_i R_{i\alpha}D_i\frac{q_i}{q_e}\frac{\nabla p_e}{p_e}}_{\text{ambipolar}} - \underbrace{\sum_i R_{i\alpha}D_i\nabla\left(\frac{p_i}{p_\alpha}\right)}_{\text{reactive}}. \tag{2.76}$$

The boundary conditions are again given by the demand that the flux perpendicular to the wall must be zero,

$$(\nabla p_\alpha)_\perp = \frac{(\vec{c}_\alpha)_\perp}{D_\alpha}. \tag{2.77}$$

As in the particle flux equation, the bulk term will vanish at the boundary, but the ambipolar and reactive terms remain in $(c_\alpha)_\perp$.

2.4.4 Implementation details

The bulk velocity $\vec{u}$ is calculated, along with the pressure field p and the plasma density ρ, by the bulk module in PLASIMO, which solves equations (2.33) and (2.37) for each of the components of $\vec{u}$, as well as the pressure field p. The equations for the components of $\vec{u}$ and for the pressure correction Δp (the pressure p is not directly calculated, but rather the correction Δp needed with respect to an approximated pressure field) are ϕ-equations. In an axially symmetric cylinder, the bulk flow problem is represented by a system of 3 ϕ-equations, with ϕ representing axial velocity u_z, radial velocity u_r, and pressure correction Δp, using the SIMPLE method (Patankar, 1980).

The temperature T is calculated by solving the energy balance which itself is another ϕ-equation, describing the balance of local energy production and thermal conduction and convection.

The control volume method is used to discretise the ϕ-equation (2.29). Each CV contains a nodal point (NP) for which the local value of ϕ is calculated. The discretised equation is obtained by integrating the ϕ-equation over a control volume and solved using a stabilised biconjugate gradient matrix solver (Barrett *et al.*, 1994)

The boundary conditions for p_α present somewhat of a problem. A literal implementation of (2.77) turned out to be very unstable. Another problem with boundary conditions where the gradient is specified, is that it is impossible to ensure a solution with a given value of p_α somewhere at the boundary (usually it is known at the coldest part of the plasma, the so-called cold-spot, which is located at the wall). In order to obtain a unique solution for ϕ-equations, at some part of the boundary the value of ϕ must be set. However, fixing the value of ϕ leaves the gradient free, which gives rise to fluxes through the wall.

The solution used here is to set the reactive and chemical terms to zero at the boundary points and specify the boundary condition $(\nabla p_\alpha)_\perp = 0$. This effectively removes the boundary points from the calculation, since the elemental flux there will automatically be zero and the value at the boundary will always be equal to the value of the first point inside the grid.

To force a unique solution, at every iteration the values of p_α are scaled so that the value at a special boundary point (the cold-spot) matches a set value (the cold-spot pressure). This is possible since any p_α field that satisfies equation (2.68) can be multiplied by a constant factor to obtain a new valid solution. The values of D_α and $\vec{c}_\alpha$, which depend on p_i, will be different in the next iteration, so the scaling procedure has to be repeated at each iteration in order to obtain a convergent solution. This is a rather ad hoc method to force the solver to pick one solution out of the available ones (since the boundary conditions themselves do not specify a unique solution), which works very well in practice.

2.5 An example calculation

The calculations presented here are for configurations similar to a Hg/Na/I metal halide lamp. The exclusion of radiation in the model description means that it cannot be a realistic description of a metal halide lamp, but the emphasis lies on the problems this lamp presents for LTE density calculations.

The reason behind the use of metal elements in lamps is to take advantage of their radiative properties. As is described by Meyer and Nienhuis (1988), one problem with metal elements in

a lamp is that most metals have low vapour pressures, so that a high wall temperature would be required to evaporate the metals. Apart from the difficulties of constructing lamps with walls that can withstand very high temperatures, another problem is presented by the fact that, after evaporation, the metal atoms and ions would seriously damage the wall. The solution is to add the metals in a compound that has a high vapour pressure at lower temperatures, so that the metals, once the compound is in the gaseous phase, are not "aggressive" enough to do damage to the wall. Many metal halide compounds have vapour pressures that are higher than those of the metals, so that when the compound is evaporated, the metals are still contained in relatively harmless molecules like NaI and ScI_3.

A metal halide lamp consists of a buffer gas, usually mercury, at an operating pressure of several bars. In addition to this, metal halide compounds are present, which at the prevailing wall temperatures have a vapour pressure of typically tens of millibars. Once evaporated, the metal halide compounds, in the form of molecules, diffuse away from the wall into the high temperature part of the discharge and dissociate. The resulting metal atoms are then responsible for the lamp's radiative output, with Hg mainly acting as a buffer gas. This principle of operation implies that the elemental densities of the metal elements in the high temperature region of the lamp, where they matter the most, are not known. From the known vapour pressures of the metal halide molecules, the densities at the wall are generally known. It is up to the model to calculate the diffusive-convective transport of the metal elements into the lamp.

2.5.1 Calculation domain and boundary conditions

The configuration for the calculation is an axially symmetric cylindrical vessel with length $L = 32$ mm and radius $R = 8$ mm. Figure 2.5 shows the layout of the grid and the boundary conditions for the temperature. Each side of the grid is labelled with a wind direction. The west and east sides represent the cylinder bottom ($z = 0$) and top ($z = L$) respectively, the south side is the cylinder axis ($r = 0$) and the north side is the outer cylinder wall ($z = R$).

The boundary conditions for the temperature are $T = 1500$ K at the east and west sides, and most of the north side. A small part of the north side, near the bottom of the cylinder, is the so-called "cold-spot" and has a lower temperature of 1200 K. This is the location where in the actual lamp the metal halide reservoir would be. The temperature at the south side, which is the axis of cylindrical symmetry, must have a zero derivative in the r direction, $dT/dr = 0$.

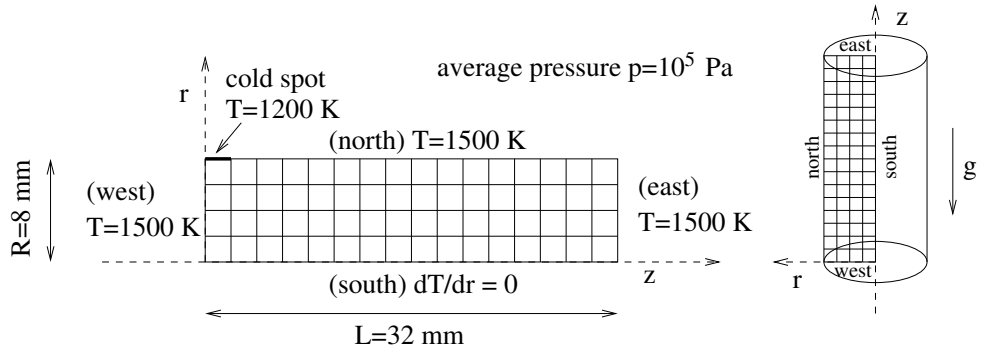

Figure 2.5: *The grid for the metal halide lamp calculations, including the boundary conditions for the temperature T. The cylindrical lamp is axially symmetric, so that the independent coordinates are z and r.*

The boundary conditions for the bulk flow can be summarised as follows: no slip (no velocity component parallel to the wall) and no flux through the wall (no velocity component perpendicular to the wall). This implies $\vec{u} = \vec{0}$ for the north, east, and west sides, and, again for reasons of symmetry, $u_r = 0$ and $du_z/dr = 0$ at the south side. The special boundary conditions for p_α at the walls are discussed in section 2.4.4, while the boundary condition at the symmetry axis is $dp_\alpha/dr = 0$.

The bulk calculations are done with a constant average pressure of 10^5 Pa (=1 bar). All calculations were done with 40 points in the z direction and 20 points in the r direction[5].

2.5.2 Mixture densities and transport coefficients

The plasma mixture in the current model contains eight species: Hg, Hg^+, Na, Na^+, I, I^+, NaI and electrons e. The following equations determine the system:

1. The partial elemental Na pressure $p_{\{Na\}}$ is determined by the solution of equation (2.68). The local LTE calculation contains an elemental constraint,
$$[Na] + [Na^+] + [NaI] = \frac{p_{\{Na\}}}{kT}.$$

2. The partial elemental I pressure $p_{\{I\}}$ is also given by equation (2.68), with the following local constraint,
$$[I] + [I^+] + [NaI] = \frac{p_{\{I\}}}{kT}.$$

3. A constant average (there are small deviations generating bulk flow) total pressure $p = 10^5$ Pa, gives a constraint for the total density,
$$[Hg] + [Hg^+] + [Na] + [Na^+] + [I] + [I^+] + [NaI] + [e] = \frac{p}{kT}.$$

4. The fourth constraint is given by the requirement of charge neutrality,
$$[Hg^+] + [Na^+] + [I^+] = [e].$$

5. The remaining equations are given by LTE balances for the following reactions
$$Hg \longleftrightarrow Hg^+,$$

6.
$$Na \longleftrightarrow Na^+,$$

7.
$$I \longleftrightarrow I^+,$$

8.
$$NaI \longleftrightarrow NaI^+.$$

[5]Test calculations using a finer grid of 80 by 20 points gave essentially the same results.

For fixed partial Na and I pressures of $5 \cdot 10^3$ Pa, the particle densities are given as a function of temperature in figure 2.6. Some temperature regions of interest can be identified:

- Between 2000 and 3000 K, NaI is dissociated. As can be seen in the thermal conductivity graph of figure 2.7, this transition causes a bump in the coefficient for thermal conductivity.
- Between 5000 and 6000 K the following transition occurs, when Na becomes fully ionised. The ionisation energy for Na, 5.1 eV, is much lower than that of either I and Hg (both near 10.5 eV), so at these temperatures the electron density is approximately equal to the Na^+ density. The ionisation of Na^+ causes another bump in the thermal conductivity.
- At 9000 K, due to the combined effects of increased temperature and the high Hg density, the Hg^+ density overtakes the Na^+ density. Above this temperatures, the dominant ion will be Hg^+. Since the I density is very low compared to Hg, the I^+ ion will not play an important role. The limiting regime where the plasma consists mainly of ions lies at temperatures above 10000 K and is outside of the scope of this calculation.

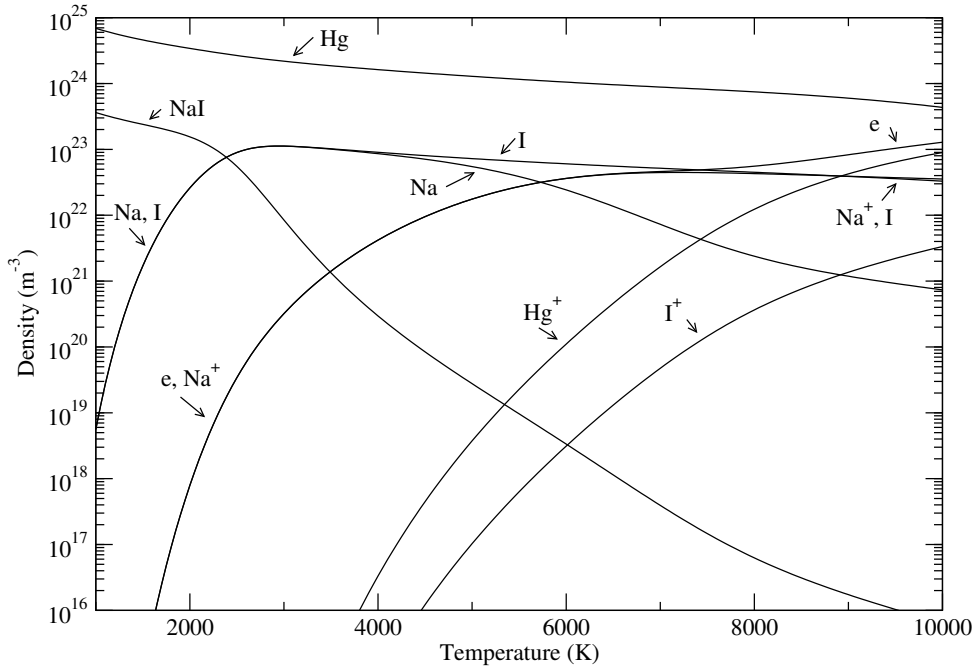

Figure 2.6: *Particle densities as function of temperature for fixed elemental Na and I partial pressures of* $5 \cdot 10^3$ *Pa.*

The PLASIMO transport coefficients module calculates quantities such as the thermal and electrical conductivities and diffusion coefficients. A discussion of the methods used to calculate these results is outside the scope of the current work, see for example Johnston (2003) and, for a more general treatment, Hirschfelder *et al.* (1964).

The result of the thermal and electrical conductivities for the current mixture, again with fixed Na and I elemental partial pressures, is shown in figure 2.7. Due to the fact that the electrical conductivity is mostly linear in n_e (see equation (2.53)) it is plotted on a logarithmic scale.

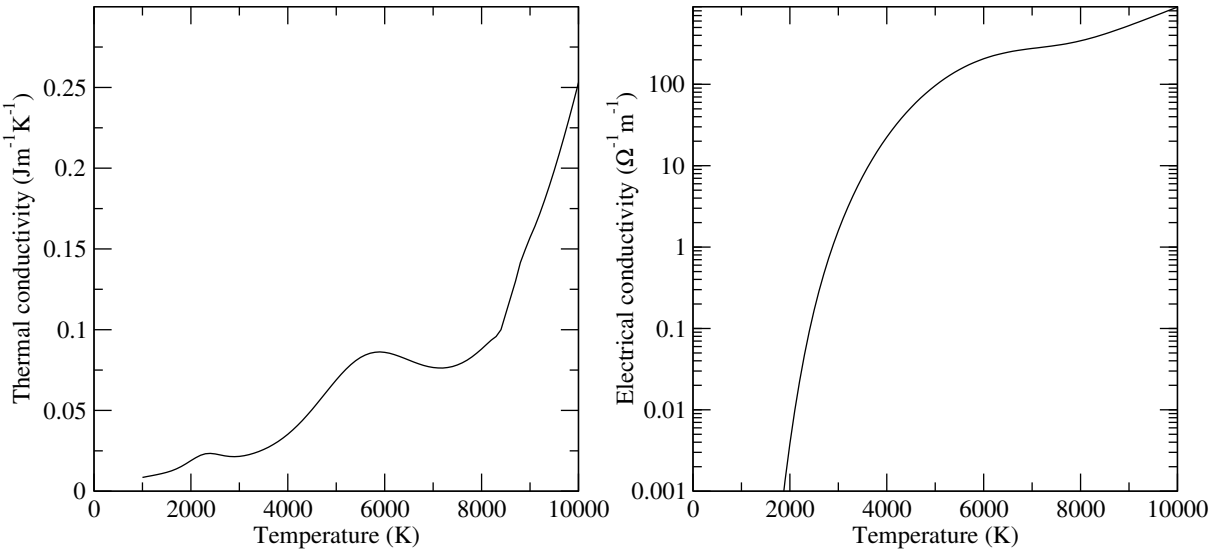

Figure 2.7: *Thermal (left) and electrical (right) conductivities of the Hg/Na/I mixture as calculated by the* PLASIMO *transport coefficients module for* $p_{\{Na\}} = p_{\{I\}} = 5 \cdot 10^3$ *Pa (Johnston, 2003).*

Finally, the diffusion coefficients, as calculated by the transport module, of the relevant particles are shown in figure 2.8. The diffusion coefficient of electrons only plays a role in the electrical conductivity, and does not appear in the elemental transport equations. Due to the insignificant density of I^+, its diffusion coefficients can be ignored as well. Important is the large difference between the diffusion coefficients of the Na atom and the NaI molecule, which is lower by an order of magnitude. Also note the slight difference between the diffusion coefficients of Na and Na^+.

2.5.3 Temperature distribution

In this limited model without radiation, three quantities determine the temperature distribution. The first is the Ohmic dissipation term Q_{Ohm} [Wm^{-3}] which describes power coupled into the plasma. The second one is the thermal conductivity λ_c, describing diffusive heat transport and the third is convective heat transport, governed by the bulk velocity $\vec{u}$.

The Ohmic dissipation is given by

$$Q_{Ohm} = \frac{1}{2}\sigma E_j^2, \tag{2.78}$$

with E_j the magnitude of the AC electric field that drives the current density j. The value of E_j is assumed to be uniform in the r-direction, and is therefore a function of z only,

$$\int_0^R \sigma(r,z) E_j(z) 2\pi r dr = I, \tag{2.79}$$

with I the total current in the z-direction. The total current is an input value, so that for each z point E_j is given by

$$E_j(z) = \frac{I}{\int_0^R \sigma(r,z) 2\pi r dr}. \tag{2.80}$$

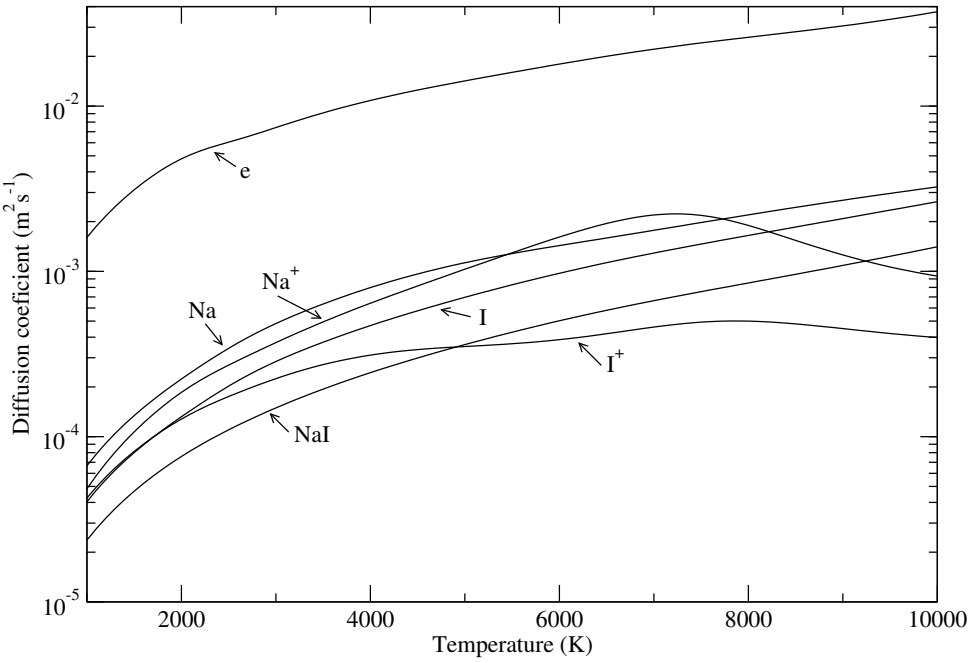

Figure 2.8: *Calculated diffusion coefficients as a function of temperature for a Hg/Na/I mixture with* $p = 10^5$ *Pa and* $p_{\{Na\}} = p_{\{I\}} = 5 \cdot 10^3$ *Pa (Johnston, 2003).*

In an actual lamp, this method for calculating $E_j(z)$ is not realistic at the bottom ($z \approx 0$) and top ($z \approx L$) since the points of electrodes, between which the current flows, are not located at $z = 0, L$, but a few millimetres from the bottom and top. Ignoring this leads to large errors in the electric field calculation, since at the low temperatures near the bottom and top walls, the electrical conductivity is so low that unrealistically large E_j values are needed in order to reach the required total current I.

To remedy this without actually adding electrodes to the model, equation (2.80) is only applied in the centre of the lamp, between the electrodes. At the top and bottom, transition regions of length $L_T = 0.2L$ are created, where the E_z field is smoothly varied from 0 at the wall to the value given by equation (2.80).

The electrical current in a typical metal halide lamp is of the order of several Amperes. However, since radiative energy losses are not considered in the current model and the only way to remove energy from the lamp is through thermal conduction through the wall, the current used in the calculations has to be significantly smaller. It turns out that a current of 0.1 A gives a temperature profile with a peak value of about 6000 K, which is a realistic value for a metal halide lamp.

Figure 2.9 gives the resulting temperature profile for a 10^5 Pa mixture with a 0.1 A current. The influence of convection is minimal, so the main parameters that determine the temperature profile are thermal conductivity and Ohmic dissipation. The axial temperature peaks at the places where the E_j transition region stops. At these points, where the tips of the electrodes would be, the current is carried by a narrow part of the plasma so that the Ohmic dissipation density is high. Note that even though it appears as if the gradients in the r direction are much less steep than those in the z direction, this is not true and merely the result of mapping the $L : R = 4 : 1$ cylinder cross section onto a square.

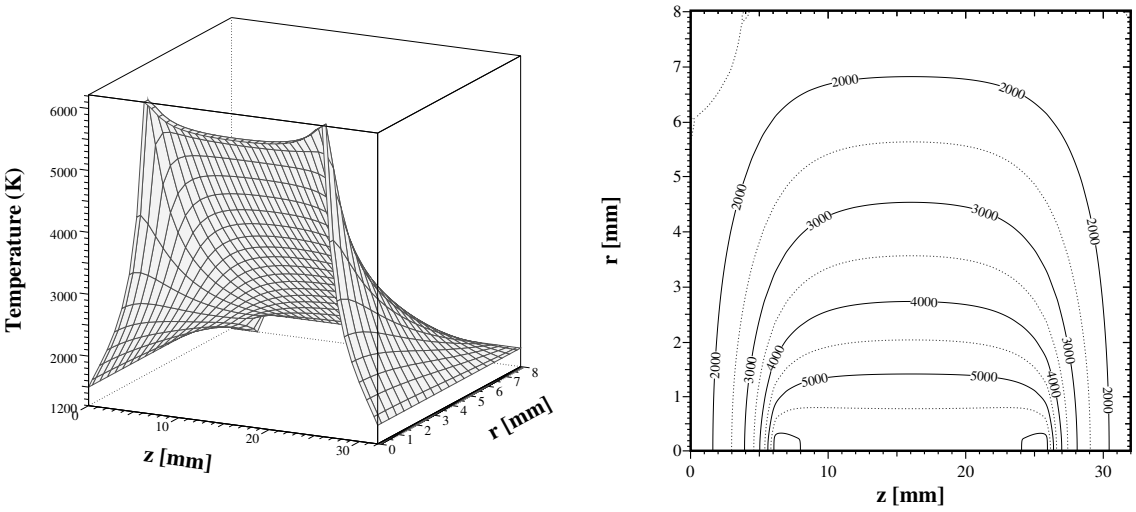

Figure 2.9: *Surface (left) and contour (right) plots of the calculated temperature profile for a* $p = 10^5$ *Pa Hg/Na/I mixture with an axial current of* 0.1 *A. In the* $z = 0, r = R$ *corner is the cold-spot at 1200 K, the other parts of the vessel wall are at 1500 K. The central value is near 6000 K. Since the electrical conductivity* σ *is strongly temperature dependent, most of the current will be carried by the hot centre of the plasma. The end points of the transition zones (at 6 mm from the top and bottom) are clearly visible.*

2.5.4 Elemental partial pressure calculations

Considering the fact that the equation for the elemental flux contains terms describing diffusive (∇p_i), convective ($\vec{u}$), ambipolar (∇p_e), and reactive ($\nabla(p_\alpha/p_i)$) effects, it makes sense to consider limiting cases in which the elemental flux equation is simpler. The diffusive and chemical terms are central to the theory and must remain, while the ambipolar term is only effective for ions and even then, as was shown in the previous section, can be approximated by multiplying the dominant ion diffusion coefficient by $(1 + Z_i)$. The convection term, therefore, is the obvious term to be eliminated in the first calculation, which can easily be achieved in the model by setting the bulk velocity to 0 m/s.

This convection-less calculation is not an entirely academic exercise; it is expected that there are real-life configurations where the elemental distribution is dominated by the diffusive and ambipolar terms and convection can be ignored.

While the temperature for the configuration was already shown in figure 2.9, figure 2.10 now shows the calculated values of $p_{\{Na\}}$, for a total pressure $p = 10^5$ Pa and a cold-spot partial pressure $p_{\{Na\}} = 10^3$ Pa. The most striking characteristic of the solution for $p_{\{Na\}}$ is that the pressure drops steeply near the walls. After dropping approximately 700 Pa, over a distance of about 2 mm from the north, east, and west walls $p_{\{Na\}}$ reaches a plateau at 300 Pa, then continues the descent to the minimal value of 170 Pa.

The $p_{\{Na\}}$ gradient can be understood by examining the various forms in which Na elements appear. Figure 2.11 shows the dimensionless quantity $[Na]/\{Na\}$ which is zero if all Na elements are in contained in molecules (NaI), near the north, east, and west walls or contained in ions (Na^+), near the axis at the south boundary, and unity if all Na elements are contained

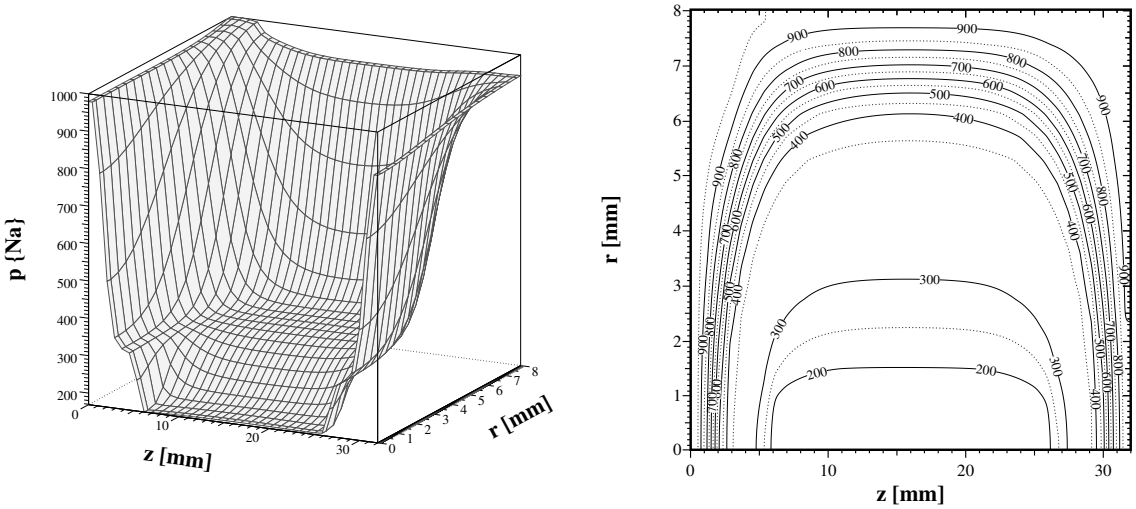

Figure 2.10: *Elemental partial pressure of Na with a cold-spot (at $z = 0, r = R$) pressure of 10^3 Pa, calculated without convection. The fact that $p_{\{Na\}}$ is slightly lower at the top than at the bottom is caused by the asymmetric location of the cold-spot.*

in atoms. It is clear to see that the region where $[Na]/\{Na\} \approx 1$ is the same region where the $p_{\{Na\}}$ value is constant. The steep gradients must therefore have something to do with the reactive term $\nabla(p_i/p_\alpha)$.

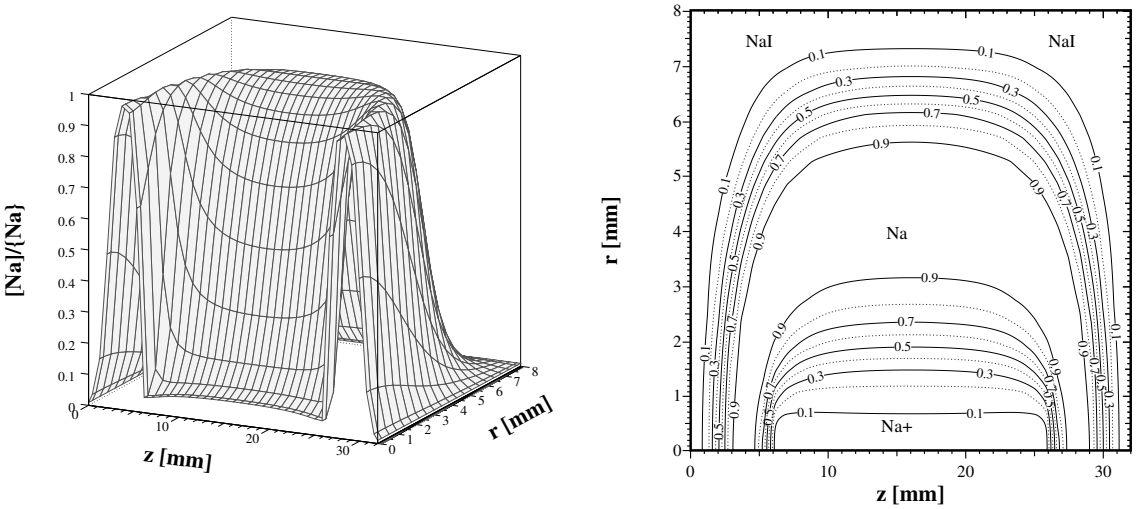

Figure 2.11: *Surface and contour plots of the fraction of Na elements in atomic form, $[Na]/\{Na\}$. Close to the north, east, and west walls, the Na elements are almost 100% in molecular NaI form. At the axis, all Na elements form Na^+ ions. In between is a ring where nearly all Na elements are in atomic form.*

The "back of an envelope" calculation to explain the steep gradients is as follows. At temperatures where there are approximately equal $[NaI]$ and $[Na]$ densities, the gradient of $[Na]$

will tend to point in the same direction as the gradient of T, since at higher temperatures the Na + I $\leftrightarrow$ NaI balance shifts to the left, while the $[NaI]$ gradient will point in the opposite direction. Ignoring Na^+, which has a very low density at temperatures where NaI still exists, and assuming that I elements are available in abundance so that the $[NaI]$ density is a function of $\{Na\}$ and T only, the $[Na]$ and $[NaI]$ gradients can be approximated by

$$\begin{aligned} \nabla[Na] &\approx \frac{1}{2}\nabla\{Na\} + \frac{\partial[Na]}{\partial T}\nabla T, \\ \nabla[NaI] &\approx \frac{1}{2}\nabla\{Na\} + \frac{\partial[NaI]}{\partial T}\nabla T \approx \frac{1}{2}\nabla\{Na\} - \frac{\partial[Na]}{\partial T}\nabla T. \end{aligned} \tag{2.81}$$

The value of $[Na]$ is proportional to $\exp(-E_d/kT)$, with $E_d = 3.1$ eV the dissociation energy of NaI, which is the most temperature sensitive term in the full equation for $[Na]$. The derivative with respect to T is therefore approximately given by

$$\frac{\partial[Na]}{\partial T} \approx \frac{E_d}{kT^2}[Na]. \tag{2.82}$$

The diffusion fluxes of Na and NaI can be obtained from equation (2.62) by neglecting the convection term, yielding

$$\vec{\Gamma}_{Na} = -D_{Na}\left(\frac{1}{2}\nabla\{Na\} + [Na]\left(\frac{E_d}{kT}+1\right)\frac{\nabla T}{T}\right), \tag{2.83}$$

$$\vec{\Gamma}_{NaI} = -D_{NaI}\left(\frac{1}{2}\nabla\{Na\} + [NaI]\left(-\frac{E_d}{kT}+1\right)\frac{\nabla T}{T}\right). \tag{2.84}$$

Figure 2.12 shows the calculated particle densities for an axial cross section (left hand side) and a radial cross section (right hand side). The point where $[Na] \approx [NaI] \approx \{Na\}/2$ is at about 1.5 mm from the walls at a temperature of about 2000 K, as can be seen in figure 2.9.

In the absence of external forces that give rise to a bulk flow, the net elemental flux should be zero as well, so that (again neglecting Na^+) $\vec{\Gamma}_{Na} + \vec{\Gamma}_{NaI} = \vec{0}$. At 2000 K, the factor $E_d/(kT) \approx 18$, so that the $+1$ addition in front of $\nabla T/T$ in equation (2.83) can be neglected. Using $[Na] = [NaI] = \{Na\}/2$, and rearranging terms then gives

$$(D_{Na} + D_{NaI})\frac{\nabla\{Na\}}{\{Na\}} = (-D_{Na} + D_{NaI})\frac{E_d}{kT}\frac{\nabla T}{T}. \tag{2.85}$$

In figure 2.8 it can be seen that at 2000 K, $D_{Na} \approx 2 \cdot 10^{-4}$ and $D_{NaI} \approx 6.5 \cdot 10^{-5}$, so that $(D_{Na} + D_{NaI})/(-D_{Na} + D_{NaI}) \approx -2$. Then, using $\nabla p/p = \nabla n/n + \nabla T/T$,

$$\frac{\nabla p_{\{Na\}}}{p_{\{Na\}}} \approx -8\frac{\nabla T}{T}, \tag{2.86}$$

which explains the steep gradients in $p_{\{Na\}}$ in the regions where the mixture goes from molecular NaI to atomic Na.

Essentially, this effect is caused by the fact that on one side NaI molecules are diffusing away from the boundary, while at the same time Na atoms diffuse towards the walls. Since the atoms have higher diffusion coefficients than the molecules, the only way to balance the Na elemental flux is to lower the $\{Na\}$ elemental density in the region where the atoms are.

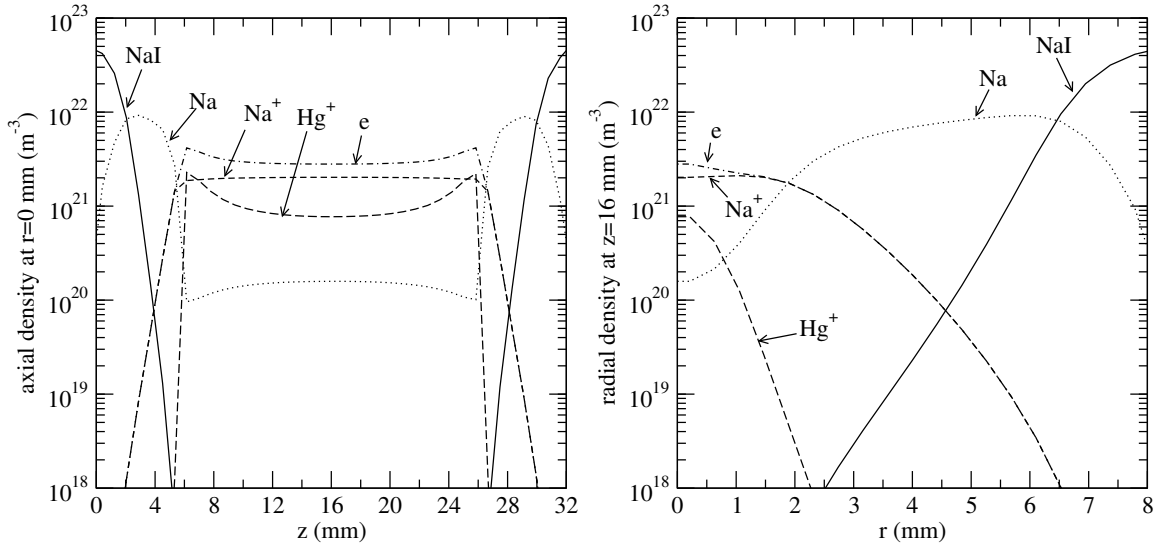

Figure 2.12: *Particle densities at the axis as a function of z (left) and halfway the z axis as a function of r (right). The plots clearly show the zones where Na appears in molecules, atoms and ions. Also note that the profiles close to walls look very similar. The plot on the left hand side for $z = 24 \ldots 32$ is almost identical to the plot for $r = 0 \ldots 8$ on the right.*

A similar effect occurs at the location where the transition is made from Na atoms to Na^+ ions. However, here is also another effect at work. The right hand side of figure 2.12 shows that there is a location with $[Na] = [Na^+]$ at $z = 16$ mm, $r = 2$ mm, at a temperature of about 4400 K. At this temperature, figure 2.8 shows that the Na^+ ions have a slightly lower diffusion coefficient than the atoms, so one would expect an increase in $p_{\{Na\}}$ rather than the observed decrease. However, due to the ambipolar term, which can be accounted for by multiplying D_{Na^+} by 2 since Na^+ is effectively the only ion, the Na^+ ions diffuse a little more quickly than the Na atoms, so that again the elemental partial pressure drops.

Adding convection to the elemental transport equations changes the solution for p_α rather a lot. Figure 2.13 shows the convection field for the current mixture. The bulk flows upwards, against the gravitational force, at the axis and downwards near the cylinder wall. At the bottom the bulk flows inwards, towards the axis, and at the top it flows outwards, towards the wall. The highest convection velocity is about 14 cm/s at the axis.

Figure 2.14 shows the solution for $p_{\{Na\}}$ with convection. The influence of the reactive and ambipolar terms, causing downward gradients from the wall, is still visible, but now there is a strong z dependence as well. Also note that the cold-spot, at the north-west corner, is no longer the location with the highest elemental partial pressure. The boundary conditions merely specify that $p_{\{Na\}} = 10^3$ Pa at the cold-spot, but do not ensure that this is also the highest value of $p_{\{Na\}}$ in the mixture. However, the bottom of the cylinder is at a temperature of 1500 K, while the cold-spot is at 1200 K, so that the NaI vapour pressure at the bottom may still be physically possible.

The cause of the axial segregation can be better understood by examining the flux density of Na elements, sketched in figure 2.15. The Na elements follow the same pattern as the bulk flow, except that during the upwards transport along the axis, the Na elements partly diffuse away towards the wall again, so that the total $\{Na\}$ density carried upwards along the axis decreases.

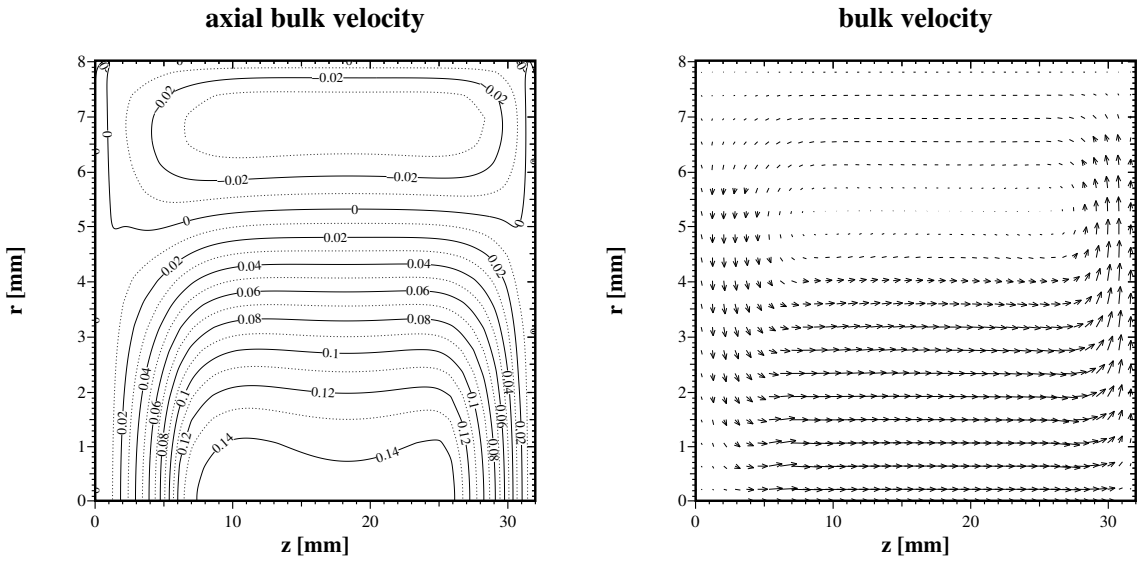

Figure 2.13: *Results of the bulk velocity calculation for a total pressure of* 10^5 *Pa. The bulk flows upwards (against gravity, which points towards the negative* z *axis) at the axis of the cylinder, with a maximum velocity of about 14 cm/s, and downwards, at about 2 cm/s, near the cylinder wall. The contour plot on the left shows the magnitude of the axial component, while the vector plot on the right gives an overview of the velocity field, where the lengths of the arrows are proportional to the velocity.*

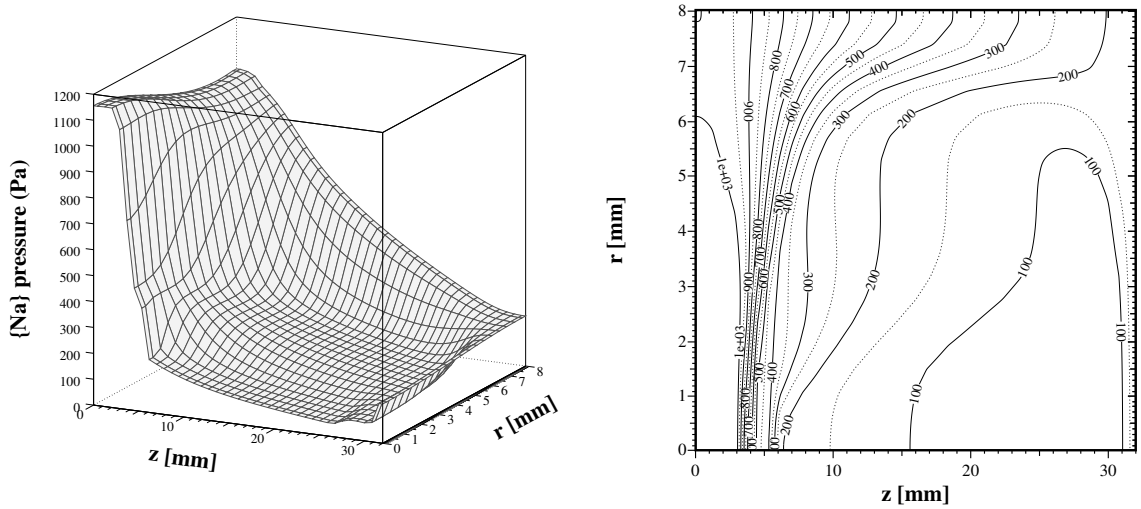

Figure 2.14: *The Na elemental partial pressure* $p_{\{Na\}}$ *with bulk convection. In contrast to the previous calculation without bulk convection, the Na pressure now goes down as a function of* z*.*

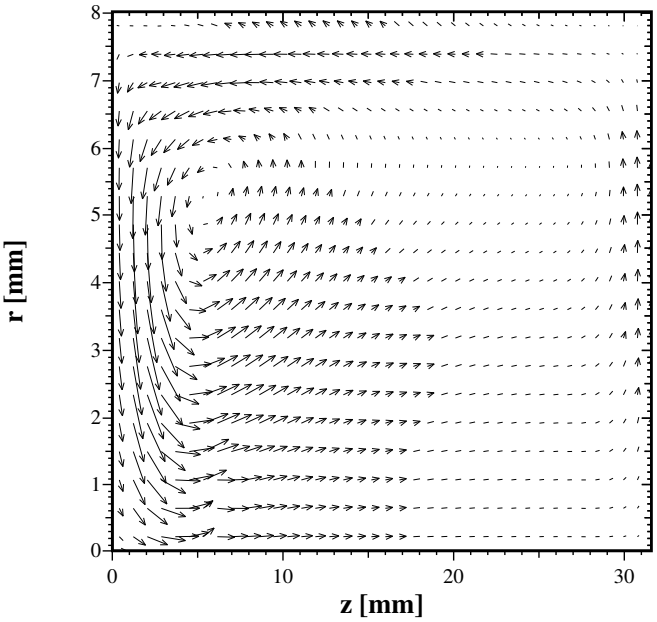

Figure 2.15: *A vector plot of the Na elemental flux density. At the bottom of the cylinder, Na elements are transported from the cylinder wall towards the axis. From there, the elements are carried upwards by the bulk flow and diffuse away from the axis, so that the total $\{Na\}$ density carried upwards diminishes.*

2.6 Discussion and conclusion

In this chapter, the standard local method (with only p and T as input parameters) for calculating LTE particle densities has been extended with a transport model for calculating the whereabouts of minority elements. For many (close to) LTE light sources only vapour pressures at the boundary or cold-spot are given, so that an elemental transport model is essential for a correct description of the chemistry.

The approach developed in this chapter, creating and solving a transport equation (written in the form of a ϕ-equation) for each elemental partial pressure p_α, works and gives specific results that can be verified using approximate calculations.

The elemental flux density equation (2.74) contains many physical quantities that are calculated in another part of a full model. In PLASIMO, a full model consists of a combination of modules that calculate a specific aspect of the plasma under investigation. A solution is obtained by iteratively letting each module do its calculation based on the currently calculated values of all plasma parameters, until certain convergence criteria are reached. Figure 2.16 shows an overview of the modules involved in an LTE densities calculation, from which it is clear that the LTE transport module directly uses results from all other modules.

The results of the LTE densities calculation in turn affect other parts of the model calculation. Solving the elemental transport equation, $\nabla \cdot \vec{\Gamma}_\alpha = 0$, for each element α, and using the model's current values for the above listed quantities, gives a new set of local p_α values for the local LTE calculation. This in turn gives new values for all densities n_i, which again affect

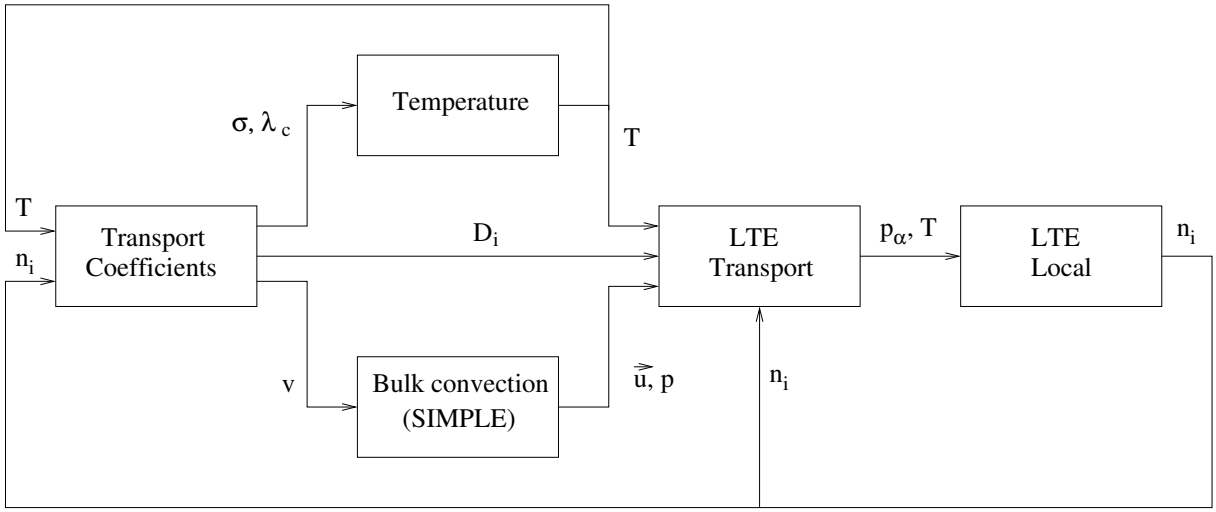

Figure 2.16: *Overview of the* PLASIMO *modules involved in an LTE densities calculation. All modules are iteratively updated until convergence is reached.*

the elemental flux (2.74) via p_i and, to a lesser extent, D_i. The LTE densities also affect the bulk calculation, since the mixture composition determines the viscosity and density, and the temperature, via the thermal and electrical conductivity. However, since the elemental transport equations deal with minority species, the influences of elemental transport on the bulk and temperature fields will generally be small. One notable exception to this rule are ions, since a minority species with a low ionisation potential, such as Na, may supply more ions than a buffer gas like Hg, as figure 2.12 shows.

The calculations without bulk convection have shown that the reactive and ambipolar terms alone have a large effect on the distribution of elements. The steep gradient of $p_{\{Na\}}$ near the walls, where the mixture switches from molecular NaI to atomic Na and I, is determined by the difference between the diffusion coefficients of Na and NaI. Closer to the centre of the plasma another gradient occurs because of the difference between Na and Na^+ fluxes, where not only the reactive term but also the ambipolar term has a strong influence. In order to correctly calculate the distribution of elements, it is therefore very important to have valid diffusion coefficients.

Bulk convection causes an axial segregation of the minority species, as figure 2.14 shows. An interesting modelling experiment would be to investigate the influence of bulk velocity on the segregation. The calculation without convection has shown that the lower limit gives a distribution that is nearly (but not quite, due to the asymmetry introduced by the cold-spot) symmetric at the top and bottom. One can imagine that at higher convection velocities — that is, at higher pressure or smaller aspect ratio $L : R$ — the importance of the radial elemental diffusion away from the axis, as illustrated in figure 2.15, is reduced. Therefore, there may be an optimum convection velocity where the axial decrease of elemental partial pressures is maximal. Unfortunately, due to the extensive manual tweaking that is currently needed to obtain convergent bulk flow solutions for the present configuration, this effect has not yet been investigated for a suitably large range of pressures and aspect ratios.

It must be mentioned that the current approach of using ϕ-equations for elemental partial pressures p_α is not the only means to calculate the distribution of elements. A coupled approach,

in which the transport equations for particles and local LTE balance and constraint equations are put together in one large matrix equation of the type $Ax = b$, is also possible. The dimension of the square matrix A would be $N_x \cdot N_y \cdot N_p$, with N_x and N_y the number of x and y grid points and N_p the number of distinct particles. The advantage of a coupled approach is that the model does not have to iterate through local (using a non-linear-equation solver) and non-local (using a ϕ-equation solver) calculation modules in order to find a consistent set of particle densities. The coupled approach, however, does not completely remove this problem. Since the balance equations are non-linear, the linear $Ax = b$ matrix equation still has to be set up and solved repeatedly in order to find a correct solution. Another disadvantage is that the coupled approach can not be implemented using the existing ϕ-equation infrastructure in PLASIMO, so that considerable extra programming effort would be needed.

A point where the current method can be improved is in the treatment of the friction term in the specific momentum balance, given by equation (2.31). In the current approach, only friction with the bulk species is accounted for, which is a fairly good approximation for neutral minority particles, but is less precise for ions, especially if the ion and electron densities are dominated by the minority elements as is the case in the Hg/Na/I mixture. A treatment that accounts for all of the $f_{ij}(\vec{u}_i - \vec{u}_j)$ terms in order to calculate particle flux densities is under development in PLASIMO, see Hartgers *et al.* (2002), but currently only used for non-LTE mixtures, where a transport equation is solved for each particle. Adapting this so-called self-consistent diffusion module for use by LTE mixtures would accomplish the twin goals of better LTE elemental diffusion treatment and tighter integration between the LTE and non-LTE parts of PLASIMO.

The omission of radiative transfer effects makes the current calculations hardly applicable to an actual metal halide lamp. However, the aim of this chapter is not to correctly model a metal halide lamp, but to develop and test methods for calculating transport-sensitive LTE densities. Still, the obtained radial temperature profile and convection field, calculated using a reduced current of 0.1 A and at the relatively low pressure of 10^5 Pa, show good agreement with the trends for a Hg/Na/Sc/I metal halide lamp (but at significantly lower Na/Sc/I partial pressures than in the current work) found by Hashiguchi *et al.* (2001).

Chapter 3

Basic radiation theory and implementation

Abstract

This chapter presents basic equations in radiation theory and outlines the design of the radiation modules in PLASIMO. The distinction between local and non-local radiative quantities is discussed, and the escape factor Λ is introduced.

3.1 Introduction

The first part of this chapter provides an overview of the basic equations and quantities in radiative transfer, which form the basis of the theory presented in the next chapters. As was mentioned in the introductory chapter, the following three chapters (4-6) first saw the light of day as scientific publications. In order to make them as self-contained as possible, and also to clarify which one of the many notational conventions in the field of radiative transfer the authors prefer, many of the basic equations are introduced in each paper. The decision was made to include these papers as chapters in this thesis without making changes. Persons reading this thesis from cover to cover may notice that some parts of the radiation theory are repeated. Casual thesis readers, which usually form a majority, will find that the following chapters are mostly self-contained. The theory in the first part of this chapter also provides a basis for a discussion of the design of the radiation modules in PLASIMO.

Like the subject of LTE density calculations in the previous chapter, the calculation of radiation properties can be split into a local (depending on locally given parameters such as temperatures and densities) and a non-local (sensitive to transport effects and details of the geometry) part, as section 3.2 shows. The local theory is explored further in section 3.3 while non-local theory is discussed in section 3.4. As such, these two sections outline the problems that will be dealt with in the following chapters. Chapter 4 is concerned with the local radiative emission and absorption properties of di-atomic molecules, chapter 5 is somewhat in the middle, touching on both local and non-local aspects of radiative transfer, while chapters 6 and 7 discuss approaches for calculating the non-local effects of radiation.

The discussion of the local and non-local aspects of radiation will make clear how radiation is connected to other aspects of plasmas. These relations must of course be considered in the design of a modular computational code like PLASIMO. Therefore, before the next chapters dive into various highly specific details of radiation calculations, the second part of this chapter,

starting at section 3.5, gives an overview of the design and implementation of the radiation modules in PLASIMO.

Since most of the concepts and equations in this chapter can be found in standard texts, they will generally be introduced without literature references. A few good standard texts are, in chronological order, Chandrasekhar (1960); Rybicki and Lightman (1979); Molisch and Oehry (1998); Rutten (2000).

3.2 The equation for radiative transfer

The equation for radiative transfer is a first order differential equation that describes the change in intensity I_ν [1] [$\mathrm{Wm^{-2}Hz^{-1}sr^{-1}}$] along a path s [m]. Being deceptively simple, it reads

$$\frac{dI_\nu}{ds} = j_\nu - \kappa I_\nu, \tag{3.1}$$

where j_ν [$\mathrm{Wm^{-3}Hz^{-1}sr^{-1}}$] is the local emission coefficient and κ [$\mathrm{m^{-1}}$] the local absorption coefficient. The convention followed in this work is to give spectral quantities, that is, quantities that are defined per frequency interval such as j_ν and I_ν, a subscript ν. Except where it is needed for clarity, the dependence of light related quantities on frequency ν is implied (e.g. κ rather than $\kappa(\nu)$).

The complex character of equation (3.1) is mostly hidden in the intensity $I_\nu(\nu, \vec{r}, \vec{\Omega})$. This quantity represents the energy per unit of time, area, solid angle, and frequency interval propagating through a surface at position $\vec{r}$ with a normal pointing in the direction $\vec{\Omega}$. With $I_\nu(\nu, \vec{r}, \vec{\Omega})$ one can compute the radiative flux Φ^ϵ_ν [$\mathrm{WHz^{-1}}$] through an arbitrary surface A corresponding to the radiation in the direction $\vec{\Omega}$ with margin $d\Omega$ (see figure 3.1),

$$\Phi^\epsilon_\nu = I_\nu(\vec{\Omega} \cdot \vec{A})d\Omega = I_\nu(\vec{A} \cdot d\vec{\Omega}), \tag{3.2}$$

where $\vec{\Omega}$ is a unit vector, $\vec{A}$ surface A times its normal vector, $(\vec{\Omega} \cdot \vec{A})$ the inner product of $\vec{\Omega}$ and $\vec{A}$, and $d\vec{\Omega}$ the vector with direction $\vec{\Omega}$ and magnitude $d\Omega$.

For a blackbody radiator in thermal equilibrium, I_ν is given by Planck's Law,

$$B_\nu = \frac{2h\nu^3}{c^2}\frac{1}{\exp(h\nu/kT) - 1}. \tag{3.3}$$

In the next section expressions for j_ν and κ in terms of local plasma properties such as densities and temperature will be given. Solutions of the equation for radiative transfer (3.1) will be examined in section 3.4.

3.3 Local radiation properties

The relation between j_ν and plasma properties can be made plausible by examining the first two terms of the equation for radiative transfer (3.1). Consider the interaction between a beam and a plasma slab, as in figure 3.2.

[1] The convention of the field of astrophysics is followed by calling this quantity intensity rather than radiance

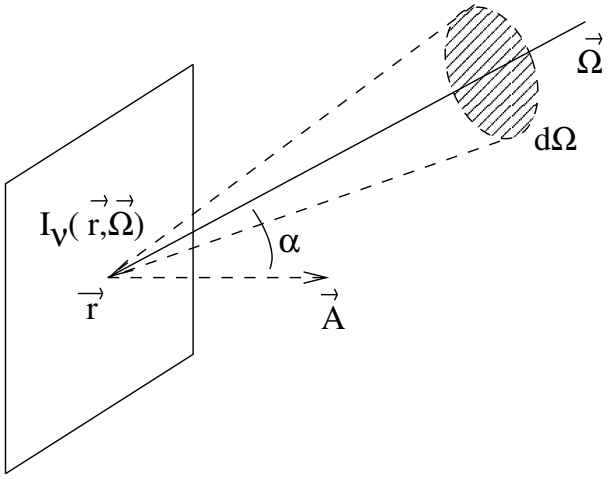

Figure 3.1: *A probe line propagating in the direction $\vec{\Omega}$ and representing the radiation within solid angle $d\Omega$. The spectral power flux Φ^{ϵ}_{ν} through surface A equals $I_{\nu}(\vec{A}\cdot\vec{\Omega})d\Omega$.*

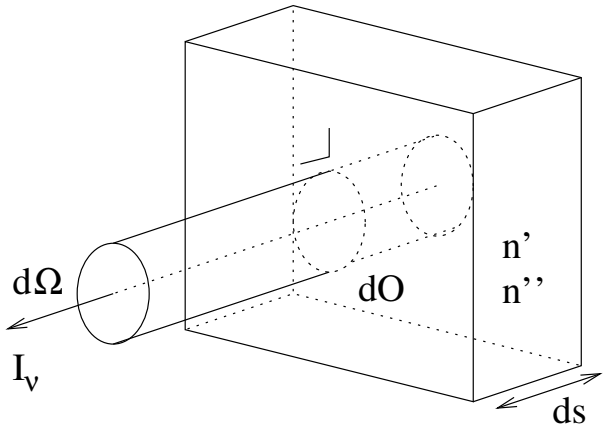

Figure 3.2: *Interaction between a plasma slab of thickness ds and a beam with cross section dO and solid angle fraction $d\Omega/(4\pi)$. Inside the plasma slab are emitting (density n') and absorbing (density n'') particles.*

The beam is characterised by its initial flux density $\Phi^{\epsilon}_{\nu,0}$, a cross section dO, and a direction margin given by the solid angle $d\Omega$. The plasma slab has a thickness ds and contains, among others, particles with density n'[2] which due to spontaneous decay add photons to the radiation field and thus to the beam. The decay probability [s^{-1}] equals A (the so-called Einstein coefficient) whereas the photon energy equals $h\nu$. The increase of the power in the beam $d\Phi^{\epsilon}$ caused by spontaneous emission from the plasma slab equals the number of photons added to the beam per unit time, times the energy per photon. The first quantity is found by multiplying the number of atoms in the beam-plasma overlap volume, $n'dOds$, by the transition frequency A and solid angle fraction $d\Omega/(4\pi)$. Combined with the energy per photon $h\nu$, this gives

$$d\Phi^{\epsilon} = n'dOdsh\nu d\Omega/(4\pi). \tag{3.4}$$

[2]The convention is to label the properties of the radiating upper state with a single prime, and those of the absorbing lower state with double primes.

Since $dI = d\Phi^{\epsilon}/(dOd\Omega)$, this means that the intensity increase equals $dI = n'dsh\nu A/(4\pi)$, so that from equation (3.1) follows that $j = n'h\nu A/(4\pi)$. Finally, not all the emitted photons have the same energy, instead the frequency distribution is given by the normalised line profile ϕ_ν[3] This implies that the spectral emission coefficient j_ν is given by

$$j_\nu = \frac{h\nu}{4\pi} n' A \phi'_\nu. \tag{3.5}$$

In the course of the transition through the slab, the beam will also loose photons due to absorption by particles with density n'', and gain some due to stimulated emission by particles with density n'. Both effects are linear in the beam intensity I_ν, and are thus accounted for by the κI_ν term in equation (3.1). Since the absorption and stimulated emission processes are also linear in the lower and upper state densities respectively, κ can be written in terms of absorption (σ_{abs}) and stimulated emission (σ_{stim}) cross sections,

$$\kappa = n''\sigma_{abs} - n'\sigma_{stim}. \tag{3.6}$$

Kirchoff's law states that in radiative equilibrium, emission equals absorption, so that $dI_\nu/ds = 0$ and, following from the equation of radiative transfer (3.1), $j_\nu = \kappa I_\nu$, or

$$I_\nu = \frac{j_\nu}{\kappa} = S_\nu, \tag{3.7}$$

introducing the source function S_ν, which is the ratio of j_ν to κ. In radiative equilibrium, the intensity I_ν is given by Planck's Law (3.3), so that the equilibrium value for κ follows from $j_{\nu,eq}/\kappa_{eq} = S_{\nu,eq} = B_\nu$,

$$\kappa_{eq} = \frac{j_{\nu,eq}}{B_\nu} = \frac{n'h\nu A\phi'_\nu}{4\pi}\frac{c^2}{2h\nu^3}\left(\exp\left(\frac{h\nu}{kT}\right) - 1\right). \tag{3.8}$$

In chapter 2 it has been shown that the equilibrium ratio between lower and upper states n'' and n' is given by the LTE Boltzmann balance (2.18),

$$\frac{n''}{n'} = \frac{g''Z''}{g'Z'}\exp\left(-\frac{E'' - E'}{kT}\right), \tag{3.9}$$

where g' and g'' are the degeneracies of the upper and lower state respectively, Z' and Z'' are the internal partition sums (as in equation (2.14)), and E' and E'' are the offset energies.

Substituting (3.9) into (3.6), setting it equal to (3.8) and dividing the left and right hand sides by n' gives

$$\sigma_{abs}\frac{g''Z''}{g'Z'}\exp\left(-\frac{E'' - E'}{kT}\right) - \sigma_{stim} = \frac{c^2}{8\nu^2\pi}A\phi'_\nu\left(\exp\left(\frac{h\nu}{kT}\right) - 1\right). \tag{3.10}$$

[3]From here on, complete frequency redistribution (CFR) will be implicitly assumed. Essentially, CFR means that the frequency distribution ϕ_ν for spontaneous emission is independent of the distribution of the absorbed radiation intensity I_ν. This is usually a valid assumption in plasmas, such as high pressure light sources, where the collision frequency is larger than the transition probability A. For a discussion of complete and partial frequency redistribution, see chapter 11 of Molisch and Oehry (1998).

The cross section for stimulated emission is thus given by

$$\sigma_{stim} = \frac{c^2}{8\pi\nu^2} A\phi'_\nu, \tag{3.11}$$

while the cross section for absorption is defined as

$$\sigma_{abs} = \frac{c^2}{8\pi\nu^2} A\frac{g'}{g''}\phi''_\nu. \tag{3.12}$$

The absorbing line profile ϕ''_ν is related to the emitting line profile ϕ'_ν according to,

$$\phi''_\nu = \frac{Z'}{Z''} \exp\left(\frac{h(\nu-\nu_0)}{kT}\right) \phi'_\nu, \tag{3.13}$$

where the central frequency ν_0 is defined by the difference in offset energies, $\nu_0 = (E' - E'')/h$. Equation (3.13) shows that if the two radiating states have internal energy distributions that gives rise to radiation at frequencies ν that depart significantly from the central frequency ν_0, the line profiles for the emitting and absorbing states are not necessarily identical. However, in LTE they are still related according to (3.13). For most atomic transitions, where the internal partition functions of the emitting and absorbing states are approximately unity and the spread in frequency $\Delta\nu$ is much smaller than the central frequency ν_0, equation (3.13) gives the standard result $\phi'_\nu \approx \phi''_\nu$, which explains why equation (3.13) is rarely found in standard texts. However, molecular radiators, which are discussed in chapter 4, have a tendency to emit radiation over such a broad frequency range that this approximation is no longer valid.

Finally, expressions for some common line profiles are given below.

- The *Doppler* profile describes broadening due to thermal motion. The emission and absorption distributions are given by

$$\phi_{\nu,D} = \frac{1}{\Delta\nu_D}\sqrt{\frac{4\ln 2}{\pi}} \exp\left(-4\ln 2\left(\frac{\nu-\nu_0}{\Delta\nu_D}\right)^2\right), \tag{3.14}$$

  with the Doppler full width at half maximum (FWHM) $\Delta\nu_D$ given by

$$\Delta\nu_D = \nu_0\sqrt{\frac{8\ln 2kT}{mc^2}}. \tag{3.15}$$

- The *Lorentz* profile describes natural distributions and collision broadening. It is given by

$$\phi_{\nu,L} = \frac{1}{\pi}\frac{\Delta\nu_L}{(\nu-\nu_0)^2 + (\Delta\nu_L)^2}, \tag{3.16}$$

  where FWHM $\Delta\nu_L$ is A in the case of natural line broadening.

- A combination of the Doppler and Lorentz line profiles is called a *Voigt* profile,

$$\phi_{\nu,V} = \frac{1}{\Delta\nu_D}\sqrt{\frac{4\ln 2}{\pi}}\frac{y}{\pi}\int_{-\infty}^{\infty}\frac{\exp(-t^2)}{y^2 + \left(\frac{\nu-\nu_0}{\Delta\nu_D}\sqrt{4\ln 2} - t\right)^2}dt, \tag{3.17}$$

  with y the ratio of Lorentz to Doppler widths,

$$y = \frac{\Delta\nu_L}{\Delta\nu_D}\sqrt{\ln 2}. \tag{3.18}$$

3.4 Non-local transfer effects

The equation for radiative transfer (3.1) is sometimes written in another form, which can be obtained by dividing (3.1) by κ,

$$\frac{1}{\kappa}\frac{dI_\nu}{ds} = \frac{dI_\nu}{d\tau} = S_\nu - I_\nu, \tag{3.19}$$

introducing optical depth τ, $d\tau = \kappa ds$. In this form, the equation reveals an important property, namely that the adjustment of intensity I_ν along a path s is so that the value of I_ν tends towards the source function S_ν (see equations (3.7) and (3.3)). Therefore, the reciprocal of the absorption coefficient, κ^{-1}, is a measure of the distance over which an incident intensity I_ν is adjusted to the local source function S_ν.

Since the source function is a local property, the magnitude of this characteristic distance provides an important boundary criterion for the (non-)locality of radiation. If absorption is so high that κ^{-1} is much smaller than characteristic distances and gradient lengths in the plasma, radiation is effectively a local effect, and the transport is due to local gradients in the source function (see for example the discussion of the high opacity limit in section 6.3.3). However, it is rarely possible to treat radiation purely locally. In large part this is due to the fact that line profiles ϕ_ν tend to have such a wide range of values that even for strongly absorbed transitions, there are still frequency intervals where κ^{-1} is significantly larger than a characteristic plasma dimension.

Returning to the original differential equation for radiative transfer (3.1), an expression for $I_\nu(s)$ can be readily written down in integral form,

$$I_\nu(s) = \int_{s_0}^{s} j_\nu(s') \exp\left(-\int_{s'}^{s} \kappa(s'')ds''\right) ds', \tag{3.20}$$

where s_0 is the starting point (may be $-\infty$), s' and s'' are integration variables, and the integral in the exponent is the optical depth $\tau(s', s)$ between points at s' and s,

$$\tau(s', s) = \int_{s'}^{s} \kappa(s'')ds''. \tag{3.21}$$

Equation (3.20) shows that the intensity I_ν at a given point s along a path is due to emission at previous points $j_\nu(s')$ attenuated by an absorption factor $\exp(-\tau(s', s))$. This is illustrated in figure 3.3.

A useful quantity in radiative transfer is the direction-averaged intensity J_ν:

$$J_\nu = \frac{1}{4\pi}\int_{4\pi} I_\nu d\Omega. \tag{3.22}$$

From the definition of J_ν (3.22) and the integral expression for I_ν (3.20), an integral equation for J_ν can be given in spherical coordinates centred around the location where J_ν is calculated,

$$J_\nu = \frac{1}{4\pi}\int_0^{\pi}\int_0^{2\pi} \sin\theta \int_0^{\infty} j_\nu(r, \phi, \theta) \exp\left(-\int_0^{r} \kappa(r', \phi, \theta)dr'\right) dr d\phi d\theta. \tag{3.23}$$

Once J_ν is known, the effects of radiative transfer on the plasma as a whole can be calculated. The reason why radiative transfer calculations are difficult, is the fact that equation (3.23)

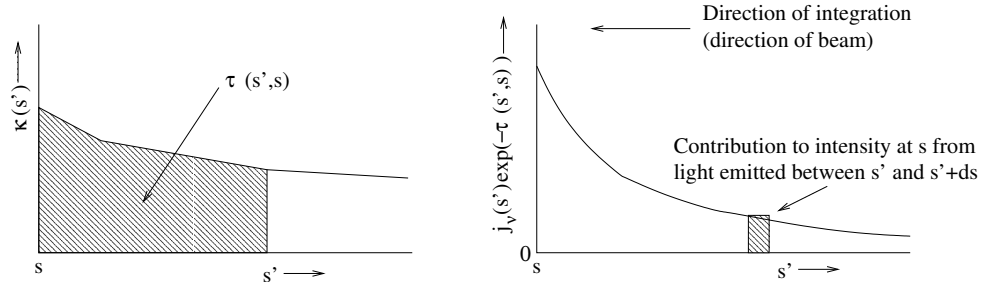

Figure 3.3: *Schematic illustration of the integral quantities in equation (3.20). On the left hand side, the optical depth between points s and s' is illustrated as the integral of κ. On the right hand side is shown how radiation emitted at s' contributes to the intensity at s with attenuation* $\exp(-\tau(s', s))$.

is an integral over the entire space where $j_\nu \neq 0$ (read: the plasma volume), which needs to be evaluated at every point in the volume. This is why two chapters in this thesis (6 and 7) are devoted to techniques to solve this problem.

In LTE, radiative transfer causes a transport of energy. The effect of radiation on the energy balance is as follows. The energy loss per unit time and per unit volume due to spontaneous emission, $(dU/dt)_{ems}$, is given by

$$\left(\frac{dU}{dt}\right)_{ems} = -\int_\nu \int_\Omega j_\nu d\nu d\Omega = -4\pi \int_\nu j_\nu d\nu. \tag{3.24}$$

This needs to be corrected for absorption and stimulated emission effects,

$$\left(\frac{dU}{dt}\right)_{abs} = \int_\nu \int_\Omega \kappa I_\nu d\nu d\Omega = 4\pi \int_\nu \kappa J_\nu d\nu, \tag{3.25}$$

so that the net influence is

$$\frac{dU}{dt} = 4\pi \int_\nu (\kappa J_\nu - j_\nu) d\nu. = 4\pi \int_\nu \kappa (J_\nu - S_\nu) d\nu. \tag{3.26}$$

The last form, with the $\kappa(J_\nu - S_\nu)$ term, shows again that in radiative equilibrium, with $J_\nu = I_\nu = S_\nu$, there is no net change in energy density U.

In LTE calculations in PLASIMO, the term dU/dt is a source term in the transport equation for the temperature.

For non-LTE, the required quantity is the change in particle densities. Realizing that each transition $n' \rightarrow n''$ involves one quantum of energy $h\nu$, the equations for dn/dt can be written down directly by dividing the previous equations in terms of energy density U by $h\nu$,

$$\frac{dn'}{dt} = -\frac{dn''}{dt} = 4\pi \int_\nu \frac{\kappa J_\nu - j_\nu}{h\nu} d\nu. \tag{3.27}$$

The possibility of having multiple transitions that overlap each other spectrally (e.g. for a given ν, j_ν is composed of the sum of $j_{\nu,i}$ of various different transitions i) makes the non-LTE case more complex. For a transition $n_i' \rightarrow n_i''$ we find

$$\frac{dn_i'}{dt} = 4\pi \int_\nu \frac{\kappa_i J_\nu - j_{\nu,i}}{h\nu} d\nu. \tag{3.28}$$

From an implementation point of view this means that the individual emission and absorption coefficients, $j_{\nu,i}$ and κ_i have to be stored as well as the summed values. When modelling an LTE plasma, one can save some computer resources by only storing the summed coefficients.

A convenient parameter to summarise the effects of emission and absorption for a given transition i is the escape factor Λ_i. There are various definitions of Λ in the literature, but here it is defined as the ratio between net emission (emission minus absorption) and spontaneous emission. For a specific frequency ν, the escape factor $\Lambda_i(\nu)$ is thus

$$\Lambda_i(\nu) = \frac{j_{\nu,i}(\nu) - J_\nu(\nu)\kappa_i(\nu)}{j_{\nu,i}(\nu)} = 1 - \frac{J_\nu(\nu)\kappa_i(\nu)}{j_{\nu,i}(\nu)} = 1 - \frac{J_\nu(\nu)}{S_{\nu,i}(\nu)}, \tag{3.29}$$

where the dependence of the various quantities on ν is emphasised. For optically thin radiation, where absorption is negligible, $\Lambda_i(\nu) \approx 1$, while for optically thick radiation, close to radiative equilibrium, $\Lambda_i(\nu) \approx 0$. If the intensity $J_\nu(\nu)$ is larger than the local equilibrium value, absorption processes outweigh emission and the escape factor is negative.

A frequency independent escape factor can be defined by integrating the nominator and denominator over ν separately,

$$\Lambda_i = \frac{\int_\nu (j_{\nu,i} - J_\nu\kappa_i)d\nu}{\int_\nu j_{\nu,i}d\nu} = 1 - \frac{\int_\nu J_\nu\kappa_i d\nu}{\int_\nu j_{\nu,i}d\nu}. \tag{3.30}$$

The usefulness of Λ can be shown by rewriting the equations for the energy and particle density source terms, equations (3.26) and (3.28) respectively, in terms of Λ:

$$\frac{dU}{dt} = -4\pi \int_\nu \sum_i j_{\nu,i}\Lambda_i(\nu)d\nu = -4\pi \sum_i \Lambda_i \int_\nu j_{\nu,i}d\nu, \tag{3.31}$$

$$\frac{dn_i'}{dt} = -\frac{dn_i''}{dt} = -4\pi \int_\nu \frac{j_{\nu,i}\Lambda_i(\nu)}{h\nu}d\nu \approx -4\pi \frac{\Lambda_i}{h\nu_{0,i}} \int_\nu j_{\nu,i}d\nu. \tag{3.32}$$

By writing $j_{\nu,i}$ as $n_i' h\nu A_i \phi_{\nu,i}'/(4\pi)$, as in equation (3.5), and using $\int_\nu j_{\nu,i}d\nu \approx n_i' h\nu_{0,i}A_i/(4\pi)$ — valid for most atomic transitions — the expressions become more elegant,

$$\frac{dU}{dt} = -\sum_i \Lambda_i n_i' h\nu_{0,i}A_i, \tag{3.33}$$

$$\frac{dn_i'}{dt} = -\frac{dn_i''}{dt} = -n_i'\Lambda_i A_i. \tag{3.34}$$

The averaged escape factor Λ_i can therefore be seen as an correction factor for the Einstein coefficient A_i of transition i.

In practice it is often more convenient to calculate the frequency averaged escape factor Λ_i not following the definition (3.30), but instead by using the spontaneous emission frequency distribution $\phi_{\nu,i}'$:

$$\Lambda_i = \int_\nu \Lambda_i(\nu)\phi_{\nu,i}'d\nu. \tag{3.35}$$

That this form is equivalent to equation (3.30) can be seen by substituting (3.29) into (3.35) to obtain

$$\Lambda_i = \int_\nu \left(1 - \frac{J_\nu\kappa_i}{j_{\nu,i}}\right)\phi_{\nu,i}'d\nu. \tag{3.36}$$

Using $\int \phi_{\nu,i} d\nu = 1$ for the first term in the integrant and again writing $j_{\nu,i} = n' h\nu A_i \phi'_{\nu,i}/(4\pi)$ in the second term then gives

$$\Lambda_i = 1 - \frac{1}{n'A} \int_\nu \frac{4\pi J_\nu \kappa_i}{h\nu} d\nu. \tag{3.37}$$

Realizing that $[4\pi J_\nu \kappa_i/(h\nu)]d\nu$ is the number of absorption events per unit of time per unit of volume in the frequency range $\nu \ldots \nu + d\nu$, and $n'A$ is the number of spontaneous emission events per unit of time per unit of volume, it is clear that equation (3.35) is an alternative representation of the frequency averaged escape factor of equation (3.30).

3.5 Design and implementation of the radiation modules

3.5.1 Modular design

The distinction between local (j_ν and κ) and non-local (J_ν) radiation quantities is clearly reflected in PLASIMO's radiation module design, which is schematically presented in figure 3.4.

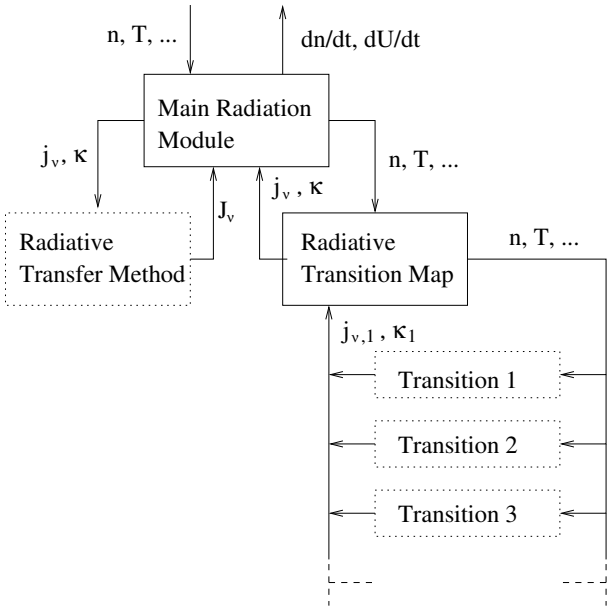

Figure 3.4: *Overview of the* PLASIMO *modules related to radiation. Boxes with dotted lines signify that the modules are plugins. For example, there are different radiative transfer methods for spherical and cylindrical configurations. Likewise, different plugins exist for radiative transitions.*

There is one main radiative transfer module, which contains a "Radiative Transition Map" and a "Radiative Transfer Method". The radiative transition map contains one or more "transition" objects, each of which describes a unique radiative transition. The radiation map, and the transitions it contains, only refer to local quantities such as densities and temperatures. On the other hand, the radiative transfer method, which is concerned with the radiation transport calculation, is generally strongly dependent on the geometry. Both the transition and transport

method modules are drawn with dotted lines, signifying that the functionality of both modules is implemented in plugins.

For a detailed treatment of PLASIMO plugins the reader is referred to chapter 3 of van Dijk (2001) or to van der Mullen *et al.* (2002). Essentially, a plugin is a unit of program code that uses selected data from the model as input and produces selected output in a prescribed format. For example, a PLASIMO transition plugin can use local values for densities n, temperature T, etc, and is required to produce values $j_{\nu,i}$ and κ_i. The actual details of the transition, for example the shape of the line profile or the value of A, are "hidden" from the framework. Likewise, a radiative transfer method plugin calculates J_ν given a set of j_ν and κ values for each grid point.

Figure 3.5 shows the place of the main radiative transport module in a PLASIMO LTE model, by extending figure 2.16 of chapter 2.

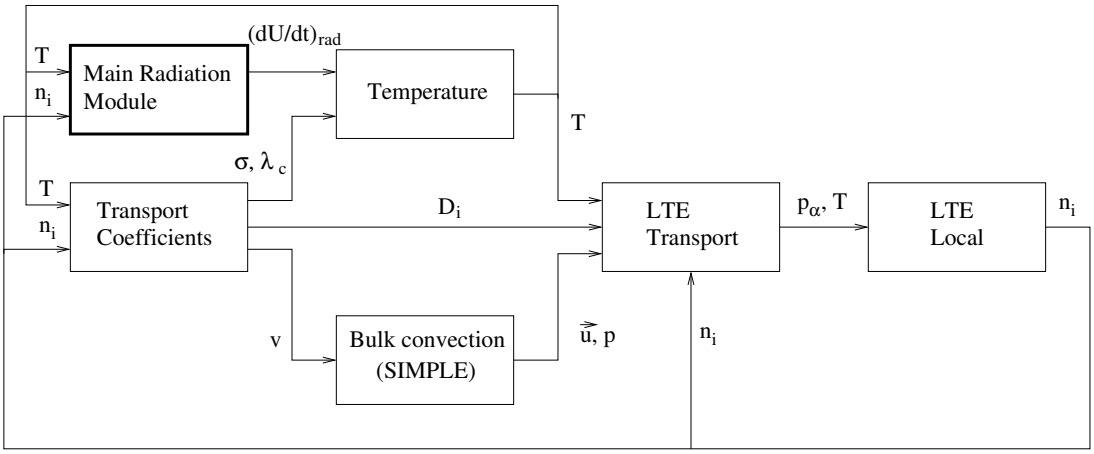

Figure 3.5: *Overview of the* PLASIMO *modules involved in an LTE calculation, including the main radiation module. The details around this radiation module, such as the Radiative Transitions Map and Radiative Transfer Method, are largely hidden from the rest of the model. In LTE, the radiation module essentially reads density and temperature values, and produces energy source terms.*

3.5.2 Frequency sampling

As figure 3.4 shows, the radiation (sub)modules deal with radiative quantities like j_ν, κ, and J_ν, which are all frequency dependent. In PLASIMO, the dependence of the radiative quantities on frequency ν is accounted for by sampling the quantities on a set of frequency points $\{\nu\}$. This approach of sampling in frequency space ν has the advantage that it is very flexible. Any spectral line profile can be used in the radiative transfer calculations, provided it can be sampled using a practical number of frequency points.

The radiative transition map contains one or more transition plugins. Each transition plugin i calculates the emission and absorption coefficients $j_{\nu,i}$ and κ_i as a function of local parameters $n_X, T, \ldots$. The transition plugin chooses the set of frequency points $\{\nu_i\}$ where $j_{\nu,i}$ and κ_i are calculated.

The radiative transition map then combines the $j_{\nu,i}$ and κ_i values for individual transitions i together into the summed values j_ν and κ. The summed values for j_ν and κ are defined on the set of frequency points $\{\nu\}$ which is the combination of all sets $\{\nu_i\}$.

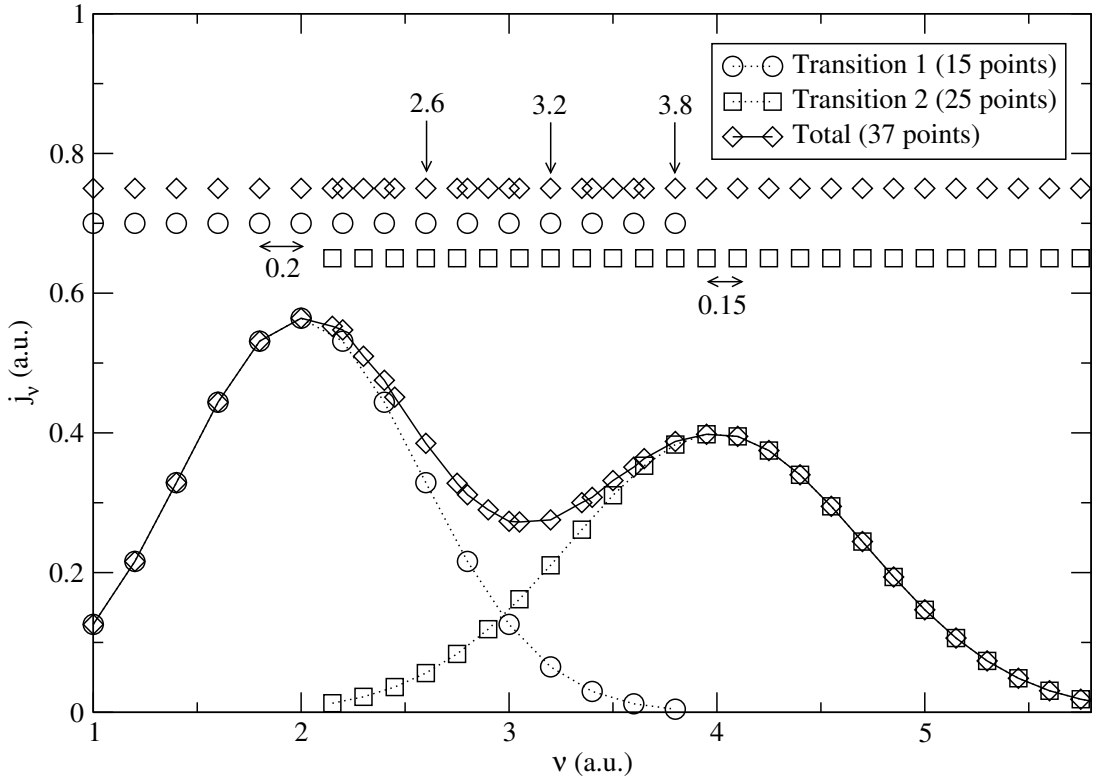

Figure 3.6: *Illustration of the way two discrete spectral functions, sampled at different frequencies ν, are combined into a single function. The first function (circles) is sampled at 15 ν points, the second function at 25 points (squares). Since both functions have 3 ν points in common, the combined function (diamonds) has a total of $25 + 15 - 3 = 37$ ν points.*

As an example of how this works, consider two sets of frequencies $\{\nu_1\}$ and $\{\nu_2\}$ which are used to discretise the spectral range of transitions 1 and 2 respectively. The emission profiles for these transitions are given schematically in figure 3.6. The first set of 15 frequency points, denoted by circles in figure 3.6 are between 1 and 4 and subsequent points are 0.2 apart (everything in arbitrary units). The second set, denoted by squares, is located between 2 and 6 and all 25 points are 0.15 apart. The two sets have three frequency values in common, at ν values of 2.6, 3.2 and 3.8. The total emission coefficient is then sampled on all unique frequency points, a set of $15 + 25 - 3 = 37$ points, denoted by the diamonds in figure 3.6. For each transition point $\nu_j \in \{\nu\}$, and for each transition i with frequency sets $\{\nu_i\}$ and emission and absorption data sets $\{j_{\nu,i}\}$ and $\{\kappa_i\}$, one of the following three conditions holds:

- The value ν_j is part of the set of frequency points of transition i, $\nu_j \in \{\nu_i\}$ for which the plugin of transition i already calculates $j_{\nu,i}$ and κ_i. No interpolation is needed.
- The value $\nu_j \notin \{\nu_i\}$ is smaller than the minimum or larger than the maximum value of the set $\{\nu_i\}$. Frequency ν_j is considered to be out of the ν-range of transition i, which therefore does not contribute to the total value of j_ν and κ at ν_j.
- The value ν_j is between the minimum and maximum values of the set $\{\nu_i\}$, but not part of the set itself, $\nu_j \notin \{\nu_i\}$. In this case, the value of $j_{\nu,i}$ and κ_i is interpolated from the nearest points in the $\{j_{\nu,i}\}$ and $\{\kappa_i\}$ sets that are supplied by the transition plugin.

3.5.3 Parallel computing

Another advantage of sampling radiative quantities on a discrete set of frequency points $\{\nu\}$, is that it makes parallelisation of the computer code rather straightforward. If there is no cross-talk between radiation at different frequencies (that is, transport of radiation at one frequency is not directly influenced by transport of radiation at another frequency), the work of the radiative transfer method may be spread out over several processors by letting each processor handle a part of the set of frequency points for which J_ν is to be calculated.

This is implemented using the Message Passing Interface (MPI) programming environment (Message Passing Interface Forum, 1994, 1995), and is schematically shown in figure 3.7. The master process is the standard PLASIMO executable. Several slave processes are run from special executable files, which do little more than set up MPI communications with the master process and load the requested radiative transfer method plugin. Then the master process calculates j_ν and κ for the frequency points in the complete set $\{\nu\}$[4] and distributes the values for subsets of $\{\nu\}$ over the available slave processes. Each slave process will calculate J_ν for its own subset of frequency points and send the result to the master process which will then assemble the complete set of $\{J_\nu\}$ values.

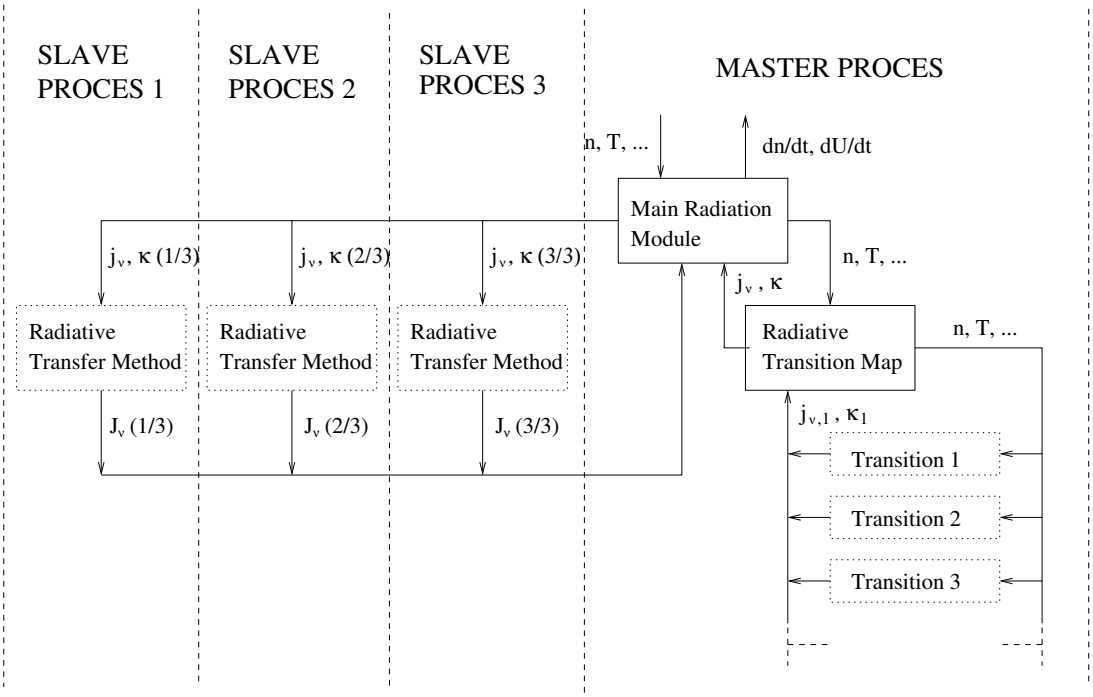

Figure 3.7: *Schematic representation of the parallelisation of the radiative transfer calculation using MPI techniques. The master process controls several slave processes (three shown), each of which runs the radiative transfer method plugin for a subset (one third) of the frequencies* $\{\nu\}$.

This parallel calculation of the effects of radiative transfer has been implemented as a "proof of concept" and has not been extensively tested or bench-marked for speed.

[4] In principle this can be parallelised as well, by having slave processes calculate j_ν and κ for subsets of $\{\nu\}$. However, usually the radiative transfer method is computationally much more expensive than the calculation of radiative transition coefficients in the radiative transition map.

Chapter 4

Semiclassical and quantum-mechanical descriptions of S_2 molecular radiation

Published as: *Harm van der Heijden and Joost van der Mullen*
J. Phys. B: At. Mol. Opt. Phys. **34** 4183-4201 (2001)

Abstract

A semiclassical theory to calculate diatomic molecular radiation emission and absorption coefficients is presented in some detail. The theory is applied to the S_2 $B^3\Sigma_u^- \rightarrow X^3\Sigma_g^-$ transition and the results are compared to a quantum-mechanical calculation. We show that disregarding fine structure, the semiclassical results compare very well to the average results of the quantum-mechanical theory. We conclude that the semiclassical theory is recommendable when fine-structure is not important since it requires less detailed data about the molecular states and transition and its results can be computed faster.

4.1 Introduction

There are many examples of plasmas in which diatomic molecular radiation plays an important role. Compared to atomic line radiators, molecules tend to emit light over a much broader frequency range which means that molecular radiation is less likely to be captured in the plasma. For some discharges this effect is desirable, for example in light sources which are optimised for visible light or UV production, and in plasma switches, where radiation emission can be a major cooling factor. In other cases, such as plasma sources in use for spectrochemical analysis or the production of beams of radicals, the energy loss due to radiation emission may be unwelcome.

In all cases, however, calculating the effect of radiation emission due to the presence of molecules is severely complicated due to the fact that the description of molecular radiation in (high pressure) discharges involves complex chemistry and requires detailed information about the available molecular states. Moreover, at high pressure most molecules exhibit a very

complex spectrum, consisting of many (often in the order of 10^6) ro-vibrational transitions, which makes radiative transfer calculations difficult.

Many high pressure molecular discharges feature favourable light source qualities, such as high efficacy and colour rendering. For example, Na_2 dimers cause the broad D_2 line in high pressure sodium lamps (de Groot and van Vliet, 1986), and S_2 is responsible for the bulk of the light emitted by the sulfur lamp (Dolan *et al.*, 1992, 1995; Turner *et al.*, 1997). The S_2 $B^3\Sigma_u^- \rightarrow X^3\Sigma_g^-$ transition creates visible light that extends from the blue to the red end of the spectrum, closely following the eye sensitivity curve. Since little energy is emitted in either the infrared or ultraviolet parts of the spectrum, high pressure sulfur discharges have very good lighting characteristics. However, a quantitatively correct theoretical description of the sulfur lamp spectrum, using a self-consistent energy balance, has so far proved difficult to obtain, due to the large number of ro-vibrational lines to be considered. It is for this reason that we investigate the feasibility of a semiclassical description of radiation generation for S_2.

The bulk of this paper is devoted to a discussion of a semiclassical theory (Lam and Gallagher, 1977; Jablonński, 1945; Sando and Wormhoudt, 1973; Hedges *et al.*, 1972; Proud and Luessen, 1986) which provides a powerful and convenient alternative means of describing these high pressure molecular radiation characteristics. Compared to a quantum-mechanical ro-vibrational description, it requires far less computation time. In this paper we examine the feasibility of applying this theory for the description of high pressure sulfur discharge spectra by comparing semiclassical calculations of emission and absorption coefficients with the result of quantum-mechanical calculations. Our aim is to determine whether the semiclassical theory allows us to quickly calculate molecular radiation characteristics without compromising significant accuracy. We focus on calculating the radiative properties of a high pressure S_2 discharge, which has attractive properties as a light source. However, the theory presented here is not restricted to light sources, and may be useful to researchers in any of the earlier mentioned fields.

To make this paper mostly self-contained, we present the basics of the semiclassical theory here, referring to existing literature on the subject for discussions of some of the more subtle points. The fundamental differences between the semiclassical and the quantum-mechanical theory are the line profile and the way in which partition functions are calculated. Section 4.2 discusses the basics of molecular radiation and frequency distribution, while in section 4.3 we present the semiclassical theory in some detail. Section 4.4 is devoted to a brief review of the quantum-mechanical approach and in section 4.5 we present semiclassical and quantum-mechanical calculations of the S_2 spectrum. Section 4.6 concludes with a discussion of the results and the applicability of both methods.

4.2 Radiation basics

The radiative emission coefficient $j_\nu(\nu)$ is related to the coefficient for absorption $\kappa(\nu)$ following Kirchhoff's law:

$$S_\nu(\nu) = \frac{j_\nu(\nu)}{\kappa(\nu)} = \frac{2h\nu^3}{c^2}\frac{1}{\exp(h\nu/kT)-1}. \tag{4.1}$$

We can generally express $j_\nu(\nu)$ for isotropic radiation as

$$j_\nu(\nu) = \frac{h\nu}{4\pi} n' A \phi'_\nu(\nu), \tag{4.2}$$

where n' is the density of the upper state (we adopt the convention of labelling upper states with a single (') prime and lower states with double (") primes), A the corresponding transition probability or Einstein coefficient and $\phi_\nu(\nu)$ a normalised line profile:

$$\int_0^\infty \phi_\nu(\nu)d\nu = 1.$$

We define the absorption cross section $\sigma_{abs}(\nu)$ as

$$\sigma_{abs}(\nu) = \frac{c^2}{8\pi\nu^2} A \frac{g'}{g''} \phi''_\nu(\nu), \tag{4.3}$$

with g', g'' the weights of the upper and lower levels. We also define a cross section σ_{stim} for stimulated emission,

$$\sigma_{stim}(\nu) = \frac{c^2}{8\pi\nu^2} A \phi'_\nu(\nu), \tag{4.4}$$

so that the following relation holds,

$$\kappa(\nu) = n''\sigma_{abs}(\nu) - n'\sigma_{stim}(\nu). \tag{4.5}$$

In the remainder of this article, we focus on the role of ϕ_ν and derive formulas for j_ν, σ_{abs}, and σ_{stim} using equations (4.2-4.4) respectively. A useful check of results developed in this paper is the equilibrium condition, with

$$\frac{n''}{g''Z''} = \frac{n'}{g'Z'} \exp(h\nu/kT),$$

where Z is the internal partition sum of the state and from which follows the requirement that

$$\frac{j_\nu(\nu)/n'}{\sigma_{abs}(\nu)\frac{g''Z''}{g'Z'}\exp(h\nu/kT) - \sigma_{stim}(\nu)} = \frac{2h\nu^3}{c^2} \frac{1}{\exp(h\nu/kT) - 1}, \tag{4.6}$$

conform equation (4.1).

4.3 Semiclassical molecular radiation

The core of a semiclassical radiation theory is the connection between a point in the phase space (for a single particle we use the spatial coordinates x, y, z and the momentum coordinates p_x, p_y, p_z or, in short, $\mathbf{r}$ and $\mathbf{p}$) of the emitting or absorbing particle and the frequency of the radiation ν. With this relation and the use of statistical mechanics, an expression for $\phi_\nu(\nu)$ can be found. More precisely, the theory states that the fraction of the line profile between ν and $\nu + d\nu$ is the same as the fraction of particles in the phase space $dxdydzdp_xdp_ydp_z = d^3\mathbf{r}d^3\mathbf{p}$ emitting or absorbing in the frequency band $\nu \ldots \nu + d\nu$.

From statistical mechanics we know that the fraction of particles in phase space $d^3\mathbf{r}d^3\mathbf{p}$ equals

$$f(r,p)d^3\mathbf{r}d^3\mathbf{p} = \frac{1}{Z} \frac{\exp(-H(\mathbf{r},\mathbf{p})/kT)d^3\mathbf{r}d^3\mathbf{p}}{h^3}, \tag{4.7}$$

with $H(\mathbf{r}, \mathbf{p})$ the Hamiltonian

$$H(\mathbf{r}, \mathbf{p}) = \frac{p_x^2 + p_y^2 + p_z^2}{2m} + V(x, y, z) = \frac{\mathbf{p}^2}{2m} + V(\mathbf{r}), \tag{4.8}$$

where $V(\mathbf{r})$ is the potential function of the system, and Z the semiclassical partition function

$$Z = \frac{1}{h^3} \int \int \exp(-H(\mathbf{r}, \mathbf{p})/kT) d^3\mathbf{r} d^3\mathbf{p}, \tag{4.9}$$

which is called semiclassical because the h^{-3} term does not appear in the purely classical treatment.

As a practical example of the semiclassical radiation theory, we now consider non-relativistic Doppler broadening of an atomic line around central frequency ν_0. The connection between phase space and frequency ν is given by

$$\nu(\mathbf{r}, \mathbf{p}) = \left(1 + \frac{p_x}{mc}\right) \nu_0, \tag{4.10}$$

with c the speed of light and where the x axis has arbitrarily been chosen as the direction in which the frequency shift is observed. Since ν only depends on the x component of $\mathbf{p}$ and not on $\mathbf{r}$ at all, we integrate over all values of the other coordinates. Using

$$\exp(-H(\mathbf{r}, \mathbf{p})/kT) = \exp(-p_x^2/2mkT) \exp(-p_y^2/2mkT) \exp(-p_z^2/2mkT),$$

we see that all terms in (4.7) cancel, except for the p_x term

$$f(p_x)dp_x = \frac{\exp(-p_x^2/2mkT)dp_x}{\sqrt{2\pi mkT}}. \tag{4.11}$$

Using $\phi_\nu(\nu)d\nu = f(p_x)dp_x$ and inserting $p_x = mc(\nu - \nu_0)/\nu_0$, $dp_x = mcd\nu/\nu_0$ into equation (4.11) we find the well-known formula for a Doppler broadened line,

$$\phi_\nu(\nu) = \sqrt{\frac{mc^2}{2\pi kT\nu_0^2}} \exp\left(-\frac{(\nu - \nu_0)^2}{2kT\nu_0^2/mc^2}\right). \tag{4.12}$$

For diatomic molecular states the situation is more complex, since with two atoms we have a 12-dimensional phase space. It is convenient to work in centre-of-mass coordinates, where the Hamiltonians are given by

$$H(\mathbf{R}) = \frac{\mathbf{P}^2}{2M},$$

$$H(\mathbf{r}) = \frac{\mathbf{p}^2}{2\mu} + V(\mathbf{r}),$$

where $\mathbf{R}, \mathbf{P}$ are the centre of mass coordinates and $\mathbf{r}, \mathbf{p}$ are the relative or reduced coordinates. The total and reduced mass are represented by M and μ respectively while $V(\mathbf{r})$ is the adiabatic potential curve of the molecular state. As with equation (4.10), we must now specify a connection between phase space coordinates and radiation frequency. We use the classical interpretation of the Franck-Condon principle (FCP), which states that an electronic transition

happens so fast that the particles do not undergo a significant change in position or kinetic energy. That is, $\mathbf{r}$, $\mathbf{R}$, $\mathbf{p}$, and $\mathbf{P}$ are kept constant. The radiation frequency then follows from the change in potential energy:

$$\nu(\mathbf{r}) = \frac{\Delta V + V'(\mathbf{r}) - V''(\mathbf{r})}{h}, \tag{4.13}$$

where $V'(\mathbf{r})$ and $V''(\mathbf{r})$ are the potential energies of respectively the upper and the lower states relative to their minimum potential energies, V_0' and V_0'', and $\Delta V = V_0' - V_0''$ is the potential difference between the two states.

We will calculate the fraction of phase space $f(r)dr$ where $|\mathbf{r}|$ has a value between r and $r + dr$. The integrations over the $\mathbf{R}$ and $\mathbf{P}$ coordinates will cancel when $f(r)dr$ is normalised, so from here on only $\mathbf{r}$ and $\mathbf{p}$ need to be considered. For $f(r)dr$ we thus find

$$f(r)dr = \frac{\sigma_{sym}}{Z} 4\pi r^2 \exp(-V(r)/kT) dr \frac{1}{h^3} \int \exp(-\mathbf{p}^2/2\mu kT) d^3\mathbf{p}, \tag{4.14}$$

where σ_{sym} is a statistical symmetry factor that equals 1 for heterogenous and $\frac{1}{2}$ for homogenous molecules. Since this factor also appears in Z, it effectively cancels in equation (4.14). It is, however, of importance for the absolute value of Z.

In general, we can integrate the $\mathbf{p}$ dependent part over all values, but in many cases it makes sense to distinguish between bound ($\mathbf{p}^2/2\mu < D(r)$) and free states ($\mathbf{p}^2/2\mu > D(r)$), where $D(r) = V(\infty) - V(r)$ is the dissociation energy. The integral over $\mathbf{p}$ space then becomes dependent on $\mathbf{r}$, for example for bound states we have

$$f(r)dr = \frac{\sigma_{sym}}{Z} 4\pi r^2 \exp(-V(r)/kT) dr \frac{1}{h^3} \int_0^{\sqrt{2\mu D(r)}} 4\pi p^2 \exp(-p^2/2\mu kT) dp,$$

which, after some manipulation, can be rewritten in a more concise form

$$f(r)dr = \frac{\sigma_{sym}}{Z} \Gamma\left(\frac{3}{2}, \frac{D(r)}{kT}\right) \left(\frac{2\pi\mu kT}{h^2}\right)^{\frac{3}{2}} 4\pi r^2 \exp(-V(r)/kT) dr, \tag{4.15}$$

with $\Gamma(\frac{3}{2}, x) = \frac{2}{\sqrt{\pi}} \int_0^x \sqrt{t} \exp(-t) dt$, the normalised incomplete gamma function of order $\frac{3}{2}$. Figure 4.1 gives a graphical representation of this fraction in phase space. Similarly, the expression for unbound states contains a factor $(1 - \Gamma(\frac{3}{2}, D(r)/kT))$.

As $r \to \infty$, $D(r)$ will go to zero and $\Gamma(\frac{3}{2}, D(r)/kT) \to 0$. On the other hand, if the thermal energy is much smaller than the dissociation energy, $\Gamma(\frac{3}{2}, D(r)/kT)$ is approximately unity, which may be the reason why in the literature this factor is often omitted (de Groot and van Vliet, 1986) or unexplained (Lam and Gallagher, 1977).

The calculation of the partition sum Z is not entirely trivial. Normalising with respect to the total phase space volume of bound states gives

$$Z_{bound} = \sigma_{sym} \left(\frac{2\pi\mu kT}{h^2}\right)^{\frac{3}{2}} \int_0^\infty \Gamma\left(\frac{3}{2}, \frac{D(r)}{kT}\right) 4\pi r^2 \exp(-V(r)/kT) dr, \tag{4.16}$$

which is finite for most molecular potentials (see appendix 4.A for details) and valid as long as the gas density is so low that the average distance $\overline{r}$ between particles is large compared to

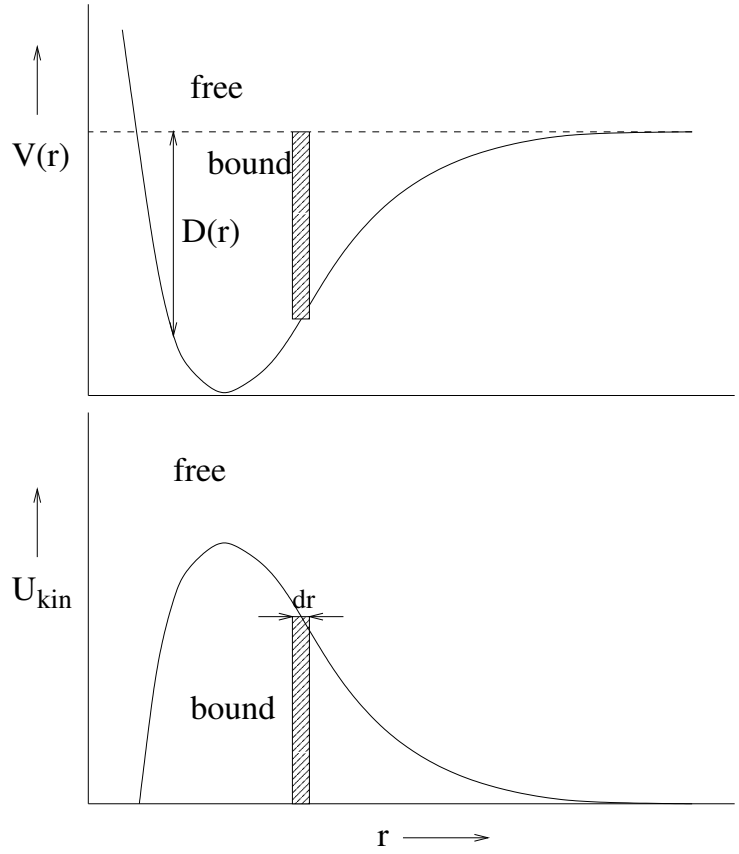

Figure 4.1: *In a molecular potential well, $U_{kin} = \mathbf{p}^2/2\mu$ has a maximum value $D(r)$, the r-dependent dissociation energy, for bound states. The fraction in phase space that is occupied by the shaded area, representing all bound states between r and $r + dr$, is proportional to $4\pi r^2\Gamma(\frac{3}{2}, D(r)/kT)dr$. The unbound states occupy a fraction $\propto 4\pi r^2(1 - \Gamma(\frac{3}{2}, D(r)/kT))dr$.*

the width of the potential well, i.e. $D(\overline{r})/kT \approx 0$. If this is not the case, these distribution statistics also have to be taken into account. These statistics are always important when adding the contribution of both bound and unbound states, which has the effect of cancelling the Γ factor,

$$Z_{total} = \sigma_{sym}\left(\frac{2\pi\mu kT}{h^2}\right)^{\frac{3}{2}}\int_0^\infty 4\pi r^2\exp(-V(r)/kT)dr. \tag{4.17}$$

This integral is certainly not finite for finite potentials, resulting in $f(r)dr = 0$. It correctly describes two particles in an infinitely large space, where the chance that the distance between them is in a finite range is zero. Equation (4.17) is, however, not applicable to an atom in a plasma, because the chance of finding the *nearest* other atom — with which it forms, by classical definition, a bound or unbound molecule — at a distance r rapidly decreases with increasing r. In appendix 4.A a formula for the more general case is derived, but under most circumstances where molecular effects are of importance we need to consider only bound states.

To complete the derivation of the semiclassical molecular radiation formula, we must equate

$\phi_\nu(\nu)d\nu$ to $f(r)dr$. From equation (4.13) we find

$$\frac{dr}{d\nu} = \left(\frac{d\nu}{dr}\right)^{-1} = h\left(\frac{d}{dr}(V'(r) - V''(r))\right)^{-1},$$

which, combined with equation (4.15) gives, for bound states,

$$\phi_{\nu,bound}(\nu(r)) = \frac{\sigma_{sym}}{Z_{bound}}\Gamma\left(\frac{3}{2}, \frac{D(r)}{kT}\right)\left(\frac{2\pi\mu kT}{h^2}\right)^{\frac{3}{2}} 4\pi r^2 \exp(-V(r)/kT)\left|\frac{d\nu}{dr}\right|^{-1}. \quad (4.18)$$

Finally, using equation (4.18) with $n'Ah\nu/4\pi$ with equations (4.2-4.4) gives the semiclassical expression for j_ν, σ_{abs}, and σ_{stim}:

$$j_\nu = n'\frac{h\nu(r)A}{4\pi}\frac{\sigma_{sym}}{Z'_{bound}}\Gamma\left(\frac{3}{2}, \frac{D'(r)}{kT}\right)\left(\frac{2\pi\mu kT}{h^2}\right)^{\frac{3}{2}} 4\pi r^2 \exp(-V'(r)/kT)\left|\frac{d\nu}{dr}\right|^{-1}, \quad (4.19)$$

$$\sigma_{abs}(\nu) = \frac{Ac^2}{8\pi\nu(r)^2}\frac{g'}{g''}\frac{\sigma_{sym}}{Z''_{bound}}\Gamma\left(\frac{3}{2}, \frac{D''(r)}{kT}\right)\left(\frac{2\pi\mu kT}{h^2}\right)^{\frac{3}{2}} 4\pi r^2 \exp(-V''(r)/kT)\left|\frac{d\nu}{dr}\right|^{-1}, \quad (4.20)$$

$$\sigma_{stim}(\nu) = \frac{Ac^2}{8\pi\nu(r)^2}\frac{\sigma_{sym}}{Z'_{bound}}\Gamma\left(\frac{3}{2}, \frac{D'(r)}{kT}\right)\left(\frac{2\pi\mu kT}{h^2}\right)^{\frac{3}{2}} 4\pi r^2 \exp(-V'(r)/kT)\left|\frac{d\nu}{dr}\right|^{-1}. \quad (4.21)$$

Note that these equations do not satisfy equation (4.6). This is due to the fact that we only consider bound-bound radiation. To take into account all four combinations of transitions between bound and free states, it is sufficient to replace Z_{bound} with Z_{total} and remove the $\Gamma(\frac{3}{2}, D(r)/kT)$ factor. Using the equilibrium condition $n'/(g'Z') = n''/(g''Z'')\exp(-\Delta V/kT)$ it can easily be verified that then equation (4.6) holds. However, as was mentioned before, calculating Z_{total} requires a special statistical treatment of the distribution of distances between atoms which is outlined in appendix 4.A.

Equations (4.19-4.21) are completely determined in terms of r. As can be seen in figure 4.2, not every value of r corresponds with a unique ν value. In fact, the spectrum is said to "fold back on itself" around points where $d\nu/dr$ changes direction. In order to compute j_ν for a given value of ν, we need to add the contributions from all radii r_i that satisfy $\Delta V + V''(r_i) - V'(r_i) = h\nu$.

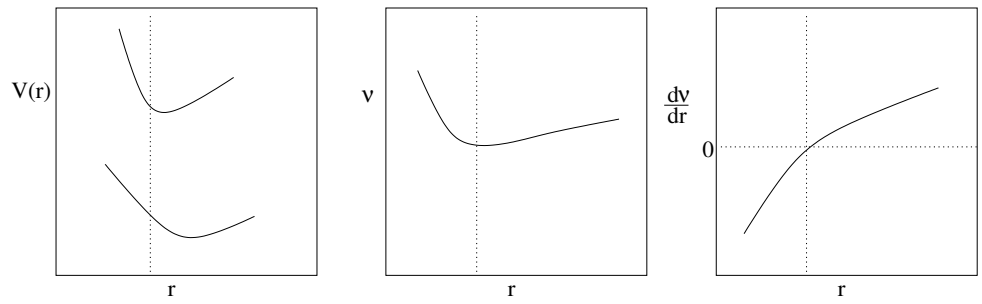

Figure 4.2: *(a) Potential energies $V(r)$ for the upper and lower states as function of r, (b) the resulting photon frequency $\nu(r)$ according to the FCP, (c) the derivative $d\nu(r)/dr$, which is the reciprocal of the semiclassical line width. The dotted line denotes the place where $d\nu/dr = 0$.*

At the folding point, where $d\nu/dr = 0$, the line profile, and therefore both j_ν and κ, becomes infinite. In reality the peak value κ_p is of course finite, but as long as $\kappa_p \ell \gg 1$, where ℓ is a characteristic distance in the plasma, the transported radiation will be in equilibrium and can be described using equation (4.1) independent of the actual value for κ_p. That is, it is only necessary to sample r points along the curve leading up to the singularity until $\kappa\ell \gg 1$. These so-called satellite lines have been discussed in literature (Kielkoff *et al.*, 1970; Szudy and Baylis, 1975).

As r goes to infinity, $d\nu/dr$ will also go to zero due to the fact that both the upper and the lower potential curve flatten out. Without influences from molecular potentials, the actual line profile $\phi_{\nu,\ell}$ is given by a normalised function like

$$\phi_{\nu,\ell} = \frac{C}{\Delta\nu} P\left(\frac{\nu - \nu_0}{\Delta\nu}\right),$$

with $\Delta\nu$ a typical line width, for example the Doppler width or the natural linewidth. As on folding points, the semiclassical approach gives a line profile with a singularity, since $\phi_\nu \propto |d\nu/dr|^{-1}$, even though the profile can still be integrated,

$$\int \phi_\nu(\nu) d\nu \propto \int \left|\frac{d\nu}{dr}\right|^{-1} d\nu = \int dr,$$

where it should be noted that the r integral is normalised by Z. So a condition for the validity of the semiclassical line profile is to stay away from the central frequency ν_0,

$$|\nu - \nu_0| \gg \Delta\nu, \tag{4.22}$$

where, in the classical context, ν_0 is defined as

$$\nu_0 = \lim_{r\to\infty} \frac{V'(r) - V''(r) - \Delta V}{h}.$$

As the theory will give us narrower lines than physically possible at high values of r, at r close to r_e the opposite may be the case. This is illustrated in figure 4.3. The semiclassical theory assumes that at every wavelength there is a possible transition, while a calculation using the exact energy levels will show that the spectrum in this region is not continuous, but consists of peaks and gaps. By overestimating the number of transitions, the semiclassical theory underestimates the effective absorption coefficient.

For values of $r < r_e$, the potential normally increases very rapidly as r decreases and the potential function data may become inaccurate. This is usually not a problem, because with increasing $V(r)$ and decreasing r, the factor $r^2 \exp(-V(r)/kT)$ in equations (4.19-4.21) quickly goes to zero.

4.4 Quantum-mechanical molecular radiation

This section contains a brief overview of the quantum-mechanical theory. More details are given in standard text books such as Steinfeld (1986) and Herzberg (1950). We again start from

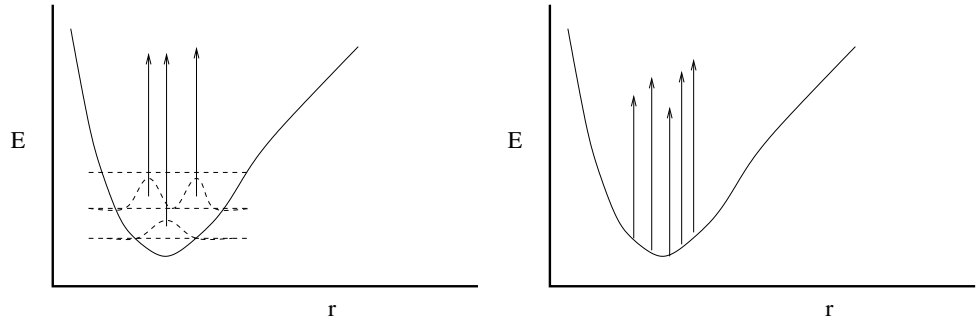

Figure 4.3: *At values of r close to the equilibrium distance, the semiclassical theory (right) overestimates the number of possible transitions. The quantum-mechanically most likely transitions (without rotational structure) are schematically represented on the left.*

the internal Hamiltonian for a diatomic molecular state in reduced centre of mass coordinates, which is given by

$$H = \frac{\mathbf{p}^2}{2\mu} + V(\mathbf{r}), \tag{4.23}$$

where, in this context, $\mathbf{p}$ is the momentum operator.

From the Hamiltonian for a molecular state we can calculate a partition function Z. As before, Z indicates a state's internal partition sum, without taking into account the state's degeneracy g or offset energy E. So the partition function Z_{mol} for the molecule as a whole is

$$Z_{mol} = \sum_i g_i Z_i \exp\left(-\frac{E_i}{kT}\right), \tag{4.24}$$

with i going over all states and Z_i and E_i respectively the internal partition sum and offset energy of state i.

In order to calculate the quantum-mechanical partition function, we must first find the eigenvalues E_i of the equation $H\Psi = E\Psi$. In the case of diatomic molecules the energy levels are specified by the quantum numbers v (vibration) and J (rotation).

Both the upper and the lower molecular state under consideration here are $^3\Sigma$ states, for which Hund's case (b) applies (Herzberg, 1950). The angular momentum apart from spin, with quantum number N, can have all integral values from 0 up, with $J = N+S, N+S-1, \ldots, |N-S|$. With the spin number S equal to 1, this means each level with a given N (except $N = 0$) consists of $2S + 1 = 3$ components. In this work, splitting of these components is not taken into account, so the $2S + 1$ term is incorporated in the degeneracy g_i of equation (4.24) (this is not valid for singlet $N = 0$ levels, but that is a minor error if $kT \gg B$). The energy of a given v, N level is then given by

$$E_{v,N} = \omega(v + \frac{1}{2}) - \omega_x(v + \frac{1}{2})^2 + \omega_y(v + \frac{1}{2})^3 + \ldots + (B - \alpha(v + \frac{1}{2}))N(N + 1) + \ldots,$$

with $\omega, \omega_x, \omega_y$ and B, α vibrational and rotational expansion terms respectively, and (...) indicating still higher order terms in v and N.

Assuming an equilibrium density distribution, the internal state partition sum is given by

$$Z_{qm} = \sum_v \sum_N g_{v,N} \exp\left(-\frac{E_{v,N}}{kT}\right). \tag{4.25}$$

The weight factors $g_{\nu,N}$ are given by

$$g_{v,N} = g_N = \omega_N(2N+1),$$

i.e. independent of v and with ω_N a statistical factor due to nuclear spin, which for bosons in a Σ electronic state is

$$\omega_N = \begin{cases} I/(2I+1) & even\ N'' \\ (I+1)/(2I+1) & odd\ N'' \end{cases},$$

where I is the half-integral nuclear spin of the molecule. Note that if $I = 0$, which is the case for S_2, even numbered N'' levels have a weight of 0, and are therefore forbidden. For the upper state the situation is reversed, with forbidden odd N' levels. This effectively halves the number of levels, and can be seen as the quantum-mechanical analog of the classical σ_{sym} factor which equals $\frac{1}{2}$ for S_2.

We now have a function for the fraction $f(v, N)$ of molecules in excited states with quantum numbers v and N:

$$f(v,N) = \frac{1}{Z_{qm}}\omega_N(2N+1)\exp\left(-\frac{E_{v,N}}{kT}\right). \tag{4.26}$$

The probability for a transition from state $v'N'$ to $v''N''$ is proportional to

$$S_{N''}^{N'} < \psi_{v'}|\psi_{v''} >^2, \tag{4.27}$$

with ψ_v a vibrational wave function, $< \psi_{v'}|\psi_{v''} >^2$ the Franck-Condon factors, and $S_{N''}^{N'}$ the Hönl-London factors.

The Franck-Condon factor defines how emission and absorption strengths, for vibrational levels v' and v'' respectively, are distributed among target levels v'' and v'. Therefore, they have the property that

$$\sum_{v''} < \psi_{v'}|\psi_{v''} >^2 = \sum_{v'} < \psi_{v'}|\psi_{v''} >^2 = 1,$$

where in the first summation v' is kept constant (emission) and in the second v'' (absorption).

Likewise, the Hönl-London factors divide emission and absorption strengths for rotational levels, so, using the fact that the weight of a rotational level is $2N + 1$, they must conform to

$$\begin{aligned} \textstyle\sum_{N''} S_{N''}^{N'} &= (2N'+1) \\ \textstyle\sum_{N'} S_{N''}^{N'} &= (2N''+1), \end{aligned}$$

where again the first summation refers to emission from N' and the second to absorption from N''. Typically, for a given rotational level N' or N'' there are three other rotational levels available for absorption or emission, with $N' - N'' = 1$, 0 or -1, respectively labelled the R, Q and P branches. The Hönl-London factors for the R, Q and P branches of a molecular $\Sigma - \Sigma$ systems, like S_2 B-X, are

$$\begin{array}{lcll} S_{N''}^{N''+1} = N''+1 & = & S_{N'-1}^{N'} = N' & (R) \\ S_{N''}^{N''} = 0 & = & S_{N'}^{N'} = 0 & (Q) \\ S_{N''}^{N''-1} = N'' & = & S_{N'+1}^{N'} = N'+1 & (P), \end{array}$$

where in the left column the factors are given relative to an emitting rotational state N', and on the right side for an absorbing state N''. Note that the fact that $S_{N''}^{N'} = 0$ for $N' = N''$ means that $\Delta N = 0$ transitions are forbidden between Σ states.

Combining equations (4.26) and (4.27) and summing over all upper and lower levels, the quantum-mechanical line profile can be written as

$$\phi'_{\nu,qm}(\nu) = \frac{1}{Z'_{qm}} \sum_{v'N'} \omega_{N'} \sum_{v''N''} S^{N'}_{N''} < \psi_{v'} | \psi_{v''} >^2 \phi_{\nu,\ell}(\nu) \exp\left(-\frac{E_{v'N'}}{kT}\right), \tag{4.28}$$

in (stimulated) emission, and

$$\phi''_{\nu,qm}(\nu) = \frac{1}{Z''_{qm}} \sum_{v'N'} \omega_{N'} \sum_{v''N''} S^{N'}_{N''} < \psi_{v'} | \psi_{v''} >^2 \phi_{\nu,\ell}(\nu) \exp\left(-\frac{E_{v''N''}}{kT}\right), \tag{4.29}$$

in absorption, where $\phi_{\nu,\ell}$ is a normalised line profile for an individual $v'N' \rightarrow v''N''$ transition. Using equation (4.3) with (4.29), we obtain the following expression for $\sigma_{abs}(\nu)$,

$$\sigma_{abs}(\nu) = \frac{Ac^2}{8\pi\nu^2} \frac{g'}{g''} \frac{1}{Z''_{qm}} \sum_{v'N'} \omega_{N'} \sum_{v''N''} S^{N'}_{N''} < \psi_{v'} | \psi_{v''} >^2 \phi_{\nu,\ell}(\nu) \exp\left(-\frac{E_{v''N''}}{kT}\right). \tag{4.30}$$

Expressions for j_ν and σ_{stim} can be formed by combining (4.28) with equations (4.2) and (4.4) respectively.

4.5 Calculations

Figure 4.4 shows the sulfur potential curves (states X and B) that have been taken into account (Kuznetsova *et al.*, 1993, 1991), along with the light wavelength as function of radius according to the FCP.

First we calculate the S_2 partition functions using equations (4.25) and (4.9) to verify that the quantum-mechanical and semiclassical methods give numerically similar results. The results are shown in figure 4.5. The semiclassical and quantum mechanical partition sums are generally in good agreement. It is also clear that up to $T \approx 4500$ K it is safe to approximate $\Gamma(\frac{3}{2}, D(r)/kT)$ with unity.

The transition probability A for the B→X transition has been calculated using an r-averaged transition dipole moment (Pradhan and Partridge, 1991); $D_{B\rightarrow X} = 0.6 \cdot q_e a_0$, with a_0 the Bohr radius. A then follows from

$$A = g_{osc} \frac{16\pi^3\nu^3}{3\epsilon_0 hc^3} |D|^2, \tag{4.31}$$

where g_{osc} is a degeneracy factor that is equal to 1 for a $\Sigma \rightarrow \Sigma$ transition.

From the potential curves in figure 4.4 the frequency ν was then calculated as function of r. From a light source point of view, the most interesting part of the spectrum is roughly between 300 and 800 nm, which corresponds to r values between 1.9 and 3 Å. This range contains no points where $d\nu/dr = 0$, so there are no singularities to be avoided.

For the quantum-mechanical calculation, the Franck-Condon values were taken from the RADEN data bank for characteristics of diatomic molecules (Kuznetsova *et al.*, 1993, 1991). For the X state the maximum value of v'' is 35, while for the B state the highest vibrational level is 17. There actually are approximately 66 bound vibrational levels in the X state, but calculations involving these higher levels are complicated due to uncertainties in the exact potential curve and the fact that the minimum of the B state is actually below the dissociation

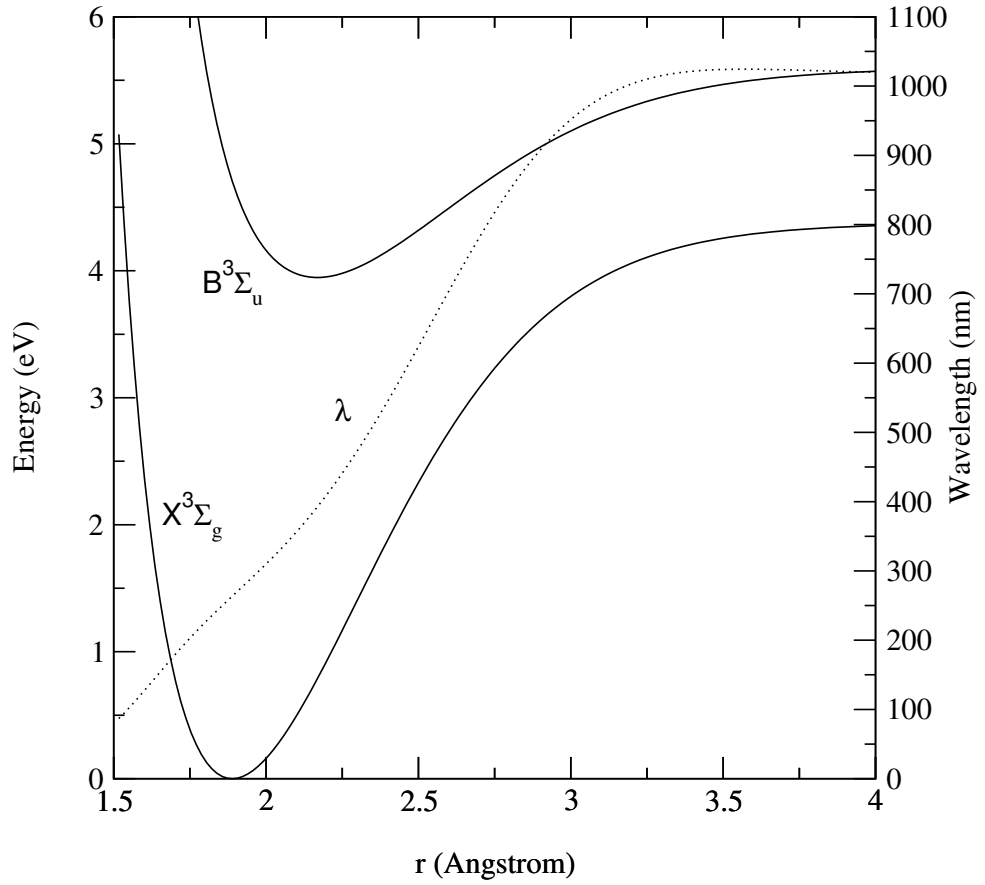

Figure 4.4: *Potential energies (values on left axis) of the diatomic sulfur $X^3\Sigma_g^-$ and $B^3\Sigma_u^-$ states. The dotted line is the wavelength (values on right axis) according to the Franck-Condon principle.*

energy of the X state. In the B state, the presence of an unbound 1_u state that crosses the B state around $v'' = 9$ may cause pre-dissociation (Quick and R.E. Weston, 1981). Moreover, detailed measurements of transitions involving high v'' levels are complicated due to a perturbing B"$^3\Pi_u^-$ state. These factors affect the semiclassical calculation as well, but, in order to correctly compare both methods, in the semiclassical calculation we use the same potential curves that were used to calculate the Franck-Condon factors without attempting to correct for these complications.

A single $v'N' \rightarrow v''N''$ transition is centred around frequency ν_0,

$$\nu_0 = E_{v'N'} - E_{v''N''} + \Delta E, \tag{4.32}$$

where ΔE is the difference in offset energy between the upper and the lower state. The quantum-mechanical data is initially collected in bins of size b, which has the effect of applying a rectangular normalised line profile $\phi_{\nu,bin}$,

$$\phi_{\nu,bin}(\nu) = \begin{cases} 1/b, & |\nu - \nu_0| \leq b/2 \\ 0, & |\nu - \nu_0| > b/2 \end{cases} . \tag{4.33}$$

Once the intensities of all possible $v'N' \rightarrow v''N''$ transitions have been calculated and collected in bins, the data is convoluted with a normalised line profile $\phi_{\nu,\ell}$, for example a Gaussian. The

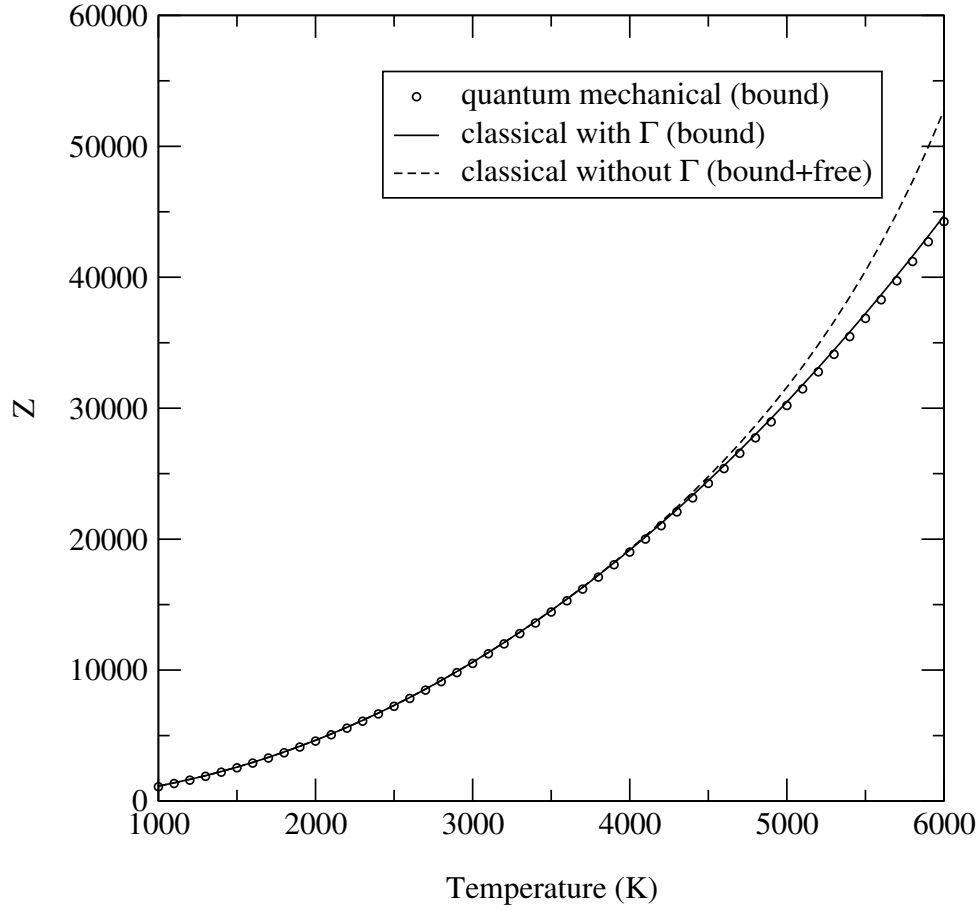

Figure 4.5: *Comparison between the quantum-mechanical and semiclassical partition functions. The semiclassical function has been plotted both with (only bound state) and without (bound and free) the* Γ *function. The latter was limited by cutting off the integration at* $r = 15$ Å*. The quantum-mechanical partition function only includes bound vibrational levels, which is the reason why the classical bound and free function starts to deviate at temperatures that are high enough for significant dissociation.*

only requirement of this profile is that its width must be significantly larger than b, the spectral resolution of the calculation. Since the results are presented as a function of wavelength rather than frequency, bin and convolution widths will also be given in terms of wavelength intervals.

Figure 4.6 shows spectra calculated using both methods on a small (2 nm) wavelength interval. The quantum-mechanical data has been collected in bins with a width of 0.01 nm, then convoluted with a Gaussian with a FWHM of 0.05 nm, preserving the sharply peaked nature of this spectrum. At this resolution, even band-heads are virtually unnoticeable and it is hard to determine visually whether the semiclassical theory gives a correct average cross section. In the following figures, we plot over a much larger wavelength interval and also increase the bin width to 0.5 nm and convolute the data with a Gaussian with FWHM=2 nm.

Figures 4.7-4.9 show a comparison of the semiclassical and quantum-mechanical absorption cross section for the S_2 B$\rightarrow$ X transition at 1000, 3000 and 5000 K respectively.

Due to the particular shapes and relative positions of the B and X potential wells, radiation absorbed in the minimum of the X potential is in the UV, while with increasing r and $V''(r)$ the

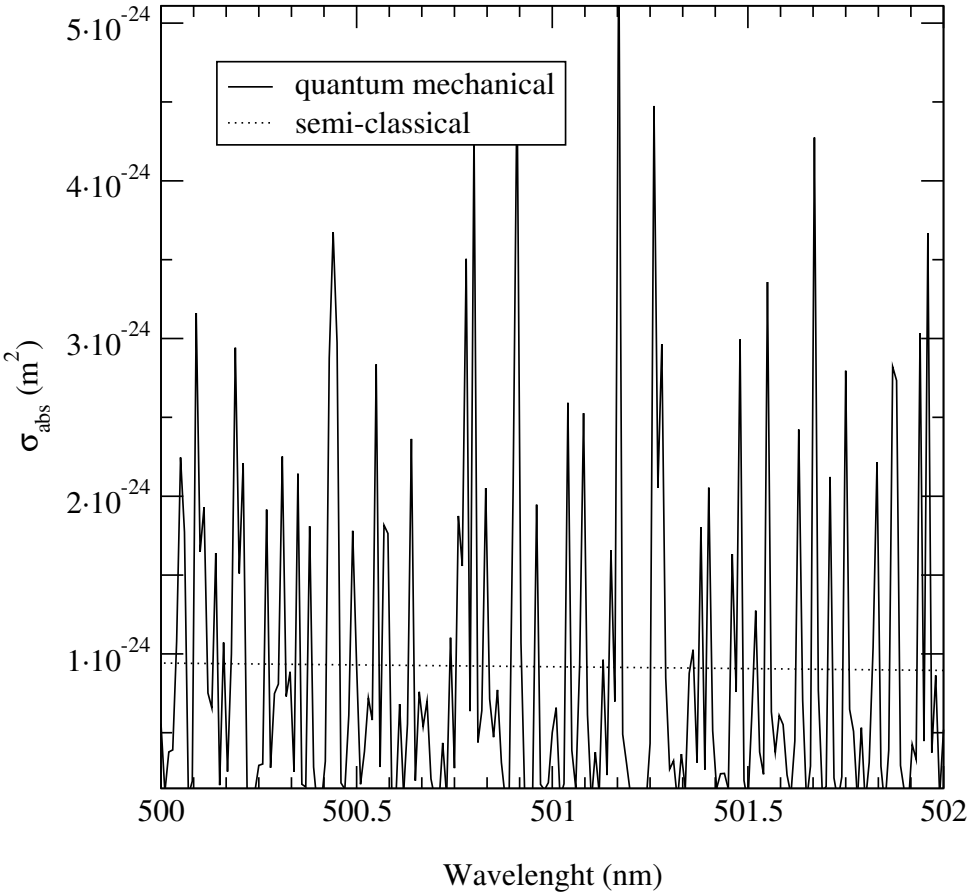

Figure 4.6: *A close up of spectra calculated using the quantum-mechanical respectively semi-classical calculated theory. The quantum mechanical data has been collected in bins with a width of 0.01 nm.*

absorbed energy shifts to higher wavelengths. That is, at low temperatures most S_2 molecules will emit and absorb mainly UV radiation, while at higher temperatures higher r values become available. Indeed, at low pressures S_2 discharges are known for UV production, whereas at the high operational pressure and temperature of the sulfur lamp, the UV absorption becomes so strong the net emitted light shifts to the visible part of the spectrum, where the S_2-X state is less opaque.

While all figures show that agreement is generally good at wavelengths between 300 and 600 nm, the quantum-mechanical cross section drops off quickly at higher wavelengths. This is due to the incompleteness of the Franck-Condon tables. The light at wavelengths above 600 nm is absorbed in high vibrational levels in the X state, while the Franck-Condon table that was used for this calculation does not list values above $v'' = 35$ for the B state. The discrepancy increases with increasing temperature as more high v'' levels become populated.

Another effect of increasing temperature is that the minimum and maximum values of σ_{abs} in the plotted wavelength interval come closer together. This can clearly be seen in figure 4.10, which shows semiclassically calculated values for σ_{abs} for temperatures from 1000 K to 6000 K. At low temperatures the lower v'' levels are heavily populated, which results in strong UV absorption. At higher temperatures, the levels are more evenly populated, resulting in less

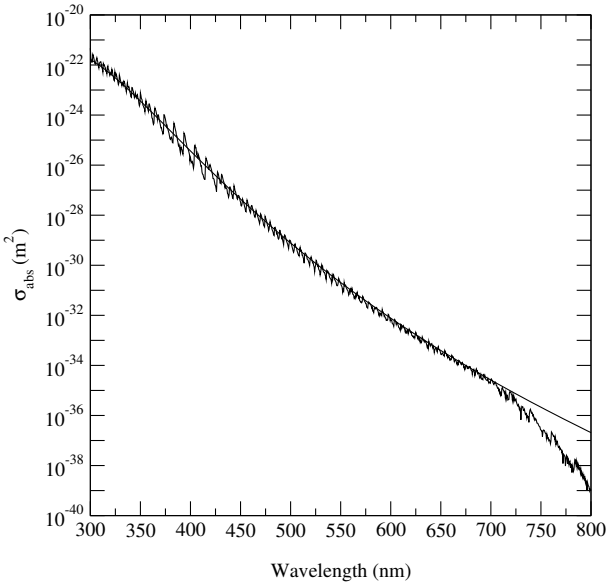

Figure 4.7: *S_2 Semiclassical (smooth line) and quantum-mechanical (jagged line) absorption cross section calculation for the $B^3\Sigma \rightarrow X^3\Sigma$ transition at 1000 K. In this and the following 2 graphs the quantum-mechanical bin width is 0.5 nm and the data is convoluted with a Gaussian with a 2 nm FWHM. The range of the y axis spans 20 orders of magnitude, indicating that practically all significant absorption is in the UV and blue regions of the spectrum.*

UV and more red absorption.

4.6 Discussion and conclusion

The calculations have shown that the semiclassical theory gives values for σ_{abs} that compare well to the average of the quantum-mechanically calculated values for the S_2 B→X transition. When computation speed is important, and the high resolution (< 1 nm) details of the spectrum are not, it is recommendable to use the semiclassical theory.

One of the additional advantages of this theory is that it does not require detailed information about the discrete energy levels and also does not depend on a Franck-Condon table. As can clearly be seen in figures 4.7-4.9, the quantum-mechanical cross sections are too low in the red spectrum. This is caused by the fact that the used table, which, to our knowledge, is the most complete one available for S_2 B→X, goes no higher than $v' = 17$ and $v'' = 35$, while in fact most of the high wavelength radiation is absorbed in higher vibrational levels v''. It must be said, however, that part of the reason the quantum-mechanical data is incomplete — the perturbing 1_u and B"$^3\Pi_u^-$ states — will also affect a semiclassical calculation to some degree. Still, it is generally easier to obtain good potential energy data than complete Franck-Condon factors.

A disadvantage of the classical method is the possible occurrence of singularities around folding points when $d\nu/dr = 0$ which causes $\phi_{\nu,bound}$, and therefore j_ν and κ, to become infinite. However, as was discussed in section 4.3, it is possible to work around these singularities provided that the actual peak value of the absorption coefficient is high enough so that the radiation at that frequency is in equilibrium.

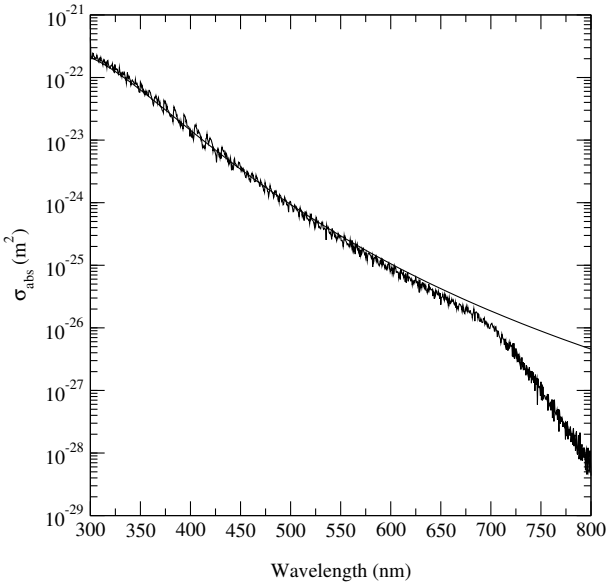

Figure 4.8: *S_2 Semiclassical (smooth line) and quantum-mechanical (jagged line) absorption cross section calculation for the $B^3\Sigma \rightarrow X^3\Sigma$ transition at 3000 K. The curve is flatter than at 1000 K, as it only spans 8 orders of magnitude. At high wavelengths the agreement between the two calculations is not as good, because the Franck-Condon table for the quantum-mechanical calculation is not complete for high v''.*

In general, the emission coefficient A is not a constant but dependent on radius r. In the quantum-mechanical treatment, this effect is ignored by the Franck-Condon approach:

$$\sigma_{abs}^{v'v''} \propto < \psi_{v'}|R_e|\psi_{v''} >^2 \approx \overline{R_e}^2 < \psi_{v'}|\psi_{v''} >^2,$$

with R_e the electronic transition moment and $\overline{R_e}$ the average value over r. In the semiclassical calculation we do not have to make this approximation, since we can simply insert an r-dependent A value in equation (4.20). Data on $R_e(r)$ for sulfur is available (Pradhan and Partridge, 1991), but we have not used it in the calculations presented here because the emphasis lies on a comparison with the quantum-mechanical results.

In conclusion, we present a simple "check list" of steps is needed to apply the semiclassical method:

- Collect data about the potential curves of the upper and the lower states. If no detailed data is available, it is possible to use an enhanced Morse (Herzberg, 1950) or the universal potential function proposed by Jhung *et al.* (1990) that is based on spectroscopic constants (ω, B, ω_x, ...) which are usually available.
- Collect data on the transition dipole moment or oscillator strength of the transition.
- Analyse $\nu(r)$ to find the r range(s) of interest and, if needed, examine folding points around $d\nu/dr = 0$.
- Consider how to limit the classical partition sum: by only considering bound states (applicable at temperatures well below the dissociation energy) or by cutting off integration at a certain radius r (at high densities). See appendix 4.A for pointers on other cases.

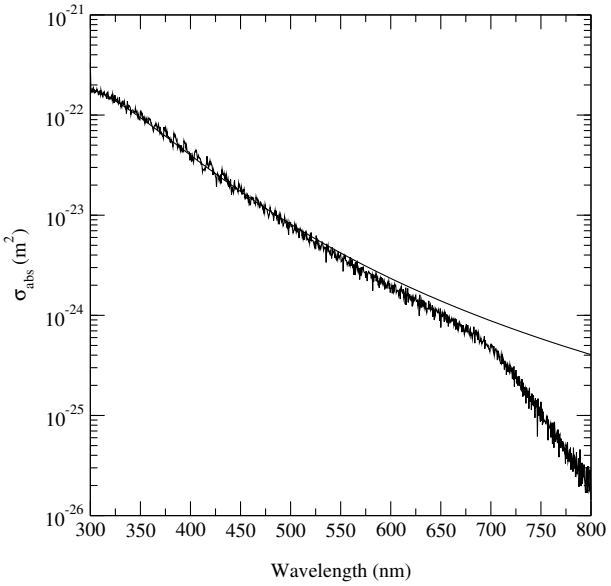

Figure 4.9: *S_2 Semiclassical (smooth line) and quantum-mechanical (jagged line) absorption cross section calculation for the $B^3\Sigma \rightarrow X^3\Sigma$ transition at 5000 K. Compared to the calculations at lower temperatures, here the v'' levels are most evenly populated, resulting in relatively flat curves. The defects in the Franck-Condon table for high v'' values are clearly visible, although there are still 2 orders of magnitude between the UV absorption peak and the value at 600 nm where the discrepancy becomes significant.*

- Test implementation of equation (4.16) by comparing it with the quantum-mechanical partition sum (4.25). This is also to insure that the temperatures of interest are high enough for the semiclassical approach.
- Test implementation of j_ν and κ equations using equation (4.1). Note that this condition only holds if both bound and free radiation is considered.

4.A Statistics

Consider a partition function for a bound state

$$Z_{bound} = \sigma_{sym} \left(\frac{2\pi\mu kT}{h^2}\right)^{\frac{3}{2}} \int_0^\infty 4\pi r^2 \exp(-V(r)/kT)\Gamma\left(\frac{3}{2}, \frac{D(r)}{kT}\right) dr.$$

This integral is finite if in the limit of high r values, $\Gamma(\frac{3}{2}, D(r)/kT)$ goes to zero faster than $1/r^3$. Since $D(r) = V(\infty) - V(r)$, we must look at the behaviour of $V(r)$ for high values of r, which will generally be

$$D(r) = V(\infty) - V(r) \propto r^{-m}.$$

A series expansion of $\Gamma(\frac{3}{2}, x)$ gives

$$\Gamma\left(\frac{3}{2}, x\right) = \frac{4}{\sqrt{\pi}} x^{\frac{3}{2}} \left(\frac{1}{3} - \frac{x}{5} + \frac{x^2}{7 \cdot 2!} - \dots\right),$$

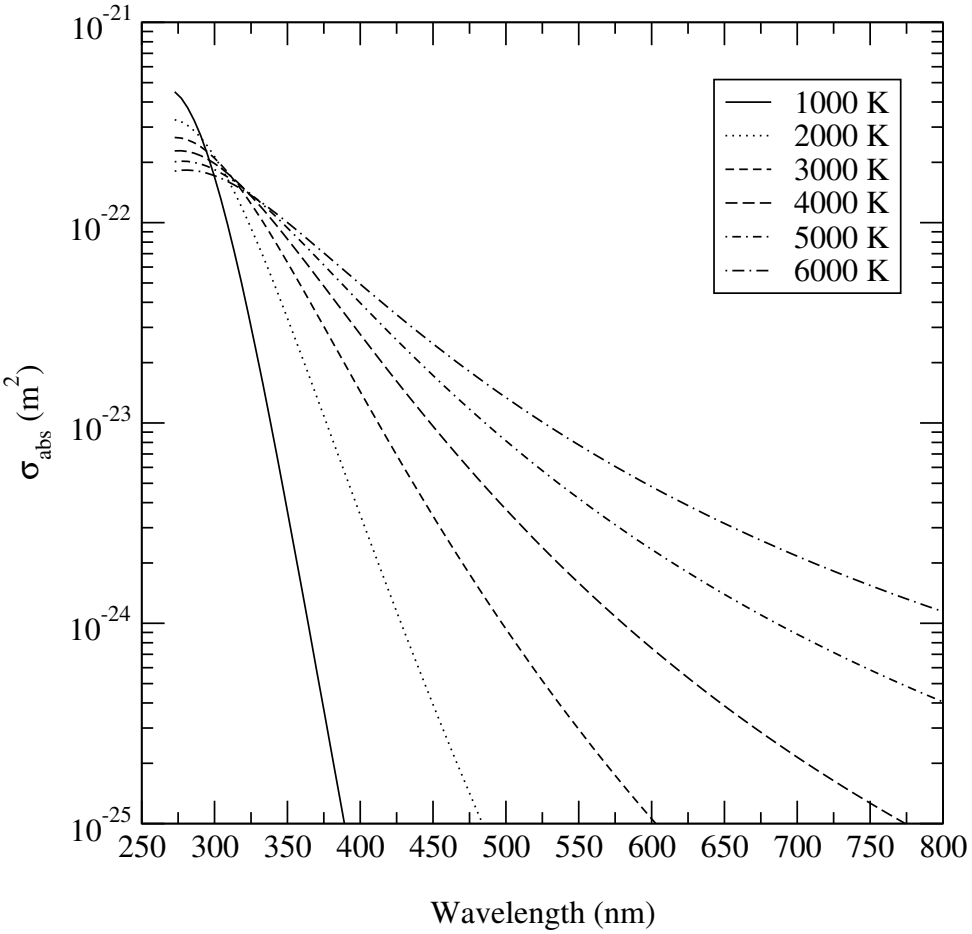

Figure 4.10: *Overview of the semiclassical absorption cross sections for temperatures between 1000 K and 6000 K. With increasing temperature, the absorption in the UV is reduced whereas the red absorption increases.*

so $\Gamma(\frac{3}{2}, D(r)/kT)$ will go to zero $\propto r^{-\frac{3}{2}m}$. The partition function is thus finite only if $m > 2$. This rules out Coulomb potentials, but most molecular potentials flatten much faster than that, with typically $m > 6$.

If the above criterion is not valid for the potential of interest, or if we want to calculate an unbound partition sum, or if the average distances between atoms are of the order of the width of the potential well, we have to put an upper limit on the r integration.

It is important to realize that the potential $V(r)$ is in fact determined by the closest other particle. We need to derive an distribution function $w(r)$, so that $w(r)dr$ gives the probability of finding the closest particle in the distance interval $r \ldots r + dr$ (Chandrasekhar, 1943). We expect $w(r)$ to be proportional to $4\pi r^2 nC \exp(-V(r)/kT)$, where n is the particle density and C is a constant to be determined later. Only one particle can be the nearest, so $w(r)$ must also be proportional to the probability of not finding the first particle at a closer range, $(1 - \int_0^r w(r')dr')$, so we have

$$w(r) = \left(1 - \int_0^r w(r')dr'\right) 4\pi r^2 nC \exp(-V(r)/kT).$$

By taking the derivative with respect to r we obtain a differential equation,

$$\frac{d}{dr}\left(\frac{w(r)}{4\pi r^2 C\exp(-V(r)/kT)}\right) = -4\pi r^2 C\exp(-V(r)/kT)\left(\frac{w(r)}{4\pi r^2 C\exp(-V(r)/kT)}\right),$$

which is easily solved:

$$w(r) = 4\pi r^2 nC\exp(-V(r)/kT)\exp\left(-\int_0^r 4\pi r'^2 nC\exp(-V(r')/kT)dr'\right).$$

The constant C must be determined from

$$\int_0^\infty w(r)dr = 1,$$

which is generally cannot be done analytically. Only in the limit where $V(r)/kT \ll 1$, so that we can ignore the potential term, can $w(r)$ be readily found,

$$w(r) = 4\pi r^2 n\exp\left(-\frac{4}{3}\pi r^3 n\right),$$

with the expectation value $< r >$, for the distance to the closest neighbour, given by

$$< r >= \int_0^\infty rw(r)dr \approx 0.554n^{-\frac{1}{3}}.$$

Chapter 5

Radiative transfer of a molecular S_2 B-X spectrum using semiclassical and quantum-mechanical radiation coefficients

Published as: *Harm van der Heijden, Joost van der Mullen, Johannes Baier and Achim Körber*
J. Phys. B: At. Mol. Opt. Phys. **35** 3633-3654 (2002)

Abstract

A fast method is presented for calculating the net emitted spectrum of a spherical sulfur plasma, from which the bulk of the radiation originates in the S_2 $B^3\Sigma_u^- \rightarrow X^3\Sigma_g^-$ molecular transition. The radiative transfer calculation needs as input the local spectral emission and absorption coefficients of the transitions. Calculations are presented using both a quantum-mechanical and a semiclassical method for generating these coefficients. It is found that the fine-structure of quantum-mechanical coefficients, which is absent in the smooth semiclassical data, may have a profound influence on the transport calculation. The circumstances where this occurs are identified and discussed. Measured spectra of the sulfur lamp are presented and compared with calculations, and a number of differences are found which may be due to an incorrect modelled temperature profile or non-LTE effects.

5.1 Introduction

In an earlier study (van der Heijden and van der Mullen, 2001) a semiclassical (SC) method for computing molecular radiation emission and absorption coefficients was presented and the results were compared to a quantum-mechanical (QM) calculation. By definition, the SC theory cannot be used to calculate the fine structure of the absorption and emission coefficients, but it does have the benefit that it is much less computationally intensive. The comparison showed that the SC data matched the QM data very well, provided the QM data was smoothed by

averaging over a wavelength or frequency interval that was large compared to the widths of the individual ro-vibrational transitions, thus removing the fine structure.

While this lack of fine structure may appear to be a serious limitation of the SC method, it is important to realize that using a full QM approach is not always desirable. The QM data needed for the calculation may simply be incomplete, leaving only the SC approach which merely requires data about the molecular potential functions — which can often be reconstructed from basic spectroscopic data (Herzberg, 1950; Jhung *et al.*, 1990) — and the transition probability. Finally, the details of the spectrum may not be of interest, for example in calculating the spectrum from a high pressure molecular light source, where the emitted spectrum spans hundreds of nanometres, and the primary concern is the spectrum's overlap with the eye-sensitivity curve and the total emitted power.

In the previous study, the SC method was indeed applied to the calculation of radiation coefficients of such a molecular light source, the high pressure sulfur lamp (Dolan *et al.*, 1992, 1995; Turner *et al.*, 1997). In this work, a method for calculating radiation transport in the sulfur lamp to obtain the emitted spectrum is discussed. Calculations are presented using both SC and QM data, where the main aim of this paper is to compare the results of both calculations and explain the differences. Spectra calculated using both methods are also compared to an experimentally obtained spectrum to determine the overall accuracy.

The sulfur lamp consists of a spherical quartz bulb (inner radius 16 mm) which is filled with typically 20 – 60 mg sulfur powder and 100 – 400 mbar (at 293 K) argon for ignition. In our experimental setup, the bulb is inside a hemi elliptical microwave cavity, as in figure 5.1. The range of microwave input power at 2.45 GHz in our experiments is between 300 and 1000 W, with an estimated 5% loss of power in the resonating cavity. Sulfur lamps can typically operate at input powers up to 2 kW. The plasma in the sulfur lamp is not entirely point-symmetric, due to the fact that the bulb is rotated at about 200 rpm and due to the not point-symmetric electric field. However, these non-symmetric effects are not expected to be important, and in the calculations a point-symmetric spherical configuration will be used.

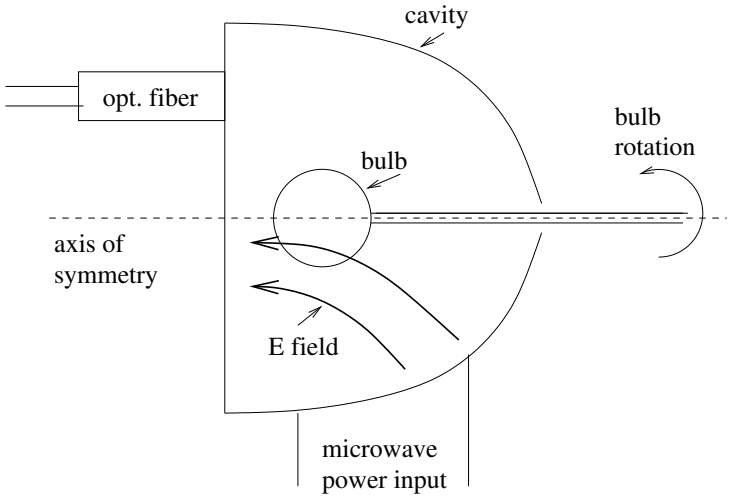

Figure 5.1: *Experimental setup of the sulfur lamp. The microwave power is coupled into a hemi elliptical cavity that contains the bulb (outer/inner radii 18/16 mm).*

Two characteristics make this plasma attractive as a light source. Firstly, the spectrum over-

laps well with the eye-sensitivity curve and contains hardly any UV or infrared radiation. Secondly, the efficiency is rather high, up to 70% of the power coupled into the plasma is emitted as visible light (but note that for practical comparisons with other light sources the efficiency of the microwave power source needs to be taken into account). The main origin of the emitted radiation is the S_2 $B^3\Sigma_u^- \rightarrow X^3\Sigma_g^-$ transition. The potential energy curves for both states are shown in figure 5.2 (Kuznetsova *et al.*, 1993, 1991).

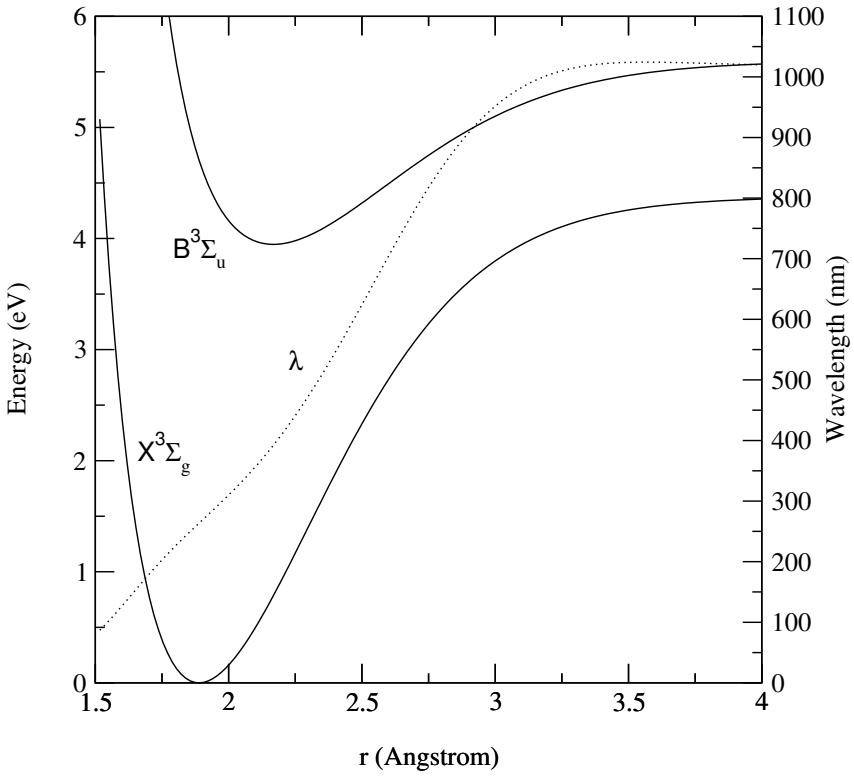

Figure 5.2: *S_2 $X^3\Sigma_g^-$ and S_2 $B^3\Sigma_u^-$ potential energy curves, with the classical radiation wavelength, $\lambda(r) = hc/(V_B(r) - V_X(r))$, plotted as function of internuclear distance r with values on the right axis.*

Van Dongen *et al.* (1998) measured electrical field strengths in the lamp's microwave cavity and, combining this with a study of the power coupling and calculations of the temperature dependence of an LTE sulfur plasma's electrical conductivity, estimate the temperature in the centre of the plasma to be approximately 4000 K. The temperature at the outside of the plasma was measured to be about 1000 K. Based on these temperatures and the amount of sulfur powder inside, operational partial pressures are estimated to be 5 bar sulfur compounds (mainly S and S_2) and 1 – 4 bar argon. This high pressure is the main argument for the assumption of LTE in the sulfur discharge.

Also working with the assumption of LTE, Körber (1998) calculated the QM spectrum of the sulfur lamp by assuming a cubic temperature profile with a central temperature of 4600 K. In order to reduce the number of individual transitions that needed to be included, Körber replaced the rotational branches of each vibrational band head with a quasi-continuous distribution. In the S_2 B-X system this is a particularly attractive technique since all branches overlap and extend to lower frequencies than that of the band head. A difference was found between the calculated

and measured spectra, with the amount of calculated radiation between 380 and 360 nm too high by a factor of 2.6, and the position of the maximum shifted from the experimentally found 525 nm to 470 nm. These effects were contributed to the quasi-continuous rotational distribution approximation.

Recently, Johnston *et al.* (2002) calculated a self-consistent temperature profile for the sulfur lamp by solving the temperature equation, again under the assumption of LTE and accounting for the effects of radiative transfer by basing the radiative transfer procedure on SC emission and absorption coefficients. Their results also indicated a central temperature, depending on microwave input power and operational pressure, of between 4000 and 4500 K, and the calculated spectra were shifted to the blue as well.

The results of Körber indicate that a quantum-mechanical calculation using "smeared out" vibrational bands results in a spectrum that does not quite fit the experiment. The question remains whether this is due to the used approximation or whether other effects are ignored, such as systems other than S_2 B-X or non-LTE effects. The work of Johnston, who employed SC radiation coefficients, poses the questions whether a different temperature profile might be found if the radiation were described using QM equations. It is our aim to investigate both questions by calculating a full QM, without the quasi-continuous rotational distribution approximation, as well as a SC spectrum and comparing both with an measured spectrum.

The calculations presented here are done with the plasma temperature profile as an input value, with subsequent density profiles according to LTE balances. The temperature profiles used in this work for evaluating the radiative transfer methods are sensible and supported by experimental evidence where available. However, in a fully self-consistent LTE model the radiation calculation, in conjunction with a model for microwave power input coupling, gives feed-back to the temperature and density profiles in an iterative manner until convergence is reached. In order to reach convergence in a reasonable amount of time, the limit on the amount of computer time that can be spend on radiation calculations is much more strict than for the non-iterative calculations presented here. In evaluating which method is most suitable for calculating the effects of radiative transfer the required computational resources are an important consideration.

In the following section the method for calculating the net emitted spectrum from a spherical plasma will be discussed. An extension of this method, to calculate not only the net emitted energy but also the internal radiative power source terms needed for a self-consistent temperature balance, will be treated in an upcoming paper. Section 5.3 contains a summary of the results for semiclassical and quantum-mechanical emission and absorption coefficients from earlier work (van der Heijden and van der Mullen, 2001). In section 5.4 spectra calculated using the semiclassical and quantum-mechanical coefficients are presented and compared to experimental spectra. Finally, section 5.5 is devoted to a discussion of the results and the conclusion.

5.2 Radiative transfer in a point-symmetric spherical configuration

5.2.1 Spherical geometry

In a point-symmetric spherical configuration, all quantities that determine the absorption and emission coefficients are a function of radius ρ alone (the symbol ρ has been chosen to avoid

confusion with the internuclear distance r in the following section). The sphere with radius R is divided into n shells around radii ρ_i ($0 \leq i < n$) between R_i and R_{i+1}, with $R_0 = 0$ and $R_n = R$. Inside these shells, all relevant quantities are assumed to be constant. Figure 5.3 shows the setup.

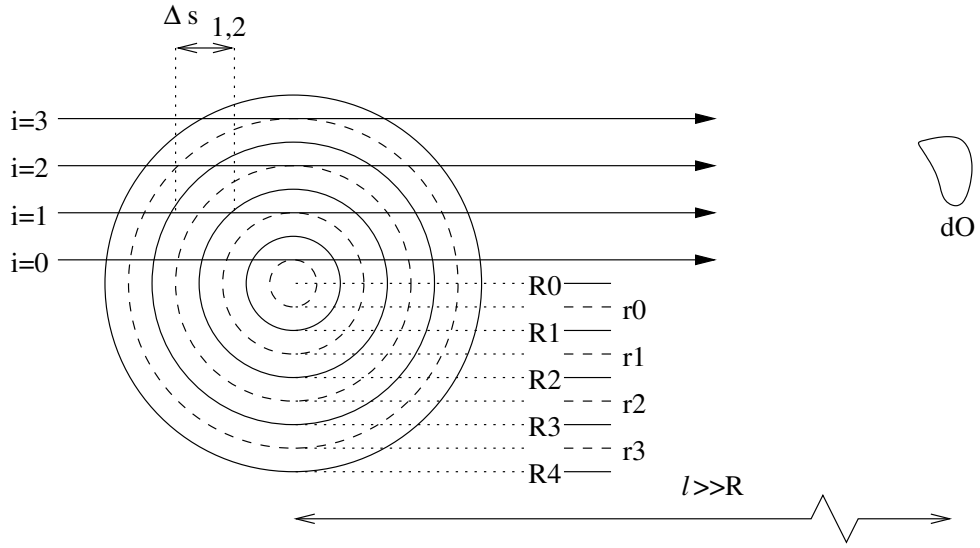

Figure 5.3: *Radiative transfer for spherical symmetry. The volume is divided in n spherical shells around radius ρ_i, bounded between R_i and R_{i+1}. The distance ℓ to the observer surface dO is large compared to outer radius R, so only "horizontal" rays (drawn arrows) reach dO. To obtain the intensities at the end of each ray, the equation for radiative transfer (5.6) is integrated.*

Also due to the symmetry, all straight paths through the lamp can be characterised by one parameter, the minimal distance y between points along the path and the centre of the sphere. By calculating the amount of light that is emitted or absorbed along these lines and weighing the resulting intensities of the rays when they leave the lamp, the overall emitted spectrum can be determined.

Consider an observer surface element dO at a large distance ℓ with corresponding solid angle $d\Omega = dO/\ell^2$. Since $\ell \gg R$, the only light rays that reach dO are those that travel horizontally in figure 5.3. In order to calculate the total spectral power $P_\nu(dO)$ (in units of W/Hz) that arrives at dO, we must evaluate all unique lines with distance y from the centre:

$$P_\nu(dO) = \int I_\nu \Omega dA = \int_0^R I_\nu(y) \frac{dO}{\ell^2} \frac{dA}{dy} dy, \tag{5.1}$$

with $I_\nu(y)$ the spectral intensity of the radiation leaving the sphere, in the direction of dO, with minimal distance to the centre y, and dA the area of the emitting surface projected on dO,

$$dA = 2\pi y dy. \tag{5.2}$$

The total emitted spectral power is obtained by integrating over the entire observer sphere: $P_\nu = 4\pi\ell^2 P(dO)/dO$, so

$$P_\nu = 8\pi^2 \int_0^R I_\nu(y) y dy. \tag{5.3}$$

We choose to calculate the intensity along probe lines i that have distances to the centre y_i corresponding to the radial discretisation ρ_i (see figure 5.3). Then, replacing the integral with a summation over i, and $dA = 2\pi y dy$ with

$$\Delta A_i = \pi(R_{i+1}^2 - R_i^2), \tag{5.4}$$

we find

$$P_\nu = 4\pi^2 \sum_{i=0}^{n-1} I_\nu(i)(R_{i+1}^2 - R_i^2). \tag{5.5}$$

Two things can be noted about this numerical scheme. First, because the radiation rays have distances y_i to the sphere centre, the number of spherical shells n that we use for discretisation is equal to the number of rays that we will need to evaluate. Each ray, depending on it's distance y_i to the centre, traverses up to $2n$ spherical shells, which makes the computational cost of this algorithm scale with n^2. Second, this scheme does not depend on equidistant ρ_i and R_i values. This property allows us to decrease the distance between ρ_i points in certain locations, for example to accommodate steep gradients near the sphere surface.

5.2.2 Integration along probe lines

The spectral intensity I_ν along a probe line is calculated by integrating the equation for radiative transfer,

$$\frac{dI_\nu}{ds} = j_\nu - \kappa I_\nu, \tag{5.6}$$

where j_ν and κ are the coefficients for emission and absorption respectively, with s representing distance along the line.

The integration goes from the point where the line enters (s_0) to where it leaves (s_1) the sphere. It can be easily verified that the following equation for the intensity $I_\nu(i)$ at the end of ray i satisfies the differential equation (5.6):

$$I_\nu(i) = \int_{s_0}^{s_1} j_\nu(s) \exp(-\tau(s)) ds, \tag{5.7}$$

with the optical depth τ given by

$$\tau(s) = \int_s^{s_1} \kappa(s') ds'. \tag{5.8}$$

Using the property that the sphere is divided in shells with constant j_ν and κ values, integrating over a distance Δs inside a shell gives

$$\int_s^{s+\Delta s} j_\nu \exp(-\kappa \cdot (s + \Delta s - s')) ds' = \frac{j_\nu}{\kappa}[1 - \exp(-\kappa \Delta s)]. \tag{5.9}$$

Since each ray will travel through a series of shells, we can use this relation to rewrite equation (5.7) as a recursive relation. Labelling the shells that ray i travels through ($n-1, n-2, \ldots, i, i+1, \ldots, n-1$) with k, we find

$$I_{\nu,k+1}(i) = I_{\nu,k}(i) \exp(-\tau_{i,k}) + \frac{j_{\nu,k}}{\kappa_k}[1 - \exp(-\tau_{i,k})], \tag{5.10}$$

with $\tau_{i,k} = \kappa_k \Delta s_{i,k}$ the optical depth of shell k as seen by line i. Using $I_\nu(i) = 0$ at the beginning of the line, we can calculate $I_\nu(i)$ at the end by applying relation (5.10) for each shell that the sphere traverses. Another way of expressing this recursive relation is by writing equation (5.10) in terms of the change $\Delta I_{\nu,k}$ of I_ν in shell k,

$$\Delta I_{\nu,k} = \left(\frac{j_{\nu,k}}{\kappa_k} - I_{\nu,k} \right) \left[1 - \exp(-\tau_{i,k}) \right]. \tag{5.11}$$

Using the fact that in LTE the ratio between j_ν and κ is fixed according to Kirchhoff's law,

$$\frac{j_\nu}{\kappa} = \frac{2h\nu^3}{c^2} \frac{1}{\exp(h\nu/kT) - 1} = B_\nu, \tag{5.12}$$

equation (5.11) clearly shows that when the intensity I_ν is higher than the Planck intensity B_ν, the change in I_ν will be negative. If the intensity is lower, the change will be positive. In both cases, the transition through the shell causes the difference between the ingoing I_ν and the shell's local B_ν to be reduced by a factor of $[1 - \exp(-\tau)]$.

Two limiting cases can now be distinguished. First, if $\tau \gg 1$, then $[1 - \exp(-\tau)] \approx 1$ and the resulting I_ν will be equal to B_ν. This has the effect that the intensity on this path has no history, that is, it is completely determined by the local B_ν. If this is valid throughout the sphere, the spectrum can be easily calculated by integrating over the solid angle (4π) and the projected surface (πR^2),

$$P_{\nu,thick} = 4\pi^2 R^2 B_\nu(T(R)), \tag{5.13}$$

where $T(R)$ is the surface temperature.

Second, if $\tau \ll 1$, the term $[1 - \exp(-\tau)]$ can be approximated as $\tau + O(\tau^2)$, so that

$$\Delta I_\nu \approx \left(\frac{j_\nu}{\kappa} - I_\nu \right) \tau \approx j_\nu \Delta s.$$

In this case absorption plays no role, and the emitted spectrum can be calculated by integrating the emission coefficient over the solid angle (4π) and the sphere volume ($4\pi\rho^2 d\rho$),

$$P_{\nu,thin} = \int_0^R 16\pi^2 \rho^2 j_\nu(\rho) d\rho. \tag{5.14}$$

5.3 Molecular emission and absorption coefficients

5.3.1 Semiclassical and quantum-mechanical systems

First the formulae for j_ν and κ will be given for the SC and QM approaches, where the reader is referred to van der Heijden and van der Mullen (2001) for a derivation. Both approaches use LTE, by assuming the population of a level at energy E is proportional to $\exp(-E/kT)$. The QM approach is valid for cases where the molecular levels can be described by quantum numbers v (vibration) and N (rotation) and does not describe fine splitting. The spectral shape of an individual ro-vibrational transition can be any normalised function of frequency ν, for example a Gaussian for Doppler broadened lines. The semiclassical formulae are valid for diatomic molecules at high pressure (order >1 bar) and at temperatures high enough so that the thermal energy is larger than the energy gaps between levels. In S_2, the vibrational energy

spacing ω is 725 cm^{-1} (corresponding to approximately 1000 K), and the rotational spacing is much smaller ($B = 0.30$ cm^{-1}).

For both approaches the following definitions are used, using single primes for quantities of the upper state and double primes for the lower state,

$$j_\nu = \frac{h\nu}{4\pi} n' A \phi'_\nu(\nu), \tag{5.15}$$

$$\kappa(\nu) = n''\sigma_{abs} - n'\sigma_{stim} = n'' \frac{c^2}{8\pi\nu^2} A \frac{g'}{g''} \phi''_\nu(\nu) - n' \frac{c^2}{8\pi\nu^2} A \phi'_\nu(\nu), \tag{5.16}$$

with A the transition probability, n the state density, g the state's degeneracy and ϕ_ν a normalised line profile.

For the semiclassical case, the upper and lower line profiles are given by (van der Heijden and van der Mullen, 2001)

$$\phi'_\nu(\nu(r)) = \frac{\sigma_{sym}}{Z'_{SC}} \Gamma\left(\frac{3}{2}, \frac{D'(r)}{kT}\right) \left(\frac{2\pi\mu kT}{h^2}\right)^{\frac{3}{2}} 4\pi r^2 \exp\left(-\frac{V'(r)}{kT}\right) \left|\frac{d\nu(r)}{dr}\right|^{-1}, \tag{5.17}$$

$$\phi''_\nu(\nu(r)) = \frac{\sigma_{sym}}{Z''_{SC}} \Gamma\left(\frac{3}{2}, \frac{D''(r)}{kT}\right) \left(\frac{2\pi\mu kT}{h^2}\right)^{\frac{3}{2}} 4\pi r^2 \exp\left(-\frac{V''(r)}{kT}\right) \left|\frac{d\nu(r)}{dr}\right|^{-1}, \tag{5.18}$$

where r is the molecule's internuclear distance, Z_{SC} the state's internal partition sum, $V(r)$ the potential energy, $D(r) = V(\infty) - V(r)$ the dissociation energy, σ_{sym} a symmetry factor (1 for heterogenous and $\frac{1}{2}$ for homogenous molecules), and $\Gamma(\frac{3}{2}, x)$ the normalised incomplete gamma function of order $\frac{3}{2}$,

$$\Gamma\left(\frac{3}{2}, x\right) = \frac{2}{\sqrt{\pi}} \int_0^x \sqrt{t} \exp(-t) dt. \tag{5.19}$$

The potential energy $V(r)$ is defined relative to the state's minimum energy V_0 and the energy difference ΔV between the upper and the lower state is defined as $V'_0 - V''_0$. According to the Franck-Condon principle, which states that an electronic transition in a molecule will occur so quickly that r and U_{kin} do not change, the change in energy is entirely due to the change in potential and thus the frequency of the radiation is given by

$$\nu(r) = \frac{\Delta V + V'(r) - V''(r)}{h}. \tag{5.20}$$

The symmetry factor σ_{sym} effectively cancels because it also appears in the classical version of the internal partition function Z_{SC},

$$Z_{SC} = \sigma_{sym} \left(\frac{2\pi\mu kT}{h^2}\right)^{\frac{3}{2}} \int_0^\infty \Gamma\left(\frac{3}{2}, \frac{D(r)}{kT}\right) 4\pi r^2 \exp\left(-\frac{V(r)}{kT}\right) dr, \tag{5.21}$$

Due to the presence of the $\Gamma(\frac{3}{2}, D(r)/kT)$ term in (5.21), it is the partition function for all bound ($U_{kin} = p^2/(2\mu) < D(r)$) levels. The partition function for both bound and free levels can be obtained by replacing the Γ term in (5.21) with unity, but in that case some other effect must be included to ensure the integral is finite. One way of obtaining this is by setting an upper

limit on the integration at $< r >$, the expected distance to the next neighbour in a plasma with particle density n (Chandrasekhar, 1943; van der Heijden and van der Mullen, 2001),

$$< r >= \int_0^\infty 4\pi r^3 n \exp\left(-\frac{4}{3}\pi r^3 n\right) dr \approx 0.554 n^{-\frac{1}{3}}. \tag{5.22}$$

By van der Heijden and van der Mullen (2001) it was shown that up to a temperature of 4500 K, the bound partition function does not significantly diverge from the one calculated using the total partition function where the integration was cut off at 15 Å (comparable to $< r >$ at the sulfur lamp's pressure and temperature). Unbound levels therefore have no large influence in this study, and in the remainder of this paper equation (5.21) is used as the semiclassical partition function.

The quantum-mechanical line profile is actually composed of many individual, possibly overlapping lines. For molecular $^3\Sigma$ states, where Hund's rule (b) applies (Herzberg, 1950), and ignoring electron spin splitting (we include the $2S+1$ degeneracy in the state degeneracies g' and g''), we have

$$\phi'_\nu = \phi_{\nu,\ell}(\nu)\frac{1}{Z'_{QM}}\sum_{v'N'}\omega_{N'}\sum_{v''N''}S^{N'}_{N''} < \psi_{v'}|\psi_{v''} >^2 \exp\left(-\frac{E_{v'N'}}{kT}\right), \tag{5.23}$$

$$\phi''_\nu = \phi_{\nu,\ell}(\nu)\frac{1}{Z''_{QM}}\sum_{v''N''}\omega_{N''}\sum_{v'N'}S^{N'}_{N''} < \psi_{v'}|\psi_{v''} >^2 \exp\left(-\frac{E_{v''N''}}{kT}\right), \tag{5.24}$$

with v the vibrational quantum number, N the quantum number for angular momentum without spin, ω_N a statistical factor due to nuclear spin, $S^{N'}_{N''}$ the Hönl-London factor, $< \psi_{v'}|\psi_{v''} >^2$ the Franck-Condon factor and $\phi_{\nu,\ell}$ the line profile for a single ro-vibrational transition $v'N' \longrightarrow v''N''$. The internal partition function is now given by

$$Z_{QM} = \sum_v \sum_N g_{v,N} \exp\left(-\frac{E_{v,N}}{kT}\right), \tag{5.25}$$

and the state degeneracy g contains a factor $2S+1$ (=3 for $^3\Sigma$ states). For S_2, ω'_N equals unity for odd and zero for even N'' levels, effectively making even N'' levels forbidden. For the upper state, the situation is reversed and odd N' levels are forbidden. The Hönl-London factors are such that only $|N' - N''| = 1$ transitions are allowed.

5.3.2 Spectral averages

We have shown (van der Heijden and van der Mullen, 2001) that the S_2 B-X absorption and emission coefficients can, averaged over a certain frequency range $\Delta\nu_{avg}$, be adequately described using a semiclassical (SC) method, that is

$$\int_{\Delta\nu_{avg}} \kappa_{SC} d\nu \approx \int_{\Delta\nu_{avg}} \kappa_{QM} d\nu, \tag{5.26}$$

where $\Delta\nu_{avg}$, the averaging frequency interval, is sufficiently large so that it contains many QM ro-vibrational lines. For S_2, the energy gap between ro-vibrational lines is of the order 0.3 cm^{-1}, corresponding to 10^{10} Hz, so that a frequency interval of order 10^{12} Hz is sufficient.

A similar averaging relation holds for the emission coefficients $j_{\nu,SC}$ and $j_{\nu,QM}$. However, with respect to the intensity I_ν that is obtained through a repeated application of equation (5.11), which is decidedly non-linear except in the limiting case of negligible absorption, this averaging will not be valid. Since $j_\nu/\kappa = B_\nu$ is a smooth function of ν, the source of non-linearity is in the exponential term. That is, the following inequality generally holds,

$$\int_{\Delta\nu_{avg}} [1 - \exp(-\tau_{SC})] d\nu \neq \int_{\Delta\nu_{avg}} [1 - \exp(-\tau_{QM})] d\nu, \tag{5.27}$$

even if equation (5.26) is satisfied. The extend to which these small structure details influence the overall characteristics of the radiative transfer is investigated in section 5.4.

5.3.3 Ro-vibrational line profiles

Up to this point, the line profiles $\phi_{\nu,\ell}$ of the individual QM ro-vibrational transitions have not been specified in detail. From equation (5.26) it follows that in the limit where the profile's FWHM is much larger than the average frequency separation between line centres, the QM coefficient's fine structure details will be smoothed out so that it becomes indistinguishable from the smooth SC coefficients. If, however, the line width is significantly smaller than the average separation, then, while equation (5.26) still holds true, the QM and SC spectra will look quite different on a small frequency scale. This is illustrated in figure 5.4, where the QM line profiles with width $\Delta\nu_{peak}$ are, for the sake of the following argument, approximated by step functions and the SC continuum is represented by the dotted line. From equation (5.26) follows that the surface under the dotted line is equal to the shaded surface under the peaks. With $\Delta\nu_{gap}$ the gap between central peak wavelengths this means that,

$$\kappa_{SC}\Delta\nu_{gap} = \kappa_{QM}\Delta\nu_{peak}, \tag{5.28}$$

where κ_{SC} is the continuous absorption coefficient and κ_{QM} is the effective (peak) absorption coefficient, which is higher by a factor ν_{gap}/ν_{peak}. Körber (1998, 1999) found that using a factor of $\nu_{gap}/\nu_{peak} = 5$ to correct the quasi-continuous approach improved the agreement of the calculated spectrum with the experimental one. However, without a detailed analysis of the actual QM coefficients, this correction factor cannot be calculated and is effectively a fit parameter.

5.3.4 Numerical aspects

The formulae in the previous sections were all given, as is the convention, in terms of frequency ν. The calculations are presented in terms of wavelength λ, which is the common representation for light sources.

While the calculation of the SC coefficients is relatively straightforward, there are a few important details in the numerical representation of QM coefficients. First, the spectrum range of interest (typically 300-800 nm) is divided in wavelength "bins" of width $\Delta\lambda_{bin}$ where the contributions from ro-vibrational lines are collected. Since the bin size is the spectral resolution of the numerical representation, care has been taken to insure that the bin size is significantly smaller than the (smallest) physical line width. At this stage, these lines effectively have a square profile ϕ_ν with value $1/\Delta\lambda_{bin}$ at wavelengths inside the bin and 0 elsewhere. Contributions from other transitions that fall into the same bin are simply added. After all ro-vibrational

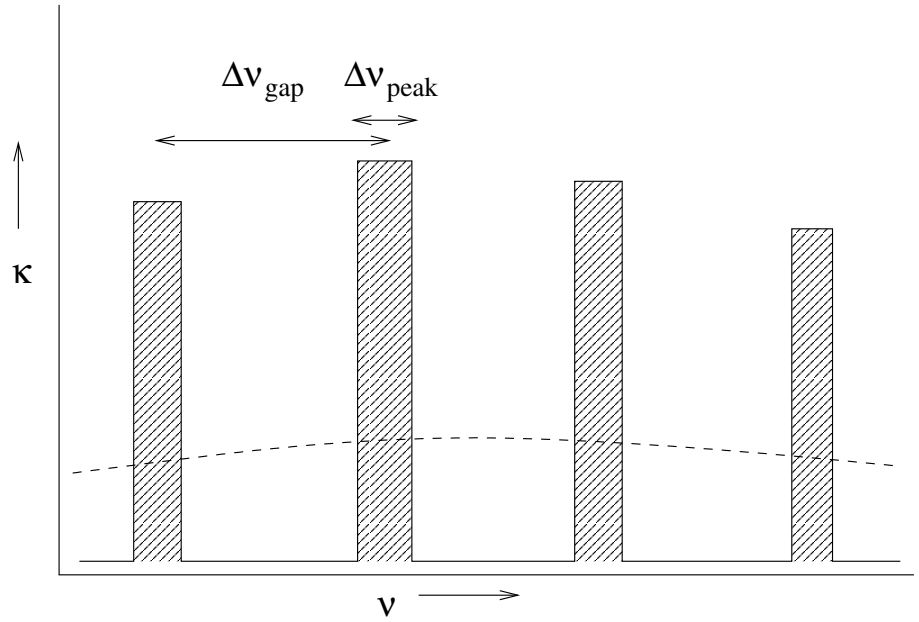

Figure 5.4: *Sketch of a discrete QM absorption spectrum, here approximated with square line profiles, and a continuous SC spectrum, plotted with a dashed line. The distance between line centres is $\Delta\nu_{gap}$ and the width of the lines is $\Delta\nu_{peak}$.*

transitions have been collected in bins this way, the spectra are convoluted with an appropriate line profile $\phi_{\nu,\ell}$.

The smallest width encountered in this study was about 1.5 pm for S_2 Doppler (Gaussian) profiles at 1000 K and 300 nm. Since this value is the absolute minimum, and tests indicated that there was little difference between spectrum calculations using a bin size of 0.2 pm and 1 pm, a bin size of 1 pm was used for all calculations involving Doppler widths. This still results in sampled spectra with $(800 - 300)/0.001 = 500,000$ points. This clearly shows that doing full fledged radiative transfer calculations using QM coefficients is not a convenient option, especially when we are not particularly interested in the sub-nanometre details of the total emitted spectrum.

5.4 Calculations

5.4.1 Calculation parameters

Due to the spherical symmetry, we need to specify all quantities relevant to the transport of radiation as a function of radius ρ only. The radius is discretised using 20 equidistant points between $\rho = 0$ and $\rho = 16$ mm.

Calculations will be done on a pure sulfur plasma at a pressure p of 5 bar. The presence of argon in the actual lamp of course influences the plasma as a whole, but we assume here that it does not significantly influence the LTE sulfur densities or line profiles. The temperature T is imposed according to the following profile,

$$T(r) = T_c - (T_c - T_w)\left(\frac{\rho}{R}\right)^a, \tag{5.29}$$

where T_c and T_w are the centre and wall temperature respectively and a is the order of the profile (high a values give flat profiles with steep gradients near the wall). From the constant pressure p and temperature profile $T(\rho)$ all particle densities follow. Specifically, we consider particles S, S^+, S^-, S_2X (ground state S_2), S_2B (excited S_2) and electron e. Sulfur forms molecules S_n with n up to > 2 at lower temperatures, but at the operational conditions (1000 – 5000 K) these molecules are not important. To obtain the densities we solve the following LTE balances,

$$S \longleftrightarrow S^+ + e \tag{5.30}$$

$$S^- \longleftrightarrow S + e \tag{5.31}$$

$$S_2X \longleftrightarrow S + S \tag{5.32}$$

using the general equilibrium expression for a balance of type $AB \longleftrightarrow A + B$

$$\frac{[A][B]}{[AB]} = \frac{Q_A Q_B}{Q_{AB}} \left(\frac{2\pi\mu_{AB}kT}{h^2}\right)^{\frac{3}{2}} \exp\left(-\frac{E_{AB}}{kT}\right), \tag{5.33}$$

where $[X]$ and Q_X represent respectively the density and the total partition function for particle X, μ_{AB} is the reduced of mass $m_A m_B/m_{AB}$ of the $A-B$ system, and E_{AB} is the internal energy offset difference between $A + B$ and AB. The total partition function Q is a Boltzmann sum over the particle's internal levels i with offset energy E_i, degeneracy g_i, and internal partition sum Z_i,

$$Q = \sum_i g_i Z_i \exp\left(-\frac{E_i}{kT}\right). \tag{5.34}$$

For reactions involving electrons with $Q = 2$ and a mass m_e that is small compared to an ion mass so that $\mu_{Ae} \approx m_e$, it can be seen that equation (5.33) is a general form of the well-known Saha equation, while in the case of the molecular reaction the expression becomes the Guldberg-Waage equation. For the balance between ground and excited S_2 states,

$$S_2X \longleftrightarrow S_2B, \tag{5.35}$$

the Boltzmann equation is used,

$$\frac{[S_2B]}{[S_2X]} = \frac{Q_{S_2B}}{Q_{S_2X}} \exp\left(-\frac{\Delta V}{kT}\right), \tag{5.36}$$

with ΔV the difference between the minimal energies of the B and X state. To complete the system of equations we add charge neutrality,

$$[S^+] = [S^-] + [e], \tag{5.37}$$

and constant pressure,

$$[S] + [S^+] + [S^-] + [S_2X] + [S_2B] + [e] = \frac{p}{kT}. \tag{5.38}$$

Figure 5.5 shows the solution of this system as a function of temperature for a pressure of 5 bar.

At room temperature, the bulb of a sulfur lamp contains sulfur in solid state, which after ignition of the argon buffer gas will evaporate and take over the plasma, as S has a lower

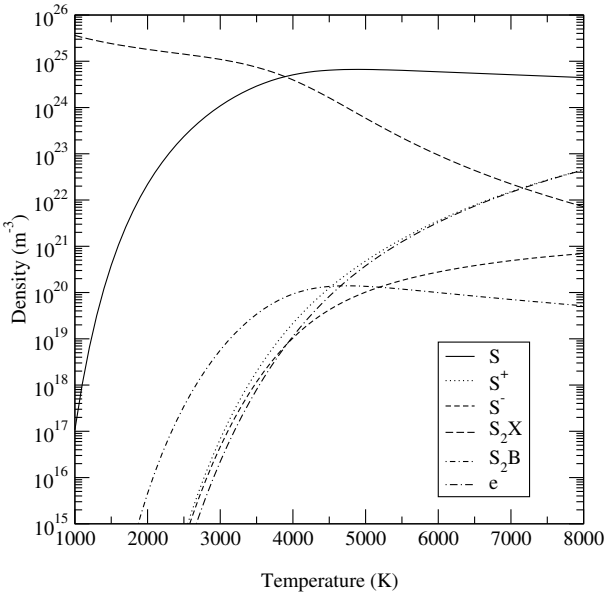

Figure 5.5: *Calculated densities of particles in a pure sulfur plasma as function of temperature at a total pressure of 5 bar.*

ionisation energy than Ar. As a consequence of this, the partial sulfur pressure under operating conditions is not directly controlled by the experimenter, but rather a consequence of the amount of sulfur available in the bulb and the temperature profile of the plasma. Figure 5.6 shows the pressure of a pure sulfur plasma for different central temperatures T_c and powers a, cf. equation (5.29). The temperature profile that has been used in the calculations, unless specified otherwise, is shown in figure 5.7 and is characterised by $T_c = 4000$ K, $T_w = 1000$ K, and $a = 3$ (van Dongen *et al.*, 1998).

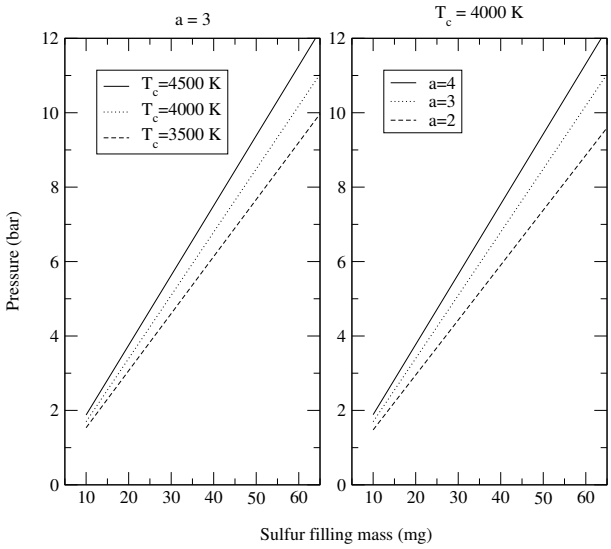

Figure 5.6: *Pressure of a pure sulfur plasma as function of sulfur mass filling for varying central temperatures T_c in a cubic profile (left) and for quadric, cubic, and parabolic profiles with $T_c = 4000K$ (right).*

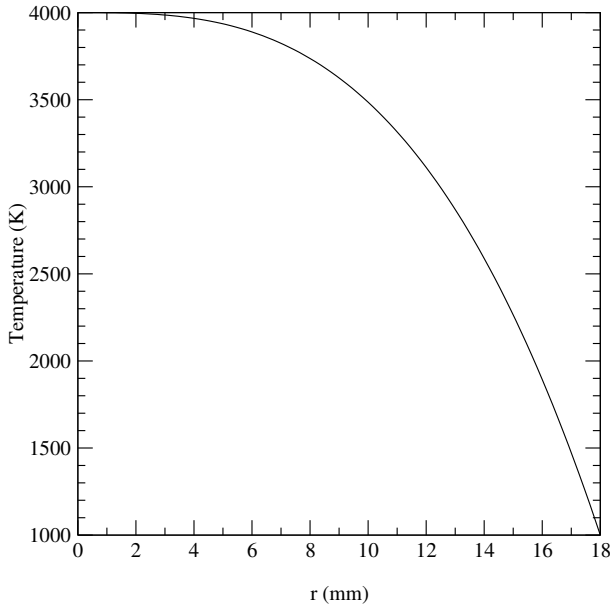

Figure 5.7: *The cubic ($a = 3$) temperature profile with $T_c = 4000$ K and $T_w = 1000$ K.*

The measurements are done with bulbs filled with 30 mg sulfur powder. Figure 5.6 shows that, for the given temperature profile, the partial sulfur pressure at operating conditions is approximately 5 bar.

5.4.2 Radiative transfer using QM and SC coefficients

Figure 5.2 shows the S_2X and S_2B potential functions, along with the classical radiation wavelength as function of internuclear distance r. Note that the wavelengths that are interesting from a lighting point of view, roughly between 300 and 800 nm, are emitted from low-lying B levels, whereas the low-lying X levels mostly absorb undesired UV radiation.

The transition probability of the B-X system is proportional to the square of the transition dipole moment $D_{BX}(r)$, which is a function of r. It is trivial to include this dependence in the semiclassical equations, but the Franck-Condon factors that are used in the quantum-mechanical method (Kuznetsova *et al.*, 1993, 1991) effectively replace $D_{BX}(r)$ with an effective $\overline{D_{BX}}$ (Herzberg, 1950). Since we are primarily interested in the comparison between SC and QM calculations, we "handicap" the SC method by using the same average dipole transition moment. In figure 5.8 the transition dipole moment $D_{BX}(r)$ is plotted against the classical wavelength $\lambda(r)$ (Pradhan and Partridge, 1991). A value of 0.83 $a_0 q_e$, corresponding to $D(r)$ at the centre of the emission spectrum, was chosen as the effective transition dipole moment.

Using a sulfur pressure of 5 bar and a cubic temperature profile with $a = 3$, $T_c = 4000$ K, and $T_w = 1000$ K, cf. equation (5.29) and figure 5.7, we calculate the emitted spectrum, integrated over the total solid angle, of the sulfur plasma. Figure 5.9 shows three spectrum calculations; one using SC coefficients, and two with QM coefficients.

The first QM spectrum was calculated with Doppler line widths (order 1.5 - 5 pm, depending on λ and T) with 1 pm bins and, in order to be able to distinguish the general shape, is plotted with a 1 nm running average. In the second QM calculation, the widths were fixed at 20 pm and it is clear that the result is much more similar to the SC calculation. At higher line widths,

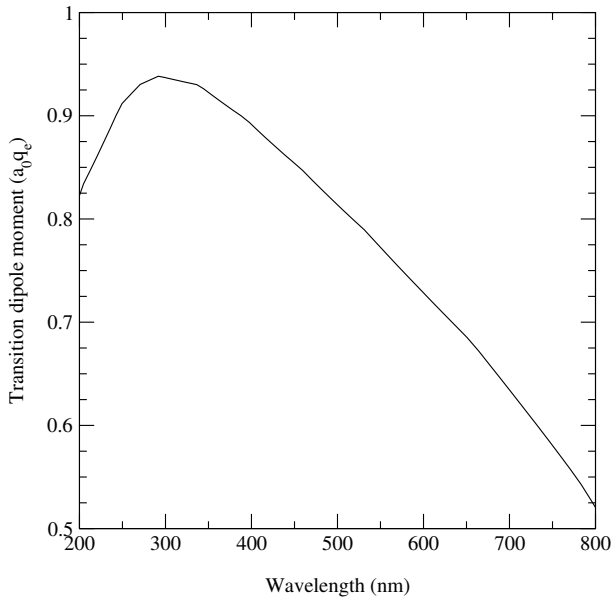

Figure 5.8: *Transition dipole moment D in atomic units as function of classical radiation wavelength.*

the results become the same except for the tail in the red part of the spectrum, where the QM Franck-Condon tables are incomplete (van der Heijden and van der Mullen, 2001). The total emitted radiation, $\int P_\lambda d\lambda$, is 389 W for the SC spectrum and 246 W for the QM spectrum. This is a substantial difference that could have a large impact on a self-consistent LTE calculation. It must be noted, however, that Doppler line widths are not necessarily correct for the plasma at hand, but rather form a lower limit of the line width.

To investigate the differences between the SC and the QM spectrum with Doppler width, which is the smallest physically relevant width, we define a diagnostic parameter $\rho_{\tau=1}(\lambda)$ that, for a given wavelength λ indicates where the optical depth equals one,

$$\int_{\rho_{\tau=1}(\lambda)}^{R} \kappa(\rho, \lambda) d\rho = 1, \tag{5.39}$$

where the integration of κ starts at the outside in the direction of the sphere's centre. The quantity $\rho_{\tau=1}(\lambda)$ is effectively a mean free optical depth into the plasma. In figure 5.10 we plot $\rho_{\tau=1}$ against wavelength for the given temperature profile, while figure 5.11 gives the corresponding temperature $T(\rho_{\tau=1})$. In both figures the quantum-mechanical data is again smoothed by a 1 nm running average for clarity. There are three wavelength ranges of interest, as indicated in figure 5.9, which will now be discussed successively.

From figures 5.10 and 5.11 it is evident that, at the low wavelengths of range I, the QM radiation originates, on average, from layers deeper in the discharge than the SC radiation. Since the deeper layers have a higher temperature, this explains why the classical spectrum is below the quantum-mechanical one for low wavelengths. With figure 5.12 this effect can be explained further. Because the absorption coefficient is a smooth function of frequency, the semiclassical radiation is optically thick for all frequencies and no radiation will travel much further than $\tau = 1/\kappa_{SC}$. However, the QM coefficients vary considerably as a function of ν and for parts of the wings of the line profiles (diagonally shaded in figure 5.12) the mean free

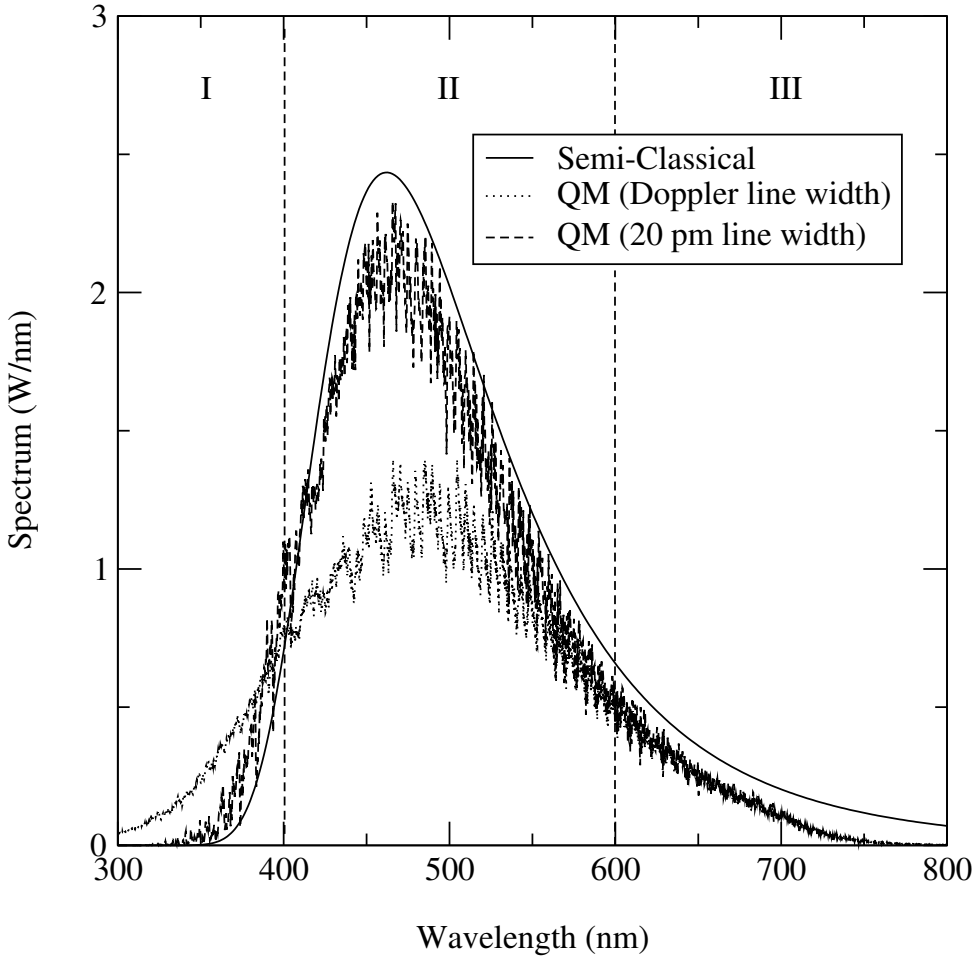

Figure 5.9: *Comparison of the QM and SC calculated spectra. Two QM spectra are given; one with Doppler line widths (with 1 pm bin size) and one with larger line widths set to 20 pm. The latter clearly resembles the SC profile. The sulfur pressure is 5 bar and the temperature profile is given by equation (5.29) with* $T_c = 4000$ *K and* $a = 3$.

optical path $1/\kappa_{QM}$ will be large enough to reach the plasma boundary.

Above $\lambda = 450$ nm, in range II, the roles are reversed and the plasma becomes thinner for the classical radiation. In this range, the classical absorption coefficient becomes sufficiently low so that a significant part of the generated radiation escapes. However, in the quantum-mechanical case, frequencies close to the central line frequency (the horizontally shaded areas in figure 5.12) are still strongly absorbed, so that less radiation escapes than in the SC case. In the spectra the crossing point between range I and II is at a lower wavelength, around 400 nm. This is caused by the fact that the most intense lines in the quantum-mechanical spectrum, which are responsible for most of the light, also have the highest absorption coefficient. This non-linear effect is not adequately represented by working with average $\rho_{\tau=1}$ values.

At still higher wavelengths, in range III, the plasma is optically open for both types of coefficients. The SC and QM spectra are in good agreement. SC is slightly higher than QM but this can be explained by the incomplete Franck-Condon table for the B-X transition (van der Heijden and van der Mullen, 2001).

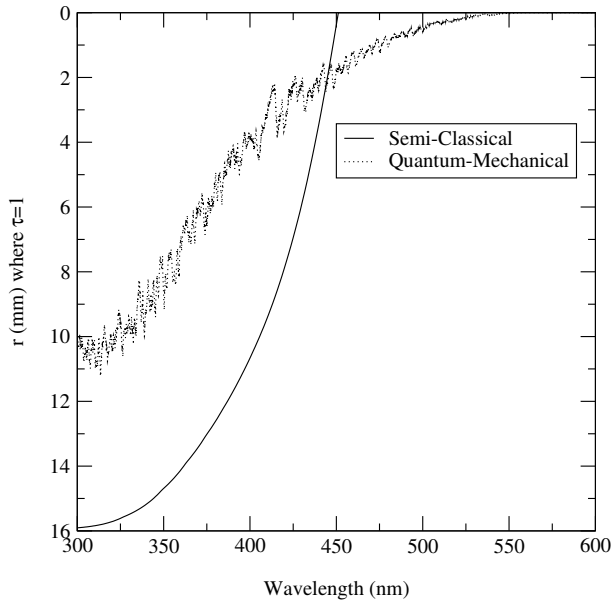

Figure 5.10: *Value of ρ where $\tau = 1$ (mean free optical path), as calculated from the outside of the sphere towards the centre. The values on the y axis represent coordinate ρ, not distance into the plasma $d = 16$ mm$-\rho$.*

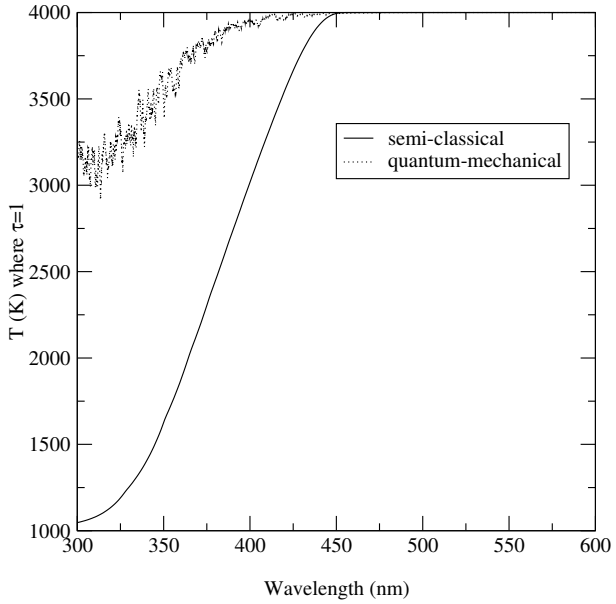

Figure 5.11: *Value of $T(\rho)$ where $\tau = 1$, as calculated from the outside of the sphere towards the centre.*

5.4.3 Optimising the quantum-mechanical calculation

Since, as was mentioned before, calculating a QM spectrum with 1000 points per nm over a range of 500 nm requires an inconvenient amount of computing power, and making use of the fact that we are only interested in the general shape of the spectrum, the calculation of a QM spectrum can be optimised.

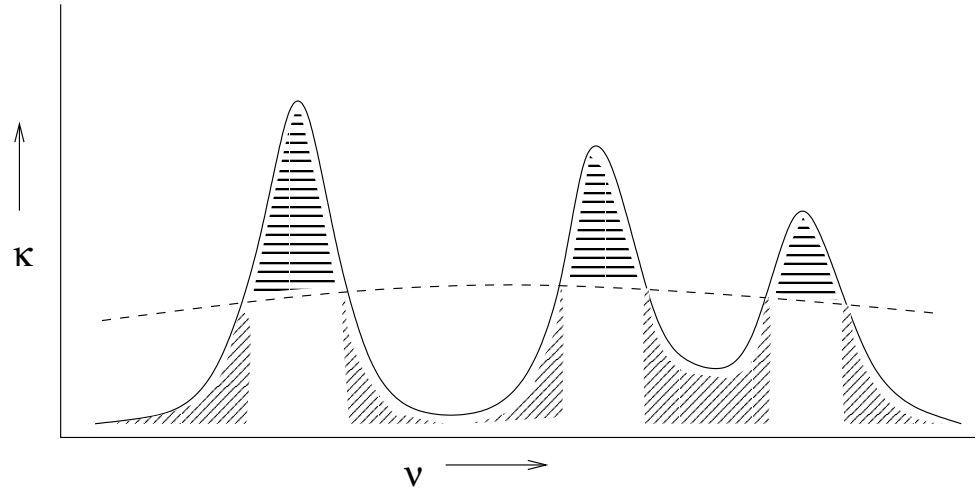

Figure 5.12: *Refined version of the sketch in figure 5.4. The wings (diagonally shaded) of the QM peaks are under the SC continuum (dashed line) and the central values (horizontally shaded) are above the continuum.*

As it is already known that the spectrum, averaged over a large enough wavelength range, is smooth, the shape of the spectrum can be determined by calculating the radiative transfer of a number of isolated "islands" of frequency or wavelength points and connecting the averaged result for these islands together to form the full spectrum.

Figure 5.13 shows how the result of a calculation with 40 islands of 250 points (each island spanning 0.25 nm). It is clear that the overall shape of the spectrum is preserved well in this approximate calculation. The total emitted radiation power is within 5% of the value from the full QM calculation. By using only 40 islands of 250 wavelength points each, instead of using 1000 points per nm over a range of 500 nm, the amount of work is reduced by a factor of 50.

5.4.4 Comparison with experimental results

Spectra of 36 mm diameter lamps with 30 mg sulfur powder and 100 mbar argon (at 293 K) have been measured for various microwave input powers. In order to calibrate the spectra, the inside of the hemi-spherical microwave cavity was coated with a paint that reflects light between 300 and 1000 nm. The radiation was guided via a glass fibre, attached off-centre to avoid direct light from the lamp, to a monolithic Zeiss spectrometer (wavelength resolution ~ 3 nm) which is sensitive in the region between 250 nm and 1000 nm. The system of integrating cavity and detection apparatus was calibrated using a 400 W halogen lamp with a well known spectral intensity distribution. For the sulfur lamp, the microwave input power was varied between 400 and 1000 W.

In figure 5.14 the measured spectra are shown and table 5.1 lists the microwave input power, radiated power and the lamp's estimated – due to not precisely known power losses in the cavity – efficiency. Two differences with the calculated spectra are immediately apparent, (i) the maxima of all experimental spectra lie considerably, about 50 nm, to the red side of both the semiclassical and the quantum-mechanical ones, and (ii) the experimental spectra show more emission in the red part, roughly above 600 nm, of the spectra.

In order to find explanations for these differences, it is useful to examine results of calcula-

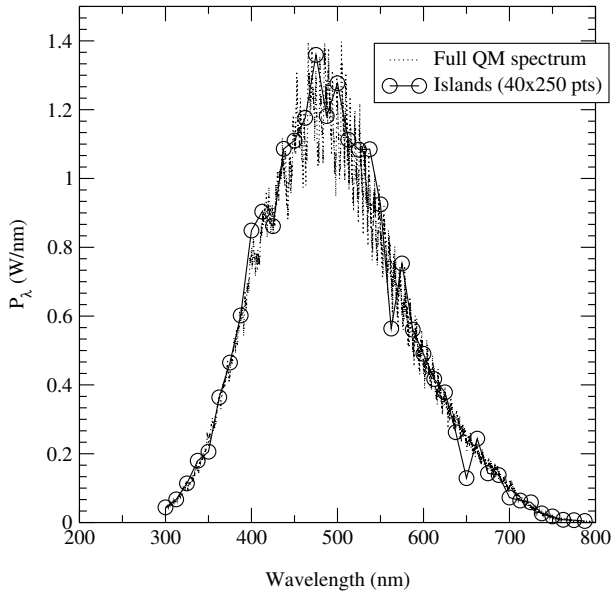

Figure 5.13: *The optimised QM method, for 40 islands of 250 points (at 1 pm intervals, so one island spans 0.25 nm) each, compared with the full QM spectrum using 500,000 points. Temperature and pressure settings are the same as in figure 5.9. The circles represent the averaged values for each island. The difference in total emitted radiation power (surface below the spectrum curve) is less than 5%.*

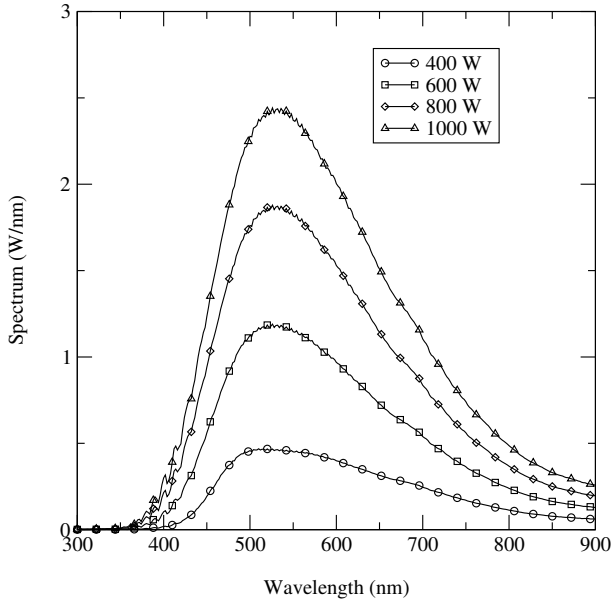

Figure 5.14: *Measured spectra for different input powers. Table 5.1 lists the emitted radiation power and efficiency. The bulb contains 30 mg sulfur powder, resulting in a 5 bar sulfur pressure at the estimated operating conditions.*

tions with varying pressures and central temperatures, which are presented in figures 5.15 and 5.16. The spectra were calculated using the optimised QM method as outlined in section 5.4.3 and plotted with a 5 point running average to make the curves more smooth. Figure 5.15 shows

Table 5.1: *Estimated lamp efficiency for as function of microwave input power. Power losses in the cavity are assumed to be 5%.*

input (W)	est. net input (W)	radiation output (W)	est. efficiency
400	380	132	35%
600	570	317	56%
800	740	502	68%
1000	950	658	69%

that increasing the pressure in the calculation has the effect of moving the maximum of the spectrum to the red. Since the absorption coefficient κ is roughly proportional to p and due to fact that the B-X system is such that κ decreases with increasing wavelength, increasing p will cause an increase in the wavelength where the plasma becomes optically open. Figure 5.16 shows that increasing the temperature generally scales the spectra, without moving the maximum or changing the overall shape significantly. This is caused by the fact that in the B-X system increased temperatures cause more emission, without significantly affecting the absorption coefficient.

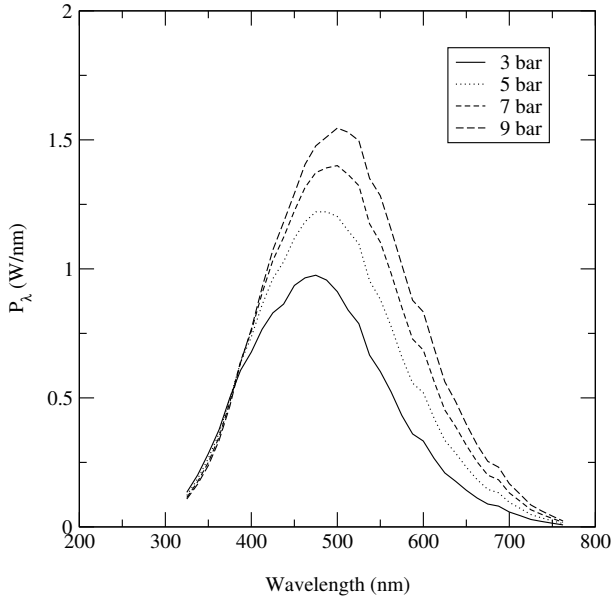

Figure 5.15: *Change of the calculated spectrum, using the optimised quantum-mechanical approach, as a function of sulfur pressure with $T_c = 4000$ K and $a = 3$. The semiclassical spectrum follows a similar trend. Note that the location of the maximum moves towards higher wavelengths with increasing pressure.*

Knowing this, the observed experimental trend of increasing total output power with increasing input power is readily explained by a rise in the central temperature. This trend does not go on indefinitely as at higher powers (over 2 kW) the temperature becomes so high that S_2 is significantly dissociated and the plasma mostly consists of atoms, ions and electrons. In the input power range of interest, however, the central plasma temperature is the main parameter that is influenced by the input power. Ideally, a calculation can be used to determine the actual

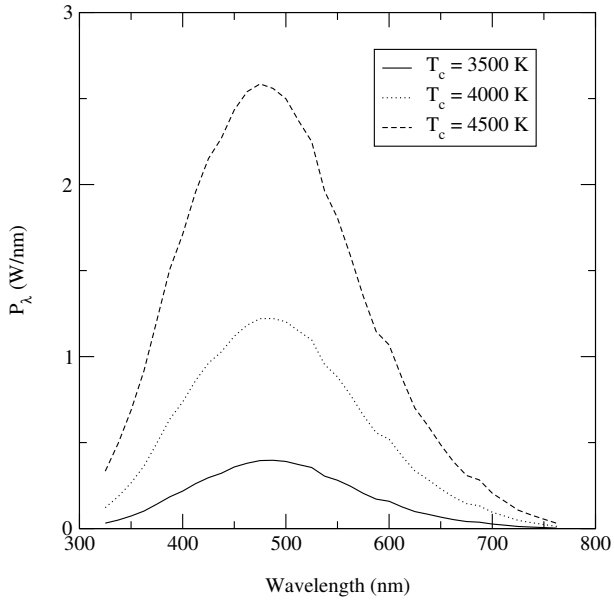

Figure 5.16: *Change of the calculated spectrum, using the optimised quantum-mechanical approach, as a function of central temperature T_c with $a = 3$ and a sulfur pressure of 5 bar. The central temperature acts as a scaling variable for the entire spectral output power.*

central temperature for each input power by fitting the calculated spectrum to the measured one.

Unfortunately, the situation is not ideal due to the two differences between calculated and measured spectra noted above. The discrepancy in the locations of the maxima could in principle be caused by an incorrect sulfur pressure in the calculations. In order to fit the calculated maximum to the observed one, the pressure has to be increased by a factor of about 2. This increase is well beyond the experimental uncertainty of the amount of sulfur powder that was put in the bulb.

A more likely explanation is a departure from LTE of the B and X vibrational levels. Certainly the electron density (typically 10^{20} m^{-3}) is low enough to cause concern about the LTE vibrational distribution of sulfur molecules that have a typical density of 10^{25} m^{-3}. One possible scenario is that S_2 B states are not created by electron excitation from the X ground state, with an energy gap of over 4 eV, but rather by association of one ground state and one excited, with 1 eV, S atom. Via heavy-heavy collisions the vibrational levels of the B state would then be populated, starting at high levels going down. As the de-excitation cascades downwards through the vibrational levels with each collision, radiation provides an escape channel so that the lowest vibrational level may not be reached. This scenario is all the more likely considering that radiation from the highly excited levels is not readily re-absorbed in the plasma. A relative enhancement with respect to LTE of the population of the higher vibrational levels could explain both the shifted maximum and the observed higher than calculated emission in the red part of the spectrum.

5.5 Conclusion

From the comparison of the semiclassical and the quantum-mechanical spectra it is obvious that the quantum-mechanical structure of the emission and absorption coefficients cannot be automatically ignored, even if only global spectral aspects are of interest. In two of the three defined regions there are notable differences between both spectra, and only in the trivial region where the radiation is optically thin is agreement guaranteed, provided a complete set of Franck-Condon coefficients is available.

It is further important to note that the sign of the difference between the two spectra generally follows the difference between the QM and SC mean free optical paths $\rho_{\tau=1}$, which changes between regions I and II. In the first region, the semiclassical method yields less emitted radiation, since the plasma is optically thick at all wavelengths, whereas a calculation based on quantum-mechanical data still shows some wavelengths, in between peak positions, where light escapes. In the second region, the semiclassical calculation yields more light than the quantum-mechanical one because the average opacity is such that light may escape but the quantum-mechanical peak values are still optically thick.

As is required, it has been shown that the differences between the SC and QM calculations disappear with increasing quantum-mechanical line widths. At 20 pm widths the differences are already small.

The method for approximating the effects of peaked absorption and emission coefficients by correcting continuous values discussed in section 5.3.2 and illustrated in figure 5.4 can only correct for the effects observed in region II, not those in region I where the wings of the line profiles are of importance.

As was noted in the introduction, radiative transfer can be rapidly done on smooth semiclassical data, but is rather involved in the case of precise quantum-mechanical absorption and emission coefficients. The optimised method for calculating quantum-mechanical radiative transfer that was outlined in section 5.4.3 can reduce the calculation time significantly. Using this technique, the microscopic (sub-nanometre) QM details are mostly ignored, as in the SC method, but the macroscopic effects (less radiation in region I and more in region II than according to the classical calculation) are preserved.

The comparison with experimental spectra shows that at low wavelengths the semiclassical calculation yields the best results, starting at roughly the same wavelength as the observed spectra, while the QM spectrum contains too much blue light.

Aside from a neglected broadening mechanism for the individual ro-vibrational transitions, the difference between the calculated and measured spectra may be caused by a departure from LTE, as was discussed in the previous section. Thirdly, the shape of the temperature profile that was used in the calculation is based on experience with high pressure LTE plasma's rather than on direct measurements on the sulfur lamp. If the temperature profile is in fact completely different, it makes any comparison between the current calculations and the measured spectra invalid. An indication that the assumed profile may be essentially correct is the fact that calculations show that the observed trend of increasing spectral output without changing the spectrum's shape as the input power increases can be attributed to an increasing central temperature.

The general observed difference between calculated and measured spectra is similar to the differences found by Körber (1998), which indicates that the quasi-continuous rotational distribution approximation used in that work was not the main cause of the deviation. Johnston *et al.* (2002) likewise calculated a self-consistent temperature profile based on SC radiative

transfer that yields a spectrum that is shifted to the blue in comparison with experiments. The self-consistent temperature profile found by Johnston is similar to the fixed one used in this work.

The temperature profile is the most important quantity when trying to explain the observed spectra. Therefore, working on the assumption of LTE, a following study will attempt to calculate a self-consistent temperature profile by solving the temperature equation while taking into account the effects of QM radiative transfer, microwave power input, and thermal conduction. A comparison with the QM spectrum that results from such a self-consistent temperature profile will be compared with the semiclassical spectrum calculated earlier by Johnston *et al.* (2002).

Chapter 6

General treatment of the interplay between fluid and radiative transport phenomena in symmetric plasmas: the sulfur lamp as a case study

Published as: *Harm van der Heijden and Joost van der Mullen*
J. Phys. D: Appl. Phys. **35** 2112-2125 (2002)

Abstract

A general ray-trace method for calculating the effects of radiative transfer in a control volume fluid code is presented. The method makes use of the structured control volume grid of the fluid code, and is suited for geometries with a point or axis of symmetry. In particular, the specific equations for spherical and cylindrical (without z dependence) configurations are developed. The application of this method to local thermal equilibrium (LTE) and non-LTE plasma models is discussed. Various opportunities for sacrificing precision for calculation speed are pointed out.
As a case study, the effects of radiative transfer in a sulfur lamp are calculated. Since an LTE description of the molecular radiation yields a computed spectrum that differs significantly from a measured one, the possibility of a non-LTE vibrational distribution of the radiating S_2-B state is investigated. The results indicate that the vibrational populations may be inversed.

6.1 Introduction

For many types of plasma applications, the transport of radiation is an important aspect that greatly influences the overall plasma characteristics. Especially in light sources, an appropriate description of radiative processes is vital in order to be able to model the plasma as a whole and in particular the relation between plasma properties and light characteristics. In many

interesting light sources, the light generated by the plasma extends over a range of frequencies with different characteristics. At some frequencies the plasma is optically thin, so that the radiation does not interact with other parts of the plasma, whereas at other frequencies the plasma may be optically thick, causing the generated photons to be absorbed near the point of origin. Between these two extremes is "medium-thick" radiation at intermediate frequencies, which influences all parts of the plasma, not just the region near its origin. This medium-thick radiation is often a determining factor in the efficiency and spectrum characteristics of the light source, and, due to its non-local nature, typically much more difficult to model than thick or thin radiation.

Various approximations can be used to account for the effects of radiative transfer. In plasmas that are not in local thermal equilibrium (LTE), radiation effectively transports particles by removing an excited particle at the location of the photon's origin and adding one at the location of absorption. At the same time, a de-excited particle is effectively transported in the other direction. One way of describing this process is by setting a fixed escape factor Λ, so that the excited particle density n^* balance contains a term $(dn^*/dt)_{rad} = -\Lambda n^* A$.

The escape factor, with a value usually in the range $0-1$, is introduced to reduce absorption processes to a local property. Together with terms for processes like convection, diffusion and chemical reactions, which depend of local values such as electron density n_e and temperature, T_e, the balance equation for n^* can be solved. While this is essentially correct, the problem is that the value of Λ is strongly non-locally determined, since it is designed to account for absorption of radiation that may originate anywhere in the plasma. Using a fixed value in the calculation means that the process of absorption is decoupled from the plasma quantities that are calculated and the model is no longer self-consistent.

In LTE the problem is similar. In this case, since all particle densities are a function of temperature, radiation acts as a source term in the temperature balance. The (nearly) optically thin radiation can be accounted for using an escape factor, $(dU/dt)_{rad,thin} = h\nu n^* \Lambda A$, while the optically thick radiation, which has a short range influence, is described using an extra term to the coefficient for heat conductivity λ_c. This approach requires that the range of radiation frequencies is divided into an optically thick and thin part, with the disadvantage that the interesting medium range is described poorly. Another drawback is the fact that whether a frequency is thick or thin is usually dependent on the location.

It is clear that for a self-consistent description of a plasma with radiative transfer, the fluid description (particle and temperature balances) must be coupled to the radiation model. On the one hand the fluid properties will determine absorption and emission coefficients which are needed for the build-up of the radiation field, on the other hand this radiation field will change local fluid properties by means of absorption processes. Due to the non-locality of radiative transfer, this involves describing radiative relations between all points of the plasma. In numerical terms, while a diffusion/convection equation on a grid with N points gives rise to a $Ax = b$ matrix equation with A an $N \times N$ sparse matrix, radiative transfer requires a $N \times N$ dense matrix for each relevant frequency. Since the critical medium-thick radiation is at different frequencies depending on the location inside the plasma, the emission and absorption frequency profiles need to be sampled liberally (much more densely than would be needed for, say, a quadrature integration). As even relatively simple frequency profiles thus require a frequency discretisation of some 50 points, this causes a sharp increase in the computational power required. This increase is compounded by the need for an iterative procedure; the radiation calculation requires

particle densities and temperature values, while the results of this calculation are source terms in the particle and temperature balance equations.

This study aims to give a general treatment of the relation between fluid and radiation aspects of symmetric plasmas. The method deals with radiation in the whole opacity range from optical open to closed radiation and is applicable to both LTE and non-LTE plasmas. The fluid aspects will be handled by a control volume (CV) method on a structured grid, whereas the generation and transport of radiation will be dealt with by a ray-trace method. This ray-trace control volume (RTCV) method makes optimal use of available symmetry to reduce the complexity of the radiative transfer problem. The essence of the ray-trace method is to discretise all available directions of radiation by using probe lines which represent a fraction of the total solid angle. The average radiation intensity combined with the local absorption coefficient determines the number of absorption processes. The RTCV radiative transfer method has been added to the modular plasma modelling toolkit PLASIMO (van der Mullen *et al.*, 2002; Janssen *et al.*, 1999).

As a case study we will present a self-consistent model of a spherical high pressure LTE sulfur lamp. In a future publication we will present the generation and transport of the 254 nm radiation in a cylindrical low pressure non-LTE mercury discharge. The details of the RTCV method differ depending on the plasma configuration. However, since the basics are the same for both cases, this paper treats both the spherical configuration (as in the present test case) and the cylindrical one that is used in a following paper.

In section 6.2 the overall numerical model is described in some detail, with an emphasis on the fluid description and the use of nodal points and control volumes. Section 6.3 contains the basics of the ray-trace method, which is applied to spherical and cylindrical configurations in section 6.4. The discussed spherical configuration is point-symmetric, that is, all local quantities are a function of radius r only. Likewise, the cylindrical configuration is considered to be infinitely long and uniform along the z axis, so that again all local quantities are a function of r alone. The equations developed in section 6.3 can be applied to more complicated geometries, but that is beyond the scope of this paper.

In the second part of this work, beginning at section 6.5, a case study is presented for the sulfur lamp. A self-consistent model for this spherical lamp has been described before by Johnston *et al.* (2002), where the details of the radiative transfer description were deferred to this paper and the theory behind the local S_2 molecular radiation generation characteristics is described by van der Heijden and van der Mullen (2001). The S_2 molecular radiation theory in van der Heijden and van der Mullen (2001) is a semiclassical (SC) description that is far less computationally intensive than a full quantum-mechanical (QM) ro-vibrational model, and was for this reason used by Johnston *et al.* (2002). Since then, a comparison between transport of SC and QM radiation has been made, using a non self-consistent sulfur model with a fixed temperature profile, showing differences between the emitted spectra (van der Heijden *et al.*, 2002). An approximate method, the so-called 'frequency islands method' was also developed to make a self-consistent (iterative) QM calculation possible. This method is applied here to study the differences with the earlier self-consistent calculation by Johnston.

6.2 Numerical model

The PLASIMO code combines several numerical techniques to provide a complete plasma model. One of the techniques is the fluid approach to describe processes like diffusion and convection.

The fluid code makes use of a control volume method and solves a general form of the diffusion and convection equation, the so called ϕ-equation, or canonical transport equation:

$$\nabla \cdot (f_\phi \rho \vec{c}_\phi \phi) - \nabla \cdot (\lambda_\phi \nabla \phi) = S_\phi, \tag{6.1}$$

where the f_ϕ factor (Janssen *et al.*, 1999) is an addition to the general form given by Patankar (1980). The first and second term of the left hand side describe convection and diffusion respectively. The right hand side contains the ϕ sources.

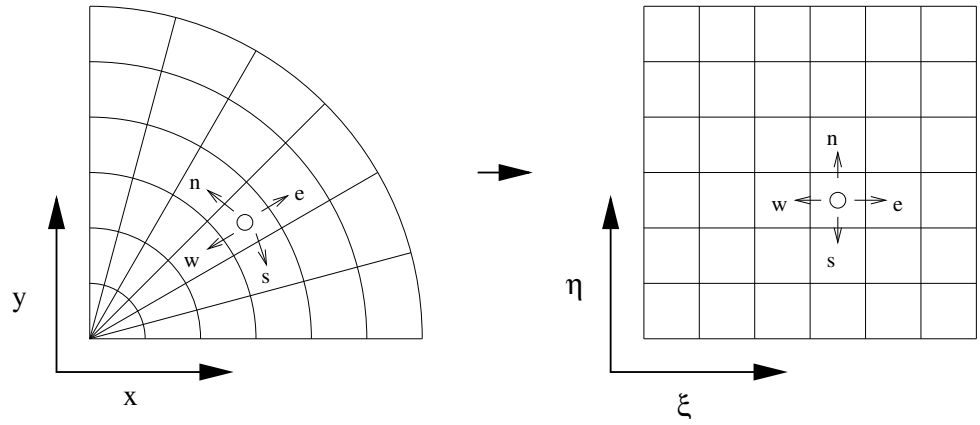

Figure 6.1: *The* PLASIMO *grid abstraction for a spherical grid. On the left hand side the real grid, where the x axis is an axis of symmetry. On the right hand side the internal square computational grid with abstract coordinates ξ and η. In the spherical context, ξ and η represent radius r and azimuth angle ϕ respectively.*

PLASIMO works with 2D grids with spherical, cylindrical or general axially symmetric geometries. Figure 6.1 shows how a real problem space (coordinates x and y) for a spherical grid is internally represented in a square grid with coordinates (ξ, η), which correspond to radius and azimuth angle (r, ϕ). For a cylindrical grid, ξ and η represent axial coordinate z and radius r, respectively.

The control volume method is used to discretise the ϕ-equation (6.1). Each CV contains a nodal point (NP) for which the local value of ϕ is calculated. The discretised equation is obtained by integrating the ϕ-equation over a control volume and solved using a stabilised biconjugate gradient matrix solver (Barrett *et al.*, 1994).

The fluid approach works well for medium or high pressure plasmas where the mean free path λ_{free} of particles is much smaller than the dimensions of the control volumes, so that one volume is influenced only by its direct neighbours. The upper limit of the dimensions of the fluid CVs is mainly determined by the gradients of quantities like temperatures and densities.

The radiative equivalent of the mean free path is the mean free photon path $\lambda_\gamma(\nu) = 1/\kappa(\nu)$, where $\kappa(\nu)$ is the radiative absorption coefficient. The absorption coefficient depends strongly on frequency ν and $\lambda_\gamma(\nu)$ can range from much smaller than a typical CV dimension ℓ, so that a fluid approach is valid, to much larger than plasma dimension L, so that emitted radiation escapes and does not interact with other parts of the plasma. The first case can be incorporated in a fluid code as a contribution to thermal conductivity (LTE) or particle diffusion (non-LTE) — an expression for this diffusive limit of radiative transfer will be derived as a validation of

the presented general method — and the second case can be accounted for as an energy (LTE) or particle density (non-LTE) source term.

The range of free photon paths $\ell < \lambda_\gamma < L$, between the respectively optically thick and thin limits, makes the fluid approach unsuitable for radiative transfer calculations. In choosing or developing an alternative method, it is important to keep in mind that fluid control volumes and the radiation quantities are linked. The fluid method yields values for temperatures and densities in the nodal points, which are used to calculate radiative absorption and emission coefficients. The radiative code in turn calculates how the absorption and emission transport energy (LTE) or particle densities (non-LTE) through the plasma and supplies the data as source terms for the fluid equations. Therefore, while the radiative transfer description cannot make use of the fluid technique of only treating the effects of a control volume's direct neighbours, it is desirable to make use of the control volume structure where possible, both from a standpoint of keeping things simple and to minimise the need to interpolate data between radiative and fluid grids.

6.3 Ray-tracing

The radiation transport calculation method treated in this paper is based on the use of a discrete number of probe lines to sample the radiation coming from different directions. This is done by solving the equation for radiative transfer along these probe lines. This equation describes the change in radiation intensity I_ν [$\mathrm{Wm^{-2}Hz^{-1}sr^{-1}}$] (note that we follow the convention of the field of astrophysics by calling this quantity intensity rather than radiance) along a path s [m], and is deceptively simple,

$$\frac{dI_\nu}{ds} = j_\nu - \kappa I_\nu, \tag{6.2}$$

where j_ν [$\mathrm{Wm^{-3}Hz^{-1}sr^{-1}}$] is the local emission coefficient and κ [$\mathrm{m^{-1}}$] the local coefficient for absorption. Like all related quantities in this paper, spectral quantities that are defined per frequency interval, such as j_ν and I_ν have a subscript ν. Except where it is needed for clarity, the dependence of light related quantities on ν is implied (e.g. κ rather than $\kappa(\nu)$).

The complex character of equation (6.2) is mostly hidden in the intensity $I_\nu(\nu, \vec{r}, \vec{\Omega})$. This quantity represents the energy per unit of time, surface, solid angle, and frequency interval propagating through a surface at position $\vec{r}$ with a normal pointing in the direction $\vec{\Omega}$. With $I_\nu(\nu, \vec{r}, \vec{\Omega})$ one can compute the radiative flux Φ^ϵ_ν [$\mathrm{WHz^{-1}}$] through a surface A corresponding to the radiation in the direction $\vec{\Omega}$ with margin $d\Omega$ (see figure 6.2),

$$\Phi^\epsilon_\nu = I_\nu(\vec{\Omega} \cdot \vec{A})d\Omega = I_\nu(\vec{A} \cdot d\vec{\Omega}), \tag{6.3}$$

where $\vec{\Omega}$ is normalised, $\vec{A}$ is surface A times its normal vector, $(\vec{\Omega} \cdot \vec{A})$ is an inner product, and $d\vec{\Omega}$ is the vector with direction $\vec{\Omega}$ and magnitude $d\Omega$.

A useful quantity in radiative transfer is the mean intensity J_ν, which is a direction-less average of intensity:

$$J_\nu = \frac{1}{4\pi} \int_{4\pi} I_\nu d\Omega. \tag{6.4}$$

The goal of the transport calculation is to calculate J_ν for all points $\vec{r}$ in the plasma, which means calculating $I_\nu(\vec{r})$ for all directions $\vec{\Omega}$. The first approximation that the numerical scheme

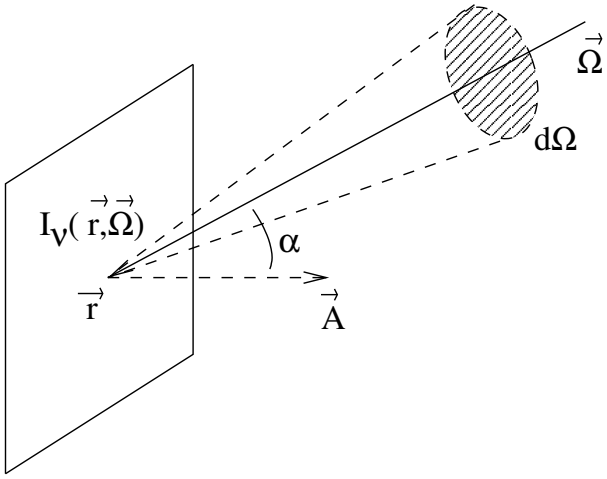

Figure 6.2: *A probe line propagating in the direction $\vec{\Omega}$ and representing the radiation within solid angle $d\Omega$. The spectral power flux Φ_ν^ϵ through surface A equals $I_\nu(\vec{A}\cdot\vec{\Omega})d\Omega$.*

uses is to employ a limited number of probe lines, indexed by i, to sample the continuum of directions $\vec{\Omega}$, e.g.

$$J_\nu = \frac{1}{4\pi}\int_{4\pi} I_\nu d\Omega \approx \frac{1}{4\pi}\sum_i I_{\nu,i}\Delta\Omega_i. \tag{6.5}$$

Section 6.3.1 outlines how the quantities I_ν and J_ν are related to quantities that are of interest to LTE or non-LTE fluid codes. In section 6.3.2 the integration of (6.2) along a probe line is discussed and section 6.3.3 discusses the limiting cases of optically thin and thick radiation. Finally in section 6.4 the theory is first applied to geometries with a circular cross section after which the equations for a spherical and infinitely long cylindrical geometry are derived.

6.3.1 Interaction of probe lines with control volumes

The way in which the radiative intensity along probe lines interacts with control volumes, and thus connects volumes that are not necessarily neighbours, depends to some degree on the plasma conditions. Here both the cases of LTE and non-LTE will be discussed.

In LTE, we consider radiative transfer as transport of energy. The quantity of importance then is the change of plasma energy density U due to radiation,

$$\left(\frac{dU}{dt}\right)_{rad} = Q_{rad} = \int_\nu \left(-4\pi j_\nu + \kappa\int_{4\pi} I_\nu d\Omega\right) d\nu. \tag{6.6}$$

For reasons of clarity the following equations will be written in spectral form. To convert a spectral quantity Y_ν to a non-spectral quantity Y an integration over ν is needed. The spectral form of Q_{rad} is thus,

$$Q_{rad,\nu} = -4\pi j_\nu + \kappa\int_{4\pi} I_\nu d\Omega = 4\pi(\kappa J_\nu - j_\nu). \tag{6.7}$$

For non-LTE, the required quantity is the change in particle densities. Let n' and n'' be the densities of respectively the upper and lower states, then the transport of radiation leads to the

following temporal change in particle densities,

$$\left(\frac{dn'}{dt}\right)_{rad,\nu} = -\left(\frac{dn''}{dt}\right)_{rad,\nu} = \frac{4\pi}{h\nu}(\kappa J_\nu - j_\nu) = \frac{Q_{rad,\nu}}{h\nu}. \tag{6.8}$$

Here use was made of the connection between power density $Q_{rad,\nu} = (dU/dt)_{rad,\nu}$ due to radiative processes and change in particle densities, $Q_{rad,\nu} = h\nu(dn'/dt)_{rad,\nu}$.

The possibility of having multiple transitions that overlap each other spectrally (e.g. for a given ν, j_ν is composed of the sum of $j_{\nu,i}$ of all different transitions i) makes the non-LTE case more complex. For a transition $n_i' \rightarrow n_i''$ we find

$$\left(\frac{dn_i'}{dt}\right)_{rad,\nu} = \frac{4\pi}{h\nu}(\kappa_i J_\nu - j_{\nu,i}). \tag{6.9}$$

From an implementation point of view this means that the individual emission and absorption coefficients, $j_{\nu,i}$ and κ_i have to be stored as well as the summed values. When modelling an LTE plasma, one can save some computer resources by only storing the summed coefficients. The transport calculation itself, which focuses on calculating J_ν or $Q_{rad,\nu}$, uses only those summed values.

Two different techniques for connecting probe lines with control volumes can be employed, by considering CV boundaries and nodal points respectively. The first method calculates Q_{rad} directly from in and out going fluxes at the boundaries, while the second one calculates J_ν at the nodal points. The two approaches are linked via equation (6.7). Here we will only discuss the CV boundary method, which is the one actually used in the calculations of section 6.6, while the alternative, the nodal point method, is outlined in appendix 6.A.

Both methods work according to the same principle; as a probe line travels through the plasma, it takes away energy from control volumes through emission and deposits energy through absorption. The boundary method reflects this principle clearly. For each volume, the difference between the power that is brought into the volume $\Phi_\nu^\epsilon(s)$ by the probe line and the power that is taken out, $\Phi_\nu^\epsilon(s+\Delta s)$ is spread over the CV volume V:

$$\begin{aligned} Q_{rad,\nu} &= \frac{1}{V}\sum_{lines} \Phi_\nu^\epsilon(s) - \Phi_\nu^\epsilon(s+\Delta s) \\ &= \frac{1}{V}\sum_{lines} I_\nu(s) A_{in}\cos\alpha_{in} d\Omega_{in} - I_\nu(s+\Delta s) A_{out}\cos\alpha_{out} d\Omega_{out}. \end{aligned} \tag{6.10}$$

The direction of the probe line is of importance, as the angle α between the probe line and the normal of the surface influences the in or outgoing flux. Note also that in the square box CVs of figure 6.3, $\alpha_{in} = \alpha_{out}$. This is not generally true for curved geometries such as rotation symmetric bodies with a circular cross-section, which we will consider later (section 6.4).

6.3.2 Integration of I_ν along probe lines

The differential equation (6.2) specifies how I_ν changes along a probe line. The solution to this differential equation, with s representing the distance along a line in the direction of $\vec{\Omega}$, is

$$I_\nu(\vec{r},\vec{\Omega}) = \int_0^\infty j_\nu(\vec{r}+s\vec{\Omega}) \exp\left(-\int_0^s \kappa(\vec{r}+s'\vec{\Omega})ds'\right) ds. \tag{6.11}$$

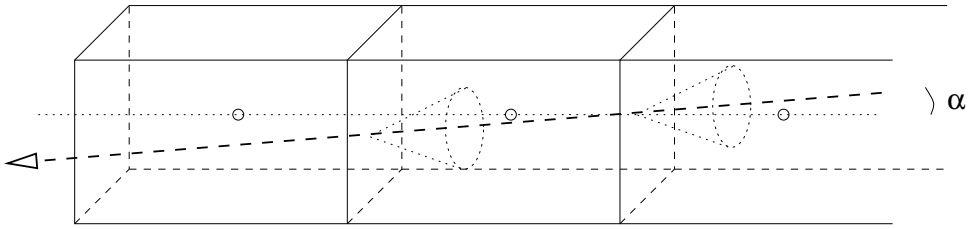

Figure 6.3: *Sketch of the CV boundary method. The boxes are control volumes, the circles are nodal points, the dashed line is a probe line, and the cones represent the solid angle associated with the probe line. The radiative energy source Q_{rad} is calculated by taking the difference of in and outgoing energy fluxes.*

It is common practice to define the optical depth τ,

$$\tau(s) = \int_0^s \kappa(\vec{r} + s'\vec{\Omega})ds'. \tag{6.12}$$

From here on we will drop the notation $j_\nu(\vec{r} + s\vec{\Omega})$ and $\kappa_\nu(\vec{r} + s\vec{\Omega})$ for local coefficients and simply write j_ν and κ.

The plasma is divided in a number of CVs, each with a central nodal point with j_ν and κ values. Therefore it makes sense to split the integral in equation (6.11) into small steps Δs. As will become clear in the following section, it is advantageous to keep κ at a constant value over length Δs and develop j_ν into a Taylor series of order 2:

$$j_\nu = j_\nu|_r + \left.\frac{dj_\nu}{ds}\right|_r \delta s + \frac{1}{2}\left.\frac{d^2 j_\nu}{ds^2}\right|_r (\delta s)^2. \tag{6.13}$$

For convenience, we define $s = 0$ around the point of the Taylor expansion so that $\delta s = s$. Taking a forward step from $s = 0$ to $s = \Delta s$ then involves (cf. equation (6.11)) the integral

$$\begin{aligned}\int_0^{\Delta s} j_\nu(s)\exp(-\kappa(\Delta s - s))ds = \\ \exp(-\tau)\int_0^{\Delta s} j_\nu(s)\exp(\kappa s)ds,\end{aligned} \tag{6.14}$$

where $\tau = \kappa\Delta s$. Using (6.13), equation (6.14) expands to $L_{fwd}(\tau)$,

$$\begin{aligned} L_{fwd}(\tau) &= \exp(-\tau)\int_0^{\Delta s} j_\nu(s)\exp(\kappa s)ds \\ &= \frac{1}{\kappa} j_\nu|_r (1 - \exp(-\tau)) \\ &\quad + \frac{1}{\kappa^2}\left.\frac{dj_\nu}{ds}\right|_r (\tau - 1 + \exp(-\tau)) \\ &\quad + \frac{1}{\kappa^3}\left.\frac{d^2 j_\nu}{ds^2}\right|_r \left(\frac{\tau^2}{2} - \tau + 1 - \exp(-\tau)\right). \end{aligned} \tag{6.15}$$

In this case the Taylor expansion is done at the starting point of the integration $s = 0 \ldots \Delta s$. The alternative is to expand j_ν around the end point of segment Δs. Labelling the end point

with $s = 0$ (so that $\delta s = s$ is still valid), the integral for $s = -\Delta s \ldots 0$ is

$$\int_{-\Delta s}^{0} j_\nu(s) \exp(\kappa s) ds. \tag{6.16}$$

This method of integrating, by looking backwards along the line, will be used in the next section to obtain the diffusive limit, so we expand it as well

$$\begin{aligned} L_{bwd}(\tau) &= \int_{-\Delta s}^{0} j_\nu(s) \exp(\kappa s) ds \\ &= \frac{1}{\kappa} j_\nu|_r \left(1 - \exp(-\tau)\right) \\ &\quad + \frac{1}{\kappa^2} \left.\frac{dj_\nu}{ds}\right|_r \left(-1 + (\tau + 1)\exp(-\tau)\right) \\ &\quad + \frac{1}{\kappa^3} \left.\frac{d^2 j_\nu}{ds^2}\right|_r \left(1 - \left(\frac{\tau^2}{2} + \tau + 1\right)\exp(-\tau)\right). \end{aligned} \tag{6.17}$$

Since each probe line consists of a number of steps Δs_k, we can use (6.15) or (6.17) to rewrite equation (6.11) as a recursive relation. Labelling the consecutive steps with k, we find

$$I_{\nu,k+1} = I_{\nu,k} \exp(-\tau_k) + L(\tau_k), \tag{6.18}$$

with $\tau_k = \kappa_k \Delta s_k$ the optical depth in step k. Using $I_\nu = 0$ at the beginning of the line (just outside the plasma), we can calculate I_ν at the end by applying relation (6.18) for each step.

6.3.3 Optically thin and thick limits

It is of interest to study the two limiting cases of optically thin ($\tau \ll 1$) and thick ($\tau \gg 1$) radiation and determine whether the ray-trace method gives correct results.

The optically thin limit can be found by developing $\exp(-\tau)$ in equation (6.15) as a Taylor series around $\tau = 0$, and replacing τ/κ with Δs. It is then found that

$$I_{\nu,k+1} = I_{\nu,k} + \left(j_\nu + \frac{1}{2}\frac{dj_\nu}{ds}\Delta s_k + \frac{1}{6}\frac{d^2 j_\nu}{ds^2}\Delta s_k^2\right)\Delta s_k = I_{\nu,k} + \overline{j_{\nu,k}}\Delta s_k, \tag{6.19}$$

where $\overline{j_{\nu,k}}$ is the average value of j_ν on segment Δs. This result can be verified by solving the optically thin version of the equation for radiative transfer,

$$\frac{dI_\nu}{ds} = j_\nu, \tag{6.20}$$

i.e. the intensity is filled linearly by the plasma, with average coefficient for emission $\overline{j_\nu}$, and loses nothing due to absorption. The intensity $I_{\nu,k+1}$ is therefore strongly influenced by the history of the probe line (that is, the emission and absorption characteristics on previous points along the line), and thus on the previous value $I_{\nu,k}$.

In the case of optically thick radiation, $I_{\nu,k+1}$ is independent of $I_{\nu,k}$, since $\exp(-\tau_k) \approx 0$. Since I_ν is locally determined, it is necessary to use the backwards integral (cf. equation (6.17)) to evaluate I_ν at an end point. The approximation $\exp(-\tau_k) \approx 0$ gives

$$I_\nu \approx \lim_{\tau\to\infty} L_{bwd}(\tau) = \frac{j_\nu}{\kappa} - \frac{1}{\kappa^2}\frac{dj_\nu}{ds} + \frac{1}{\kappa^3}\frac{d^2 j_\nu}{ds^2}. \tag{6.21}$$

Since the optically thick limit implies that the photon free path $1/\kappa$ is much smaller than control volume dimension ℓ we can develop this case a little further without having to deal with possible curvature of the actual geometry. We consider a (locally) flat surface A, with probe lines coming both from the left and the right, as in figure 6.4.

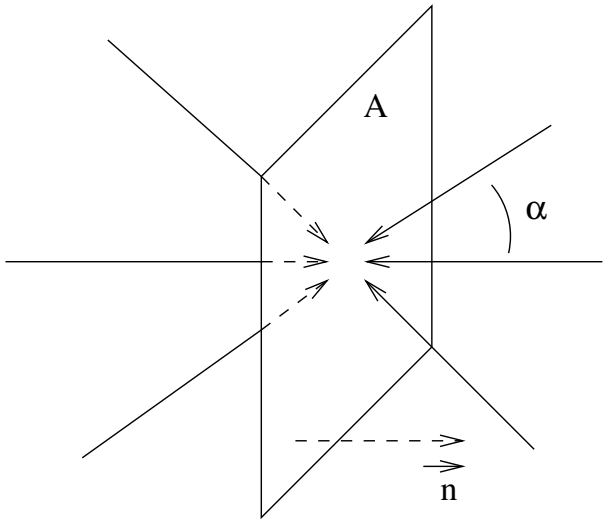

Figure 6.4: *Lines from both sides (angle α) contribute to the net flux through surface A.*

For each line coming from the left of the surface there is a matching line coming from the right. The intensity according to equation (6.21) is the same for both lines, except for a sign change in dj_ν/ds.

The net contribution to the flux for each pair of lines will therefore only contain the first derivative of j_ν, since both the zeroth and second order terms cancel. For dj_ν/ds we write

$$\frac{dj_\nu}{ds} = \nabla j_\nu \cdot \vec{\Omega}, \tag{6.22}$$

where $\vec{\Omega}$ is the unit vector in the direction of the probe line. Using equation (6.3), the contribution of one left-right pair of probe lines to the flux is then

$$d\Phi_\nu^\epsilon = \frac{2}{\kappa^2}(-\nabla j_\nu \cdot \vec{\Omega})(\vec{A} \cdot d\vec{\Omega}), \tag{6.23}$$

where the flux is measured as positive if it is going in the direction of the surface normal vector $\vec{n}$. Let α be the angle between $\vec{n}$ and the direction of the probe line $\vec{\Omega}$, so that $(\vec{A} \cdot d\vec{\Omega}) \propto \cos\alpha$. The part of the total solid angle $d\Omega$ associated with $d\alpha$ is $2\pi \sin\alpha d\alpha$, which is a ring with radius $\sin\alpha$ around $\vec{n}$. Adding the contributions of $(-\nabla j_\nu \cdot \vec{\Omega})$ on this ring has the effect that all components of $\vec{\Omega}$ cancel except the one in the direction of $\vec{n}$, so that $\vec{\Omega}$ can be replaced with $\vec{n}\cos\alpha$. For one angle α, the contribution to the flux is then given by

$$d\Phi_\nu^\epsilon(\alpha) = \frac{4\pi}{\kappa^2}(-\nabla j_\nu \cdot \vec{n})A\cos^2\alpha \sin\alpha d\alpha. \tag{6.24}$$

Integrating α from 0 to $\pi/2$ then gives the total flux in the diffusive limit, in the direction of $\vec{n}$,

$$\Phi_\nu^\epsilon = \frac{4\pi}{3\kappa^2}(-\nabla j_\nu \cdot \vec{n})A, \tag{6.25}$$

and the energy flux density $\vec{\Gamma}^{\epsilon}_{\nu}$ is

$$\vec{\Gamma}^{\epsilon}_{\nu} = -\frac{4\pi}{3\kappa^2}\nabla j_\nu = -\frac{4\pi}{3\kappa}\nabla S_\nu. \tag{6.26}$$

The last equality, with source function $S_\nu = j_\nu/\kappa$ is justified since κ is treated as a constant. The above equation indeed represents the fluid like flux density as generated by diffusion.

6.3.4 Discretisation

The details of the discretisation are of importance in order to obtain the correct limits. Figure 6.5 shows the discretisation for the boundary method. All relevant quantities j_ν, dj_ν/ds and κ (the term containing $d^2 j_\nu/ds^2$ can be omitted since it is not necessary to describe the diffusive limit) are defined at the boundaries. For example, at boundary R_i in figure 6.5, $\kappa = (\kappa_{i-1} + \kappa_i)/2$, $j_\nu = (j_{\nu,i-1} + j_{\nu,i})/2$, $dj_\nu/ds = (j_{\nu,i} - j_{\nu,i-1})/\Delta s$. To go from one boundary to the other requires two steps, since all values change at the nodal point. In the first step, going from a boundary towards the nodal point, L_{fwd} is used, while in the second step, from the nodal point towards a boundary, L_{bwd} is used.

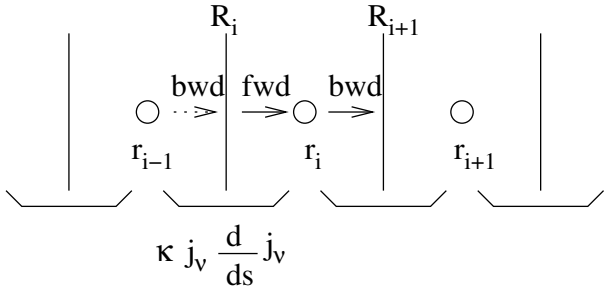

Figure 6.5: *Discretisation for the boundary method. All relevant quantities are defined at the boundaries. To go from one boundary to the next, two steps are needed. Note that in the boundary method it is possible to ignore $d^2 j_\nu/ds^2$ and still obtain the correct diffusion limit.*

If the optical thick limit, where dj_ν/ds plays a role, is not of interest, the calculation can be made faster by ignoring this term. The expressions for L_{fwd} and L_{bwd} are then reduced to $(1 - \exp(-\tau))j_\nu/\kappa$.

6.4 Spherical and cylindrical geometry

In this section the details of ray-tracing will be discussed for spherical and infinitely long cylindrical geometries. Both geometries have circular cross sections (CCS) with at the centre an axis or point of symmetry. We will first discuss the ray-tracing in the circular cross section where all quantities that determine absorption and emission are a function of radius r only.

Consider a point P inside the circular cross section, at a distance r from the centre. In figure 6.6(a) probe lines are drawn coming from six different directions towards point P. Due to the symmetry (all points on the dotted line have the same local values), these probe lines can be freely re-arranged as two sets of parallel lines, as in (b). Finally, (c), by starting one line of each pair from the opposite sphere boundary a single set of parallel lines is obtained. Therefore,

the intensities from all discretised directions in a point-symmetric sphere can be calculated by integrating the intensity I_ν along each line in one set of parallel probe lines.

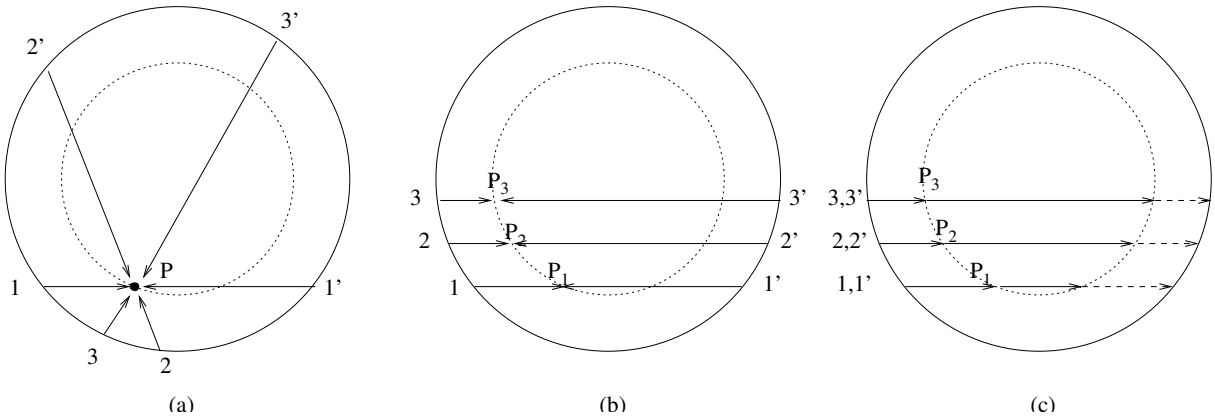

Figure 6.6: *In the symmetric circular cross section, probe lines may be re-arranged into a set of parallel lines.*

The cross section with radius R_{wall} is divided into n shells around nodal point radii r_i ($0 \leq i < n$) between boundaries R_i and R_{i+1}, with $R_0 = 0$ and $R_{n+1} = R_{wall}$, the outer radius of the sphere (see figure 6.7).

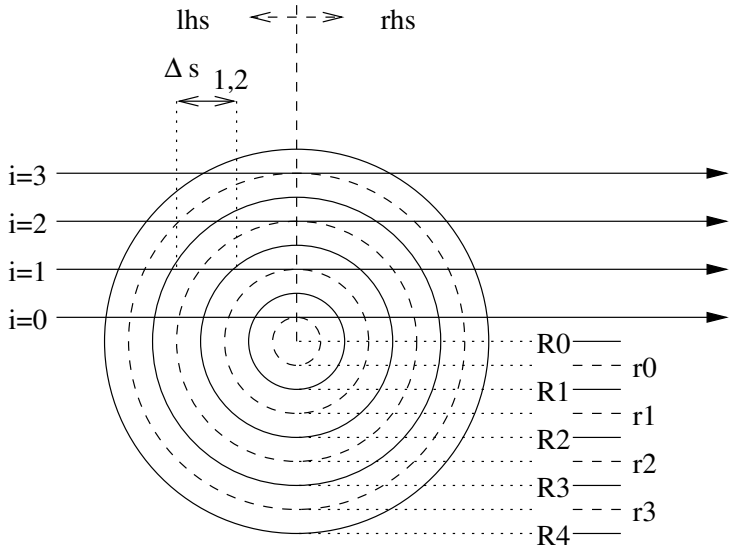

Figure 6.7: *Circular cross-section of the three dimensional spherical or cylindrical configuration. The drawn lines represent CV boundaries, the dashed lines indicate the radii of nodal points.*

All straight paths through the sphere can be characterised by one parameter, the minimal distance y between the line and the centre of the circle. We choose to calculate the intensity along probe lines i that have distances to the centre y_i corresponding to the radial discretisation r_i (see figure 6.7). The number of probe lines is therefore directly linked to the number of nodal r points of the grid. Note that probe line i with $y = r_i$ traverses all shells r_j for $j \geq i$ twice, once on the left hand side and once on the right hand side (the path through the shell around

$r_{j=i}$ is divided in two steps). The length of the path, $\Delta s_{i,j}$ of probe line i through the volume around r_j, is given by

$$\Delta s_{i,j} = \begin{cases} \sqrt{R_{j+1}^2 - r_i^2} - \sqrt{R_j^2 - r_i^2}, & j > i, \\ \sqrt{R_{j+1}^2 - r_i^2}, & j = i. \end{cases} \tag{6.27}$$

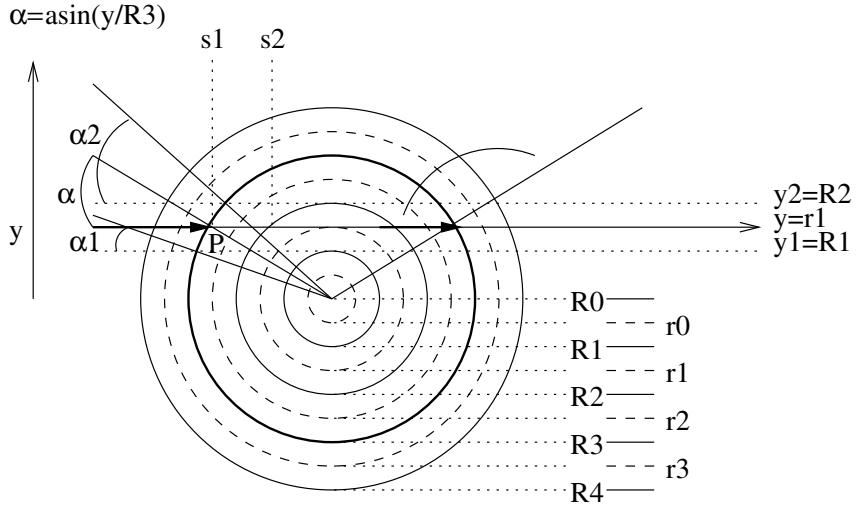

Figure 6.8: *Ray-tracing in the CCS; it is shown how propagating along the probe line the value of Δs and the angle of incidence α changes. At the outer region Δs is small and at the inside it is relatively large. As an example the α value is given which belongs to the intersection at point P between the probe line $y = r_1$ and surface of $r = R_3$. Apart from that it can be seen which range in α is associated with this intersection; a margin which is obtained by a parallel shift of the probe line. This α determines the size of the solid angle associated with the line.*

Equation (6.27) shows how propagating along a trace line belonging to $y_i = r_i$ changes the metric. Note that the angle of incidence changes as well. The relation between angle of incidence α, the radial position, and distance to centre y for a probe line in a circular cross section is illustrated in figure 6.8. The vertical spacing between parallel probe lines determines the range in α angles that a single probe line represents. For example in figure 6.8, the probe line $i = 1$ at height $y = r_1$ represents all lines with values of y between R_1 and R_2. When crossing a surface at radius R_3, the angle with the surface varies between $\alpha_1 = \arcsin(y_1/R_3)$ and $\alpha_2 = \arcsin(y_2/R_3)$. Generally,

$$\sin\alpha = \frac{y}{R}, \tag{6.28}$$

and, taking the derivative of α on both sides,

$$\cos\alpha d\alpha = \frac{dy}{R}, \tag{6.29}$$

which will be used later to simplify the derived expressions. It should be realized that the change in α, obtained by the fictitious parallel displacement of the probe line, determines the (discretisation) of the solid angle. This can be seen by making use of the symmetry in the CCS. The margin obtained by the parallel displacement can equally well be obtained by staying in

point P (fig. 6.8) and rotating the probe line over the range grazing R_2 and R_1. The exact value of the corresponding solid angle depends on the general (spherical or cylindrical) symmetry.

The elegance of the ray-trace method is that instead of looking subsequently for each plasma location what kind of intensities are coming from all the possible directions, we first select lines along which the intensity development is computed. After that we compute which control volumes are visited by these lines and under which directions the CV boundaries are irradiated.

The transition from a circular cross section to a three dimensional spherical or cylindrical configuration involves choosing an appropriate system of coordinates for the representation of the solid angle and, for the boundary method, the in-product of the probe line direction $\vec{\Omega}$ with the surface normal vector $\vec{n}$. For both configurations, the solid angle will be written in (localised) spherical coordinates as

$$d\Omega = \sin\theta d\theta d\phi, \tag{6.30}$$

where θ is the angle between the probe line and the zenith direction $\vec{z}$ which will be chosen, locally or globally, for both configurations. The translation of CCS angle α to θ and ϕ also depends on the configuration.

6.4.1 Spherical geometry

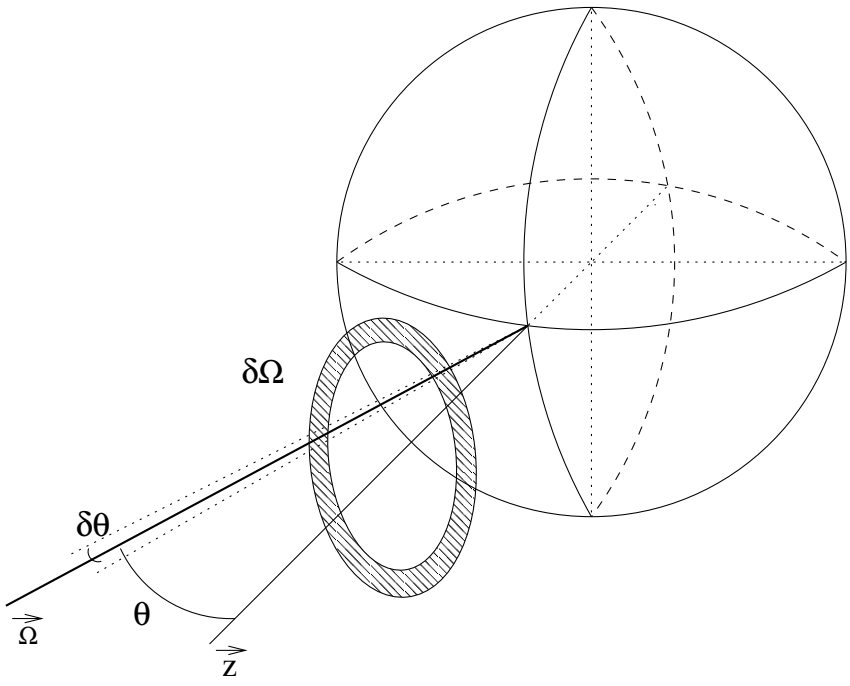

Figure 6.9: *Fraction of solid angle $d\Omega$ for a probe line in a spherical configuration. The angle θ is identical to α in the circular cross section, while $d\phi$ can be replaced by 2π (shaded area).*

In the spherical configuration, we choose the local surface normal as zenith direction $\vec{z}$, as in figure 6.9. The fact that this reference axis coincides with the surface normal means that $\theta = \alpha$ and $(\vec{\Omega} \cdot \vec{n}) = \cos\theta$. Because of the spherical symmetry, there is no ϕ dependence so $d\phi$ can

be replaced with 2π (represented by the ring in figure 6.9). Substituting $d\Omega = 2\pi \cos\theta d\theta$ into equation (6.3), using $A = 4\pi R^2$, we find for the power flux in the boundary method

$$d\Phi^{\epsilon}_{\nu} = 8\pi^2 R^2 I_{\nu} \sin\theta \cos\theta d\theta. \tag{6.31}$$

The $\sin\theta d\theta$ factor in this expression arises from the solid angle $d\Omega$, while the $\cos\theta$ factor is due to the inner product $(\vec{\Omega} \cdot \vec{n})$. The expression needs to be integrated over the range of Ω represented by probe line i. It is an advantage of the boundary method for a spherical configuration that an analytical expression for this integrand can be found by using equations (6.28) and (6.29) with $\alpha = \theta$,

$$d\Phi^{\epsilon}_{\nu} = 8\pi^2 I_{\nu} y dy. \tag{6.32}$$

Integrating from $y = R_i$ to $y = R_{i+1}$ is now trivial,

$$\int_{R_i}^{R_{i+1}} \frac{d\Phi^{\epsilon}_{\nu}}{dy} dy = 4\pi^2 (R^2_{i+1} - R^2_i) I_{\nu}, \tag{6.33}$$

which shows another property of the boundary method; the integral over $A(\vec{\Omega}\cdot\vec{n})d\Omega$ is a constant for two subsequent boundaries, so that $(\Phi^{\epsilon}_{\nu,in}(i) - \Phi^{\epsilon}_{\nu,out}(i))/V$ cf. equation (6.10), can be written as $4\pi^2(R^2_{i+1} - R^2_i)(I_{\nu,in} - I_{\nu,out})/V$. The contribution of probe line i to Q_{rad} in the CV around r_j thus depends on the difference between the ingoing and the outgoing intensity I_{ν}. We define $\Delta I^{lhs}_{\nu,i,j}$ and $\Delta I^{rhs}_{\nu,i,j}$ as the change in intensity I_{ν} over the path segment $\Delta s_{i,j}$, cf. equation (6.27), for the left and right hand side of figure 6.7 respectively.

Combining the contributions from the left and right hand side in one summation, and remembering that the control volume around r_j is only visited by probe lines with $i \leq j$, we find for the boundary method

$$Q_{rad,\nu}(r_j) = \frac{4\pi^2}{V(r_j)} \sum_{i=0}^{j} (R^2_{i+1} - R^2_i)[\Delta I^{lhs}_{\nu,i,j} + \Delta I^{rhs}_{\nu,i,j}], \tag{6.34}$$

with $V(r_j) = \frac{4}{3}\pi(R^3_{j+1} - R^3_j)$.

6.4.2 Cylindrical geometry

For a cylindrical configuration, the cylinder axis is chosen as zenith direction $\vec{z}$, as shown in 6.10. The angle ϕ is now the angle between $\vec{n}$ and the projection of Ω in the circular cross-section. That is, $\phi = \alpha$ as long as only the horizontal cross-section is considered. The "true" angle between Ω and $\vec{n}$ is a function of both θ and ϕ.

Due to the reduced symmetry, compared to the spherical case, it is no longer possible to immediately integrate over ϕ, so that $d\Omega = \sin\theta d\theta d\phi$ cannot be simplified at this point. The in-product between probe line direction $\vec{\Omega}$ and surface normal $\vec{n}$ is now given by $\sin\theta\cos\phi$. Substituting this and $A = 2\pi r \Delta z$, with Δz an arbitrary length of the cylinder, into equation (6.3) we find

$$d\Phi^{\epsilon}_{\nu} = 2\pi r \Delta z I_{\nu} \sin^2\theta \cos\phi d\theta d\phi. \tag{6.35}$$

Now ϕ has the integration range $-\pi \ldots \pi$. With equation (6.29) and $\alpha = \phi$ this integral can be simplified,

$$d\Phi^{\epsilon}_{\nu} = 4\pi \Delta z I_{\nu} \sin^2\theta d\theta dy, \tag{6.36}$$

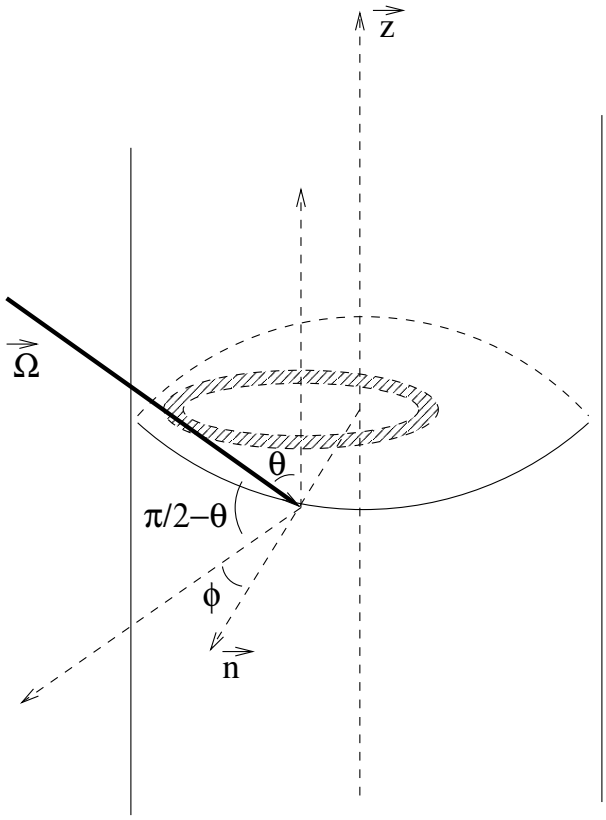

Figure 6.10: *Fraction of solid angle $d\Omega$ for a probe line in cylindrical configuration. The ring denotes an area of the solid angle with constant θ. The angle ϕ is identical to α in the CCS.*

where y has the integration range $0 \dots R_{wall}$ and the expression is multiplied by 2 to account for the fact that the complete range is actually $-R_{wall} \dots R_{wall}$. Integrating y from R_i to R_{i+1}, to calculate the contribution of line i, then gives

$$\int_{R_i}^{R_{i+1}} \frac{d\Phi_\nu^\epsilon}{dy} dy = 4\pi\Delta z(R_{i+1} - R_i) I_\nu \sin^2\theta d\theta. \tag{6.37}$$

It is important to realize that the path through a cylindrical shell from $r = R_j + 1$ to $r = R_j$ now depends on the angle θ. That is,

$$\Delta s_{i,j}^{cyl} = \frac{\Delta s_{i,j}}{\sin\theta}, \tag{6.38}$$

with $s_{i,j}$ the circular cross section expression as given by equation (6.27). As a consequence, $\Delta I_{\nu,i,j}$ is also dependent on angle theta.

Again combining the contributions from the left and right hand side in one summation, we find

$$\frac{dQ_{rad,\nu}(r_j,\theta)}{d\theta} = \frac{4\pi\Delta z \sin^2\theta}{V(r_j)} \sum_{i=0}^{j} (R_{i+1} - R_i)[I_{\nu,i,j}^{lhs}(\theta) + I_{\nu,i,j}^{rhs}(\theta)], \tag{6.39}$$

with $V(r_j) = \pi(R_{j+1}^2 - R_j^2)\Delta z$, so that Δz cancels. To obtain $Q_{rad,\nu}$ a numerical integration over θ is needed,

$$Q_{rad,\nu}(r_j) = \int_0^\pi \frac{dQ_{rad,\nu}(r_j,\theta)}{d\theta} d\theta = 2\int_0^{\pi/2} \frac{dQ_{rad,\nu}(r_j,\theta)}{d\theta} d\theta. \tag{6.40}$$

6.5 Self-consistent calculation for the LTE sulfur lamp

In a future study we will apply the ray-trace control volume interaction method to the well known cylindrical low pressure mercury lamp which is a non-LTE lamp. Here the method is applied to the LTE sulfur lamp which consists of a spherical quartz bulb (inner radius 16 mm) which is filled with typically 20 – 60 mg sulfur powder and 100 – 400 mbar (at 293 K) argon for ignition. It is a microwave driven discharge with input power typically between 300 W and 2 kW. The operational pressures vary, depending on the bulb filling, roughly between 5 and 10 bar. In this test case, we will consider a sulfur lamp with, under operating conditions, a sulfur pressure of 5 bar. This is equivalent to a powder filling of about 30 mg (van der Heijden *et al.*, 2002).

Two characteristics make this plasma attractive as a light source. Firstly, the spectrum overlaps well with the eye-sensitivity curve and contains hardly any UV or infrared radiation. Secondly, the efficiency is rather high, up to 70% of the power coupled into the plasma is emitted as visible light (but note that for practical comparisons with other light sources the efficiency of the microwave power source needs to be taken into account). The reason for this favourable emission characteristic lies in the fact that the main origin of the emitted radiation is molecular in nature: the S_2 $B^3\Sigma_u^- \rightarrow X^3\Sigma_g^-$ transition.

In the present LTE model we consider the local particle densities a known function of the partial pressures p and temperature T. The only transport equation that needs to be solved is the one for the temperature. Ignoring convection, we find with $\phi = T$,

$$-\nabla \cdot (\lambda_c \nabla T) = Q_{Ohm} + Q_{rad}. \tag{6.41}$$

with λ_c the thermal conductivity and Q_{Ohm} and Q_{rad} the power density sources [Wm^{-3}] for electromagnetic power coupling and radiative transfer. Note that under normal conditions, with microwave power coupled into the plasma and part of the generated radiation escaping, $Q_{Ohm} > 0$ and $Q_{rad} < 0$.

In figure 6.11 the LTE densities of the sulfur particles are shown as a function of temperature for a partial sulfur pressure of 5 bar. (van der Heijden *et al.*, 2002; Johnston *et al.*, 2002). Figure 6.12 shows the temperature dependence of the electrical conductivity σ and the thermal conductivity λ_c as a function of temperature for the sulfur-argon mixture (Johnston *et al.*, 2002).

The temperature equation (6.41) is solved iteratively. Alternately, based on the current temperature profile the source terms Q_{Ohm} and Q_{rad} are calculated. After this, a new temperature profile is obtained by solving equation (6.41). This is done until the temperature profile converges with a maximum relative change $< 10^{-8}$, which is typically obtained after 100–200 iterations.

6.5.1 Ohmic source term

The local electromagnetic power density $Q_{Ohm}(r)$ is determined by

$$Q_{Ohm}(r) = \frac{1}{2}\sigma(r)E(r)^2, \tag{6.42}$$

with $\sigma(r)$ the local electrical conductivity and $E(r)$ the magnitude of the AC electric field strength. The electric field strength is related to the field strength E_{wall} at the outer wall of the

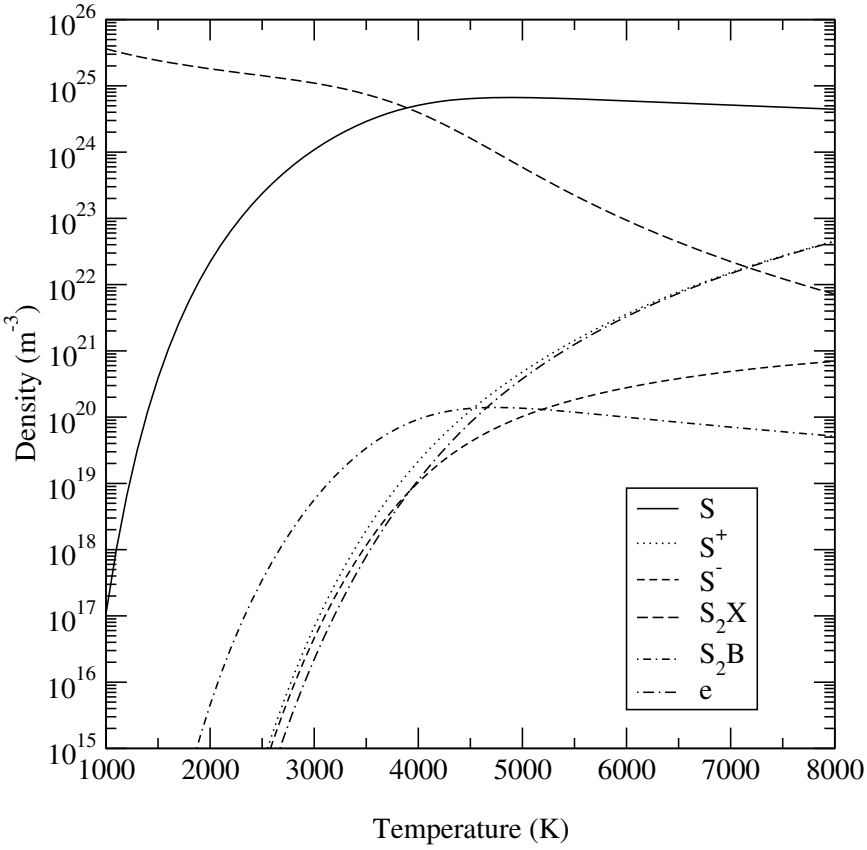

Figure 6.11: *LTE densities of the sulfur particles as a function of temperature for a sulfur pressure of 5 bar. Note that the argon buffer gas is not included in this mixture.*

plasma,

$$E(r)^2 = E_{wall}^2 \exp\left(-2\int_r^R \frac{dx}{\delta(x)}\right), \tag{6.43}$$

where the factor 2 in the exponent is due to the square and $\delta(x)$ is the skin depth,

$$\delta(x) = \sqrt{\frac{2}{\mu_0 \sigma(x)\omega}}, \tag{6.44}$$

where ω is the radial field frequency, $2\pi \cdot 2.45$ GHz. The total input power P_{Ohm} is obtained by integrating equation (6.42) over the entire plasma volume,

$$P_{Ohm} = 2\pi \int_0^R \sigma(r) E(r)^2 r^2 dr. \tag{6.45}$$

By substituting equation (6.43) into (6.45) it can be seen that P_{Ohm} is proportional to E_{wall}^2. The value of E_{wall}^2 is scaled by the model to obtain the specified value for input power P_{Ohm}.

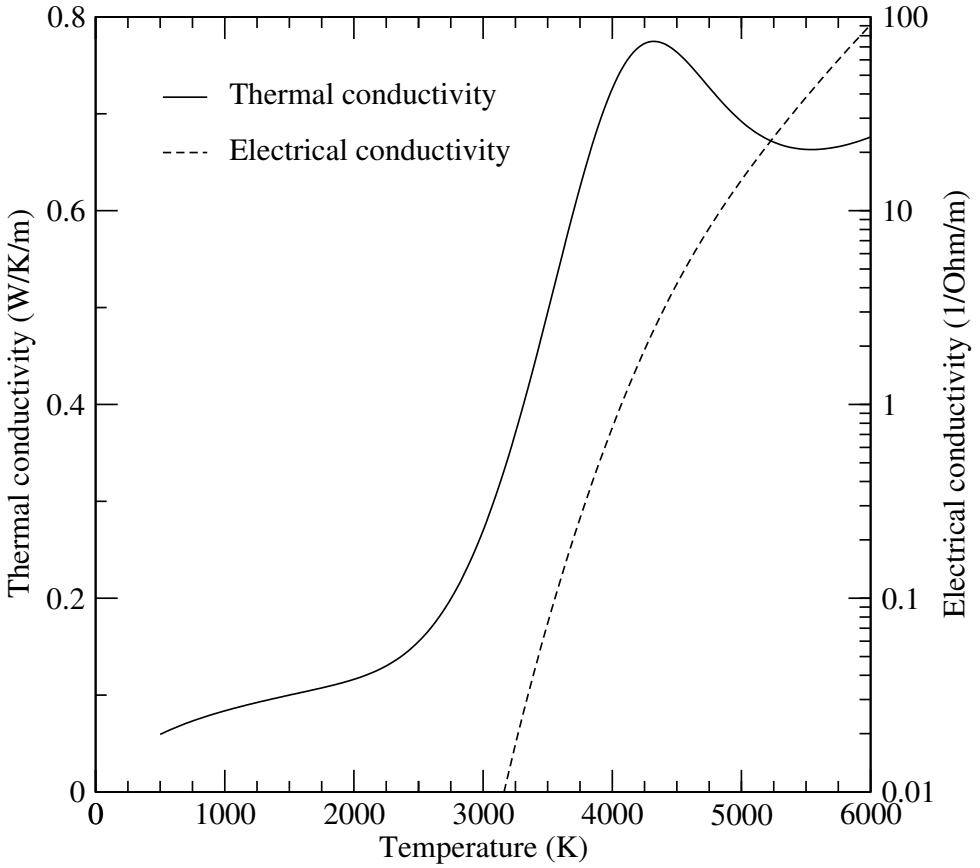

Figure 6.12: *Thermal and electrical conductivity of the sulfur-argon mixture as a function of temperature. The argon pressure is 2 bar, the sulfur pressure is 5 bar.*

6.5.2 Radiation source term

The radiation source term Q_{rad} is calculated using the boundary method as outlined in the previous sections. The local terms j_ν and κ for the S_2 B-X transition are calculated using a semiclassical and quantum-mechanical approach, for which the reader is referred to earlier work (van der Heijden and van der Mullen, 2001; van der Heijden *et al.*, 2002). For completeness, the relevant equations are summarised here.

For both approaches the following definitions are used, using single primes for quantities of the upper state and double primes for the lower state,

$$j_\nu = \frac{h\nu}{4\pi} n' A \phi'_\nu(\nu), \tag{6.46}$$

$$\kappa(\nu) = n''\sigma_{abs} - n'\sigma_{stim} = n''\frac{c^2}{8\pi\nu^2} A \frac{g'}{g''}\phi''_\nu(\nu) - n'\frac{c^2}{8\pi\nu^2} A \phi'_\nu(\nu), \tag{6.47}$$

with A the transition probability, n the state density, g the state's degeneracy and ϕ_ν a normalised line profile.

For the semiclassical case, the upper and lower line profiles are given by

$$\phi'_\nu(\nu(r)) = \frac{\sigma_{sym}}{Z'_{SC}} \Gamma\left(\frac{3}{2}, \frac{D'(r)}{kT}\right) \left(\frac{2\pi\mu kT}{h^2}\right)^{\frac{3}{2}} 4\pi r^2 \exp\left(-\frac{V'(r)}{kT}\right) \left|\frac{d\nu(r)}{dr}\right|^{-1}, \tag{6.48}$$

$$\phi''_\nu(\nu(r)) = \frac{\sigma_{sym}}{Z''_{SC}}\Gamma\left(\frac{3}{2}, \frac{D''(r)}{kT}\right)\left(\frac{2\pi\mu kT}{h^2}\right)^{\frac{3}{2}} 4\pi r^2 \exp\left(-\frac{V''(r)}{kT}\right)\left|\frac{d\nu(r)}{dr}\right|^{-1}, \tag{6.49}$$

where r is the molecule's internuclear distance, Z_{SC} the state's internal partition sum, $V(r)$ the potential energy (defined relative to the potential well), $D(r) = V(\infty) - V(r)$ the dissociation energy, σ_{sym} a symmetry factor ($\frac{1}{2}$ for S_2), and $\Gamma(\frac{3}{2}, x)$ the normalised incomplete gamma function of order $\frac{3}{2}$. Finally, Z_{SC} is the classical version of the internal partition function,

$$Z_{SC} = \sigma_{sym}\left(\frac{2\pi\mu kT}{h^2}\right)^{\frac{3}{2}}\int_0^\infty \Gamma\left(\frac{3}{2}, \frac{D(r)}{kT}\right) 4\pi r^2 \exp\left(-\frac{V(r)}{kT}\right) dr. \tag{6.50}$$

The quantum-mechanical line profile is actually composed of many individual, possibly overlapping lines. For molecular $^3\Sigma$ states, where Hund's rule (b) applies (Herzberg, 1950), and ignoring electron spin splitting (we include the $2S+1$ degeneracy in the state degeneracies g' and g''), we have

$$\phi'_\nu = \phi_{\nu,D}(\nu)\frac{1}{Z'_{QM}}\sum_{v'N'}\omega_{N'}\sum_{v''N''} S^{N'}_{N''} < \psi_{v'}|\psi_{v''} >^2 \exp\left(-\frac{E_{v'N'}}{kT}\right), \tag{6.51}$$

$$\phi''_\nu = \phi_{\nu,D}(\nu)\frac{1}{Z''_{QM}}\sum_{v''N''}\omega_{N''}\sum_{v'N'} S^{N'}_{N''} < \psi_{v'}|\psi_{v''} >^2 \exp\left(-\frac{E_{v''N''}}{kT}\right), \tag{6.52}$$

with v the vibrational quantum number, N the quantum number for angular momentum without spin, ω_N a statistical factor due to nuclear spin, $S^{N'}_{N''}$ the Hönl-London factor, $< \psi_{v'}|\psi_{v''} >^2$ the Franck-Condon factor and $\phi_{\nu,D}$ the Doppler line profile for a single ro-vibrational transition $v'N' \longrightarrow v''N''$. The internal partition function is now given by

$$Z_{QM} = \sum_v\sum_N g_{v,N}\exp\left(-\frac{E_{v,N}}{kT}\right). \tag{6.53}$$

For S_2, ω'_N equals unity for odd and zero for even N'' levels, effectively making even N'' levels forbidden. For the upper state, the situation is reversed and odd N' levels are forbidden. The Hönl-London factors are such that only $|N' - N''| = 1$ transitions are allowed.

Since the S_2 B-X spectrum stretches over approximately 500 nm and Doppler profiles at temperatures between 1000 and 5000 K require 10^{-3} nm resolution, a quantum-mechanical calculation for each iteration in a model that requires over 100 iterations to converge is not desirable. In van der Heijden *et al.* (2002) an optimised method was presented, which reduces the calculation time by only evaluating effects of radiative transfer in selected "islands" of wavelength points. For example, the calculation is performed at 10^{-3} nm resolution for the range 300 ± 0.25 nm, then again for the range 310 ± 0.25 nm. Then the average of the Q_{rad} values for these islands is taken so that the overall shape of the spectrum can be determined. It was found that the error introduced by this approximation is less than 5%.

6.6 Results

First, the influence of the number N_r of r points in the computational grid was investigated. Calculations with N_r between 10 and 60 show that with increasing N_r the results (both in the

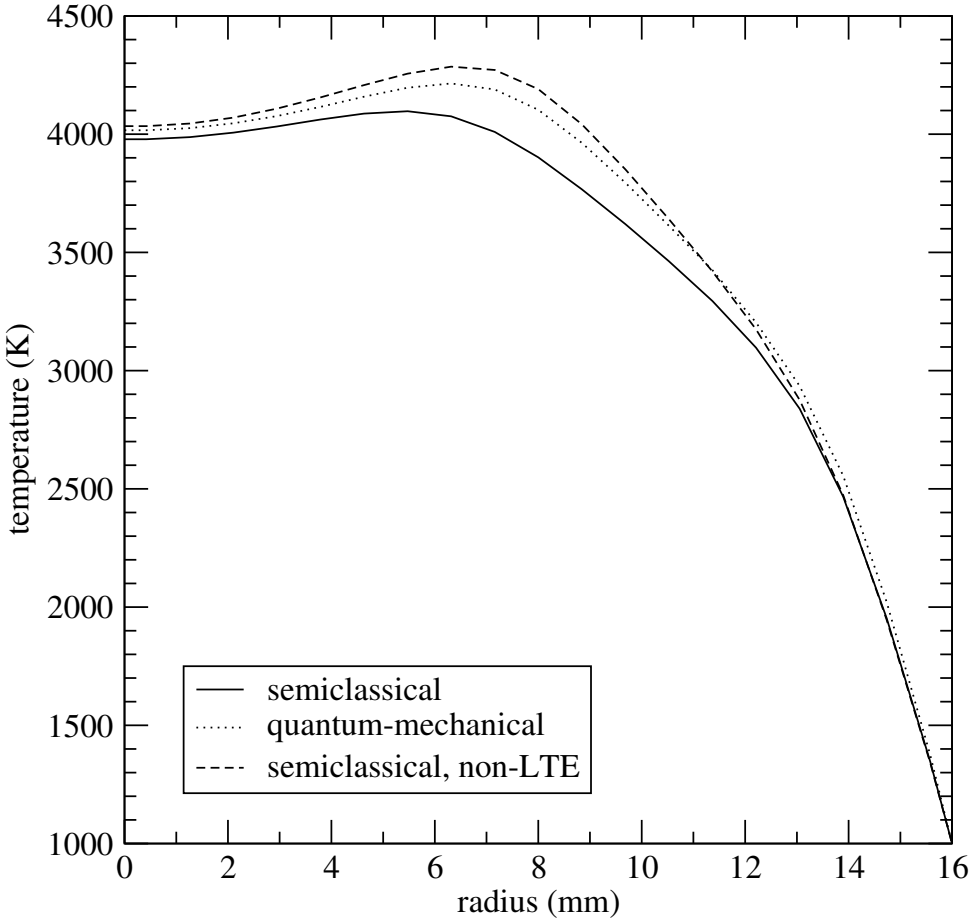

Figure 6.13: *Calculated temperature profiles for 800 W input power using SC and QM radiative transfer.*

calculated temperature profile and the emitted spectrum) converge towards a certain limiting solution. Both the calculation time per iteration and the number of iterations required to reach convergence increase linearly with N_r. Even at $N_r = 10$ the maximum difference per r point with the limiting solution at large N_r is less than 1%, so that a much larger number of r points is not needed. The rest of the calculations presented in this section are done at $N_r = 20$.

Figure 6.13 shows the calculated temperature profiles for calculations using semiclassical and quantum-mechanical values for j_ν and κ. For the optimised quantum-mechanical calculation, 40 islands of 250 points at 10^{-3} nm resolution were used (van der Heijden *et al.*, 2002). The input power was set at 800 W.

Figure 6.14 shows the calculated emitted spectra P_λ [W/nm], which is calculated by integrating the Q_{rad} source terms to obtain the total radiative losses,

$$P_\lambda = -\int_0^R 4\pi r^2 Q_{rad,\lambda} dr. \tag{6.54}$$

For comparison, a measured spectrum with 800 W input power is also plotted (van der Heijden *et al.*, 2002; Johnston *et al.*, 2002).

In earlier calculations with a fixed temperature profile (van der Heijden *et al.*, 2002), it was found that the QM calculation gives a slightly lower (60%) efficiency than the SC one

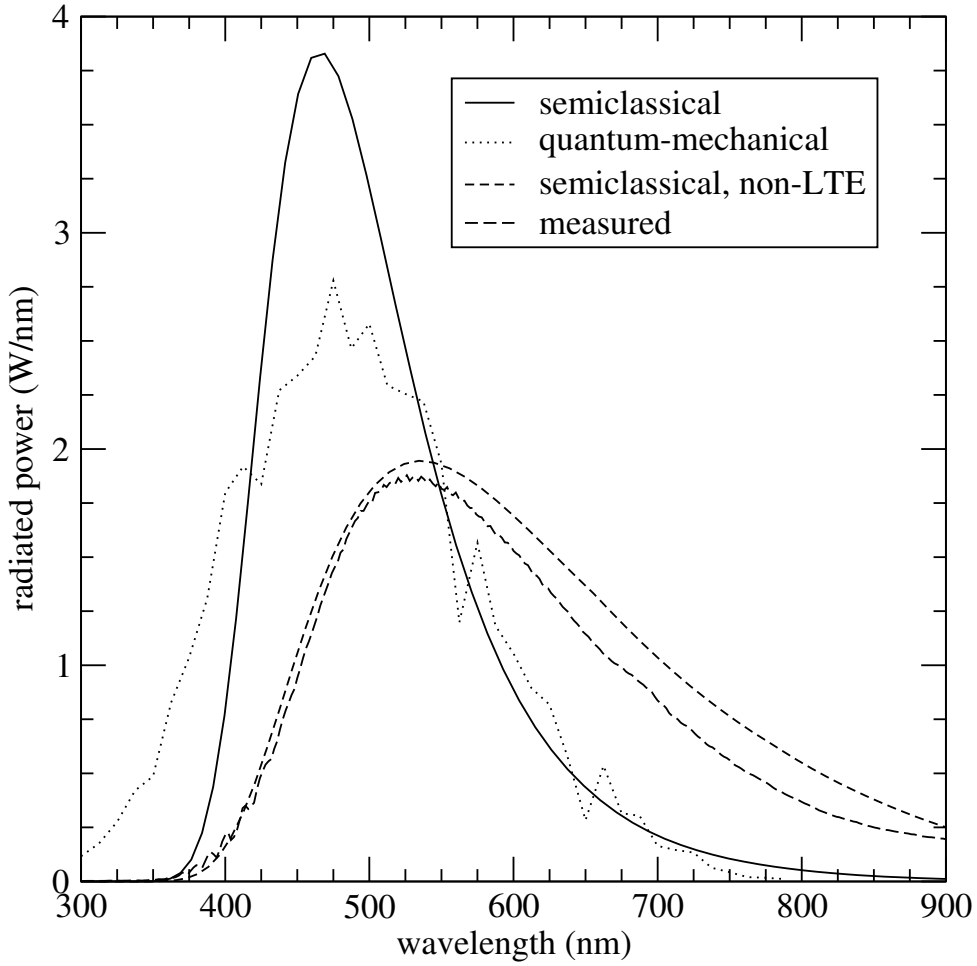

Figure 6.14: *Calculated SC and QM spectra for 800 W input power, compared with a measured spectrum. The SC, QM, and experimental total radiated power values are 558 W, 537 W, and 501 W respectively.*

(70%). It was also found that the radiative losses scale with the central temperature. The current model with a self-consistent temperature profile shows that the QM calculation gives a slightly higher peak value for the temperature, so that the difference in efficiencies is reduced. The SC calculation is still the most efficient with 558 W (70%), which is slightly higher than the QM radiated power of 537 W (67%). The difference is, however, of the same order of magnitude as the error in the optimised quantum-mechanical method (5%). The measured spectrum contains 501 W (63%), but it must be noted that the input power of 800 W also includes power losses in the cavity, which are estimated to be between 5% and 10%. Correcting for this gives a measured efficiency between 66% and 70%.

While the calculated efficiencies are in general agreement with the measured one, the same cannot be said for the overall spectrum shape. As shown in calculations with fixed temperature profiles, both the SC and QM calculations show too much blue light and too little in the red part of the spectrum. A calculation using a self-consistent temperature profile does not correct this problem, as can be seen in figure 6.14. Therefore, we investigate the effects of a possible non-LTE distribution of the vibrational states in the S_2-B molecule. Specifically, we assume that the

main source of S_2-B molecules is association of one ground state and one excited S atom, rather than excitation of a S_2-X molecule. The reason behind this assumption is that electron induced excitation from the bottom of the well of the S_2-X molecule requires approximately 4 eV, while excitation of a S atom requires less than 1 eV.

Instead of a Boltzmann distribution that is tied to the density in the well of the S_2-B potential curve, we consider a distribution that is tied to the density of S_2-B molecules in high vibrational states. That is, the vibrational states are populated according to a "trickle down" scenario, where the density of the v vibrational state is proportional to the density of the $v+1$ state. Consider a process with frequency f_c that causes a $v+1 \rightarrow v$ transition. In between these events, it is possible that the molecule spontaneously makes a radiative transition to the S_2-X state. The chance that this happens is A/f_c, where A is the transition probability. Therefore, the connection between densities of different vibrational states $v+1$ and v is given by

$$n(v) = n(v+1)\left(1 - \frac{A}{f_c}\right). \tag{6.55}$$

This description can also be translated to the semiclassical description. In the SC theory, an expression for dn/dr is needed, so that $dn/dr\Delta r$ is the density of molecules with internuclear radius r in the range $r..r+\Delta r$. The semiclassical analog of a $v+1 \rightarrow v$ transition is a change Δr in r so that $V(r+\Delta r) - V(r) = hc\omega_0$ where ω_0 is the separation (in wave numbers) between vibrational levels. The relation between $n(r)$ and $n(r+\Delta r)$ is thus

$$n(r) = n(r+\Delta r)\left(1 - \frac{A}{f_c}\frac{V(r+\Delta r) - V(r)}{hc\omega_0}\right). \tag{6.56}$$

By rewriting this as $(n(r+\Delta r) - n(r))/\Delta r$, the differential form is found,

$$\frac{dn(r)}{dr} = n(r)\frac{A}{f_c}\frac{1}{hc\omega_0}\frac{dV(r)}{dr}. \tag{6.57}$$

The differential form has an analytical solution,

$$n(r) = C\exp\left(\frac{A}{f_c hc\omega_0}V(r)\right), \tag{6.58}$$

where C is a normalisation constant. In comparison with the Boltzmann distribution, which contains a term $\exp(-V(r)/(kT))$, equation (6.58) no longer contains an explicit temperature dependence (there is of course an implicit dependence in f_c) and the minus sign in front of $V(r)$ is gone, since now the densities $n(r)$ are tied to the densities at high values of $V(r)$.

The result of a calculation with a semiclassical non-LTE S_2-B population is also given in figures 6.13 and 6.14. In the crude non-LTE treatment, the factor f_c is effectively a fit parameter. The calculations presented here are done with $f_c = 4 \cdot 10^7$ Hz. In figure 6.14 it can be seen that the calculated spectrum agrees much better with the measured one. The calculated temperature profile has a slightly higher peak value than the profile from the QM calculation.

Finally, in order to gain insight into the origin of the emitted spectrum, we plot the radiative sources from a SC calculation, weighed by a volume factor of $4\pi r^2 dr$,

$$\frac{dP_\lambda}{dr} = 4\pi r^2 Q_{rad,\lambda}, \tag{6.59}$$

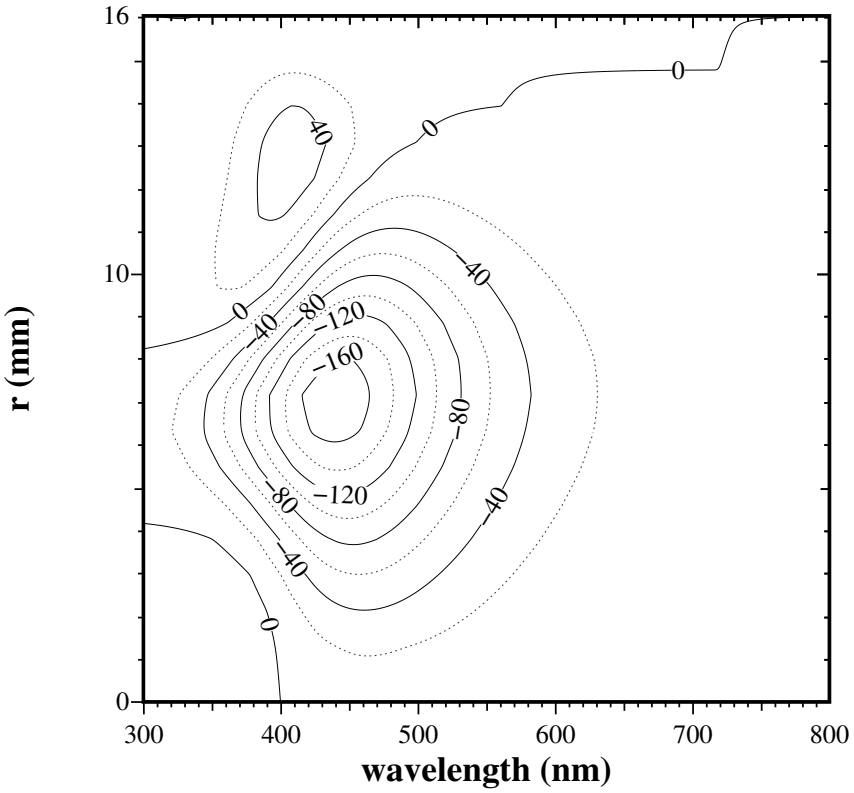

Figure 6.15: *Contour plot of the calculated spectral sources weighed with CV volume, $dP_\lambda(r)/dr = 4\pi r^2 Q_{rad,\lambda}$. Negative numbers mean the plasma looses energy due to (locally) escaping radiation and positive numbers signify that emission is less than absorption.*

as a function of r and λ (see figure 6.15). The centre of the plasma hardly contributes to the spectrum. This is due to the fact that at high temperatures S_2 is dissociated and also a result of the weighing with $4\pi r^2$. At wavelengths above 500 nm, all P_λ values are close to zero or negative for all values of r, indicating that there are no regions where absorption is significantly larger than emission. Indeed, this is the optically thin part of the spectrum. Below 400 nm, the P_λ values are relatively small. This due to the fact that the optically thick part of the spectrum plays a minor role in the transport of energy via radiation.

The most interesting wavelength range is between 400 and 500 nm. Around $r \approx 7$ mm there is a plasma region that looses a lot of energy due to radiation. Not all this radiation escapes the plasma, since around $r \approx 13$ mm there is a region that absorbs more radiation below 450 nm than it emits. This relatively cool part of the plasma partly blocks the blue part of the spectrum.

6.7 Conclusion

A general method has been given to describe the interaction between the radiation field and fluid transport phenomena of plasmas. The method which is especially useful for plasmas for lighting is based on a self-consistent merging of a ray-trace and control volume method. Even

though the test case presented here is a plasma in LTE, the difference between LTE and non-LTE plasma descriptions is small from the point of view of a radiative transfer code.

For the geometries discussed here, the sphere and infinitely long cylinder, the radiative transfer calculation does not require a separate grid, but works with the nodal points and control volumes as used in the fluid code. The method is specifically suited for systems which have an axis or point of symmetry. For more complex geometries lacking these kinds of symmetries, this method is not very suited and a Monte Carlo method is probably preferable.

The radiative transfer method does not require that the radiation is either optically thin or thick, but describes everything between these extreme cases. Furthermore, it has been shown that the description yields the well-known analytical results for optically thick and thin radiation. The method can also describe multiple radiative transitions simultaneously. In the case of LTE it is of no importance to what extent any given transition contributes to the radiative power source term, and, as outlined in section 6.3.1, in non-LTE this information can be retrieved after the calculation of the radiative power source terms.

At the basis of the radiation method is the calculation of light intensity along a probe line. Depending on the nature of the problem (predominantly thick or thin radiation, for example) and the required accuracy, the precision and computational cost of the integration of I_ν along the probe line can be adjusted by choosing the number of terms taken in the Taylor expansion of $j_\nu(s)$ (cf. equation (6.13)). For example, if thick radiation plays a minor role, using only the zeroth order term in j_ν might be sufficient. In the present study of the S_2 radiation, adding the first order term caused a difference in the resulting emitted spectral power that is below 1%.

Two methods are presented for linking the intensity along a probe line to the effects of radiation inside a given control volume: the boundary and the nodal point methods (the latter is treated in the appendix). The boundary method, used in the case study for a spherical S_2 plasma, is a little more involved than the nodal point method. It has the advantage that the interdependence between solid angle fraction, probe line direction, and control volume boundary normal — which determine the in- or outgoing radiative flux due to a probe line — results in relatively simple expressions for geometries like a sphere and an infinitely long cylinder. The nodal point method is preferable for more complex geometries, since it does not require the evaluation of an in-product between a vector and a surface normal for each control volume boundary.

In an earlier study of the sulfur lamp (van der Heijden and van der Mullen, 2001) it has been shown that with a given temperature profile, a QM radiation calculation yields a slightly lower (60%) efficiency than a SC one (70%). However, the self-consistent calculations in this study show less of a difference. The temperature profile for a QM radiation model has a slightly higher peak value (4200 K) than the profile that is calculated with SC radiation. Since the emitted radiative power scales with temperature (van der Heijden and van der Mullen, 2001) this raised temperature reduces the efficiency difference to a value smaller than the calculation error of the optimised quantum-mechanical approach. The measured spectrum shows a slightly lower efficiency, but it must be noted that the reported 800 W input power does not account for losses in the microwave cavity, which are estimated between 5% and 10%.

More serious is the discrepancy, in both the SC and QM calculations, between the calculated and measured spectrum shape. The calculations show too much light at blue wavelengths and too little in the red part of the spectrum. It has been shown that a crude non-LTE approximation for the distribution of vibrational levels in the emitting S_2-B molecule can largely correct this discrepancy. It is therefore likely that the S_2-B vibrational states are not populated according to

a Boltzmann distribution.

6.A Nodal point approach

In the main text we dealt with the boundary method. Here a brief outline will be given of the nodal point method in which the intensity I_ν is not evaluated at the CV boundaries, but rather at the nodal point in order to calculate the mean intensity there:

$$J_\nu = \frac{1}{4\pi} \sum_{lines} I_\nu \Delta\Omega. \tag{6.60}$$

Note that, in contrast to the previous method, this time the direction of the probe line is not taken into account. To obtain Q_{rad} for LTE, the difference between emission and absorption is calculated,

$$Q_{rad,\nu} = 4\pi j_\nu - \kappa \sum_{lines} I_\nu d\Omega, \tag{6.61}$$

whereas for non-LTE, it is more convenient to directly apply equation (6.8).

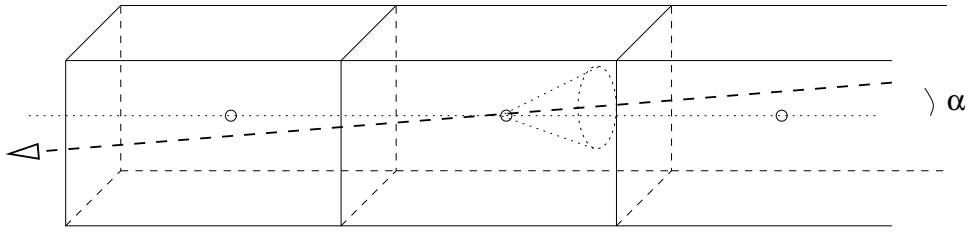

Figure 6.16: *Sketch of the nodal point method. In this method, the line intensity I_ν is evaluated at the nodal points, not at the CV boundaries.*

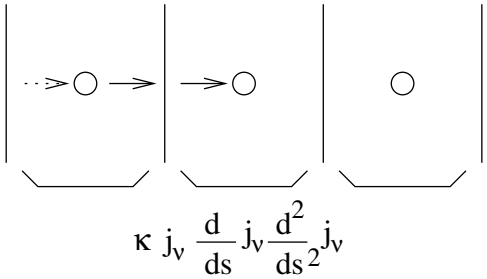

Figure 6.17: *Discretisation for the nodal point method. All relevant quantities are defined at the nodal points.*

In the nodal point approach, all quantities must be defined in the nodal point, as shown in figures 6.16 and 6.17. To move from one nodal point to the next two steps are needed: when approaching a nodal point, L_{bwd} is used, while L_{fwd} is used on leaving a nodal point. It is important to note that in this case it is not possible to ignore the $d^2 j_\nu / ds^2$ term in equation (6.17) in order to calculate the correct diffusive limit. In the boundary method this was not necessary, since the difference between in and out going fluxes was taken, which effectively calculates a derivative. In contrast, the nodal point method evaluates I_ν only at nodal points, so the scheme is less precise by design.

6.A.1 Spherical geometry

The agreement between the nodal point en boundary methods is that the same probe lines are ray-traced. Thus the intensity as function of radial position is the same. The difference lies in the treatment of the locally dependent quantisation of the direction. Instead of discretising the product of solid angle and projection we now deal with discretisation of the solid angle only. One should realize once more that this discretisation of the solid angle is not performed at the boundary but in the nodal point. From equation (6.60) we find,

$$dJ_\nu = \frac{1}{4\pi} I_\nu 2\pi \sin\theta d\theta, \tag{6.62}$$

which cannot be rewritten in terms of y and dy using equations (6.28) and (6.29). Therefore, the integration boundaries of θ for the contribution of probe line i to J_ν at the nodal point r_j, are $\theta_{i,j}$ and $\theta_{i+1,j}$, with

$$\theta_{i,j} = \begin{cases} \arcsin(R_i/r_j), & j > i, \\ \pi/2, & j = i. \end{cases} \tag{6.63}$$

The contribution of line i, on the rhs or lhs, to $J_\nu(r_i)$ is then

$$J_\nu(i,j) = \frac{1}{2} I_{\nu,i,j}[\cos(\theta_{i,j}) - \cos(\theta_{i+1,j})]. \tag{6.64}$$

Combining all probe lines, and adding lhs and rhs contributions, we find

$$J_\nu(r_j) = \frac{1}{2} \sum_{i=0}^{j} [I^{lhs}_{\nu,i,j} + I^{rhs}_{\nu,i,j}][\cos(\theta_{i,j}) - \cos(\theta_{i+1,j})]. \tag{6.65}$$

6.A.2 Cylindrical geometry

In the nodal point approach we again start with $dJ_\nu = \frac{1}{4\pi} I_\nu \sin\theta d\theta d\phi$. Now ϕ of probe line i at nodal point r_j is bounded between $\phi_j(R_i)$ and $\phi_j(R_{i+1})$, with $\phi_j(x)$ given by

$$\phi_{i,j} = \begin{cases} \arcsin(R_i/r_j), & j > i, \\ \pi/2, & j = i. \end{cases} \tag{6.66}$$

The contribution of line i at angle θ, on the rhs or lhs, to $J_\nu(r_i)$ is given by

$$dJ_\nu(i,j,\theta) = \frac{2}{4\pi} \sin\theta d\theta (\phi_{i+1,j} - \phi_{i,j}) I_{\nu,i,j}, \tag{6.67}$$

where again a factor of 2 is added since only half the actual ϕ range is taken into account. The contribution of all lines at angle θ, on the lhs and rhs, is then

$$\frac{dJ_\nu(r_j,\theta)}{d\theta} = \frac{1}{2\pi} \sin\theta \sum_{i=0}^{j} [I^{lhs}_{\nu,i,j}(\theta) + I^{rhs}_{\nu,i}(\theta)](\phi_{i+1,j} - \phi_{i,j}), \tag{6.68}$$

and $J_\nu(r_j)$ is given by

$$J_\nu(r_j) = 2 \int_0^{\pi/2} \frac{dJ_\nu(r_j,\theta)}{d\theta} d\theta. \tag{6.69}$$

Comparing the two methods with each other teaches that with regard to the boundary method we loose in the nodal point method the simple expression of the in-product of solid angle and surface. That makes the method less transparent. The advantage is that this method can easily be extended to the 2 dimensional cylindrical case and even further to non-structured meshes.

Chapter 7

Validating the radiative transfer modules

Abstract

In this chapter two new methods for calculating the effects of radiative transfer are introduced: (i) a (quasi) analytical method that is applicable to uniform plasmas in spherical or cylindrical coordinates, and (ii) a general Monte Carlo method. Both methods, which may also find applications in their own right (the Monte Carlo method is used in chapter 8), are used to validate the Ray-Trace Control Volume (RTCV) method developed in the previous chapters. The results are shown to be in agreement.

7.1 Introduction

In chapter 3 the definition of the escape factor is given in equation (3.29),

$$\Lambda_i(\nu) = \frac{j_{\nu,i} - J_\nu \kappa_i}{j_{\nu,i}} = 1 - \frac{J_\nu \kappa_i}{j_{\nu,i}} = 1 - \frac{J_\nu}{S_{\nu,i}}. \tag{7.1}$$

Substituting equation (3.23) for the direction-averaged intensity J_ν,

$$J_\nu = \frac{1}{4\pi} \int_0^\pi \int_0^{2\pi} \sin\theta \int_0^\infty j_\nu(r,\phi,\theta) \exp\left(- \int_0^r \kappa(r',\phi,\theta) dr' \right) dr d\phi d\theta, \tag{7.2}$$

into equation (7.1) leads to an integral equation for the frequency-dependent escape factor,

$$\Lambda(\nu) = 1 - \frac{\kappa}{j_\nu} \frac{1}{4\pi} \int_0^\pi \int_0^{2\pi} \sin\theta \int_0^\infty j_\nu(r,\phi,\theta) \exp\left(- \int_0^r \kappa(r',\phi,\theta) dr' \right) dr d\phi d\theta, \tag{7.3}$$

where the origin of the spherical coordinate system (r,ϕ,θ) is located at the point where $\Lambda(\nu)$ is to be calculated.

The above equation (7.3) is quite unwieldy, which is why in chapter 6 an alternative numerical approach for the calculation of J_ν is presented. In this chapter the validity of this ray-trace control volume (RTCV) approach will be tested using a variety of methods and test cases.

The first test case will be relatively simple; a sphere or cylinder with uniform and monochromatic emission and absorption coefficients. As will be shown in section 7.2, this test case has

a solution for $\Lambda(\nu)$ in the form of a single integral which in some cases can be evaluated analytically and is in all cases rather trivial numerically. In section 7.3 a Monte Carlo method for calculating the effects of radiative transfer will be introduced.

At that point, three different radiative transfer methods will have been introduced; the RTCV method from chapter 6, an analytical formulation (section 7.2), and a Monte Carlo implementation (section 7.3), all of which will be compared with each other in section 7.4.

As in the treatment of the RTCV method in chapter 6, this chapter will present radiative transfer method equations and calculations for monochromatic radiation. Specifically, the test cases involve the calculation of the monochromatic escape factor $\Lambda(\nu)$ (7.1) that was introduced in chapter 3. These methods can be applied to general radiation problems by discretising the frequency space (as discussed in section 3.5.2) and using equations (3.30) or (3.35). It is a consequence of this technique of frequency sampling that if a radiative transfer method works for a single frequency, it will work for an arbitrary set of frequencies.

7.2 Analytical solutions for uniform j_ν and κ

The analytical solution for the case of uniform emission and absorption coefficients can be derived by rewriting the definition of the escape factor (3.28) in the following manner

$$\left(\frac{dn(\vec{r})}{dt}\right)_{rad,\vec{r}} = \left(\frac{dn(\vec{r})}{dt}\right)_{ems,\vec{r}\to\infty} + \sum_{\vec{r'}} \left(\frac{dn(\vec{r})}{dt}\right)_{ems,\vec{r}\to\vec{r'}} - \sum_{\vec{r'}} \left(\frac{dn(\vec{r'})}{dt}\right)_{abs,\vec{r'}\to\vec{r}}. \quad (7.4)$$

The first two terms describe radiation emitted at point $\vec{r}$, split into the part that escapes from the vessel ($\vec{r} \to \infty$) and the part that is absorbed inside the vessel at point $\vec{r'}$ ($\vec{r} \to \vec{r'}$). The third term in (7.4) represents absorbed radiation, which is also written as a summation over all locations $\vec{r'}$ where the absorbed radiation is emitted ($\vec{r'} \to \vec{r}$). This is illustrated in figure 7.1.

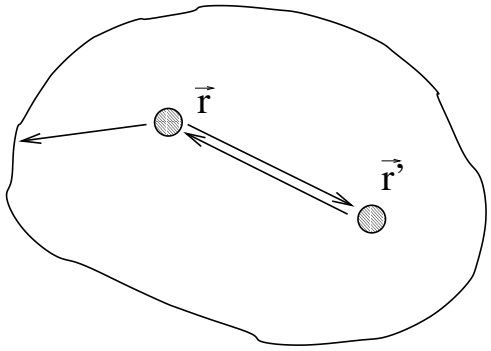

Figure 7.1: *Radiation emitted from point $\vec{r}$ can be divided into radiation that reaches the boundary of the configuration (vessel) and radiation that is absorbed at a location $\vec{r'}$ inside the vessel. In case of uniform emission and absorption, the emission from $\vec{r}$ that is absorbed near $\vec{r'}$ is balanced by the absorption at $\vec{r}$ of radiation that is generated at $\vec{r'}$.*

Consider two points $\vec{r}$ and $\vec{r'}$; both points have the same emission coefficient j_ν, the same absorption coefficient κ and the optical depth between them is $\kappa|\vec{r}-\vec{r'}|$. Therefore, the intensity of radiation generated in $\vec{r}$ and absorbed at $\vec{r'}$ must be equal to the radiation emitted at $\vec{r'}$ and landing in $\vec{r}$. Finally, due to symmetry the solid angle $d\Omega(\vec{r})$ as seen from $\vec{r'}$ is the same as

$d\Omega(\vec{r'})$ from $\vec{r}$. It follows that $(dn(\vec{r})/dt)_{\vec{r}\to\vec{r'}} = (dn(\vec{r'})/dt)_{\vec{r'}\to\vec{r}}$, i.e. what is emitted at $\vec{r}$ and absorbed in $\vec{r'}$ is the same as what is emitted in $\vec{r'}$ and absorbed in $\vec{r'}$. Therefore, all terms in the summations of equation (7.4) cancel and the net rate of change is determined only by the amount of radiation that reaches the edge of the configuration,

$$\left(\frac{dn(\vec{r})}{dt}\right)_{rad,\vec{r}} = \left(\frac{dn(\vec{r})}{dt}\right)_{ems,\vec{r}\to\infty}. \tag{7.5}$$

The mathematical derivation starts with equations (7.1) and (3.22),

$$\Lambda(\vec{r}) = 1 - \frac{\kappa J_\nu(\vec{r})}{j_\nu} = 1 - \frac{\kappa}{j_\nu}\frac{1}{4\pi}\int I_\nu(\vec{r},\vec{\Omega})d\Omega. \tag{7.6}$$

The intensity $I_\nu(\vec{r},\vec{\Omega})$ of radiation at $\vec{r}$ from the direction of $\vec{\Omega}$ is, using s as the integration parameter along $\vec{\Omega}$, given by (following equation (3.20))

$$I_\nu = \int_0^\infty j_\nu \exp(-\kappa s)ds = \int_0^{\rho(\vec{r},\vec{\Omega})} j_\nu \exp(-\kappa s)ds = \frac{j_\nu}{\kappa}\left(1 - \exp(-\kappa\rho(\vec{r},\vec{\Omega}))\right). \tag{7.7}$$

In the first step of equation (7.7), the integral $\int_0^s \kappa ds'$ is replaced by κs since κ is constant. In the second step, the integration of s is cut off at the distance between $\vec{r}$ and the boundary of the vessel, $\rho(\vec{r},\vec{\Omega})$, since there are no contributions to I_ν from beyond this point. Substituting the result of the integration (7.7) into equation (7.6) gives

$$\Lambda = \frac{1}{4\pi}\int \exp(-\kappa\rho(\vec{r},\vec{\Omega}))d\Omega. \tag{7.8}$$

Equation (7.8) represents mathematically what was argued earlier, i.e. that in order to calculate the escape factor, only the radiation that escapes from the plasma needs to be considered. The fraction of radiation which leaves the vessel must travel a distance $\rho(\vec{r},\vec{\Omega})$ un-absorbed. This fraction is given by $\exp(-\kappa\rho(\vec{r},\vec{\Omega}))$. Since the distance to the edge depends on the direction $\vec{\Omega}$ in which the radiation is emitted (except in special locations such as the centre of a sphere) and the radiation emission is isotropic, this fraction must be averaged over the solid angle margin of the direction $\vec{\Omega}$.

The mathematical derivation somewhat obscures the simple argument that inside the vessel emission and absorption exactly cancel due to the uniformity of j_ν and κ, so that only emission to the outside is relevant. In the next sections, expressions will be derived for $\rho(\vec{r},\vec{\Omega})$ and the integral (7.8) for spherical and cylindrical configurations.

7.2.1 Spherical geometry

Since both the spherical and cylindrical configurations have circular cross sections, first an expression for ρ in the 2D circular plane is derived. In figure 7.2, $\rho(r,\phi)$ is shown for a circle with radius R, where ϕ is defined as the angle between $\vec{\rho}$ and the radial direction $\vec{e_r}$. Solving $R^2 = (\rho\sin\phi)^2 + (r + \rho\cos\phi)^2$ for ρ gives,

$$\rho(r,\phi) = \sqrt{R^2 - r^2\sin^2\phi} - r\cos\phi. \tag{7.9}$$

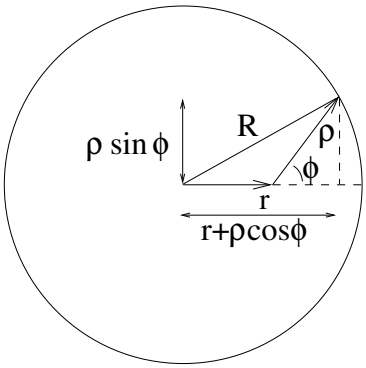

Figure 7.2: *The distance-to-boundary function ρ in a circular cross section is a function of radius r and angle ϕ.*

This result is easily extended for the spherical configuration. As can be seen in figure 7.3, the parameters are still r and ϕ. The part of the solid angle $d\Omega$ that corresponds to the parameter interval $[\phi, \phi + d\phi]$ is $2\pi \sin\phi d\phi$. Substituting equation (7.9) and the spherical expression for $d\Omega$ into equation (7.8) gives

$$\Lambda_{sphere}(r) = \frac{1}{2}\int_0^\pi \exp\left(-\kappa\left(\sqrt{R^2 - r^2\sin^2\phi} - r\cos\phi\right)\right)\sin\phi d\phi. \tag{7.10}$$

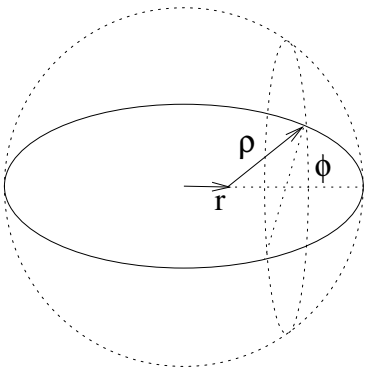

Figure 7.3: *Distance to boundary $\rho(r, \phi)$ in a spherical configuration. The only parameters are r and ϕ. The solid angle associated with interval $[\phi, \phi + d\phi]$ is $d\Omega = 2\pi \sin\phi d\phi$.*

Two limiting cases of (7.10) are of interest. In the centre of the sphere, at $r = 0$, all paths to the boundary have length $\rho = R$,

$$\Lambda_{sphere}(r = 0) = \frac{1}{2}\int_0^\pi \exp(-\kappa R)\sin\phi d\phi = \exp(-\kappa R). \tag{7.11}$$

At the edge of the sphere, the escape factor will be higher. Substituting $r = R$ into equation (7.9) gives

$$\rho(R, \phi) = R(\sqrt{\cos^2\phi} - \cos\phi), \tag{7.12}$$

that is, $\rho = 0$ for $0 \leq \phi \leq \pi/2$ and $\rho = -2R\cos\phi$ for $\pi/2 \leq \phi \leq \pi$. The escape factor at the edge of the sphere is thus given by

$$\Lambda_{sphere}(r = R) = \frac{1}{2} + \frac{1}{2}\int_{\pi/2}^{\pi} \exp\left(2\kappa R\cos\phi\right)\sin\phi d\phi = \frac{1}{2}\left(1 + \frac{1 - \exp(-2\kappa R)}{2\kappa R}\right). \quad (7.13)$$

Note that the escape factor for $r = R$ goes to $1/2$, not 0, as $\kappa R \to \infty$. This is due to the fact that at the surface of the sphere, half the total 4π solid angle is always open. The escape is therefore at least $1/2$, plus a small part, $(1 - \exp(-2\kappa R))/(4\kappa R)$, due to radiation that travels through the sphere to the other side. The escape factors for $r = 0$ (7.11) and $r = R$ (7.13) as well as for intermediate r values are plotted as a function of κR in figure 7.4.

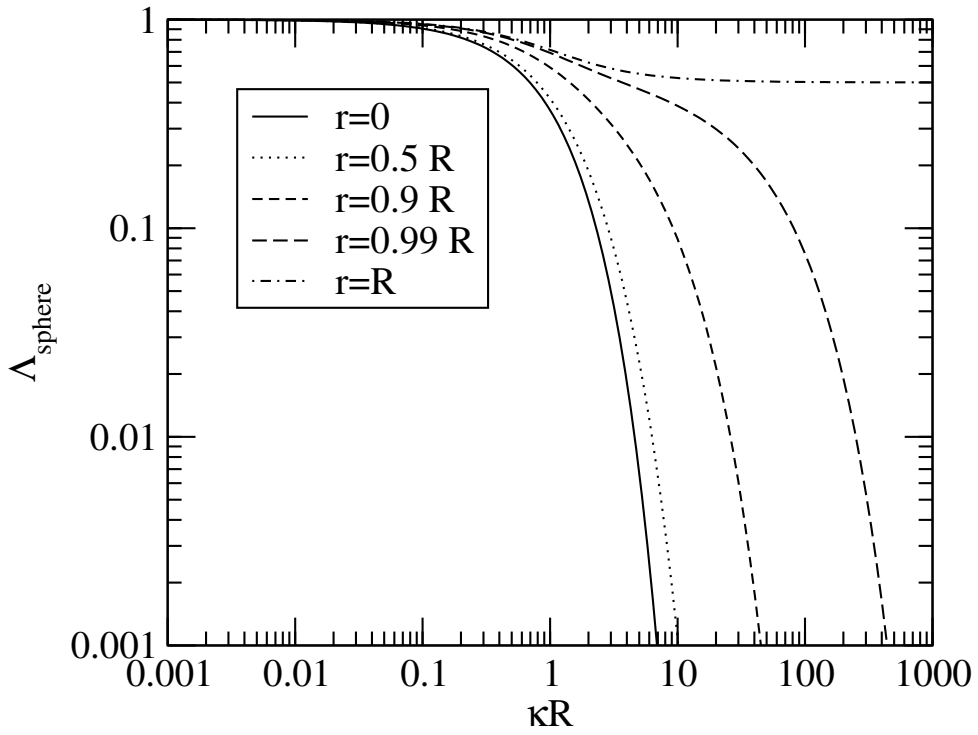

Figure 7.4: *Escape factors in a spherical configuration (radius R) for various values of r as a function of optical depth κR.*

7.2.2 Infinitely long cylinder

The infinitely long cylinder is slightly more complicated. Let θ be the angle between the direction of ρ and the horizontal circular cross section (see figure 7.5). Then for the cylinder, ρ is a function of 3 variables (r, ϕ, θ) and given by

$$\rho(r, \phi, \theta) = \frac{\rho(r, \phi)}{\sin\theta} = \frac{\sqrt{R^2 - r^2\sin^2\phi} - r\cos\phi}{\sin\theta}. \quad (7.14)$$

The solid angle interval $d\Omega$ associated with $d\phi d\theta$ is $d\Omega = d\phi \sin\theta d\theta$, so that the escape factor is given by

$$\Lambda_{cyl} = \frac{1}{4\pi} \int_0^{\pi} \int_0^{2\pi} \exp\left(-\kappa \frac{\sqrt{R^2 - r^2 \sin^2\phi} - r\cos\phi}{\sin\theta} \right) d\phi \sin\theta d\theta. \tag{7.15}$$

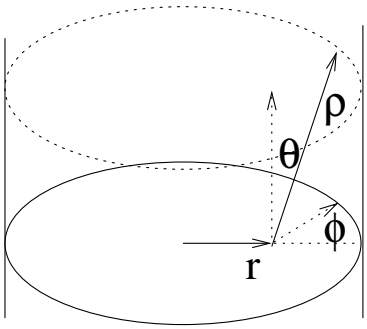

Figure 7.5: *Distance-to-boundary function $\rho(r, \phi, \theta)$ in a cylindrical configuration.*

The values for Λ_{cyl} at $r = 0$ and $r = R$ can not be computed as easily as in the spherical case. However, it is instructive to compare the cylindrical escape factor for $r = 0$,

$$\Lambda_{cyl}(r = 0) = \int_0^{\pi/2} \exp\left(-\frac{\kappa R}{\sin\theta} \right) \sin\theta d\theta, \tag{7.16}$$

with its spherical counterpart (7.11). Radiation is much more trapped in a cylinder with radius R than in a sphere with the same radius. This is due to the fact that radiation emitted roughly in the direction of the cylinder axis ($\theta \approx 0$ or $\theta \approx \pi$) has a much smaller chance of reaching the cylinder boundary than radiation that is emitted in the axial plane ($\theta \approx \pi/2$).

7.3 A Monte Carlo implementation for radiative transfer calculations

This section deals with a Monte Carlo implementation for the calculation of the effects of radiative transfer. The purest form of Monte Carlo calculations in physics is a — if implemented properly — statistically justified *pars pro toto* approach, that is, a limited number of physical processes is taken as representative of all processes. These individual physical processes may be complicated and quite impossible to describe as a whole analytically. Thus the advantage of Monte Carlo methods is that the physicist is less dependent on limits in the field of (applied) mathematics, and more on computational resources — which are more susceptible to economic factors than mathematical breakthroughs.

A distinction is made between two main Monte Carlo methods,

- *Event-based method.* This is the "traditional" Monte Carlo application in radiative transfer (House and Avery, 1969), in which a number N of photon emission events are randomly generated, and the path of the photons is followed. Based on the statistical behaviour of the set of N photons, the behaviour of all photons is inferred.

- *Integration based method.* In this case individual photons are not followed, but the integral equation for J_ν (7.2) is evaluated using Monte Carlo integration techniques. A set of N single numerical integrals is used to evaluate the quadruple integral (7.2).

All methods require a good random generator, and it is often recommended to simultaneously use multiple instances of the same random generator with different seed values. The generator used in the current work is described by Brok *et al.* (2002) and Matsumoto and Nishimura (1988).

7.3.1 An event-based method

The "event-based" Monte Carlo codes generate for each grid point two (usually integer, but some variations works with "fractional photons") numbers, representing the number of emission N_{ems} and absorption N_{abs} events for that grid point. The escape factor is then simply calculated using

$$\Lambda = \frac{N_{ems} - N_{abs}}{N_{ems}}. \tag{7.17}$$

Even though there are several variations possible, the procedure is roughly the same for all event-based methods:

1. *Generate a location for an emission event.*
   Three random numbers are needed to select a location for an emission event. If the emission probability is uniform over the entire region of interest, selecting a random location is rather straightforward in Cartesian coordinates (but many other coordinate systems are not trivial, see for example the item below). However, if the emission is not uniform, volume elements have to be weighed with the emission coefficient.

   The general way to do this weighing is by using a probability distribution function for location (x, y, z),

   $$p(x, y, z) = C j_\nu(x, y, z) dx dy dz, \tag{7.18}$$

   where C is a normalisation constant,

   $$C^{-1} = \int_{z_0}^{z_1} \int_{y_0}^{y_1} \int_{x_0}^{x_1} j_\nu(x, y, z) dx dy dz, \tag{7.19}$$

   with the integration over the entire volume under consideration (here represented by coordinate boundaries x_0, x_1, etc.). For each coordinate, one can then define cumulative distributions,

   $$\begin{aligned} c_x(x) &= C \int_{z_0}^{z_1} \int_{y_0}^{y_1} \int_{x_0}^{x} j_\nu(x', y', z') dx' dy' dz' \\ c_y(y) &= C \int_{z_0}^{z_1} \int_{y_0}^{y} \int_{x_0}^{x_1} j_\nu(x', y', z') dx' dy' dz' \\ c_z(z) &= C \int_{z_0}^{z} \int_{y_0}^{y_1} \int_{x_0}^{x_1} j_\nu(x', y', z') dx' dy' dz', \end{aligned} \tag{7.20}$$

   which provide a mapping for x, y, and z to a number in the range [0,1]. A random location, properly weighed with emission coefficient j_ν can then be generated using the inverted cumulative distributions,

   $$(x, y, z) = (c_x^{-1}(\texttt{rand1}), c_y^{-1}(\texttt{rand1}), c_z^{-1}(\texttt{rand1})), \tag{7.21}$$

where `rand1` represents a call to a function (Matsumoto and Nishimura, 1988) that generates a random number in the interval $[0, 1)$ (so that the equation above contains three random numbers).

However, since there are generally no analytical expressions for the inverted cumulative distributions in (7.20) it is quite cumbersome to implement this method.

Another algorithm, more easily implemented but computationally more costly, is the rejection method. Assuming the Monte Carlo code works internally with a Cartesian grid with constant x, y, z spacings, so that each cell has an equal volume, the choice for any given cell must be weighed only with the cell's emission coefficient j_ν. The algorithm consists of three steps, some of which may be repeated a number of times before a result is returned:

(a) Select a random cell

(b) Generate a random number in $[0, 1)$ and check if this number is smaller than the value of $j_\nu / j_{\nu,max}$, where $j_{\nu,max}$ is the maximum value of j_ν in all grid cells. If not, go back to the first step and generate a new random cell.

(c) The grid cell passed the statistical test. Now generate a random location (x, y, z) inside this cell.

This algorithm is statistically equivalent to the general method outlined above, and obviously easier to implement. In a sense, the algorithm is a Monte Carlo code inside a Monte Carlo code, since it replaces mathematics (the inverted cumulative distributions of equation (7.20)) with even more dice rolling. Every cell that is rejected by the test in the second step will cost some time. The chance of immediate success (no repeated generation of a random grid cell) is easily calculated,

$$p_{success} = \frac{1}{j_{\nu,max} V} \int_{z_0}^{z_1} \int_{y_0}^{y_1} \int_{x_0}^{x_1} j_\nu(x, y, z) dx dy dz, \tag{7.22}$$

with V the total volume. Thus the success rate is high if j_ν is evenly distributed, without large deviations from the average, and low if it has a large $j_{\nu,max}$ value compared to the average. The Monte Carlo code presented here uses the rejection method to generate a random location.

2. *Generate a direction in which the photon travels.*
Working in a local spherical coordinate system at the emission location, selecting a direction requires two random numbers to determine elevation θ and azimuth ϕ. This is not as straightforward as it might seem, since (θ, ϕ) directions are not uniformly distributed. In order to generate a proper random direction, it is important to account for the "direction density" around given protect values of (θ, ϕ).

   Consider a sphere with a radius of unity. The fraction of the sphere's surface for values around (θ, ϕ) is $\sin\theta d\theta d\phi$. This infinitesimal surface is a measure of the "direction density". Normalising by dividing by 4π, gives the distribution function $p(\theta, \phi)$ for the probability of a direction represented by the vector $(1, \theta, \phi)$ in spherical coordinates,

$$p(\theta, \phi) = \frac{1}{4\pi} \sin\theta d\theta d\phi. \tag{7.23}$$

As shown in the discussion of random locations, for each parameter a cumulative distribution is defined which provides a weighed mapping to a number in the range [0,1],

$$c_\theta(\theta) = \int_0^{2\pi}\int_0^{\theta} p(\theta',\phi')d\theta' d\phi' = \frac{2\pi}{4\pi}\int_0^{\theta}\sin\theta' d\theta' = \frac{1}{2}(1-\cos\theta),$$
$$c_\phi(\phi) = \int_0^{\phi}\int_0^{\pi} p(\theta',\phi')d\theta' d\phi' = \frac{2}{4\pi}\int_0^{\phi} d\phi' = \frac{\phi}{2\pi}, \tag{7.24}$$

which results in the following algorithm,

$$\theta = \arccos(1-2\texttt{rand1}),$$
$$\phi = 2\pi\texttt{rand1}. \tag{7.25}$$

3. *Trace the photon.*
   Another common aspect of the various event variants is the use of optical depths τ. From the integral solution (7.2) it is obvious that the influence of $j(r,\phi,\theta)$ at distance r is attenuated by a factor $\exp(-\tau(r))$. Therefore, the photon created in an emission event will be absorbed after travelling an optical depth τ which is randomly distributed according to $p(\tau) = \exp(-\tau)d\tau$. Integrating $p(\tau')$ from 0 to τ gives the cumulative distribution $c(\tau) = 1-\exp(-\tau)$. Unfortunately, except in the case of uniform absorption (no variation in κ) τ cannot be easily linked to a geometrical distance without performing the integral κds along a path s.

The least complicated variant of event based methods is as follows. A random emission point is picked using the rejection method as outlined in point (1). Then a random direction is generated using equation (7.25), and finally an optical depth τ is chosen using $c^{-1}(\tau)$,

$$\tau = -\ln(1-\texttt{rand1}). \tag{7.26}$$

Then κds is integrated from the grid point in the random direction until the integral value is equal to τ. At this point, an absorption event is generated.

7.3.2 An integration based method

In the integration based method, not a single grid point is chosen according to emission probability, but the equation for radiative transfer is integrated from plasma volume boundary to boundary.

Consider a path segment through a grid point volume with length d. Inside the volume, the values for j_ν and κ are constant. With $dI_\nu/ds = j_\nu - \kappa I$, the change in I_ν from beginning to end of segment length d is given by

$$\Delta I_\nu = \left(\frac{j_\nu}{\kappa} - I\right)\left(1-\exp(-\kappa d)\right). \tag{7.27}$$

In the optically thin limit of $\kappa \to 0$ this expression has a limit that is separately implemented, for numerical stability. Using $1-\exp(-x) \approx x$,

$$\lim_{\kappa\to 0}\Delta I = jd. \tag{7.28}$$

The integration algorithm involves the following steps:

1. First a random grid point (x, y, z) is picked (unlike in the case of event based methods, this point is not weighed with j_ν) along with a random direction (θ, ϕ) using (7.25). The tracer then calculates the indices of all grid points that are visited by a line in the direction (θ, ϕ) that goes from grid edge to edge and through point (x, y, z) (see figure 7.6 for example tracer output). It also calculates the distances d_i of the line that lies within the volume surrounding the grid point i.

2. Start with $I_{\nu,0} = 0$ at the outside, before the first grid point.

3. For each grid point i along the traced path, update the intensity I_ν by using equation (7.27). The intensity I_ν at the grid point is added to the point's J_ν data and the point's sample counter N is increased.

Note that in this algorithm no emission or absorption "events" are recorded. Instead, the aim is to calculate a value for J_ν by sampling I_ν from random directions. After a number of lines have been traced, J_ν is calculated by dividing the summed I_ν value of the point by the sample size N (the number of times a volume was visited).

7.3.3 Monte Carlo calculations

The job of the Monte Carlo tracer code is to quickly calculate which discrete grid volumes i are visited by following a line from a certain point in a certain direction, and to calculate the distances d_i that are traversed inside the volumes.

The tracer has been implemented for general 3D grids. It is possible to efficiently do calculations for 2D and 1D grids by setting the number of z and/or y grid points to 1.

The output of the Monte Carlo tracer code is shown for a two dimensional 10 x 10 grid in figure 7.6. In the left hand side of figure 7.6, ten point to point traces are shown for emission-to-event paths as outlined in section 7.3.1. The right hand side shows traces from edge to edge, which are used for the integration based approach of section 7.3.2. In both graphs, the locations where the trace lines cross a grid volume boundary are marked. The distances between these marks are the values d_i.

As a test of the event and integration methods, calculations will be done on a one dimensional grid with uniform j_ν and κ. The escape factor $\Lambda(x)$ for this problem can be found from equation (7.8) by realizing that in one dimension, there are only two possible directions so that the integral $1/(4\pi) \int d\Omega$ can be replaced by two terms,

$$\Lambda(x) = \frac{\exp[-\kappa(x - x_0)] + \exp[-\kappa(x_1 - x)]}{2}, \tag{7.29}$$

where $(x - x_0)$ and $(x_1 - x)$ are the distances to the left and right boundaries of the 1D grid. By setting $x_0 = -1/2$ and $x_1 = 1/2$, so that $L = x_1 - x_0 = 1$, $\Lambda(x)$ can be written as

$$\Lambda(x) = \exp(-\kappa/2) \cosh(\kappa x). \tag{7.30}$$

Because there are only two different directions on a 1D grid, the integral method is not really a Monte Carlo method in this case, since no random numbers are used to generate a direction. Instead, the integral is evaluated once from x_0 to x_1 and once from x_1 to x_0.

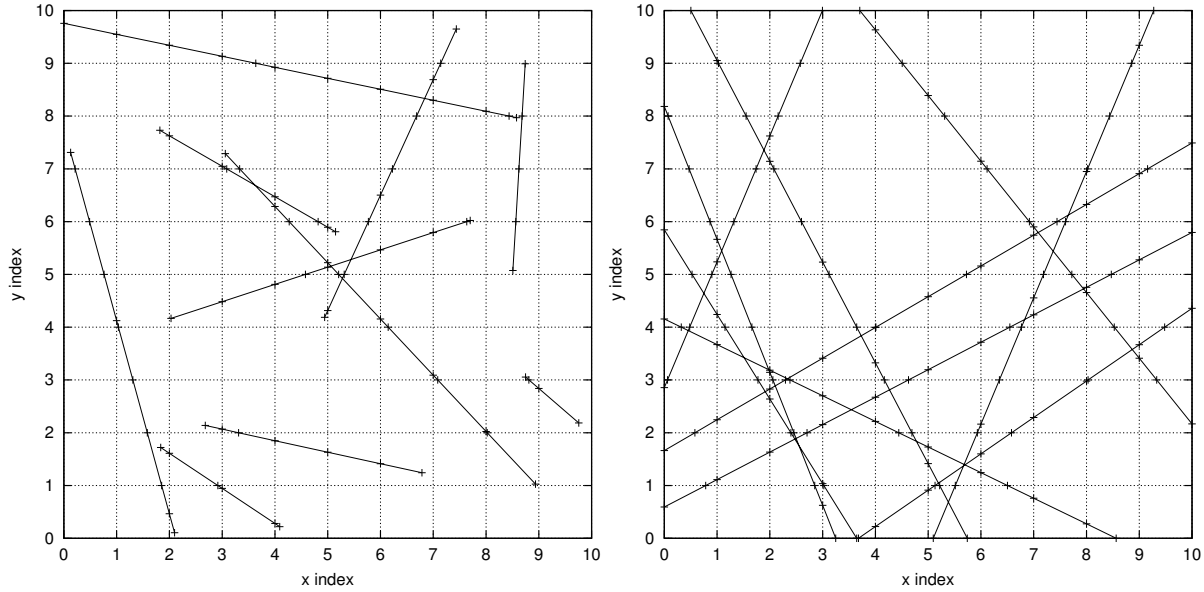

Figure 7.6: *Example output of the Monte Carlo tracer for (left hand side) point to point traces, as used in an event based method, and (on the right hand side) edge-to-edge traces, as used in an integration based method. The traces are done on a two dimensional 10 x 10 grid. The markers (+) signify transitions across volume boundaries.*

Figure 7.7 shows the results for this problem with $\kappa L = 1$ (left) and $\kappa L = 4$ (right) on a 1D grid with 20 points. What is remarkable is that even using $N = 10^5$ emission-absorption events, the result is rather poor. Only the calculations with 10^6 and 10^7 events give reasonable approximations. However, the computation times are much larger than the computation time for the integration method. Based on the finding that the integration method is much faster, the validation calculations are done using the integral method only.

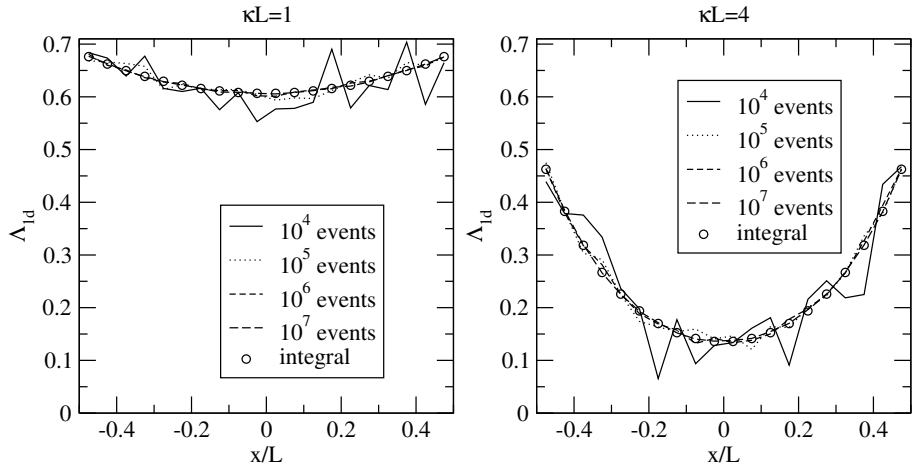

Figure 7.7: *Monte Carlo event method calculations for uniform j_ν and κ on a 1D grid with 20 points. Even using $N = 10^5$ emission-absorption events, the result differs visibly from the known analytical solution. The analytical solution is not plotted, but the $N = 10^7$ events and the integration calculations are very good approximations.*

7.4 Test calculations and discussion

In this section sample calculations will be presented to validate the RTCV and Monte Carlo radiative transfer methods. The calculations will be done in spherical and infinitely long cylindrical configurations, using uniform (so that the analytical solution of section 7.2 can be used) and — more realistic — non-uniform distributions of j_ν and κ.

The Monte Carlo implementation that is presented in the previous section only works with finite rectangular grids. In order to do Monte Carlo calculations for spherical and infinitely long cylindrical grids, a few special tricks are needed.

For a calculation in a point-symmetric sphere with N_r radius points, a 3D cubic grid with $2N_r \times 2N_r \times 2N_r$ points is created. The physical boundaries of this grid are ($-R \ldots R$, $-R \ldots R$, $-R \ldots R$) for the (x, y, z) coordinates. For each point (x_i, y_j, z_k) in this grid, $r_{ijk} = \sqrt{x_i^2 + y_j^2 + z_k^2}$ is calculated and is rounded to the nearest value r_n in the set of N_r radius points. Then the values of $j_\nu(r_n)$ and $\kappa(r_n)$ are assigned to this point.

After the calculation, the escape factor Λ_{ijk} is calculated for each point in the grid. Via the mapping of r_{ijk} to the nearest radius points r_n, the escape factor Λ_{ijk} is used to calculate the average escape factor Λ_n of point r_n.

For a calculation in a cylindrical configuration the procedure is similar. For a finite cylinder, with N_r radius points and N_z axial points, a 3D grid with $2N_r \times 2N_r \times N_z$ points is created. Then, similar to the case for the spherical configuration, by rounding $r_{ij} = \sqrt{x_i^2 + y_j^2}$ to the nearest radius point r_n, all (x_i, y_j, z_k) points are mapped to 2D (r_n, z_k) points.

For the infinite cylinder a grid with only 2 axial points is created; the dimensions are thus $2N_r \times 2N_r \times 2$. Two points in the axial direction is the minimum for 3D grids; if $N_z = 1$ the tracer code defaults to 2D behaviour, without the option of moving in the $\vec{z}$ direction. The special trick involves setting the physical boundaries of this grid to something like ($-R \ldots R$,$-R \ldots R$,$0 \ldots 10^6 R$), so that the length of the cylinder is effectively infinite. The escape factor $\Lambda(r_n)$ is calculated by taking the average value of Λ_{ijk} at both z points for each value of r_{ij}.

7.4.1 Uniform emission and absorption coefficients

As a first test, both the Monte Carlo method and the RTCV will be checked against the analytical expression for the uniform j_ν and κ test case for spherical and infinitely long cylindrical configurations. The actual radius of the sphere or cylinder in question is not directly important; the determining parameter for the escape factor function $\Lambda(r/R)$ is the optical depth κR. The value of j_ν is fixed at 1 (arbitrary units).

First a calculation is presented for $\kappa R = 4$ using the Monte Carlo method in a cylindrical grid only. The aim of this calculation is to investigate how quickly the Monte Carlo result converges towards a solution as the number of integration lines (N) is increased. The results of the calculations using the Monte Carlo integration method for an infinitely long cylindrical grid using $N_r = 20$ and $\kappa R = 4$ are shown in figure 7.8. The results for $N = 100$ are very imprecise, which is not surprising since this gives only $N/N_r = 5$ line integrations per point. With $N = 200$ the statistics are better, while the differences between $N = 500$, $N = 1000$ and $N = 5000$ are very slight. To be on the safe side, all Monte Carlo calculations are done using $N = 10000$ integrations.

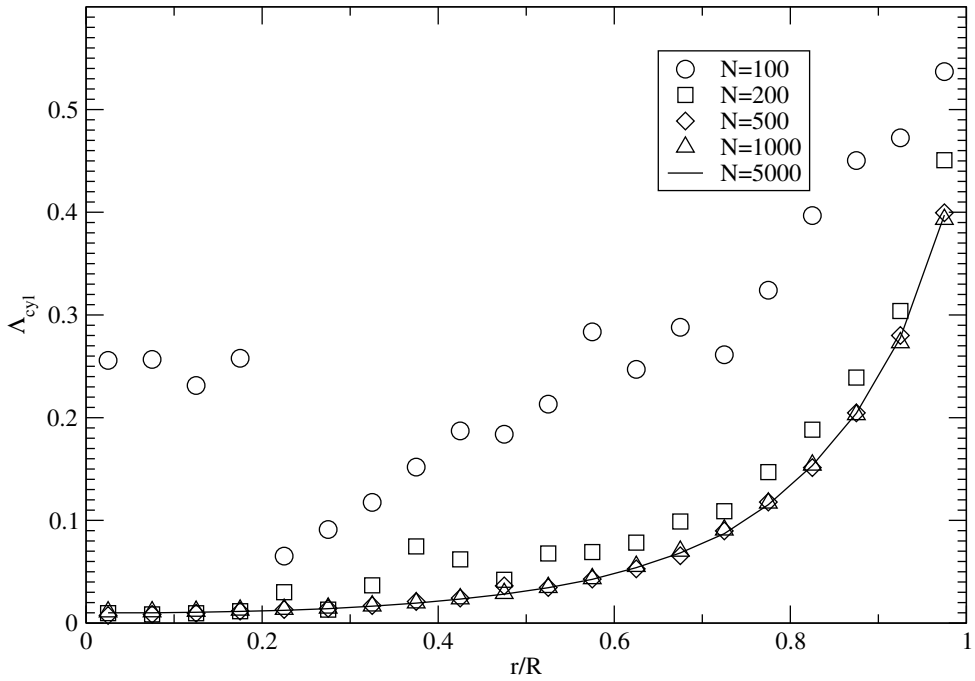

Figure 7.8: *Test calculations for uniform j_ν and κ in a cylindrical configuration with $\kappa R = 4$ using the Monte Carlo integration method, with a varying number of integration lines N.*

Now the results of the analytical expressions, the RTCV method, and the Monte Carlo implementation will be compared. Figure 7.9 shows the results of calculations for $\kappa R = 1$, 2, and 4 in a spherical configuration, and figure 7.10 shows calculations for the same setup in a cylindrical configuration.

As was discussed in connection with equations (7.11) and (7.16), for equal values of κR radiation is more trapped in a cylindrical configuration than in a spherical one.

The agreement between the three different methods is very good. A slight elevation of the RTCV values can be found near $r = 0$. It is a weakness in the RTCV method that the control volume at the centre of the circular cross section is visited by only one trace line, which gives rise to a small error.

7.4.2 Non-uniform emission and absorption coefficients

The second test case involves non-uniform, parabolic emission and absorption parameters,

$$\begin{aligned} j_\nu(r) &= 1 - \left(\frac{r}{R}\right)^2, \\ \kappa(r) &= \kappa_0 \left(1 - \left(\frac{r}{R}\right)^2\right). \end{aligned} \tag{7.31}$$

For this problem no analytical solution is available, so only the RTCV and Monte Carlo methods will be compared.

Figure 7.11 shows the results of calculations for $\kappa_0 R = 1$, 2, and 4 in a spherical configuration, while figure 7.12 shows the results for the same problem in a cylindrical configuration. Again the agreement between the RTCV and the Monte Carlo methods is very good.

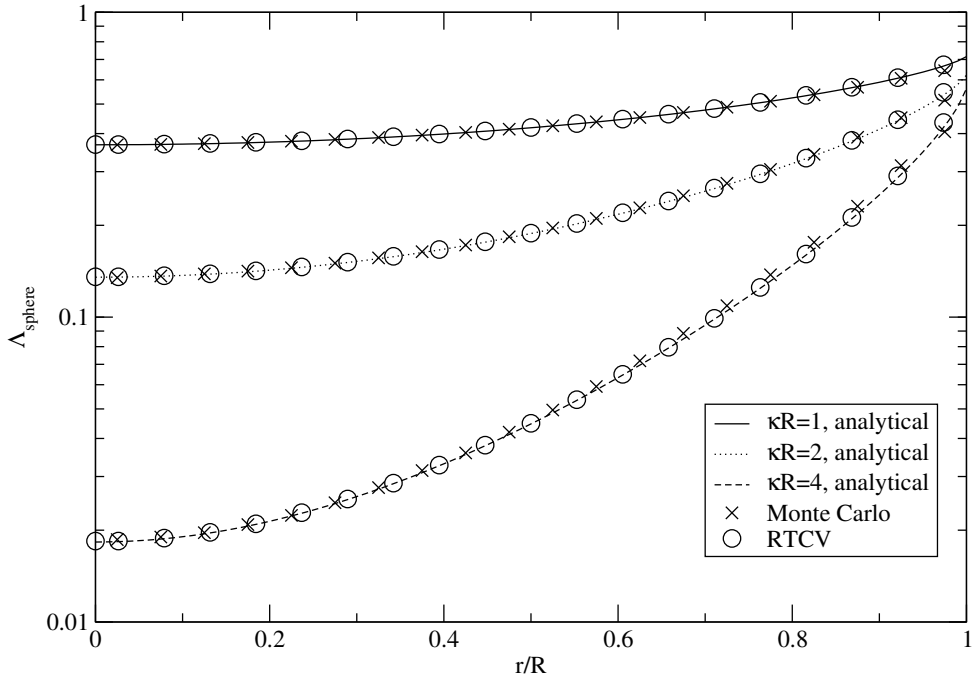

Figure 7.9: *Test calculations for uniform j_ν and κ in a spherical configuration. Λ_{sphere} is plotted as function of r/R for $\kappa R = 1$, 2, and 4.*

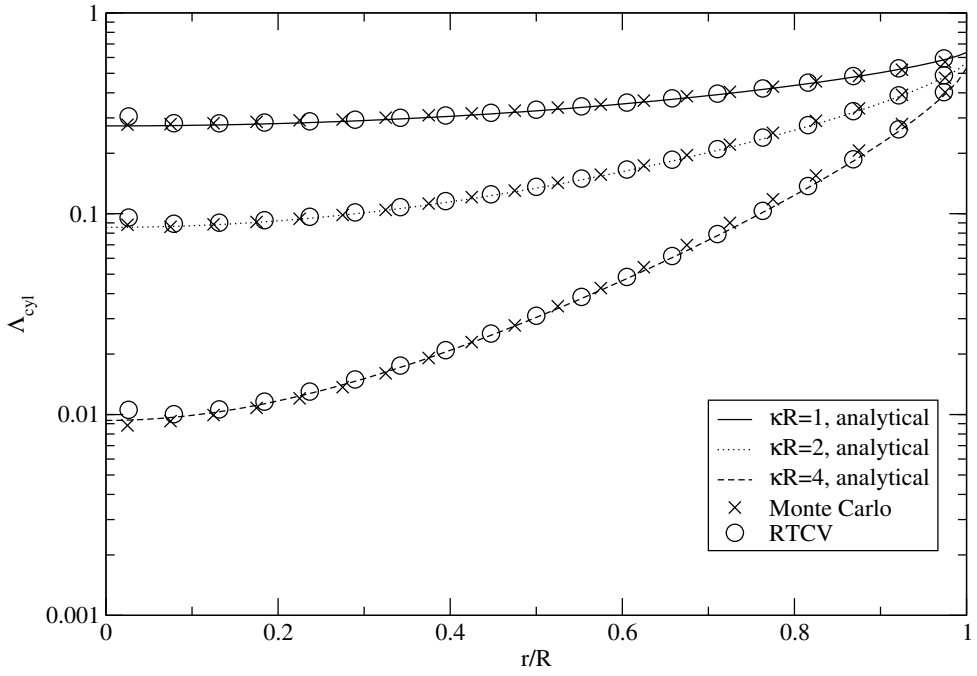

Figure 7.10: *Test calculations for uniform j_ν and κ in a cylindrical configuration. Λ_{cyl} is plotted as function of r/R for $\kappa R = 1$, 2, and 4.*

The calculations in this section have validated the implementations for the RTCV and Monte Carlo radiative transfer codes. Analytical solutions are obviously the fastest way to calculate escape factors, but that approach is hampered by the fact that analytical solutions are available

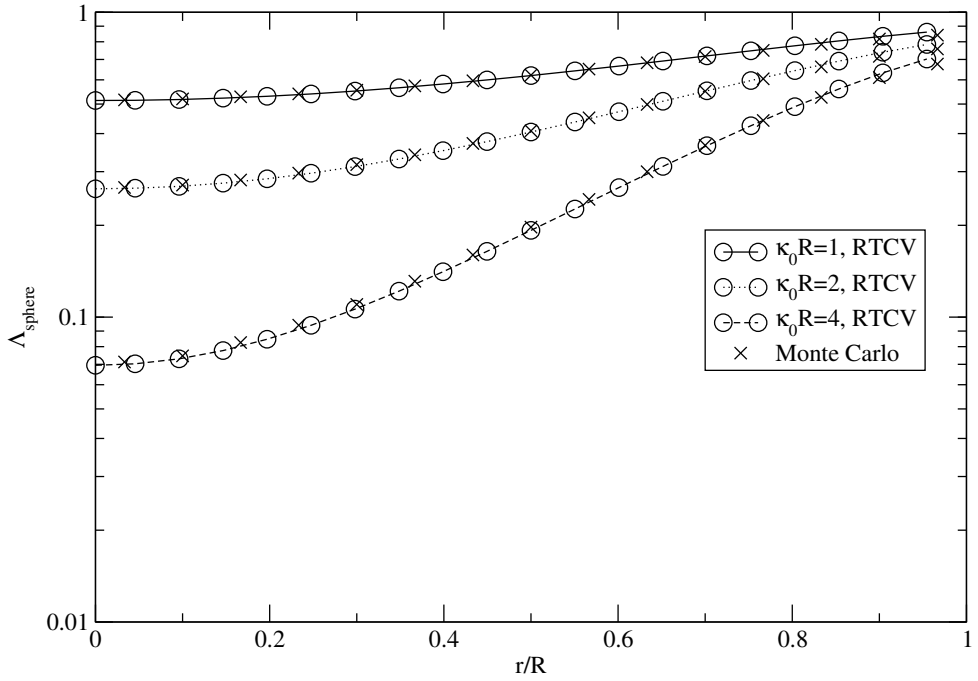

Figure 7.11: *Test calculations for non-uniform (parabolic)* j_ν *and* κ *profiles in a spherical configuration.* Λ_{sphere} *is plotted as function of* r/R *for* $\kappa_0 R = 1$*, 2, and 4, with* $\kappa(r) = \kappa_0(1-(r/R)^2)$.

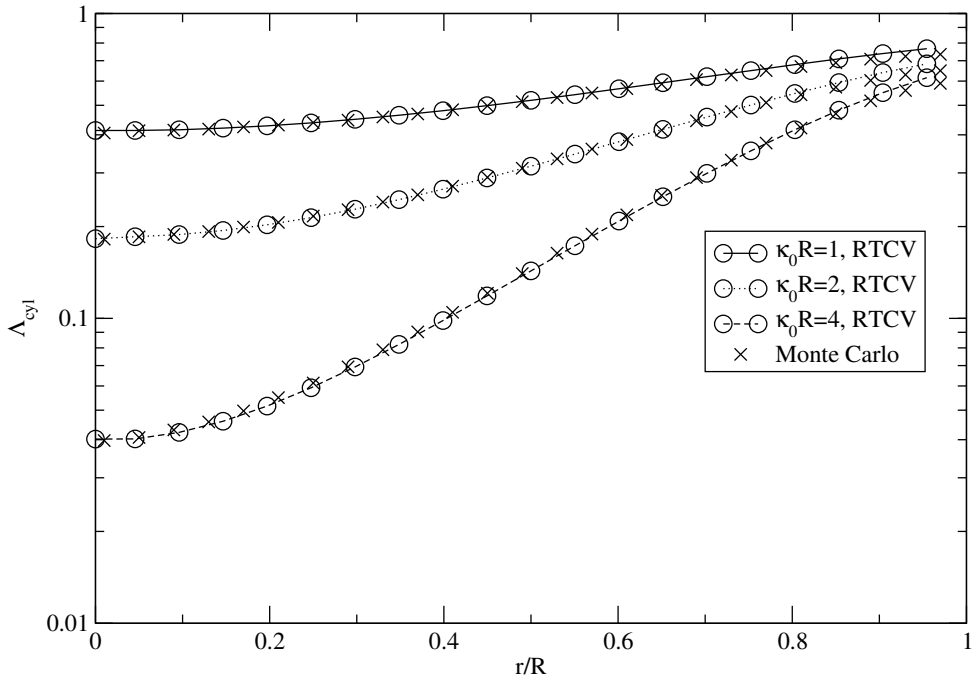

Figure 7.12: *Test calculations for non-uniform (parabolic)* j_ν *and* κ *in a cylindrical configuration.* Λ_{cyl} *is plotted as function of* r/R *for* $\kappa_0 R = 1, 2$ *and 4, with* $\kappa(r) = \kappa_0(1-(r/R)^2)$.

for a few special cases only .

The Monte Carlo codes suffer no such drawbacks. In fact, Monte Carlo radiative transfer

techniques are practically the only option for problems in arbitrary 3D configurations or involving more complex photon processes. Such problems are, for example, found in medical diagnostics applications (de Jong, 2001).

The price one pays for the general applicability of Monte Carlo methods is efficiency. Using special pre- and post-processing methods, the Monte Carlo integration code developed in this chapter can be used efficiently for problems with spherical or cylindrical symmetry. However, it is still not as efficient as the RTCV method, since it depends on a statistical sampling of the total 4π solid angle. In contrast, the RTCV method has the sampling of the directions of the beams built in.

Chapter 8

Radiative transfer of laser-induced fluorescence in an expanding hydrogen plasma

Contains text from: *H.W.P. van der Heijden, M.G.H. Boogaarts, S. Mazouffre, J.A.M. van der Mullen, and D.C. Schram*
Time-resolved experimental and computational study of two-photon laser-induced fluorescence in a hydrogen plasma
Phys. Rev. E **61** 4402–4409 (2000)

Abstract

The time dependence of the fluorescence light emission of atomic hydrogen in an expanding plasma beam after pulsed excitation with a nanosecond laser is studied, both experimentally and computationally. Ground state H atoms in an expanding Ar/H cascaded arc plasma are excited to the $p = 3$ level using two-photon laser excitation at 205 nm. The resulting fluorescence is resolved in time with a fast photo multiplier tube to investigate the occurrence of quenching or radiation trapping. At distances larger than 30 mm from the nozzle, a fluorescence decay time of (10 $\pm$ 0.5) ns is measured, indicating that there is a complete ℓ-mixing of the p=3 sub-levels. Close to the expansion source, where densities are highest, increased decay times are measured. A theoretical investigation using a Monte Carlo radiative transport calculation shows that this is likely due to radiative trapping of the resonant $p = 3 \rightarrow 1$ radiation.

8.1 Introduction

Fluorescence from laser induced two-photon excitation provides a powerful method to measure ground state densities of atoms or molecules with a large energy gap between ground and first excited state. The technique has found important applications in, among other things, combustion and low-temperature plasma research, and has been applied to a variety of species (Bokor *et al.*, 1981; Bischel *et al.*, 1981; Heaven *et al.*, 1982; Hansen *et al.*, 1987).

By measuring the fluorescence light emitted from the excited state, a signal proportional to the ground state density is obtained. If the decay of the excited level is purely governed by radiative processes, the proportionality constant is independent of plasma parameters and therefore needs to be calibrated only once. The most common exception to this condition is formed by (electron) collision induced transitions (quenching). These result in a shorter lifetime of the excited state and therefore a lower fluorescence signal. In order to use two-photon laser induced fluorescence (LIF) as a means to study ground state densities, it is necessary to not only calibrate the fluorescence signal, but also to ascertain the absence of quenching. In this work the term quenching is used for the overall collision-induced (thus radiation-less) decay of the excited-state population, including both downward and upward transitions (electron excitation).

In our group, two-photon LIF is used to investigate the density of H ground state atoms in an expanding cascaded arc argon/hydrogen plasma, by two-photon excitation of the hydrogen ground state to the $p = 3$ state at 205 nm (Bokor *et al.*, 1981). The excitation is monitored by detection of the resulting fluorescence on the Balmer-α transition at 656 nm. An overview of this scheme is given in figure 8.1.

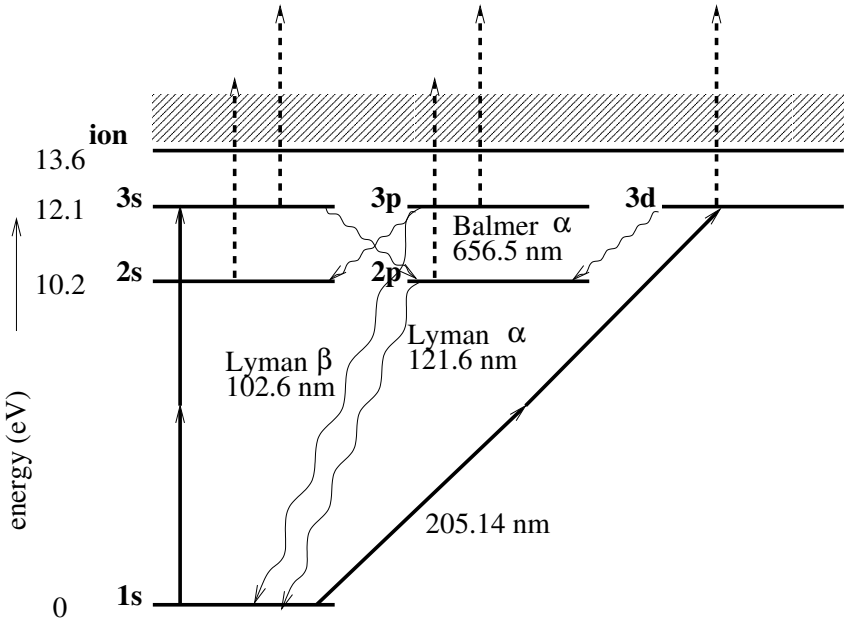

Figure 8.1: *Scheme of the hydrogen two-photon excitation (solid arrows) from $1s$ to $3s$ and $3d$. The laser photons are also capable of ionising excited H states (dashed arrows). The Balmer-α 656 nm fluorescence radiation is measured.*

This chapter will discuss an experimental investigation of the occurrence of quenching of the H $p = 3$ state in the expanding plasma by measuring the fluorescence radiation from the $3 \rightarrow 2$ transition as a function of time. However, as the results will show, an increase was found in the decay times, rather than a shortening due to quenching. This indicates that radiative trapping may be a significant effect. To investigate this further, the Monte Carlo radiative transfer model of chapter 7 is used. A complete quantitative calculation of the effects of radiative transfer in a LIF experiment requires a time-dependent model, which is beyond the scope of this sample application of the steady-state Monte Carlo radiative transfer code. However, it is instructive to qualitatively compare the result of the Monte Carlo code with the result of other approximations

that have been used to estimate the importance of radiative trapping in expanding plasmas.

The experimental method and setup are described in detail in a separate paper (Boogaarts *et al.*, 2002), therefore section 8.2 gives only a short summary of the setup. Since we measure short signals — decay times of perhaps 10 ns or less if there is quenching — special attention is given to the time-resolved diagnostics. In section 8.3 the experimental results are presented and discussed. In section 8.4 a theoretical density profile for the expanding hydrogen plasma is presented, and sections 8.5 and 8.6 are devoted to a radiative transport calculation using the Monte Carlo method of chapter 7 to investigate the effects radiation trapping. Finally, section 8.7 contains concluding remarks.

8.2 Experimental setup

The cascaded arc plasma source has been extensively discussed in the literature (van de Sanden *et al.*, 1992, 1995, 1996). In this work, the arc was operated at 40 A with 3 slm argon and 0.5 slm H_2 flow rates. The plasma expands from a nozzle into a roots-blower pumped vacuum vessel with a background pressure of 14 Pa. In the cascaded arc, the plasma is expected to burn on hydrogen whereas argon is mainly present as a buffer gas. Due to the high power density in the cascaded arc, it is expected that a considerable part of H_2 will be dissociated. The determination of the dissociation degree is one of the main goals of the plasma beam H ground state density measurements that are performed in our group (Boogaarts *et al.*, 2002; Mazouffre *et al.*, 2001; Mazouffre, 2001). The set up is constructed so that the measurements can be made at various positions in the plasma beam. The electron density n_e will drop substantially as the plasma moves away from the nozzle while the electron temperature T_e is expected to remain close to 0.3 eV.

A frequency doubled Nd:YAG laser (Spectra-Physics GCR230) is used to pump a tunable dye laser (Spectra-Physics PDL-3) producing 615 nm light at 50 Hz. Part of the dye laser light is frequency doubled in a KDP crystal and then mixed with the remaining 615 nm light in a BBO crystal to obtain a 205 nm linearly polarised laser beam. The average laser pulse energy is measured using a calibrated power meter at the beginning of the beam. Behind the plasma an uncalibrated UV sensitive SiC diode is placed in the beam to measure pulse energies on a shot by shot basis. The laser typically produces 0.5 mJ, 5 ns pulses of tunable 205 nm radiation with a spectral bandwidth of 0.2 cm^{-1}. The laser beam is focused into the plasma in a direction perpendicular to the expansion, as illustrated in figure 8.2. Two lenses are positioned so that light from the region where the laser beam is focused is imaged with a one-to-one ratio on a slit mask (width 0.4 mm) in a direction again perpendicular to both the laser beam and the expansion axis. The light then passes through a Balmer-α filter and enters the photomultiplier tube (PMT).

The Hamamatsu R5783P-01 photosensor module, which is based on the R5600P-01 'metal package' photomultiplier, has been used for all reported time-resolved measurements. The photomultiplier is very fast, has a gain of up to 10^6, and is guaranteed to be linear within 1% for signals that are up to 10 times stronger than those measured in this investigation.

Time integrated measurements are done by measuring the photomultiplier output using a LeCroy 612A charge integrator. Time-resolved measurements are done on a Hewlett Packard HP54111D digitising oscilloscope that is connected to the PMT anode with a 50 Ω coaxial cable. The oscilloscope samples at 1 GHz and has a bandwidth of 500 MHz. Figure 8.3 shows

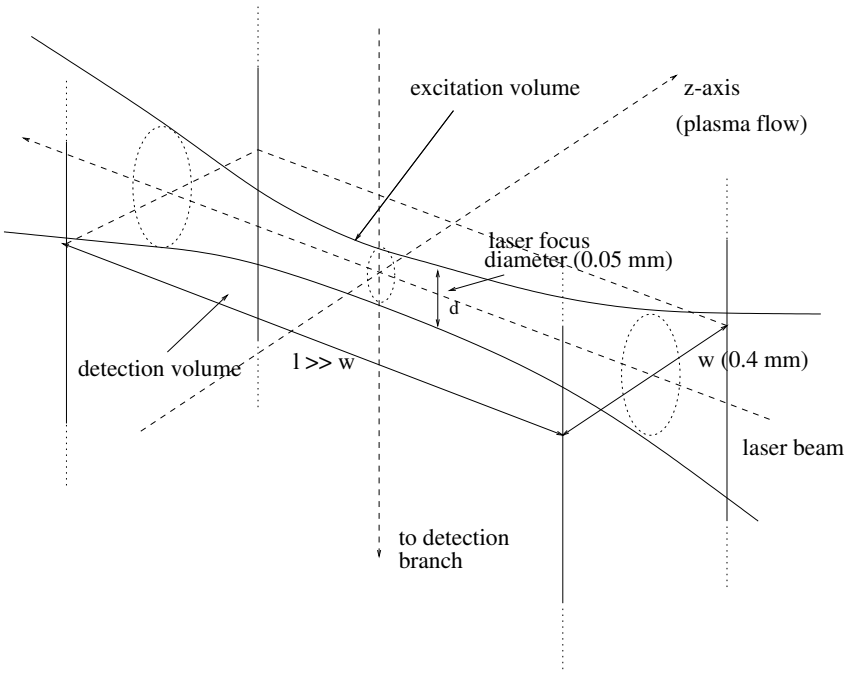

Figure 8.2: *Overview of the excitation and detection volumes. The plasma expands in the z direction. The relevant dimensions for the excitation and detection volumes are d (≈0.05 mm) and w (0.4 mm) respectively.*

the averaged single photon response of the photosensor module as measured with the oscilloscope. This data has been used to deconvolute the measured fluorescence decay data. The main peak has a full-with-at-half-maximum (FWHM) of about 1.5 ns, significantly shorter than the fluorescence decay time of 10 ns.

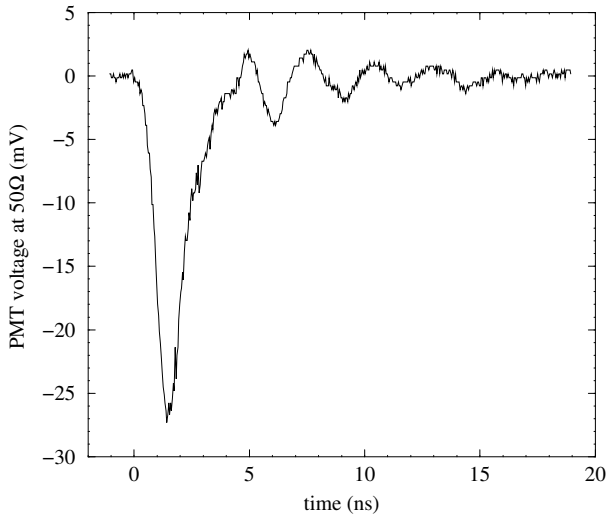

Figure 8.3: *Averaged single photon response of the R5783P-01 photosensor module.*

8.3 Experimental results and discussion

Even in the absence of quenching, it is not immediately obvious what the radiatively governed decay time of the H $p = 3$ state should be. Due to two-photon selection rules the laser can only create excited 3s and 3d sub-states. The actual fluorescence decay time now depends on the channels for de-excitation that are available to those sub-states. There are two general scenarios; (i) the sub-states remain isolated, in which case the 3s and 3d populations will decay with a natural lifetime of 150 ns and 15.5 ns respectively (see table 8.1 for a list of radiative transition frequencies and decay times), and (ii) there is a coupling between the 3s, 3p and 3d sub-states, so that these states will be mixed and populated according to their respective statistical weights, and the decay time will be the average radiative decay time of 10 ns. Note that in the calculation of the averaged decay time, it was assumed that the densities are sufficiently low to prevent trapping of resonant Lyman radiation in the detection volume.

Table 8.1: *Radiative transition frequencies and lifetimes for the $p = 3$ sub-levels and average value of all sub levels(Wiese* et al.*, 1969).*

Transition	A (10^8 s^{-1})	$\tau(10^{-9}$ s)
3s⟶2p	0.0631	158.5
3p⟶2s	0.2245	44.45
3p⟶1s	1.672	5.981
3d⟶2p	0.645	15.50
avg. 3⟶1,2	0.998	10.02

In figure 8.4 we present a typical deconvoluted observed H fluorescence signal. The measurement was done at 2 cm from the nozzle. After deconvolution, the decay time was obtained using an exponential fit resulting in a value of 10.3 ± 0.5 ns.

Figure 8.5 shows the result of a measurement of the fluorescence decay time at various positions along the expansion symmetry axis. The decay times were again obtained by computer fits to the deconvoluted time-resolved signals. The errors in the values are about 0.5 ns.

The fact that a decay time of 10 ns is found indicates that a fast mechanism exists that mixes the excited 3s, 3p and 3d states so that all $p = 3$ sub-states are populated according to statistical weights (scenario (ii)). One might argue that the natural decay time is in reality 15.5 ns (from the 3d→2p transition) and that the observed fluorescence is quenched to 10 ns, but this can be discounted since the same decay time has been found for a large range of ground state and electron densities. Close to the arc nozzle (positions 0–10 mm), the decay times seem to be slightly higher. This may be caused by resonant Lyman-β radiation trapping in the plasma region with relatively high H density ($\approx 10^{21}$ m^{-3}), which will be investigated in the following section. Otherwise all decay times are near 10 ns, so the measurements show no signs of quenching.

In the work Preppernau *et al.* (1995), H $p = 3$ lifetime measurements were performed, where hydrogen atoms were created by photo-dissociating C_2H_2. At low C_2H_2 pressures (≈ 10 mTorr) a lifetime of 15.7 ± 1.5 ns — corresponding to scenario (i) — was found using a computer fit, while at 150 mTorr the lifetime is close to 10 ns. The authors fit the experimental lifetime data with a model in which the collisional quenching effects are split up into a sub-level mixing rate

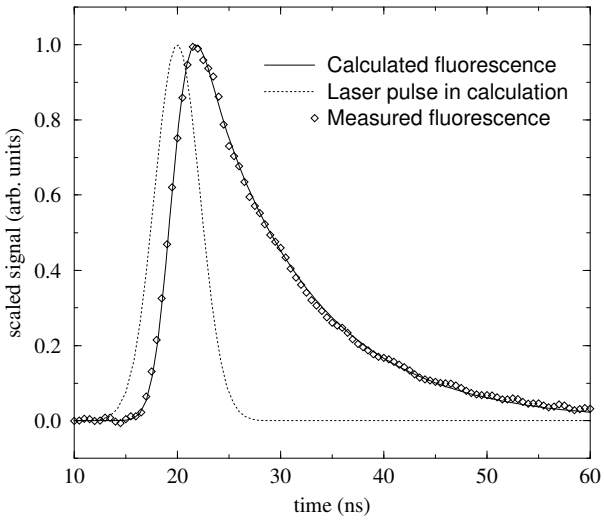

Figure 8.4: *Comparison of the modelled response (solid curve, see the original paper by van der Heijden* et al. *(2000) for a description of the model) with a deconvoluted measurement at $z = 2$ cm distance from the arc nozzle (diamonds). The Gaussian function with a peak at 20 ns represents the modelled laser intensity (arb. units). The decay time is 10 ns.*

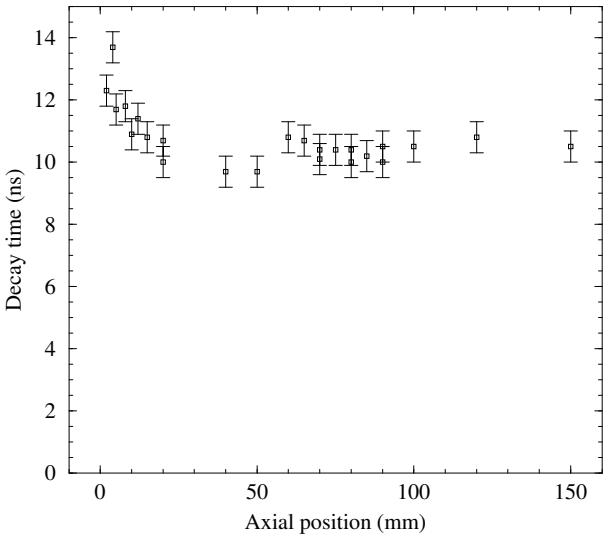

Figure 8.5: *Fitted decay times of the deconvoluted time-resolved fluorescence signals as a function of axial position.*

and a rate for collisional de-excitation of all $p = 3$ sub-levels. In our case, the sub-level mixing could be caused by unscreened electric fields that do not extend outside the Debye sphere or by the laser beam electric field, both of which are not considered in the model described by Preppernau *et al.* (1995). Other possible causes for increased mixing in our case could be the higher electron density and hydrogen-argon collisions.

8.4 Hydrogen density profiles

To a good approximation, the axial dependence of the hydrogen density can be described by a function of the form (see Mazouffre *et al.* (2001); Mazouffre (2001))

$$n(z) = n_H \frac{z_0^2}{(z + z_0)^2}, \tag{8.1}$$

where n_H is a normalising constant, to be determined later, z is the distance from the arc nozzle, and z_0 is the nozzle radius. For the current arc, with an opening angle of 45^o, Mazouffre (2001) reports $z_0 = 3.0 \pm 0.2$ mm. The expanding plasma can therefore be seen as originating from a point source that is located 3 mm inside the nozzle, as illustrated in figure 8.6.

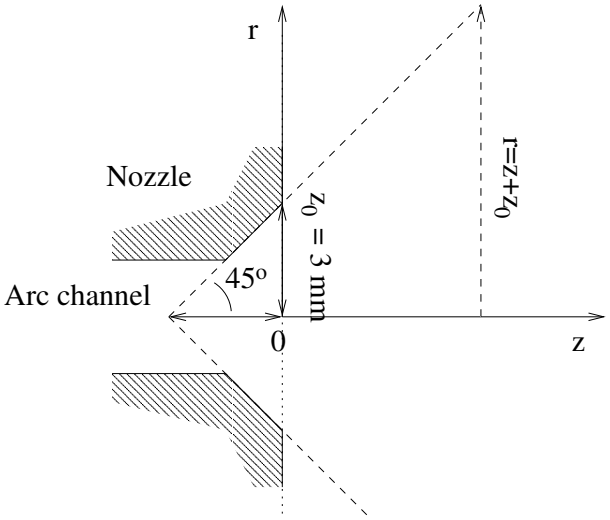

Figure 8.6: *Schematic drawing of the cascaded arc nozzle. The plasma flows in the direction of the z axis and expands radially at an angle of 45^o with the z axis. The radius of the plasma is therefore given by $r = z + z_0$.*

The radial dependence of n is approximated by a Gaussian distribution, with a $1/e$ value at $r = \alpha(z + z_0)$,

$$n(z, r) = n(z) \exp\left(-\left(\frac{r}{\alpha(z + z_0)}\right)^2\right), \tag{8.2}$$

where α is a dimensionless parameter that determines which part of the Gaussian distribution (8.2) falls within the body of the circular cone with a half-top angle of 45^o that represents the expanding plasma in figure 8.6. With $\alpha = 1$, the density at the radial boundaries at the cone is $1/e$ times the value at the axis, with still significant densities outside the conical expansion. For values of α smaller than unity the plasma is less spread out in the radial direction, and consequently a larger part of the Gaussian distribution is inside the cone with the 45^o half-top angle.

The normalisation constant n_H is related to the hydrogen flux Φ_H [s^{-1}][1]

$$\Phi_H(z) = v_z(z) \int_0^\infty 2\pi r n(z,r) dr, \tag{8.3}$$

where v_z is the axial velocity of the expanding plasma. Integrating equation (8.2) over r gives

$$\Phi_H(z) = n_H \alpha^2 z_0^2 v_z(z) \pi. \tag{8.4}$$

Rewriting this as an equation for n_H gives

$$n_H = \frac{\Phi_H}{\pi \alpha^2 z_0^2 v_z} = \frac{2\Phi_{H_2} D_{H_2}}{\pi \alpha^2 z_0^2 v_z}, \tag{8.5}$$

with Φ_{H_2} the known H_2 flux into the cascaded arc, and introducing D_{H_2} the dissociation degree of H_2 which is defined as (neglecting hydrogen ion densities)

$$D_{H_2} = \frac{[H]}{2[H_2] + [H]}. \tag{8.6}$$

Substituting (8.5) into (8.2) gives for the density profile $n(z,r)$,

$$n(z,r) = \frac{2\Phi_{H_2} D_{H_2}}{\pi (z+z_0)^2 v_z} \exp\left(- \left(\frac{r}{\alpha (z+z_0)} \right)^2 \right). \tag{8.7}$$

Measurements (Mazouffre, 2001, chap. 6) indicate that the axial velocity v_z close to the nozzle is approximately 4000 m/s, and that $n(0,0) = n_H \approx 2 \cdot 10^{21}$ m^{-3}. With $\Phi_{H_2} = 0.5$ slm ($= 2.24 \cdot 10^{20}$ H_2 particles per second), and rewriting (8.5) as

$$D_{H_2} = \frac{n_H \alpha^2 z_0^2 v_z \pi}{2\Phi_{H_2}}, \tag{8.8}$$

this gives for the dissociation degree $D_{H_2} \approx 0.5\alpha^2$. While the exact value of the dissociation degree is still a matter of debate, the value for $\alpha = 1$, which is based on a simple expansion density profile and experimentally obtained values for the axial hydrogen atom density n_H and velocity v_z close to the nozzle, is quite reasonable. It has been suggested that the dissociation degree might be still lower than 0.5 and closer to 0.1[2]. In the current model, this can be approximated by narrowing the expanding plasma radial FWHM, which in turn is done by reducing α. For example, a value of $\alpha = \sqrt{0.2} \approx 0.45$ describes a more narrow beam with 5 times less H atoms in it and thus a dissociation rate that is 5 times lower.

The density profile for $D_{H_2} = 0.5$, $\alpha = 1$, $v_z = 4000$ m/s and $\Phi_{H_2} = 0.5$ slm is plotted in figure 8.7 as a function of radius r and axial position z, up to 20 mm from the nozzle.

[1] In the equations here, fluxes are defined in particles per second. The link with flow rates in standard cc or litre per second or minute (sccs, sccm, slm) is 1 sccs = 10^{-6} $m^3 s^{-1}$ $\cdot 1.013 \cdot 10^5$ Pa / ($k \cdot 273$ K) = $2.69 \cdot 10^{19}$ particles/s, 1 sccm = 1/60 sccs, 1 slm = 1000/60 sccs.

[2] This is thought to be caused, at least partly, by a scattering in the outward radial direction of H atoms after collisions with the slower Ar atoms

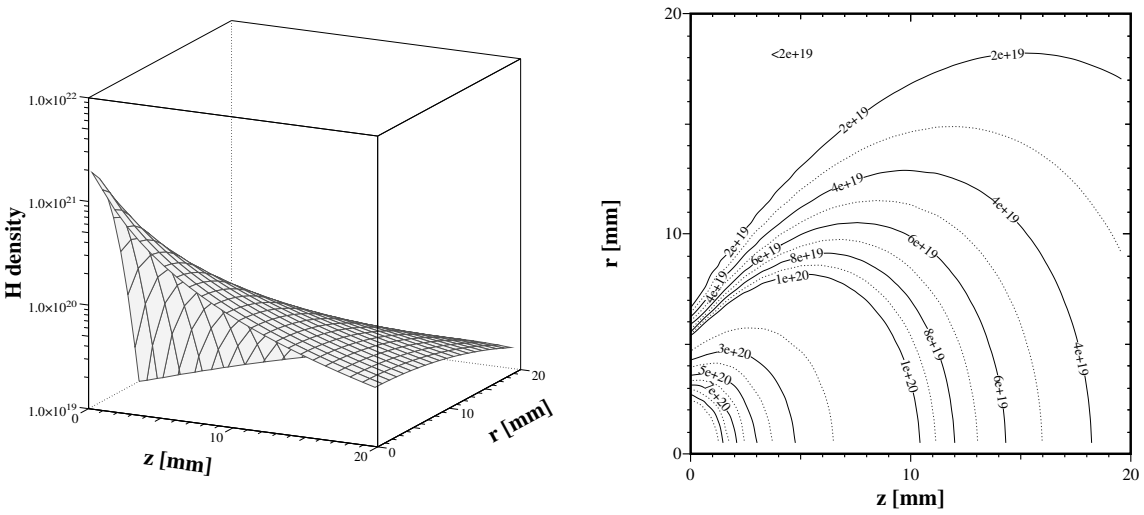

Figure 8.7: *Surface (left) and contour (right) plots of the hydrogen density profile for a H_2 flow rate of 0.5 slm, dissociation degree $D_{H_2} = 0.5$, radial profile parameter $\alpha = 1$, and a constant axial velocity of 4000 m/s.*

8.5 Radiation trapping calculations for an expanding plasma

In this section, the escape factor $\Lambda_{3\to1}$ will be calculated for a hydrogen plasma with a ground state density distribution given by equation (8.7). The calculations are done using the integrating Monte Carlo method of chapter 7 on a grid with 20 points in both the axial and the radial direction, using $2 \cdot 10^5$ trace lines. Such a calculation typically takes a few seconds on a current PC.

The excited state density is taken to be a fixed fraction of the ground state density. This is a departure from the actual situation in laser induced fluorescence experiments, since then only the part of the plasma that is caught in the laser beam is significantly excited. Although the Monte Carlo code allows arbitrary excited state distribution functions, this section does not attempt to describe a realistic LIF radiation problem. Instead, the focus of this section will be a qualitative investigation of radiative trapping effects by analysing the results of escape factor calculations for a plasma with a constant excited state density fraction, while the specifics of a LIF problem are postponed until the next section.

First the influence of the line profile ϕ_ν is investigated. In the expanding hydrogen plasma, the main broadening effect is Doppler broadening, which gives rise to a Gaussian profile $\phi_{\nu,D}$ with a FWHM that is proportional to the square root of the temperature (see eqns. (3.14) and (3.15)). The plasma heavy particle temperature drops from approximately 4000 K at the nozzle to 1000 K at 10 mm. Since the Doppler width is proportional to the square root of the temperature, this factor of 4 in temperature values results in a factor of 2 in widths. In the calculations, a constant value of 3000 K is used, which is a representative value for the "interesting" range $z \approx 0 \ldots 5$ mm where radiation trapping effects may occur.

Figure 8.8 shows the frequency dependent escape factor $\Lambda(\nu_0)$ as calculated by the Monte Carlo code for the density profile of figure 8.7, where ν_0 is the central frequency of the Doppler line profile at 3000 K. As is to be expected, close to the nozzle the radiation trapping is the most

severe (the escape factor is nearly zero) while further away, at lower hydrogen densities, the escape factor approaches unity again.

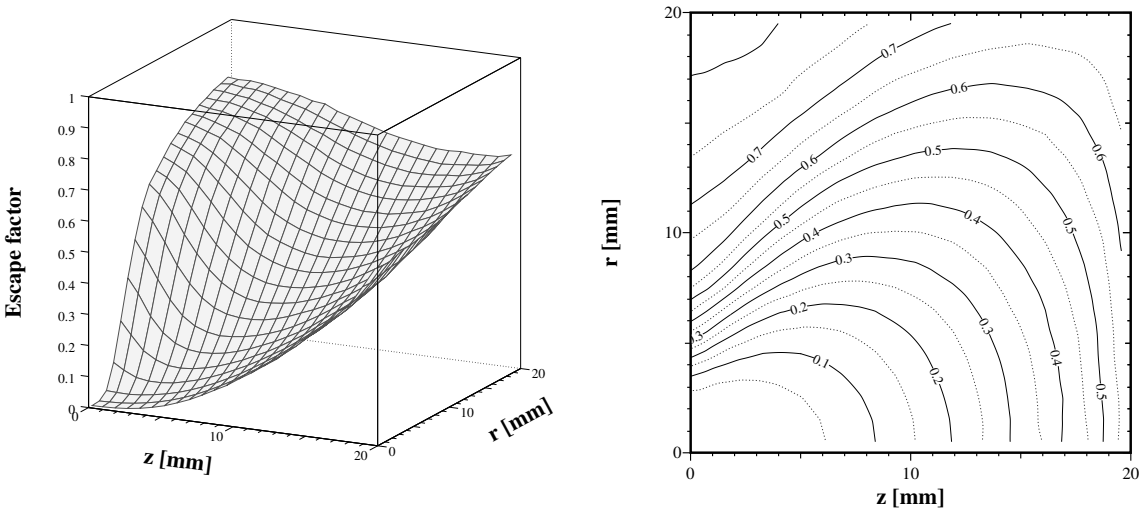

Figure 8.8: *Escape factor $\Lambda_{3\to1}(\nu)$ of the hydrogen $3 \to 1$ transition for $T = 3000$ K, at the centre of the Doppler emission profile, $\nu = \nu_0$. Compare this to the frequency-averaged escape factor in figure 8.9.*

The frequency-averaged escape factor $\Lambda_{3\to1}$, using Doppler broadened emission and absorption profiles $\phi_{\nu,D}$ (3.14) with a constant temperature of 3000 K is calculated from equation (3.35),

$$\Lambda_{3\to1} = \int_{\nu} \Lambda_{3\to1}(\nu)\phi_{\nu,D}d\nu, \tag{8.9}$$

and shown as function of z and r in figure 8.9. In this calculation, $\phi_{\nu,D}$ is discretised using 10 ν points, distributed over one half of the symmetrical profile. Comparing figures 8.8 and 8.9, it is clear that the escape factor $\Lambda(\nu_0)$ at the central line frequency is a good indicator of the frequency-averaged escape factor. On the z axis, the $3 \to 1$ transition is still almost completely trapped ($\Lambda \approx 0$), although the effect is somewhat less pronounced than in figure 8.8 since the radiation in the wings of the emission profile has a higher chance of avoiding re-absorption.

One may notice that even in regions where the hydrogen density is so low that the plasma is optically open, for example in the top-left ($z \approx 0$, $r \approx 20$ mm) corner of figure 8.8 or 8.9, the escape factor is significantly lower than unity. This apparent opacity is due to absorption of radiation generated in nearby parts of the plasma with a higher excited state density. Mathematically, this effect can be explained as follows. The escape factor is defined as

$$\Lambda(\nu) = 1 - \frac{\kappa J_\nu}{j_\nu}, \tag{8.10}$$

where κ and j_ν are locally determined while J_ν is determined non-locally. In the present case, the centre of the plasma generates so many photons that κJ_ν competes with the local emission j_ν so that $\Lambda(\nu)$ is significantly lower than 1.

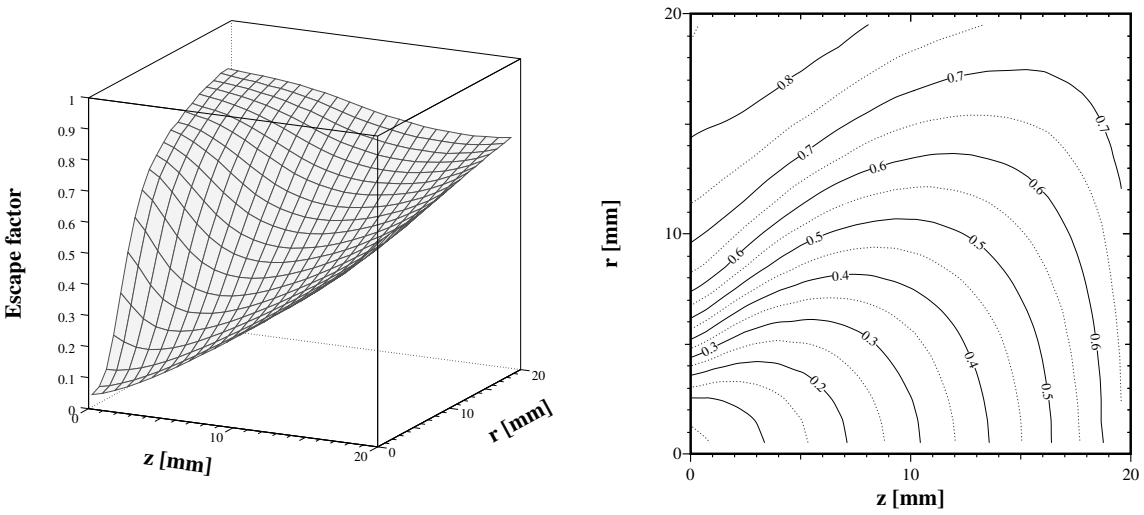

Figure 8.9: *Frequency averaged escape factor* $\Lambda_{3\rightarrow 1}$ *of the hydrogen* $3 \rightarrow 1$ *transition for* $T = 3000$ *K (using a Doppler line profile).*

As can be seen in figure 8.7, the density profile has a conical shape. However, in the past the effects of radiative trapping in expanding cascaded arc produced plasmas have been investigated using radiative transfer models for infinitely long cylinders (Buuron *et al.*, 1994). In such an approximation, for each z value of interest in the expanding plasma a radiative transfer calculation is done for an infinitely long cylinder with $j_\nu(r)$ and $\kappa(r)$ determined by $n(z, r)$.

A problem with this approximation is that in the infinitely long cylinder, radiation emitted in the direction of the z axis does not escape. For the expanding plasma, radiation emitted in the positive z direction travels through regions with increasingly lower densities, so that the escape factor is expected to be increased. The infinitely long cylinder approximation indeed gives a lower escape factor than the Monte Carlo calculation for a conical expanding plasma, as is shown in figure 8.10.

8.6 Radiation trapping calculations for laser-induced fluorescent radiation

From figure 8.9 it is clear that the effect of radiation trapping is present and that therefore, in the absence of other effects, a time-dependent LIF experiment will show increased decay times close to the arc nozzle. However, from the radiation trapping calculations in the previous section it is not possible to quantify this effect.

By using a uniform excitation profile (that is, the excited state density is a fixed fraction of the ground state density) the configuration remains axially symmetric. In reality, as figure 8.2 shows, this symmetry is removed if the laser beam is perpendicular to the z axis.

Moreover, in case of a strongly localised peak in the $j_\nu(\vec{r})$ spatial distribution, as might be induced by a laser beam, the escape factors in the vicinity (within a few times the typical distance $1/\kappa$) will be decreased due to the "artificially" increased J_ν value. The escape factors

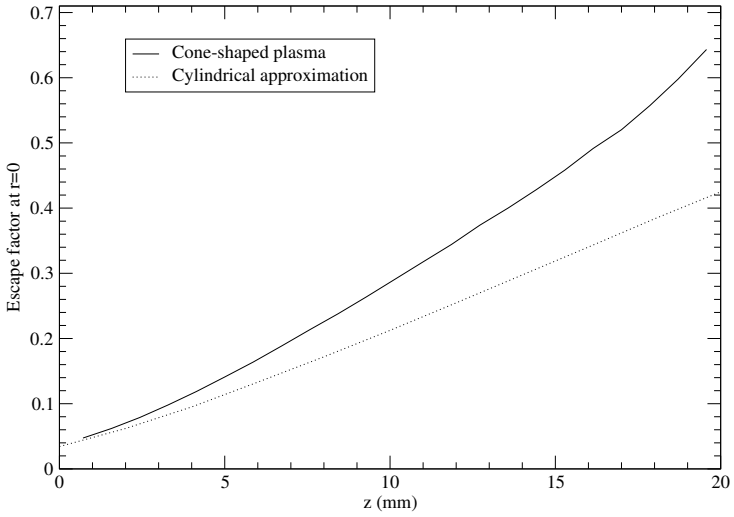

Figure 8.10: *Frequency averaged escape factors on the axis ($r = 0$) as a function of z for an expanding, cone-shaped plasma and for the infinitely long cylinder approximation. The infinitely long cylinder approximation results in lower escape factors and thus higher decay times.*

may even become negative, indicating that there are more absorption than emission processes.

In fact, in the first few nanoseconds of the laser induced excitation decay, the excitation region will broaden spatially because of this effect. At the centre of the excited region there will be a net decay of the excited state density, while in the neighbouring regions this density will go up. The effect is similar to the time-dependent problem of conductive heat transport in a solid body that is started with a non-uniform temperature distribution. However this is not the only effect at work; thermal motion will also quickly increase the initial excitation volume (van der Heijden *et al.*, 2000).

As figure 8.2 shows for a radial scan, the laser beam traverses the plasma in the radial direction at a constant value of z. It is also possible to direct the beam along the axis z itself. By measuring the shifts in the central transition frequencies, Mazouffre (2001) determined the velocity components v_r and v_z with radially and axially directed laser beams respectively. Both configurations are illustrated in figure 8.11. To avoid confusion with the z and r coordinates in the expanding plasma, axial and radial coordinates ζ and ρ are used for the laser beam. For the axially directed beam at the axis, $\zeta = z$ and $\rho = r$, while for the radial beams ζ is pointed in the direction of r and the ρ axis is parallel with the z axis.

Instead of doing a radiative transfer calculation for the whole 40 mm diameter and 20 mm length cylinder that contains the first 20 mm of the expanding plasma as in the previous section, now only the cylinders (see figure 8.11) that contain the part of the plasma near where the laser beam is located — and where the excited H atoms will be initially — will be considered.

First of all a choice must be made for the dimension of the excited state distribution. Since the emitting state density is caused by the laser excitation, the lower limit for this is the laser focal diameter of 0.05 mm. In the current calculations, the excited state density is taken to be a Gaussian distribution with FWHM $R_{exc} = 0.1$ mm. This value is chosen so that it is somewhat larger than the laser focal diameter (0.05 mm), in order to account for expansion effects as described above.

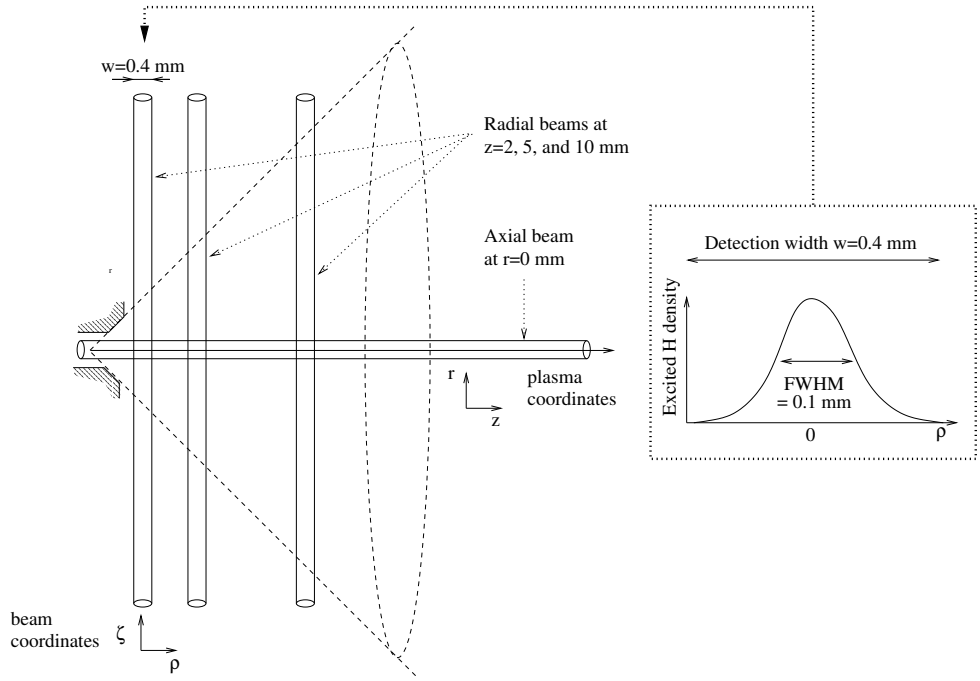

Figure 8.11: *Schematic overview of the expanding cone-shaped plasma, with three radially directed laser beams (at $z = 2$, 5 and 10 mm) and one axial laser beam (along the z axis). A laser beam, with internal coordinate system ζ (axial distance) and ρ (radius), excites a region of the plasma with a FWHM in the ρ direction of 0.1 mm. The radiation is measured in a detection window with width $w = 0.4$ mm (see also 8.2).*

The probability that a photon emerges from a particular point in the plasma is proportional to the emitting state density. A spatially averaged escape factor $\Lambda(\zeta)$ is thus given by

$$\Lambda(\zeta) = \frac{4 \ln 2}{\pi R_{exc}^2} \int_{-\infty}^{\infty} \Lambda(\zeta, \rho) \exp\left(- \ln 2 \left(\frac{\rho}{R_{exc}/2} \right)^2 \right) 2\pi\rho d\rho. \tag{8.11}$$

The radial escape factors (for the vertical laser beams in figure 8.11) are shown in figure 8.12. The axial escape factor (for the horizontal laser beam in figure 8.11) is shown as a function of z in figure 8.13, along with the $r = \zeta = 0$ values from the radial calculations for various values of z. There is no significant difference between the escape factors obtained from calculations with beams in the radial or axial directions.

8.7 Conclusion

The calculations in section 8.5 have shown that (a) there is significant radiation trapping in the first 20 mm of the expanding plasma and (b) there is "artificial" trapping in the outer parts of the plasma, in the lower density regions, due to absorption of radiation emitted from the dense centre. The latter effect, which causes a lowering of the escape factor, makes escape factor calculations using a uniform excited density fraction unsuitable for LIF problems, which are characterised by a strongly localised excited population. The difference can be seen by

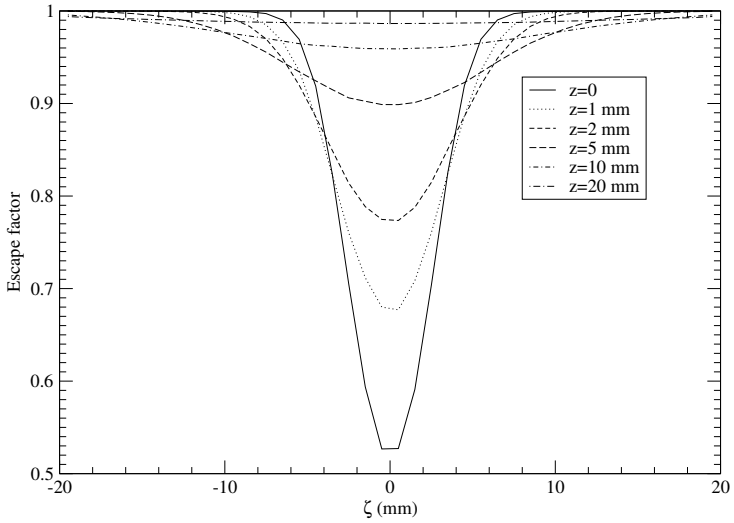

Figure 8.12: *Escape factors along radial laser beams as function of ζ at various axial positions z. The points where $\zeta = 0$ lie on the z axis ($r = 0$) in plasma coordinates. The calculated escape factors $\Lambda(\zeta, \rho)$ have been averaged over ρ using equation (8.11).*

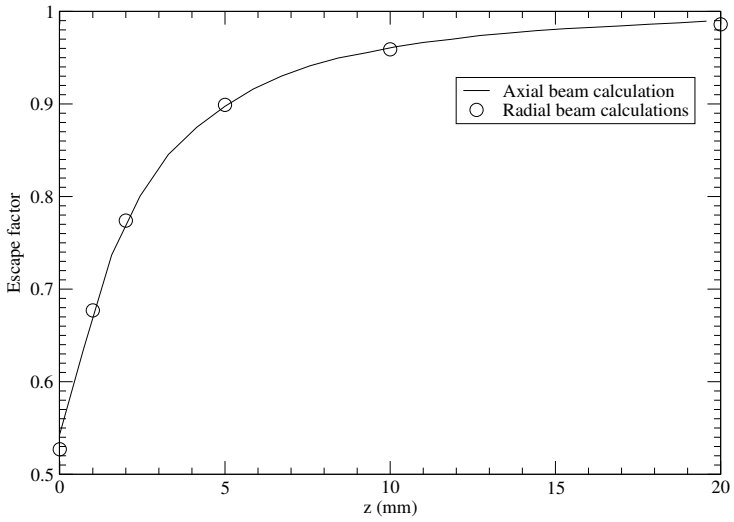

Figure 8.13: *Escape factors as function of $\zeta = z$ for the axial laser beam The calculated escape factors $\Lambda(\zeta, \rho)$ have been averaged over ρ using equation (8.11), and the points at $\zeta = 0$ from figure 8.12 have been added for comparison (circles).*

comparing the axial escape factors for the cone-shaped plasma profile in figure 8.10 with the axial escape factors in figure 8.13.

It was also found that using cylindrical approximations for the cone-shaped expanding plasma gives escape factors that are up to 30% too low (see figure 8.10).

In the radiation trapping calculations for laser-induced excited densities, no discernable difference was found between axially and radially applied beams. The decay time τ of the $p = 3$ density is related to the frequency and spatially averaged escape factor $\Lambda_{3\to1}$ in the

following manner,

$$\tau = \frac{1}{\frac{2}{18}A_{3s\to 2p} + \frac{6}{18}(A_{3p\to 2s} + \Lambda_{3\to 1}A_{3p\to 1s}) + \frac{10}{18}A_{3d\to 2p}} \approx \frac{10\text{ ns}}{0.44 + 0.56\cdot\Lambda_{3\to 1}}, \qquad (8.12)$$

using sublevel mixing scenario (ii) and the values from table 8.1. Figure 8.14 (left) shows τ as a function of $\Lambda_{3\to 1}$.

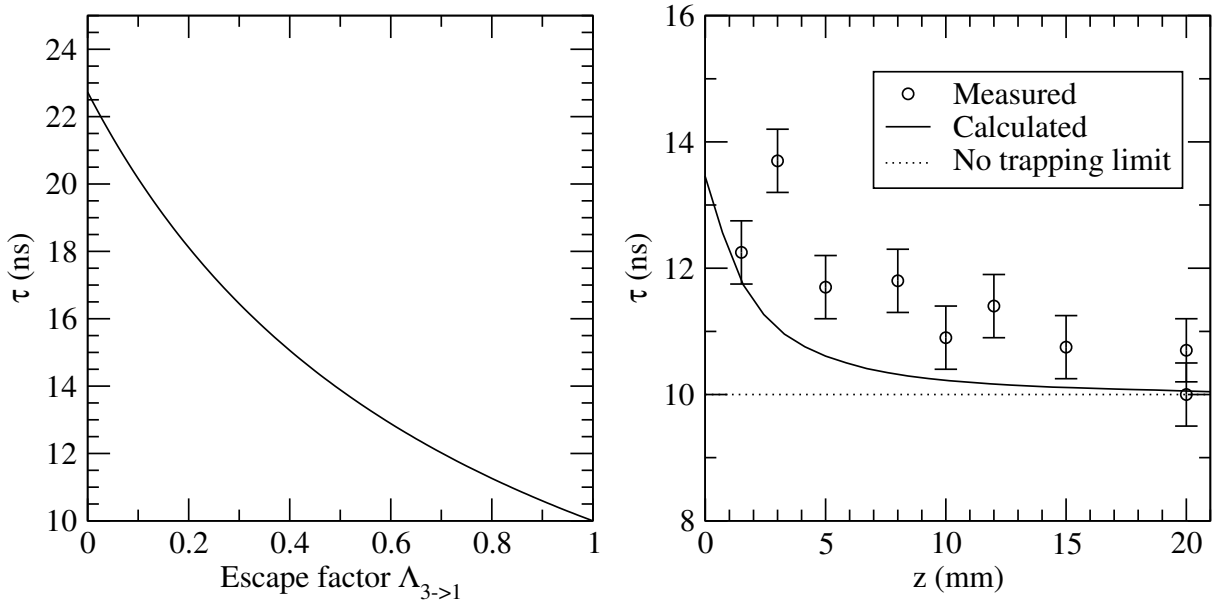

Figure 8.14: *Left: decay time τ as a function of escape factor $\Lambda_{3\to 1}$ (8.12). Right: Measured and calculated decay times as function of distance from the nozzle z. For the calculated decay times, the axial escape factors from figure 8.13 have been used.*

The reason for the discrepancy between the measured and the calculated decay times in figure 8.14 is that LIF problems are inherently time dependent, with the initially strongly localised excited density distribution being smeared out over an increasingly large volume. To modify the steady state Monte Carlo radiative transfer code developed in chapter 7 for time dependent problems would go beyond the scope of this sample application.

Chapter 9

General conclusion

The modular plasma simulation model PLASIMO has been extended for LTE density calculations using elemental diffusion equations (chapter 2), and a system of modules has been designed and implemented for doing radiative transfer calculations (chapter 3). Various radiation modules have been implemented for, and applied to, the sulfur lamp, including a module for molecular emission and absorption coefficients (chapter 4), and a general Ray-Trace Control Volume method for calculating the effects of radiation transport (chapters 5 and 6). This general transport method has been tested using analytical expressions and a Monte Carlo code, which were developed in chapter 7. Finally, the Monte Carlo code has been used in chapter 8, to investigate the possibility of radiation trapping in a Laser Induced Fluorescence experiment on an expanding hydrogen plasma produced by a cascaded arc source.

The most important conclusions are now presented per chapter:

- *Chapter 2: Particle densities in local thermal equilibrium.*
  For high pressure plasmas where the species are added to the mixture via localised "salt" reservoirs, a transport treatment is necessary to calculate the species densities. The elemental diffusion theory developed here has been implemented in PLASIMO and is applied to a Hg/Na/I mixture. It was found that the results differ strongly between calculations with and without bulk convective flow. As a follow-up study, it is of interest to further investigate the influence of the bulk velocity.

- *Chapter 3: Basic radiation theory and implementation.*
  The use of frequency sampling in PLASIMO means that the local and transport-sensitive parts of the radiation calculation are decoupled. This has tremendous benefits for a modular design. It also makes parallelisation of the computer code easier.

- *Chapter 4: Semiclassical and quantum-mechanical descriptions of S_2 molecular radiation.*
  The semiclassical theory is very elegant and, for high densities, very accurate. It can also save computation time, since semiclassical spectra are smooth and thus need not be sampled at extremely high resolutions (of the order of Doppler widths) like quantum-mechanical molecular radiation coefficients.

- *Chapter 5: Radiative transfer of a molecular S_2 B-X spectrum using semiclassical and quantum-mechanical radiation coefficients.*
  Optimising the QM calculation drastically improves calculation speeds with a limited

cost in precision. With a fixed temperature profile it is possible to calculate an emission spectrum for the sulfur lamp which agrees with experimental results as far as total emitted power is concerned. However, the calculation does not accurately reproduce the shape of the spectrum.

- *Chapter 6: General treatment of the interplay between fluid and radiative transport phenomena in symmetric plasmas: the sulfur lamp as a case study*.
  The Ray-Trace Control Volume (RTCV) radiative transfer method is efficient en designed for use in an existing control volume code such as PLASIMO. In the application to the sulfur lamp, it was found that even a self-consistent calculation using quantum-mechanical or classical molecular emission and absorption coefficients still can not completely reproduce the experimentally obtained S_2 spectrum. A non-LTE "experimental calculation" gives promising results.

- *Chapter 7: Validating the radiative transfer modules*.
  Analytical equations are developed for calculating the escape factor in spherical or cylindrical configurations with uniform emission and absorption coefficients. These equations may also find use in "quick-and-dirty" radiative trapping calculations. A simple Monte Carlo method is developed and implemented. It is found that integration based Monte Carlo methods are much more efficient than event based ones. The cost of using an integration method is that some of the effects, such as scattering, that can be accounted for in event based methods are lost. Even a Monte Carlo integration method is significantly slower than the RTCV method, since the RTCV method makes use of pre-determined sets of lines with known solid angle "weights", while the Monte Carlo method relies on sampling the weights by using random directions, which necessarily involves tracing more lines. However, the Monte Carlo method has the advantage of not being limited to a spherical or infinitely-long cylindrical configuration.

- *Chapter 8: Radiative transfer of laser-induced fluorescence in an expanding hydrogen plasma*.
  Monte Carlo calculations suggest that radiation trapping may be important and explain the increasing fluorescence decay times close to the cascaded arc nozzle. A comparison of escape factors calculated using a cone-shaped density profile (which resembles the expanding plasma) and an idealized infinitely long cylindrical profile (which has been used in the past since it simplifies the radiative transfer problem), shows that the latter calculation gives escape factor values that are too low.

Bibliography

vanden Abeele, D., 2000, *An Efficient Computational Model for Inductively Coupled Air Plasma Flows under Thermal and Chemical Non-Equilibrium*, Ph.D. thesis, Katholieke Universiteit Leuven.

Barrett, R., M. Berry, T. F. Chan, J. Demmel, J. Donato, J. Dongarra, V. Eijkhout, R. Pozo, C. Romine, and H. V. der Vorst, 1994, *Templates for the Solution of Linear Systems: Building Blocks for Iterative Methods, 2nd Edition* (SIAM, Philadelphia, PA).

Benoy, D., 1993, *Modelling of Thermal Argon Plasmas*, Ph.D. thesis, Eindhoven University of Technology.

Benoy, D., J. van der Mullen, B. van der Sijde, and D. Schram, 1991, J. Quant. Spectrosc. Radiat. Transfer **46**, 195.

Beulens, J., D. Milojevic, D. Schram, and P. Vallinga, 1991, Phys. Fluids B **3**, 2548.

Biberman, L., 1947, Zh. Eksp. Teor. Fiz. **17**, 416.

Biberman, L., 1949, Zh. Eksp. Teor. Fiz. **17**, 584.

Bischel, W., B. Perry, and D. Crosley, 1981, Chem. Phys. Lett. **82**, 85.

Bokor, J., R. Freeman, J. White, and R. Storz, 1981, Phys. Rev. A **24**, 612.

Boogaarts, M., S. Mazouffre, G.J.Brinkman, H. van der Heijden, P. Vankan, J. van der Mullen, D. Schram, and H. Döbele, 2002, Rev. Sci. Instrum. **73**, 73.

Brok, W., J. van Dijk, and J. van der Mullen, 2002, *Theory, Design and Implementation of the EPG Monte Carlo Code*, Technical Report, Group Elementary Processes in Discharges, Eindhoven University of Technology.

Buuron, A., D. Otorbaev, M. van de Sanden, and D. Schram, 1994, Phys. Rev. E **50**, 1383.

Chandrasekhar, S., 1943, Rev. Mod. Phys. **15**, 86.

Chandrasekhar, S., 1960, *Radiative Transfer* (Dover, New York).

van Dijk, J., 2001, *Modelling of Plasma Light Sources*, Ph.D. thesis, Eindhoven University of Technology.

van Dijk, J., A. Hartgers, J. Jonkers, and J. van der Mullen, 2001, J. Phys. D: Appl. Phys. **34**, 1499.

van Dijk, J., M. van der Velden, and J. van der Mullen, 2002, J. Phys. D: Appl. Phys. **35**, 2748.

Dolan, J., M. Ury, and W. Wood, 1992, *A novel high efficacy micro-wave powered light source*,

6th Int. Symp. on the Science and Technology of Light Sources, Budapest.

Dolan, J., M. Ury, and W. Wood, 1995, U.s. patent 5404076.

van Dongen, M., A. Körber, H. van der Heijden, J. Jonkers, R. Scholl, and J. van der Mullen, 1998, J. Phys. D: Appl. Phys. **31**, 3095.

Goedheer, W. J., 1978, *Models for a steady-state plasma in a gas blanket*, Ph.D. thesis, Utrecht University.

de Groot, J., and J. van Vliet, 1986, *The high-pressure sodium lamp* (Kluwer Technical Books, Deventer).

Hansen, S., G. Luckman, G. Nieman, and S. Colson, 1987, Appl. Phys. Lett. **51**, 898.

Hartgers, A., G. Janssen, and J. van der Mullen, 2002, J. Phys. D: Appl. Phys. (submitted) .

Hartgers, A., and J. van der Mullen, 2001, J. Phys. D. **34**, 1907.

Hashiguchi, S., K. Hatase, S. Mori, and K. Tachibana, 2001, *Time-dependent two-dimensional fluid model of a metal-halide lamp*, Proc. 9th Int. Symp. on Sci. & Technol. of Light Sources (Ithaca, USA).

Heaven, M., T. Miller, R. Freeman, J. White, and J. Bokor, 1982, Chem. Phys. Lett. **86**, 458.

Hedges, R., D. Drummond, and A. Gallagher, 1972, Phys. Rev. A **6**, 1519.

van der Heijden, H., J. Baier, A. Körber, and J. van der Mullen, 2002, J. Phys. B: At. Mol. Opt. Phys. **35**, 3633, *Chapter 5 of this thesis*.

van der Heijden, H., M. Boogaarts, S. Mazouffre, J. van der Mullen, and D. Schram, 2000, Phys. Rev. E **61**, 4402, *Partly in chapter 8 of this thesis*.

van der Heijden, H., and J. van der Mullen, 2001, J. Phys. B: At. Mol. Opt. Phys. **34**, 4183, *Chapter 4 of this thesis*.

van der Heijden, H., and J. van der Mullen, 2002, J. Phys. D: Appl. Phys. **35**, 2112, *Chapter 6 of this thesis*.

Herzberg, G., 1950, *Spectra of diatomic molecules* (Van Nostrand, Princeton, NJ).

Hirschfelder, J., C. Curtiss, and R. Bird (eds.), 1964, *Molecular Theory of Gases and Liquids* (Wiley & Sons, New York).

Holstein, T., 1947, Phys. Rev. **72**, 1212.

Holstein, T., 1951, Phys. Rev. **83**, 1159.

Holt, E., and R. Haskell (eds.), 1965, *Foundations of Plasma Dynamics* (The Macmillan Company, New York).

House, L., and L. Avery, 1969, J. Quant. Spectrosc. Radiat. Transfer **9**, 1579.

Jablonński, A., 1945, Phys. Rev. **68**, 76.

Janssen, G., 2000, *Design of a general plasma simulation model*, Ph.D. thesis, Eindhoven University of Technology.

Janssen, G., J. van Dijk, D. Benoy, M. Tas, K. Burm, W. Goedheer, J. van der Mullen, and

D. Schram, 1999, Plasma Sources Sci. Technol. **8**, 1.

Jhung, K., I. Kim, K. Oh, and K. Hahn, 1990, Phys. Rev. A **42**, 6497.

Johnston, C., 1999, The sulphur lamp - design of a numerical model, SAI Report, Eindhoven University of Technology, ISBN 90-5282-942-X.

Johnston, C., 2003, *(title to be announced)*, Ph.D. thesis, Eindhoven University of Technology.

Johnston, C., H. van der Heijden, G. Janssen, J. van Dijk, and J. van der Mullen, 2002, J. Phys. D: Appl. Phys. **35**, 342.

de Jong, H., 2001, *Accelerated Monte Carlo simulation for scatter correction in SPECT*, Ph.D. thesis, Utrecht University.

Jonkers, J., 1998, *Excitation and Transport in Small Scale Plasmas*, Ph.D. thesis, Eindhoven University of Technology.

Jonkers, J., M. Bakker, and J. van der Mullen, 1997, J. Phys. D: Appl. Phys. **30**, 1928.

Kielkoff, J., J. Davis, and J. Gwinn, 1970, J. Chem. Phys. **53**, 2605.

Klots, C., and V. Anderson, 1972, J. Chem. Phys. **56**, 120.

Körber, A., 1998, *Modelling the spectrum of a S_2 high pressure discharge*, 8th Int. Symp. on the Science and Technology of Light Sources, Greifswald.

Körber, A., 1999, *The physics of light emission from sulphur lamps*, Master Class on Hot Topics in Plasma Physics and Technology Socrates CLTPP-4, Eindhoven.

Kuznetsova, L., E. Pasyuk, and A. Stolyarov, 1991, Mass Spectrom. Rev. **10**, 91.

Kuznetsova, L., E. Pasyuk, and A. Stolyarov, 1993, Russian J. Phys. Chem **67**, 2046.

Lam, L., and A. Gallagher, 1977, J. Chem. Phys. **66**, 3350.

Matsumoto, M., and T. Nishimura, 1988, ACM Trans. on Modeling and Computer Simulation **8**(1), 3.

Mazouffre, S., 2001, *Transport Phenomena in Plasma Expansions Containing Hydrogen: A Laser Spectroscopic Study*, Ph.D. thesis, Eindhoven University of Technology.

Mazouffre, S., M. Boogaarts, I. Bakker, P. Vankan, R. Engeln, and D. Schram, 2001, Phys. Rev. E **64**, 016411.

Message Passing Interface Forum, 1994, The International Journal of Supercomputer Applications and High Performance Computing **8**.

Message Passing Interface Forum, 1995, Mpi: A message-passing interface standard (version 1.1), Technical report, URL `http://www.mpi-forum.org`.

Meyer, C., and H. Nienhuis, 1988, *Discharge Lamps* (Kluwer Technical Books, Deventer).

Molisch, A. F., and B. P. Oehry, 1998, *Radiation Trapping in Atomic Vapours* (Oxford University Press, Oxford).

van der Mullen, J., D. Benoy, J. van Dijk, K. Garloff, A. Hartgers, H. van der Heijden, G. Janssen, C. Johnston, and M. Tas, 2002, *The Plasma Simulation Model Plasimo* (Eindhoven University of Technology), URL `http://plasimo.phys.tue.nl`.

Patankar, S. (ed.), 1980, *Numerical Heat Transfer and Fluid Flow* (New York: McGraw-Hill).

Payne, M., , J. Talmage, G. Hurst, and E. Wagner, 1974, Phys. Rev. A **9**, 1050.

Payne, M., and J. Cook, 1970, Phys. Rev. A **2**, 1238.

Pradhan, A., and H. Partridge, 1991, Chem. Phys. Lett. **255**, 163.

Preppernau, B., K. Pearce, A. Tserepi, E. Wurzberg, and T. Miller, 1995, Chem. Phys. **196**, 371.

Proud, J., and L. Luessen (eds.), 1986, *Radiative Processes in Discharge Plasma* (Plenum, New York).

Quick, C., and J. R.E. Weston, 1981, J. Chem. Phys. **74**, 4951.

Rutten, R., 2000, *Radiative Transfer in Stellar Atmospheres* (lecture notes Utrecht University), 7th edition, URL `http://www.astro.uu.nl/~rutten/`.

Rybicki, G., and A. Lightman, 1979, *Radiative Processes in Astrophysics* (Wiley-Interscience, New York).

van de Sanden, M., J. de Regt, G. Janssen, J. van der Mullen, D. Schram, and B. van der Sijde, 1992, Rev. Sci. Instrum. **63**, 3369.

van de Sanden, M., R. Severens, J. Gielen, R. Paffen, and D. Schram, 1996, Plasma Sources Sci. Technol. **5**, 268.

van de Sanden, M., R. Severens, R. Meulenbroeks, M. de Graaf, Z. Qing, D. Otorbaev, R. Engeln, J. Gielen, J. van der Mullen, and D. Schram, 1995, Surface and Coatings Technology **74-75**, 1.

Sando, K., and J. Wormhoudt, 1973, Phys. Rev. A **7**, 1889.

Steinfeld, J., 1986, *Molecules and Radiation* (MIT Press, Cambridge, MA).

Szudy, J., and W. Baylis, 1975, J. Quant. Spectrosc. Radiat. Transfer **15**, 669.

van Trigt, C., 1976a, Phys. Rev. A **13**, 726.

van Trigt, C., 1976b, Phys. Rev. A **13**, 734.

Turner, B., M. Ury, Y. Leng, and W. Love, 1997, J. Illuminating Engng Soc. , Winter, 10.

Waymouth, J., 1971, *Electric Discharge Lamps* (M.I.T. Press, Cambridge).

Wiese, W., M. Smith, and B. Miles, 1969, *Atomic Transition Probabilities* (National Bureau Standards, Washington D.C.).

Software references

Motivation

In a letter dated 5 February 1676, Sir Isaac Newton wrote to his colleague Robert Hooke, "If I have seen further it is by standing on the shoulders of giants." Before one is able to climb onto the shoulders of giants, these giants have to be visible and accessible, hence the need for a publicly available library of scientific literature.

However, in software it still is a revolutionary idea to make not only the binary machine instructions of a program available, but the underlying source code as well. Binary machine instructions are next to useless for a human interested in understanding or extending a computer program. The software industry was and is dominated by corporations that sell computer-readable, but not human-readable programs (often for a limited period of time or otherwise strongly restricted) and keep the source code of the programs a closely guarded secret. However, in recent years open source software (OSS) has emerged as a viable alternative to proprietary software. As the name implies, open source programs are distributed including source code, usually free of charge and with a license that permits the user to read and change the program. This openness allows peer-review of the correctness of the program, much like in modern science, and empowers users to change the programs to suit their needs.

Only freely available open source software has been used for this research and in the writing of this thesis. The references for the packages used are listed in the following section.

References

The principal operating system used in the development of PLASIMO and the creation of this thesis consists of the Linux[1] kernel, originally written by Linus Torvalds, and the unix-like GNU system from the GNU project[2].

This thesis was created using the following open source programs:

- The author's favourite editor is Bram Moolenaar's improved vi clone, vim[3], which is used in both creating the computer source code and writing the thesis.
- The thesis is typeset in LaTeX[4] which is based on Donald E. Knuth's TeX[5] typesetting language. LaTeX was first developed in 1985 by Leslie Lamport, and is now being maintained

[1] http://www.kernel.org
[2] http://www.gnu.org
[3] http://www.vim.org
[4] http://www.latex-project.org
[5] http://www.tug.org

and developed by the LaTeX3 Project.

- Printable and viewable content is made by converting the TeX dvi file to PostScript using dvips(k) by Radical Eye Software. The PostScript content is converted to PDF using GNU Ghostscript[6].
- The illustrations are made with xfig[7], which was originally written by Supoj Sutanthavibul.
- Most of the 2D plots in this thesis are created using Grace[8], currently maintained by Evgeny Stambulchik. The surface and contour plots of 3D data are mostly made with Kenny K. H. Toh's plotmtv[9]. The venerable gnuplot[10] is also used on occasion.
- The background for the cover of the thesis was created using the GNU Image Manipulation Program (GIMP)[11] by Peter Mattis, Spencer Kimball, and many others.

The following open source software projects are important tools in the development of PLASIMO and other model codes used in this thesis:

- PLASIMO is written in C++ and the principal compiler is the C++ compiler from the GNU Compiler Collection (gcc)[12], which was originally written by Richard M. Stallman.
- A significant body of code is written in the scripting language Python[13] by Guido van Rossum and others. Python, extended with the fast, compact, multidimensional array language facility Numeric[14], has been used for the calculation of quantum-mechanical radiation coefficients and as a front end for the Monte Carlo engine (which is written in C++ for efficiency).
- The PLASIMO code utilises the C++ template library TBCI[15] which implements basic data structures like complex numbers, dynamic vectors, static vectors, different types of matrices like full matrices, band matrices, sparse matrices, etc. The TBCI project is led by Kurt Garloff.
- The graphical user interface (GUI) of PLASIMO uses the cross platform GUI library wxWindows[16] by Julian Smart, Robert Roebling, Vadim Zeitlin, Robin Dunn, et al. The use of wxWindows allows the compilation of the same PLASIMO source code for Linux (or other Unix-like operating systems) and Microsoft Windows.
- Dimitri van Heesch's doxygen[17] is used to generate developer's documentation of the PLASIMO source code.

[6] http://www.ghostscript.com
[7] http://www.xfig.org
[8] http://plasma-gate.weizmann.ac.il/Grace/
[9] ftp://ftp.x.org/contrib/applications/
[10] http://www.gnuplot.info
[11] http://www.gimp.org
[12] http://gcc.gnu.org
[13] http://www.python.org
[14] http://www.pfdubois.com/numpy/
[15] http://plasimo.phys.tue.nl/TBCI/
[16] http://www.wxwindows.org
[17] http://www.doxygen.org

Summary

For a good understanding of the properties of plasmas it is of great importance to treat the generation and transport of radiation. Especially for light sources this is vital, because an efficient lamp converts a significant percentage of its input energy into radiated light, which makes radiation losses a dominant term in the energy balance. Due to the complexity of the problem of radiative transfer, often approximate methods are used, such as treating radiation as a local loss term only. However, the continuing increase of computing power enables researchers to add fully non-local radiation descriptions to plasma models.

The first subject is the calculation of particle densities in plasmas in local thermal equilibrium (LTE). The subject matter is split into a local part, where the main parameters are pressure and temperature, and a non-local, transport-sensitive part. The latter is of importance in plasmas like metal halide lamps, where the densities of some species are determined by transport effects around "salt reservoirs" at a so-called cold-spot temperature.

The bulk of this thesis describes the design and application of a modular radiation generation and transport model. It has been designed to be linked with a control volume fluid model that describes other aspects of the plasma, such as chemistry, diffusion, and convection. The basis of the radiation transport code is a ray-tracing method which connects control volumes via probe lines along which radiation energy is transported. The fluid part of the model generates the local values that are needed by the radiation generation part to calculate the local emission and absorption coefficients. The radiative transfer part then calculates how these local coefficients cause exchange of energy (in an LTE description) or particle state densities (in a non-LTE description) within the plasma and feeds the results back to the fluid code. The non-local, coupled problem of radiative transfer and fluid interaction is a demanding one and great care has been taken to optimise the methods and algorithms, especially with regard to making optimal use of available symmetry in the plasma configuration.

Current lighting research focuses on molecules in high pressure (close to) LTE plasmas. Molecular spectra can span the full visible range of wavelengths, which makes these molecules attractive for use in light sources. A substantial part of this thesis is devoted to the description of molecular radiation generation and transport. The standard quantum-mechanical method for molecular radiation generation is compared to a semiclassical treatment, which, due to its relative simplicity, can significantly reduce computational requirements. The application of the linked radiation and fluid descriptions to a high pressure sulfur lamp shows that radiative transfer has a strong influence on the lamp's energy balance.

Finally the developed radiative transfer techniques are applied to a plasma that is not a light source; an argon/hydrogen cascaded arc plasma. The time dependence of the fluorescence light emission of atomic hydrogen in an expanding plasma beam after pulsed excitation with a nanosecond laser is studied, both experimentally and computationally. Ground state H atoms in

an expanding Ar/H cascaded arc plasma are excited to the $p = 3$ level using two-photon laser excitation. The resulting fluorescence is resolved in time with a fast photo multiplier tube and, under certain circumstances, increased decay times are found. A theoretical investigation using a Monte Carlo radiative transport calculation indicates that the observed increase is probably due to radiative trapping of the resonant $p = 3 \rightarrow 1$ transition.

Samenvatting

Voor een goed begrip van de eigenschappen van een plasma is het van groot belang om stralingsgeneratie en -transport te beschrijven. In het bijzonder is dit van belang voor lichtbronnen aangezien een efficiënte lamp een significant deel van de aangeleverde energie converteert naar licht. Gezien de complexiteit van het stralingstransportprobleem worden er echter vaak benaderende methodes gebruikt, zoals bijvoorbeeld het behandelen van straling als puur lokale verliesterm. Echter het toenemende rekenvermogen van computers stelt onderzoekers meer en meer in staat om volledige niet-lokale stralingstransport beschrijvingen te koppelen aan plasma modellen.

Het eerste onderwerp is de berekening van deeltjesdichtheden in plasma's in lokaal thermisch evenwicht (LTE). Het onderwerp is gesplitst in een lokaal gedeelte, waar de hoofdparameters de druk en temperatuur zijn, en een niet-lokaal, transport-gevoelig deel. Het laatste is van belang in plasma's zoals metaal halogenidelampen, waar de dichtheden van enkele deeltjessoorten afhankelijk zijn van transporteffecten rond "zout reservoirs" met een zogenaamde *cold-spot* temperatuur.

Het grootste deel van dit proefschrift beschrijft het ontwerp en de toepassing van een modulair stralingsgeneratie en -transport model. Het is ontworpen om gekoppeld te worden aan een controle volume vloeistofmodel dat andere eigenschappen van het plasma zoals chemie, diffusie en convectie beschrijft. De basis van de stralingstransport code is een *ray-tracing* methode die controle volumes via *probe* lijnen, waarlangs stralingsenergie wordt getransporteerd, met elkaar verbindt. Het vloeistof gedeelte van het model genereert de waarden waarmee het stralingsgeneratie deel de lokale emissie- en absorptiecoëfficiënten uitrekent. Het stralingstransport deel berekent dan hoe deze lokale coëfficiënten transport van energie (in een LTE beschrijving) of deeltjes (in een non-LTE beschrijving) binnen het plasma veroorzaken en voert de resultaten terug naar de vloeistof code. Het niet-lokale, gekoppelde probleem van stralingstransport en vloeistof interactie is aanzienlijk. Daarom is veel zorg besteed aan het optimaliseren van de methodes en algoritmes, met name met betrekking tot het optimaal gebruik maken van de beschikbare symmetrie in de plasmaconfiguratie.

Huidig lichtbronnen onderzoek spitst zich toe op moleculen in hogedruk (dichtbij) LTE plasma's. Moleculaire spectra kunnen het volledige zichtbare spectrum omvatten, waardoor deze moleculen geschikt zijn voor gebruik in lichtbronnen. Een aanzienlijk deel van dit proefschrift is gewijd aan de beschrijving van moleculaire stralingsgeneratie en -transport. De standaard quantum-mechanische methode voor moleculaire stralingsgeneratie wordt vergeleken met een semiklassieke theorie die, door de relatieve eenvoud, aanzienlijk minder rekenkracht vergt. De toepassing van de gekoppelde stralings- en vloeistofbeschrijvingen op een hogedruk zwavellamp laat zien dat stralingstransport een grote invloed heeft op de energiebalans van de lamp.

Tot besluit worden de ontwikkelde stralingstransport technieken toegepast op een plasma dat geen lichtbron is: een argon/waterstof cascadeboog plasma. De tijdsafhankelijkheid van de fluorescente lichtemissie van atomair waterstof in een expanderende plasma straal, na gepulste excitatie met een nanoseconde laser, wordt zowel experimenteel als theoretisch bestudeerd. Grondtoestand H atomen in een expanderend Ar/H cascadeboog plasma worden ge-exciteerd naar het $p = 3$ niveau met twee-foton laser excitatie. De resulterende fluorescentie wordt met behulp van een snelle *photo multiplier tube* als functie van de tijd gemeten, waarbij onder bepaalde omstandigheden toegenomen vervaltijden gevonden worden. Een theoretisch onderzoek met een Monte Carlo stralingstransportberekening geeft aan dat deze toename waarschijnlijk veroorzaakt wordt door stralingsinvangst van de resonante $p = 3 \rightarrow 1$ overgang.

Acknowledgements

This thesis is the result of five years of research in plasmas and plasma modelling, performed in the group Equilibrium and Transport in Plasmas and sponsored by the Dutch Technology Foundation STW as project ETN.3892.

I owe many thanks to my project leader and co-promotor Joost van der Mullen, for valuable lessons about physics, modelling, and getting things done. I'm also grateful for his non-stop flow of encouragements and suggestions (and, at times, curses) that helped to keep the project going.

Thanks also go to the group leader and my first promotor, Daan Schram, for useful discussions about plasma physics and his many corrections and suggestions for the thesis text.

It was a pleasure to work with Jeroen Jonkers in the initial stages of the project, and with Colin Johnston on what became known as "the sulfur project". I would also like to thank Achim Körber at Philips Aachen and Marco Haverlag at Philips Eindhoven for many useful discussions on plasma light sources.

Last but not least I want to thank the other members of the modelling team, past and present, Jan van Dijk, Kurt Garloff, Bart Hartgers, and Ger Janssen, for their help during the course of this project.

Harm van der Heijden, November 2002.

About the author

Harm van der Heijden was born in Helmond on March 23 1973 and grew up in the village of Panningen. From 1991 he studied physics at the Eindhoven University of Technology until he graduated cum laude in 1997. From 1997 to 2002 he worked as a Ph.D. student at the Eindhoven University of Technology in the group Equilibrium and Transport in Plasmas.